

## Waves and Turbulence in Core-Annular Pipe Flow

Li, H.

**DOI**

[10.4233/uuid:afabf9e1-a8f3-4fcd-a3b7-6000d8f71766](https://doi.org/10.4233/uuid:afabf9e1-a8f3-4fcd-a3b7-6000d8f71766)

**Publication date**

2023

**Document Version**

Final published version

**Citation (APA)**

Li, H. (2023). *Waves and Turbulence in Core-Annular Pipe Flow*. [Dissertation (TU Delft), Delft University of Technology]. <https://doi.org/10.4233/uuid:afabf9e1-a8f3-4fcd-a3b7-6000d8f71766>

**Important note**

To cite this publication, please use the final published version (if applicable).  
Please check the document version above.

**Copyright**

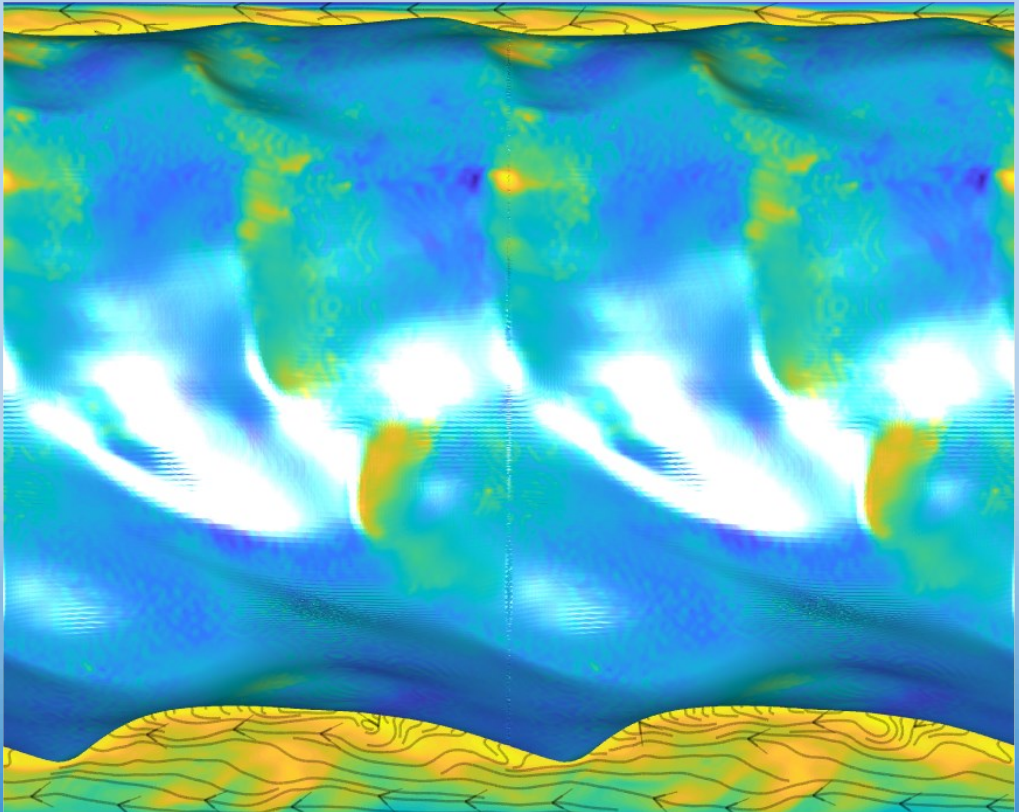
Other than for strictly personal use, it is not permitted to download, forward or distribute the text or part of it, without the consent of the author(s) and/or copyright holder(s), unless the work is under an open content license such as Creative Commons.

**Takedown policy**

Please contact us and provide details if you believe this document breaches copyrights.  
We will remove access to the work immediately and investigate your claim.

# ***Waves and Turbulence in Core-Annular Pipe Flow***

**Haoyu Li**



# **Waves and Turbulence in Core-Annular Pipe Flow**

## **Dissertation**

for the purpose of obtaining the degree of doctor  
at Delft University of Technology,  
by the authority of the Rector Magnificus Prof. dr. ir. T.H.J.J. van der Hagen,  
chair of the Board for Doctorates,  
to be defended publicly on  
Thursday, 14 December 2023, at 15:00 o'clock  
by

**Haoyu LI**

Master of Science in Fluid Mechanics,  
Shanghai Jiao Tong University, China  
born in Luohe, China

This dissertation has been approved by the promotor.

Composition of the doctoral committee:

Rector Magnificus,	chairperson
Prof. dr. ir. R.A.W.M. Henkes	Delft University of Technology, promotor
Dr. ir. M.J.B.M. Pourquié	Delft University of Technology, copromotor

Independent members:

Prof. dr. P. Poesio	Università degli Studi di Brescia, Italy
Prof. dr. R.M. van der Meer	University of Twente
Prof. dr. ir. N.G. Deen	Eindhoven University of Technology
Prof. dr. S. Kenjereš	Delft University of Technology
Prof. dr. ir. W.S.J. Uijttewaal	Delft University of Technology

Prof. dr. ir. G. Ooms has contributed greatly to the preparation of this dissertation.

Keywords: Liquid-liquid flow, multiphase flow, pipe flow

Copyright © 2023 by Haoyu Li

ISBN 978-94-6384-519-9

An electronic version of this dissertation is available at

<http://repository.tudelft.nl/>.



知行合一

*Unity of Knowledge and Action*

Yangming Wang (1508)



# Table of Contents

Summary .....	xi
Samenvatting .....	xiii
<b>1</b> Introduction.....	15
1.1 Background .....	16
1.2 Flow description.....	17
1.2.1 Flow pattern map.....	17
1.2.2 Pressure drop and holdup ratio .....	19
1.2.3 Levitation mechanism for horizontal pipe.....	21
1.2.4 Interfacial waves .....	22
1.2.5 CFD simulations .....	24
1.3 About this thesis .....	24
References .....	26
<b>2</b> 1D/2D/3D RANS for CAF.....	29
2.1 Introduction.....	30
2.2 Experimental and numerical method .....	32
2.2.1 Lab experiments .....	32
2.2.2 Governing equations .....	33
2.2.3 Numerical method.....	34
2.2.4 Considered base conditions .....	35
2.2.5 Key parameters.....	36
2.2.6 Verification of the simulations .....	36
2.3 1D results.....	39
2.4 2D results.....	40
2.5 3D Results .....	42
2.5.1 Simulation set-up .....	42
2.5.2 Turbulence characteristics .....	43
2.5.3 Levitation mechanism .....	44
2.5.4 Interfacial waves .....	47
2.6 Comparison of simulations with experiments .....	49
2.7 Conclusions .....	52
References .....	54
<b>3</b> Friction factors for CAF .....	57
3.1 Introduction.....	58
3.2 Modelling approach.....	59
3.2.1 Governing equations .....	59
3.2.2 Numerical method.....	60
3.2.3 Basic simulation set-up .....	61
3.2.4 Key parameters.....	61
3.2.5 Force balance .....	62
3.2.6 Mechanistic models.....	63
3.3 Pressure drop in various experiments .....	65
3.4 Effect of pipe section length.....	67
3.5 Two-phase versus single-phase results .....	68
3.6 Concentric single-phase results.....	72
3.7 Eccentric single-phase results .....	76
3.8 Comparison with experiments and DNS.....	78

3.9	Conclusions .....	81
	References .....	83
<b>4</b>	Interfacial wave growth .....	85
4.1	Introduction.....	86
4.2	Modelling approach.....	87
4.2.1	Governing equations .....	87
4.2.2	Numerical method.....	88
4.2.3	Parameters .....	90
4.3	Wave stability curves.....	90
4.3.1	Vertical laminar-laminar core-annular flow.....	90
4.3.2	Laminar-turbulent core-annular flow.....	92
4.4	Wave growth behaviour .....	95
4.4.1	Energy budget for the linear instability .....	95
4.4.2	Flow pattern during unstable stage .....	97
4.4.3	Comparison with experiment.....	100
4.4.4	Fully developed waves .....	103
4.5	Conclusions .....	106
	References .....	107
<b>5</b>	Vertical CAF.....	109
5.1	Introduction.....	110
5.2	Modelling approach.....	111
5.2.1	Governing equations .....	111
5.2.2	Numerical method.....	111
5.2.3	Key parameters.....	113
5.2.4	Basic simulation set-up .....	113
5.2.5	Force balance .....	114
5.3	RANS results .....	115
5.3.1	Water-only pipe flow.....	115
5.3.2	Two-phase flow .....	116
5.4	Comparison of RANS results with experiments and DNS .....	120
5.4.1	Fanning friction factor.....	121
5.4.2	Holdup ratio .....	121
5.4.3	Water annulus .....	122
5.4.4	Stresses.....	124
5.5	Conclusions .....	126
	References .....	128
<b>6</b>	RANS/LES/DNS for CAF .....	131
6.1	Introduction.....	132
6.2	Method .....	133
6.2.1	Governing equations .....	133
6.2.2	Numerical method.....	134
6.2.3	Considered base conditions .....	135
6.2.4	Key parameters.....	135
6.2.5	Averaging.....	136
6.3	RANS and DNS for single phase pipe flow .....	137
6.3.1	DNS at $Re_D=5300$ .....	137
6.3.2	Comparison between DNS/ RANS for single phase pipe flow .....	139
6.4	RANS and DNS for annulus flow with fixed wavy interface ...	141

6.4.1	Geometry and mesh .....	141
6.4.2	Averaged flow .....	142
6.5	RANS and DNS for two-phase CAF without gravity .....	144
6.6	RANS, DNS, and experiments for two-phase horizontal CAF with gravity .....	146
6.7	Conclusions .....	150
	References .....	152
<b>7</b>	Conclusions and recommendations .....	155
7.1	Conclusions .....	156
7.2	Recommendations .....	158
	Appendix .....	161
	A. ....	161
	Flow envelope .....	161
A.1	Introduction .....	162
A.2	Governing equation and numerical method .....	162
A.2.1.	Governing Equations .....	162
A.2.2.	Numerical method .....	162
A.2.2.1.	Interface capturing method .....	162
A.2.2.2.	Simulation set-up and mesh verification .....	164
A.3	Results .....	166
A.3.1.	Comparison of numerical, modelling and experimental results .....	166
A.3.2.	3D single-phase RANS simulation .....	170
A.3.3.	Comparison of DNS/RANS .....	172
A.4	conclusions .....	173
	References .....	174
	Acknowledgements .....	177
	Curriculum Vitae .....	179
	List of publications .....	181



# Summary

When a very viscous liquid (like oil) and a far less viscous liquid (like water) both flow through a pipeline, under certain conditions, the more viscous liquid will migrate to the core of the pipe, while being surrounded by an annulus with the less viscous liquid. This typical flow pattern, referred to as core-annular flow (CAF), was discovered a few decades ago and has drawn much attention from researchers. The less viscous liquid functions as a lubrication layer to reduce the pressure drop, which thus requires far less energy to transport a certain amount of viscous liquid than when the annulus flow is absent. Often oil is used for the laminar core flow and water is used for the laminar or turbulent annulus flow. The main research question in this PhD thesis is how the turbulence in the annulus and the waves at the interface determine the key hydraulic parameters that characterize the core-annular flow. Thereto, a large number of Computational Fluid Dynamics (CFD) simulations were carried out. These are mainly 1D, 2D, and 3D RANS simulations (Reynolds-Averaged Navier Stokes, with the Launder & Sharma low-Reynolds number  $k - \epsilon$  model)), but also some DNS were carried out (Direct Numerical Simulations). The simulation results are also compared with experiments carried out in the Delft lab.

Four crucial hydraulic quantities are involved in the core-annular flow study, namely: pressure drop, hold up ratio, watercut, and total flow rate. The pressure drop can be non-dimensioned to a Fanning friction factor. From the Fanning friction factor, the lubrication strength of CAF is shown, since the value of the Fanning friction factor is comparable to water only pipe flow under the same mixture-based Reynolds number. The holdup ratio indicates the apparent slip effect between the oil and water; its value is between 1 and 2, because water somewhat accumulates in the core-annular flow. In both the numerical simulations and lab experiment, two parameters are set as input and two parameters appear as output. Understanding the correlation between the four parameters can help to properly design the pipe flow system. The study of the correlation between these four parameters will be presented in Chapter 3 and in the Appendix.

The effect of gravity on the CAF depends on the inclination of the pipe. For horizontal pipe flow, gravity acts perpendicular to the pipe wall and introduces a buoyancy force on the oil core. Our simulation starts with concentric oil-water CAF with a flat interface. This flow configuration is unstable for a horizontal pipe and will finally develop into an eccentric oil core with a wavy interface. The waves create a downward force to balance the buoyancy force. Due to the movement of the oil core, a secondary flow will appear in the water layer. From our simulation results, we found how the inertia effect redistributes the pressure on the interface, creating a net downward pressure force that balances the buoyancy force, and prevents the oil core to touch the upper pipe wall. This part will be illustrated in Chapters 2 and 3. For the vertical pipe, gravity acts in the streamwise direction. Detailed DNS simulations were presented by Kim & Choi (2018). In Chapter 5, we repeat the work of Kim & Choi by using RANS, and find a rather good agreement for the Fanning friction factor and holdup ratio between RANS and DNS. Different is that the waves in the RANS simulations are more regular and that RANS predicts higher turbulence than DNS.

To study the effect of interface waves on the core-annular flow, single-phase simulations for the turbulent water annulus flow are performed. We define a wavy oil interface and impose it as a solid inner wall, based on the assumption that the highly viscous oil core is traveling with little deformation. This approach allows for rather fast and accurate simulations with easy parameter variation, since the shape of the solid oil core interface can be imposed artificially. In Chapter 3, we study the influence of the wave length, wave amplitude, and oil core eccentricity on two important parameters: the pressure drop (or Fanning friction factor) and the holdup ratio. We found how the presence of waves with a larger amplitude increased the form stress on the oil core, which makes the pressure drop higher

than for the condition with a flat interface. We also found that the Fanning friction factor for sufficiently large wave amplitude is close to the water only pipe flow.

In the unstable stage, the growth of the interfacial waves is caused by the linear/non-linear instability of the oil-water interface. There are many analytical studies on laminar-laminar interface instability. In Chapter 4, we studied the wave growth in laminar-turbulent conditions (i.e. laminar core and turbulent annulus). We disturbed the initial wave and tracked the linear and non-linear growth of waves. By using periodic boundary conditions, we are able to vary the wave length, and obtained the wave growth rate as a function of the wave length. By studying the energy budget, we found the wave for laminar-turbulent core-annular flow is initiated by the inertia term, which is different from the laminar-laminar core-annular flow, where the viscous term is the major source of instability. Compared to laminar-laminar CAF, the inertia term in laminar-turbulent CAF also causes much higher disturbance energy, for which waves grow much easier and the fully saturated wave amplitude is larger.

Chapter 6 shows that, like for single phase pipe flow, also for CAF the RANS prediction for the turbulent kinetic energy is smaller than the DNS prediction. The Reynolds stress profile in RANS is close to the DNS prediction. There is close agreement between the averaged velocity and turbulence profiles obtained in the two-phase (core-annulus) and the single-phase (annulus) approaches. The Fanning friction factor in the DNS and RANS simulations is about 30% higher than the value measured in the Delft lab in the horizontal pipe. The experimental flow is much more concentric than the DNS and RANS predictions, though DNS is more concentric (and thus closer to the experiment) than RANS. The cause for the differences between simulations and experiments is not clear yet. It might be due to the still relatively low turbulence level in the water annulus, giving transitional flow rather than fully developed turbulent flow. The higher Fanning friction factor in the experiments than in the simulations can be due to a higher turbulence level in the experiment, which in turn can influence the core position.



# Samenvatting

Wanneer er zowel een visceuze vloeistof (zoals olie) als een minder visceuze vloeistof (zoals water) door een pijpleiding stromen, zal onder bepaalde omstandigheden de meer visceuze vloeistof naar de kern van de pijp migreren, terwijl het wordt omringd door een ring met de minder visceuze vloeistof. Dit typische stromingspatroon, dat aangeduid wordt als kern-ringstroming, werd enkele decennia geleden ontdekt en heeft veel aandacht getrokken van onderzoekers. De minder visceuze vloeistof fungeert als smeerlaag om de drukval te verminderen, wat dus veel minder energie vergt om een bepaalde hoeveelheid visceuze vloeistof te transporteren dan wanneer de smeerlaag ontbreekt. Vaak wordt olie gebruikt voor de laminaire kernstroming en water voor de laminaire of turbulente ringstroming. De voornaamste onderzoeksvraag van dit proefschrift is hoe de turbulentie in de ringstroming en de golven op het grensvlak de hydraulische parameters bepalen die de kern-ringstroming beschrijven. Daartoe is een groot aantal Computational Fluid Dynamics (CFD) berekeningen uitgevoerd. Dit zijn voornamelijk 1D, 2D, en 3D RANS berekeningen (Reynolds-Averaged Navier Stokes, met het Launder & Sharma lage-Reynolds getal  $k - \epsilon$  model), maar er zijn ook Direkte Numerieke Simulaties (DNS) uitgevoerd. De rekenresultaten worden ook vergeleken met experimenten uitgevoerd in het laboratorium in Delft.

Vier cruciale hydraulische parameters zijn betrokken bij de kern-ringstromingsstudie, namelijk: drukval, ophopingsverhouding, waterbijdrage, en totale stromingsdoorzet. De drukval kan dimensieloos worden weergegeven als de Fanning wrijvingsfactor. Via deze wrijvingsfactor wordt het smeringseffect van de ringstroming duidelijk, aangezien de waarde vergelijkbaar is met enkel waterstroming in de pijp, bij dezelfde waarde van het gemengde Reynoldsgetal. De ophopingsverhouding geeft de schijnbare slip tussen olie en water weer; de waarde ligt tussen 1 en 2, omdat water zich enigszins ophoopt in een kern-ringstroming. In zowel de numerieke simulaties als het laboratoriumexperiment worden twee parameters ingesteld als invoerwaarde en twee parameters volgen dan als uitvoerwaarde. Het begrijpen van de correlatie tussen de vier parameters kan helpen om het leidingstroomstelsel correct te ontwerpen. Het onderzoek naar de correlatie van deze vier parameters wordt gepresenteerd in Hoofdstuk 3 en in de bijlage.

Het effect van de zwaartekracht op de kern-ringstroming hangt af van de hoekoriëntatie van de pijp. Bij horizontale pijpstrooming werkt de zwaartekracht loodrecht op de pijpwand en introduceert dit een opwaartse kracht op de oliekern. Onze simulatie begint met concentrische olie-water kern-ringstroming met een vlak grensvlak. Deze stromingsconfiguratie is onstabiel voor een horizontale pijp en zal zich uiteindelijk ontwikkelen tot een excentrische oliekern met een golvend grensvlak. De golven creëren een neerwaartse kracht om de opwaartse kracht te compenseren. Door de beweging van de oliekern ontstaat er een secundaire stroming in de waterlaag. Uit onze studie wordt gevonden dat het traagheidseffect de druk op het golvende grensvlak herverdeelt, waardoor een netto neerwaartse drukkracht ontstaat die de drijfkracht in evenwicht houdt, waarbij wordt voorkomen dat de oliekern de bovenkant van de pijpwand raakt. Dit deel wordt geïllustreerd in Hoofdstukken 2 en 3. Voor de verticale buis werkt de zwaartekracht in stromingsrichting. Gedetailleerde DNS zijn gepresenteerd door Kim & Choi (2018). In Hoofdstuk 5 herhalen we het werk van Kim & Choi door het uitvoeren van RANS simulaties, en er wordt een goede overeenkomst gevonden tussen DNS en RANS voor de Fanning wrijvingsfactor en voor de ophopingsverhouding. Een verschil is dat de golven in de RANS aanpak regelmatig zijn en dat RANS meer turbulentie geeft dan DNS.

Om de effecten van de grensvlaktgolven op de kern-ringstroming te bestuderen, worden enkelfasige simulaties voor de turbulente water ringstroming uitgevoerd. We definiëren een golvend olie grensvlak en leggen deze op als een vaste binnenwand, gebaseerd op de aanname dat de zeer viskeuze oliekern voortbeweegt met weinig vervorming. Deze aanpak maakt het mogelijk om relatief snel heel

nauwkeurige simulaties uit te voeren met een gemakkelijke parametervariatie, aangezien de vorm van het vaste grensvlak met de oliekern kunstmatig kan worden opgelegd. In Hoofdstuk 3 bestuderen we de invloed van de golflengte, golfamplitude en excentriciteit van de oliekern op twee belangrijke parameters: de drukval (of de Fanning wrijvingsfactor) en de ophopingsverhouding. We vinden dat de aanwezigheid van golven met een zekere amplitude de vormweerstand op de oliekern verhoogt, waardoor de drukval hoger is dan de toestand met een vlak grensvlak. We vinden ook dat de Fanning wrijvingsfactor bij voldoende grote golfamplitude dicht ligt bij de waarde waarbij alleen water door de pijp stroomt.

In de onstabiele fase wordt de groei van de grensvlaktgolven veroorzaakt door de lineaire/niet-lineaire instabiliteit van het olie-water grensvlak. Er zijn veel analytische studies uitgevoerd voor de laminaire-laminaire instabiliteit van het grensvlak. In Hoofdstuk 4 hebben we de golfgroei bij laminaire-turbulente condities bestudeerd (dus met een laminaire kernstroming en een turbulente kernstroming). We verstoorde de initiële golf en volgden de lineaire en niet-lineaire groei van golven. Door periodieke randvoorwaarden te gebruiken kunnen we de golflengte variëren en de golfgroeisnelheid verkrijgen als een functie van de golflengte. Door het energiebudget te beschouwen, vinden we dat de golf voor laminaire-turbulente kern-ringstroming wordt geïnitieerd door de traagheidsterm, hetgeen verschilt van de laminaire-laminaire kern-ringstroming, waarbij de visceuze term de belangrijkste bron van instabiliteit is. In vergelijking tot laminaire-laminaire kern-ringstroming, zorgt de traagheidsterm bij laminaire-turbulente kern-ringstroming ook voor een hogere storingsenergie, waarbij golven makkelijker groeien en een hogere eindamplitude van de golven wordt bereikt.

Hoofdstuk 6 laat zien dat de RANS voorspelling van de turbulente kinetische energie bij kern-ringstroming, net zoals bij enkelfasige pijpstrooming, lager is dan de DNS waarde. Het profiel van de Reynoldsspanning met RANS ligt dicht bij de DNS vorm. Er is een goede overeenstemming tussen de gemiddelde snelheids- en turbulentieprofielen zoals verkregen in de aanpak met enerzijds twee fasen (kern en ring) en anderzijds een enkele fase (voor de ring). De Fanning wrijvingsfactor in de DNS en RANS simulaties is ongeveer 30% hoger dan de waarde gemeten in de horizontale pijp in het laboratorium in Delft. De experimentele strooming is veel concentrischer dan de DNS en RANS voorspellingen, hoewel DNS concentrischer is (en dus dichter bij het experiment ligt) dan RANS. De oorzaak voor de verschillen tussen simulaties en experimenten is nog niet duidelijk. Het kan te wijten zijn aan het nog steeds relatief lage turbulentieniveau in de waterlaag, waardoor een laminaire/turbulente overgangsstrooming ontstaat in plaats van volledig ontwikkelde turbulente strooming. De hogere Fanning wrijvingsfactor in de experimenten dan in de simulaties kan te wijten zijn aan een hoger turbulentieniveau in het experiment, wat op zijn beurt een effect kan hebben op de positie van de kern.

# 1

## Introduction

## 1.1 Background

Pipelines are widely used in the industry, in the built environment, and at home for the transport of fluids and solid particles. This can be under single phase or under multiphase flow conditions, and under laminar or under turbulent flow conditions. Although the “pipe” is a simple configuration, the flow through it can be complex, particularly when considering turbulent, multiphase flow. The present thesis is devoted to the latter: considered is the multiphase flow of two liquids with a large difference in viscosity and a moderate difference in density, in which the less viscous liquid is turbulent, though a horizontal or a vertical pipe.

Since decades the petroleum industry has been using pipeline systems for the transport of gas, condensate/oil, and water through pipeline systems. This can be for transport from the reservoir to the central processing facilities, but also for transport between different processing units at a refinery or chemical plants. There is an increasing concern in society for the environmental impact of the production and use of fossil fuels. As part of this, research programmes are in place to develop technologies that can manage the CO<sub>2</sub> that is related to processes of production and use of hydrocarbon products. For example, Carbon Capture Use and Storage (CCUS) will be part of measures required to realize a Net Zero Emissions world in the near future (by 2050). Most likely oil products from fossil fuels will be part of that future, not primarily as energy source through combustion, but as a resource for chemical products.

When transporting very viscous crude oil, also referred to as “heavy oil”, the pressure drop along the pipeline can become very large, requiring a large pump capacity. A heavy crude typically has a viscosity that is a factor 100 to 10000 higher than the viscosity of water, which makes the transportation very energy intense. There are several ways to mitigate this problem such as heating the oil, adding hydrocarbon diluent, or mixing the crude oil with a lighter oil. These methods are all meant to reduce the viscosity, but they come with a significant cost. An alternative way to reduce the transport power is to make use of a specific two-phase flow pattern known as Core-Annular Flow (CAF), as shown in Figure 1.1. In the CAF flow pattern, the more viscous liquid (e.g. oil) is located in the centre of the pipe, while the less viscous fluid (e.g. water) will form an annulus layer in between the pipe wall and the viscous core. The low-viscous annulus serves as a lubrication layer. When using the core-annular flow pattern for viscous oil transport, the pressure drop will be comparable to what is found at the same volumetric flow rate of only water would be transported through the pipe.

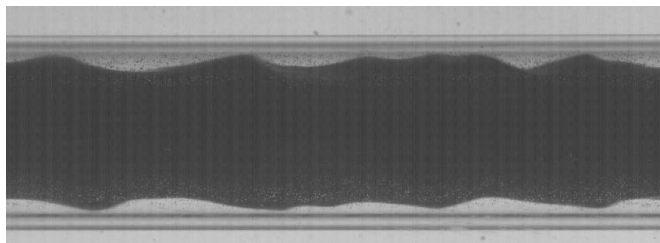


**Figure 1.1. Core-Annular Flow (CAF) captured using a high-speed camera for the experiment at Delft University of Technology, as carried out as part of the present research (pipe wall and water annulus are transparent, oil is black). Pipe diameter 2.1 cm, total flow rate is 0.43 L/s, watercut is 20%.**

The idea of using core-annular flow to transport highly viscous oil was first described by Clark and Shapiro (1949). They added an 8% to 15% volumetric flow rate of water, and the transportation of viscous petroleum was found to be greatly facilitated. They also added a surface-active agent and phosphate to mitigate the problem that the oil and water form a water-in-oil emulsion. Later, Clifton &

Handley (1958) proposed to introduce only 1% of water into the pipeline system and remove the water before the stream enters the pump, to prevent emulsification. In the past decades, there were various successful industrial experiences with CAF for oil transportation, as reviewed by Joseph et al. (1997). An example is CAF in the 38.6 kilometre long Shell pipeline near Bakersfield, California which has been in operation for 12 years.

## 1.2 Flow description

For the industrial application of CAF, it is important to know under what conditions the CAF flow pattern will be maintained, i.e. without having oil fouling of the pipe wall or transition to other flow patterns. Besides, since the main advantage of the CAF flow pattern is its low pressure drop, it is also interesting to know how the pressure drop reduction correlates with the flow throughput. The flow pattern consists of two regions: the viscous oil core which stays laminar, and the water annulus which can be either laminar or turbulent. Core-annular flow has very interesting flow physics, such as the levitation mechanism for horizontal pipe flow, the interface wave growth mechanism, and the interaction between the turbulent water layer and the laminar oil core.

Over the past decades, many research studies have been undertaken for core-annular flow. The literature was focused on various aspects of such flow, which are discussed below.

### 1.2.1 Flow pattern map

In the two-phase oil-water pipeline system, multiple flow patterns are possible (see Figure 1.2). The flow patterns can be categorized into two main types. One is well-separated flow, including core-annular flow, stratified flow, or slug flow; in this flow type, there is a clear interface between the two phases. Another type is emulsion flow, either oil emulsion into water or water emulsion into oil; in this flow type the interface is smeared and plugs appear. Core-Annular Flow only appears under specific flow conditions. When the oil/water flow rates are increased or decreased, different flow patterns will appear. For horizontal pipes, when the density difference between oil and water is too high, it is possible to find oil fouling on the upper pipe wall leading to stratified flow. The transition from CAF to other flow patterns or fouling will give an enormous increase in pressure drop.

Charles et al. (1961) studied the flow pattern map for concentric oil-water pipe flow. Experiments were done for a horizontal pipe with an equal oil and water density. They determined the flow pattern map with different oil and water flow velocities. With increasing watercut, 5 flow patterns were observed: water drops in oil, core-annular flow, oil slugs in water, oil plugs in water, and oil drops in water. They found that a too low oil velocity will give oil slug flow for a vertical pipe and stratified flow for a horizontal pipe. A high oil velocity will give oil emulsion into water, because of the high shear between oil and water. Lower and upper oil velocity boundaries for a stable CAF flow pattern were reported. Both the upper and lower velocity limit increased with increasing pipe diameter. The lower velocity limit is independent of the oil viscosity, while the upper velocity limit increased with oil viscosity and interface tension.

Bai et al. (1992) did experiments for a vertical pipe, and constructed flow pattern maps for both upward flow and downward flow. Six flow patterns were identified: oil in water dispersion, oil stuck to the wall, bamboo wave/corkscrew, disturbed bamboo wave, oil slug flow and oil bubbly flow. Two types of CAF were found: “bamboo wave” for upward flow and “corkscrew wave” for downward flow. The “bamboo wave” was almost steady (with respect to the interface reference frame), and the wave length decreased with increasing oil velocity. The “bamboo wave” covered a large area for upward flow in the flow pattern map, and the maximum pressure drop reduction existed in the bamboo wave region.

Oliemans & Ooms (1986) did experiments in a horizontal pipe to show that higher velocities of oil

and water are required to obtain the core-annular flow pattern in comparison with the vertical pipe. Sotgia et al. (2008) did experiments for the horizontal pipe with two different pipe diameters: 26 mm and 40 mm. Five flow patterns were found: dispersed flow, CAF, slug flow, wavy stratified flow, and corrugated annular flow. The core annular flow region in the flow pattern map is larger for the 26 mm pipe than for the 40 mm pipe. A broad buffer zone was found between CAF and dispersed flow. Besides, they differentiated corrugated CAF from wave CAF. Wavy CAF would transfer into corrugated CAF when the water flow rate is lower, and the oil flow rate is higher. A critical oil superficial velocity exists, above which only corrugated CAF is observed; here stratified flow never happened even not at very low water flow rates. More recently Hu et al. (2020) studied flow pattern maps for the horizontal pipe with a diameter of 14 mm, in which two types of oil were used. For the more viscous oil they found that CAF covered a larger region in the flow pattern map.

A linear stability analysis can be used to determine the transition criterion from Perfect Core-Annular Flow (PCAF) to other flow patterns. PCAF has a flat oil-water interface, which is the ideal and most effective appearance of CAF. Using a linear stability analysis, Joseph et al. (1984) found that laminar-laminar PCAF with equal density is stable when the more viscous fluid is located in the core. Preziosi et al. (1989) studied the long wave instability and showed that the flow is always stable when interfacial tension is neglected. Hu et al. (1990) performed a linear stability analysis for two liquids with equal density. For different viscosity ratios, the neutral curves for the wave number versus the Reynolds number were obtained; the stable and unstable regions can be determined from these curves. Beerens et al. (2014) verified the results of Hu et al. (1990) by performing 2D CFD simulations. Several flow pattern transition criteria for horizontal pipe were studied by Brauner & Maron (1992). The boundary for stable stratified flow is obtained from a linear stability analysis. The transition line from PCAF to oil plug flow, from segregated stratified flow to dispersed stratified flow, and the stability condition for fully dispersed flow were described by simple mechanistic models. Brauner & Maron (1999) provide an Eötvös number as a criterion for the transition. When the Eötvös number is smaller than one, the pipeline operates in the micro-gravity regime, and the horizontal CAF is stable; otherwise, the flow will evolve to stratified flow. Bannwart (2001a,b) derived a similar criterion: the flow is stable when the Eötvös number is smaller than eight, based on the assumption that the capillary effect balances the buoyancy force. According to Bannwart (2001a,b), the same criterion can also be applied to a vertical pipe, because under this criterion surface tension will compensate the stretch effect of the buoyancy to prevent that the oil phase is broken into oil slugs/plugs. Rodriguez & Bannwart (2008) studied the transition criteria for horizontal and vertical pipes. They found that surface tension is important for predicting the stability region. They derived the transition criterion again in terms of the Eötvös number, and further simplified the criterion into a maximum wave length for the vertical pipe. According to Sotgia et al. (2008), however, the above studies are limited, because there are also conditions where the surface tension is less important. They found that the flow pattern transition point is close to the point where the pressure drop reduction factor is maximum, and they related the transition point to the Froude number. An “equivalent velocity -  $\omega_i$ ” is defined as the transition criterion, which is only dependent on the flow properties.

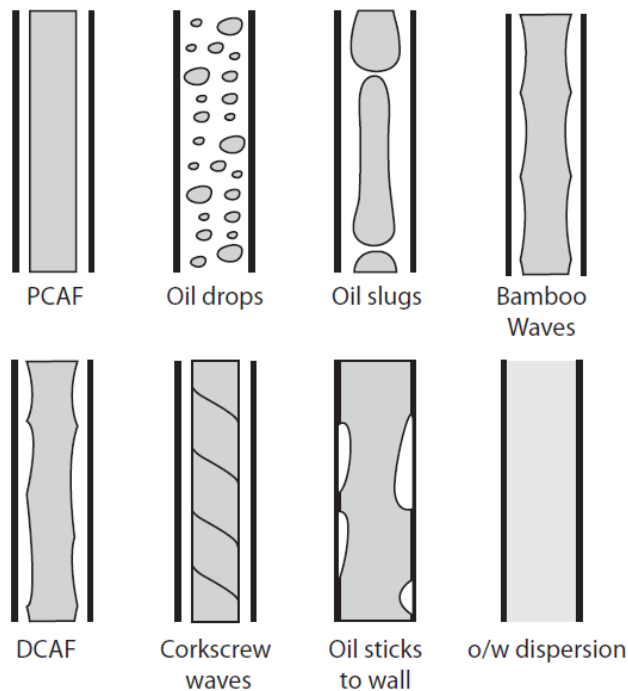


**Figure 1.2. Flow patterns that can occur for oil-water flow in a pipe (graph reproduced from the Master Thesis by Beerens, 2013).**

### 1.2.2 Pressure drop and holdup ratio

Four parameters are involved in the study of core-annular flow, namely: watercut, pressure drop, total flow rate, and holdup ratio. The holdup ratio is a dimensionless parameter, which represents the slip effect between the oil and water layers. In the core-annular flow pattern, the holdup ratio is always larger than 1 and smaller than 2, because of water accumulation in the pipe. In experiments or numerical simulations, two of them are set as input parameters, while the two others are output parameters. To predict the correlation between these parameters, empirical models are available in the literature and some of them were well summarized by Ghosh et al. (2009).

Russell and Charles (1959) derived an equation to relate the flow rate with the viscosity and pressure drop; the interface location where the flow rate is maximum is used. The model, however, predicted a too high pressure drop. Bentwich et al. (1970) did a theoretical study of the eccentricity in laminar-laminar CAF. The oil flow rate decreased with eccentricity at fixed pressure drop. There is an optimum water holdup where the pressure drop reduction factor is maximum; this optimum value decreased with eccentricity.

Ooms et al. (1983) used the lubrication model and performed numerical simulations to calculate the pressure drop as function of wave form. Oliemans et al. (1987) extended the work to the turbulent region of the water annulus. Due to the introduction of the turbulent viscosity, the pressure drop increased by 30% compared with the laminar results from Ooms et al. (1983). But the model still underpredicted the pressure drop, which is suspected to be a consequence of using the lubrication theory and ignoring the inertia effect. Furthermore, Oliemans et al. (1987) calculated the water holdup from photographs taken from experiments, and they proposed an empirical correlation between the water holdup fraction ( $Hw$ ) and the watercut fraction ( $Cw$ ), namely:  $Hw = Cw[1 + (1 - Cw)^5]$ . The pressure gradient for a 5 cm pipe was found to be correlated with the mixture velocity to the power 1.8, when the

mixture velocity is larger than 0.5 m/s.

Arney et al. (1993) derived an empirical formula between the water holdup ( $Hw$ ) and the watercut ( $Cw$ ) by fitting experimental data taken from the literature:  $Hw = Cw[1 + 0.35(1 - CW)]$ . A strong dependence of the friction factor on the oil holdup is found. A theoretical value for the friction factor is derived for a vertical pipe. At higher Reynolds numbers, the model agrees well with the experimental results, but at lower Reynolds numbers, a larger scatter was observed. Huang et al. (1994) extended the study by including the effect of eccentricity. They used a  $k - \varepsilon$  model for turbulence. They found that the friction factor increased with eccentricity, and the water holdup is insensitive to the eccentricity. The friction factor as a function of Reynolds number is computed and compared with the experimental data from Arney et al. (1993). In both studies, the waviness was ignored. The model of Arney et al. (1993) was improved by Shi et al. (2017a,b); the Froude number is included into the model to account for the effect of eccentricity and oil fouling. More recently Hu et al. (2020) presented a model with a modified friction factor, including the effects of wall roughness, eccentricity, and oil fouling.

Bannwart (2001a,b) proposed a model to predict the water holdup fraction based on the wave speed. They relate the wave speed with the oil and water superficial velocities and holdup ratio. They found a constant holdup ratio of 1.23 for horizontal pipe with a diameter of 28.4 mm. This is only slightly lower than the value of 1.39 reported by Bai et al. (1992). The pressure drop is modeled with the total flow rate and a two-phase multiplier, which includes the effect of turbulence and the interface waviness. An empirical value is used for the two-phase multiplier based on experimental results. In the model, the pressure drop compared well with the experiment, but the holdup ratio was set to 1, which is not very physical.

The two-fluid model was used by Brauner (1991) for various flow conditions for water/oil, namely laminar-laminar, turbulent-laminar and turbulent-turbulent. Both the holdup fraction and pressure drop can be predicted from their model. The pressure drop depends on both the Lockhart-Martinelli parameter and the watercut. The pressure drop reduction factor increased with increasing oil viscosity, which shows that the CAF flow pattern is more efficient for highly viscous oil. But the effect of waviness is ignored. Ullman & Brauner (2004) derived a new closure formula for the wall and interface shear stress in the two-fluid model. The interfacial stress is modeled based on the velocity difference between the oil and water, instead of the core velocity (Brauner, 1991). The effect of gravity in inclined pipes and the effect of small waviness were also considered in the modeling of the interface shear stress. But the holdup ratio is considered as a constant value of 1.16 for highly viscous oil, which is lower than found in experiments (Bai et al., 1992).

Most of the theoretical models start with PCAF. The prediction of the pressure drop is usually based on the traditional single phase pipe flow with a modified friction factor. Tripathi et al. (2017) did experiments and proposed a different empirical relationship between pressure drop, holdup ratio and oil/water flow rates. They found that it is reasonable to assume that the annulus behaves as a Couette flow driven only by the oil core velocity. The friction factor depends only weakly on the shear Reynolds number and the wave height. The pressure drop is modeled using the oil core velocity and the fitted friction factor. They used a constant holdup ratio, being 1.35 based on experiments. They also mentioned that the viscous stress and form drag both contribute to the total shear stress; the expected form drag contribution to the total stress is more than 20%..

Another interesting topic is the optimum watercut where the pressure drop is maximum. Bai et al. (1992) mentioned that the minimum pressure drop is located in the wavy core-annular flow pattern. Russell & Charles (1959) found that the optimum watercut for pressure reduction is between 8% and 10%. Sotgia et al. (2008) found that for most cases, a 10% watercut is optimum for the highest



pressure drop reduction. The maximum pressure drop reduction factor decreased with pipe diameter. Ullman & Brauner (2004) predict the watercut range for the largest pressure drop reduction to be between 8% to 12%. Bannwart (2001a,b) reported a watercut range from 9% to 14%.

### 1.2.3 Levitation mechanism for horizontal pipe

For horizontal pipe flow, because of the smaller density of oil than water, an upward buoyancy force will be acting on the oil core. Ooms & Poesio (2003) describe how different types of forces can balance the buoyancy force.

Ooms & Becker (1972) used lubrication theory and found that the interfacial waves at the top and bottom need to be asymmetric to produce a downward viscous force to balance the buoyancy force. Ooms et al. (1983) developed a lubrication film model. In this model, wave characteristics and eccentricity were artificial input parameters, and the oil core was assumed to be solid. The model showed that the pure lubrication force is able to balance the buoyancy force, for which interfacial ripples and high eccentricity are required. The pressure varied significantly at the top layer, while it showed little variance at the bottom layer. Oliemans et al. (1987) extended the model into the turbulent region by adapting the Prandtl mixing length model for the turbulent viscosity.

Ooms & Poesio (2003) used hydrodynamic lubrication theory to investigate the levitation mechanism for two wave shapes as found from the literature: the bamboo wave and the snake wave. They found for the snake wave that the net lubrication force is acting opposite to the buoyancy force, while for the bamboo wave it is acting in the same direction as the buoyancy force. Therefore, the lubrication theory is not suitable to explain the levitation mechanism for the bamboo wave. In their study the wave shape is imposed artificially. The secondary flow for the snake wave shape was shown and the levitation forces as a function of wave length and flow velocity were also presented.

To calculate the development of interfacial waves, Ooms et al. (2007) performed a simulation using hydrodynamic lubrication theory. The core was assumed to consist of a rigid core centre and a highly viscous surrounding core layer, for which the surface tension at the oil-water interface was ignored. Their simulation results show that, when the density difference is zero, the artificially eccentric core will gradually become concentric under the effect of lubrication force, and the interface shape does not change much compared to the initial state. When the density difference is non-zero, the concentric core gradually developed into an eccentric core, for which a stable CAF was obtained, and the lubrication force was balancing the buoyancy force. The wave shape changed from a symmetric shape to a non-symmetric shape. Besides, the core eccentricity decreased with increasing pressure gradient.

Ooms & Poesio (2014) performed an analytical study for Stokes flow with the following assumptions: small eccentricity, thin water layer, and small wave amplitude. They found that the vertical viscous force balanced the buoyancy force and the force came from the azimuthal velocity component. For a symmetric core shape, the balancing force vanished. In their study, the pressure force did not contribute to the vertical force because of the assumptions.

In the lubrication theory of Ooms et al. (1983), a saw-tooth wave shape was applied. Bai et al. (1996), however, argued that the saw-tooth wave shape is not possible, because the high pressure at the wave crest will smoothen the sharp part of the wave. To demonstrate this, Bai et al. (1996) carried out simulations in which the oil core is assumed to be solid, though the Young-Laplace relation is used to determine the shape of the interface along the solid body. A self-similar wave shape was found in which the wave slope is sharper in front of the crest than behind the wave crest. It was emphasized by Bai et al. (1996) that the inertia effect cannot be ignored for the levitation mechanism. Ooms et al. (2012) extracted the wave shape from Bai et al. (1996), and imposed the wave shape as a rigid inner boundary for the 3D annulus flow. Simulations were done with different artificial eccentricities and

Reynolds numbers. At high Reynolds numbers and with eccentricity, the total hydrodynamic force integrated over the interface was found acting downward, while at low Reynolds numbers the force switched its direction and acted upward. Viscous force and pressure force were both calculated. The viscous force is always acting opposite to the buoyancy force, but its contribution is only very small. This verified the statement of Bai et al. (1996) that, at least at high Reynolds number, the levitation mechanism is dominated by inertia instead of the viscous forces from the lubrication theory.

To further investigate this, Ooms et al. (2013) performed 3D simulations for horizontal core-annular flow, using the Volume of Fluid method (VOF) for capturing the interface. Both the oil core and water annulus are laminar. They found that the wave amplitude is higher at the top, while at the bottom the interface is almost flat. At high Reynolds numbers, the inertia term is necessary to provide the levitation. At very low Reynolds numbers, an eccentric core-annular flow was still stable even when excluding the inertia terms from the governing equations. The levitation mechanism was explained by the re-distribution of pressure on the interface, in which the net pressure force was balancing the buoyancy force. The flow details were also shown; the recirculation zone near the wave trough is important for the pressure re-distribution.

Bannwart (2001a,b) studied the surface tension force for the cross section of the pipe. In the model the boundary force is balanced by surface tension and drag force, so that the oil core is analogous to a bubble. The core shape is obtained from the curvature of the interface. In the model the streamwise wave was ignored.

#### 1.2.4 Interfacial waves

It is shown in the previous section that interfacial waves are important to maintain the levitation of the oil core for horizontal pipes. Perfect Core-Annular Flow is difficult to achieve in vertical pipes. In most cases, waves can grow at the interface, and the flow undergoes a transition from Perfect Core-Annular Flow (PCAF) to Wavy Core-Annular Flow (WCAF). The waviness makes the hydraulic parameters and flow physics quite different from what is found with the flat interface in PCAF.

The formation of waviness is due to the interface instability (linear or non-linear instability mechanisms). Various linear stability studies have been undertaken for laminar-laminar 2D PCAF with small disturbances; here the Navier-Stokes equations are linearized and an eigenvalue problem is solved for the Orr-Sommerfeld equation. Hickox (1971) studied the stability of two fluids in a straight tube and found that a long wave disturbance is always unstable and leads to interfacial waves with finite amplitude. According to Hickox (1971), the instability is caused by the viscosity difference, while the interface tension and density difference have less influence. Shertok (1976) found that the long wave instability is prevailing at lower oil/water superficial velocities, whereas the short-wave instability leading to the formation of oil droplets is dominant at higher superficial velocities. Ooms (1971) analyzed the stability of laminar-laminar core-annular flow, while ignoring the effect of viscosity on the flow stability, and two types of instability are found: one is the Kelvin-Helmholtz instability, which is due to the apparent difference in flow velocity near the interface, and the other one is capillary instability, induced by the surface tension. Ooms (1972) found that these two instabilities can be reduced when the water layer is thinner. Preziosi et al. (1989) found that surface tension stabilizes short waves (wave number is larger than 1) in core annular flow. Long waves are destabilizing the flow and will lead to oil droplets in the water annulus. With increased Reynolds number, the long wave capillary instability can be stabilized by shear. However, when the Reynolds number is above a critical value, a second capillary instability causes the emulsion of oil into water. Therefore, upper and lower branches of the critical Reynolds number exist in relation to the neutral stability curve. This stabilization phenomenon agrees well with the experiment from Charles et al. (1961).

To study the mechanism of instability, Hu & Joseph (1989) used the energy equation, and they found that three physical effects are involved: surface tension, interface stress, and wave Reynolds stress. At small Reynolds numbers, surface tension can cause instability, while the other two effects stabilize the flow. At large Reynolds numbers, surface tension stabilizes the flow, and the other two effects destabilize the flow. For even higher Reynolds numbers, the wave Reynolds stress in the water is the main source of instability. The wavy core-annular flow pattern in the experiment by Charles et al. (1961) is regarded as a stable flow, where the destabilizing Reynolds stress and the stabilizing interface viscosity compensate each other. Bai et al. (1992) found a new flow pattern with bamboo waves in their vertical pipe flow experiment. Energy budgets show that the bamboo wave is induced by interfacial viscous friction, the surface tension is only slightly destabilizing, and the wave Reynolds stress stabilizes the flow. Miesen et al. (1992) focused their analysis on disturbances with an intermediate wave length. A rather good agreement is found when comparing the dispersion relationship with the experimental wave distribution. Boomkamp & Miesen (1996) found five instability types for two-phase parallel flow. In particular, they argue that stable core-annular flow, as found in the stability analyses by Preziosi et al. (1989), Hu & Joseph (1989) and Miesen et al. (1992), is due to the stabilizing effect of the presence of the jump in viscosity near the interface. Water emulsion into the oil is classified as a shear-induced instability, which stems from the wall boundary layer in the annulus flow when there is a transition from laminar flow to turbulent flow. When the wave amplitude becomes significant, non-linear effects can saturate the linear instability. Papageorgiou et al. (1990) studied the non-linear stability of axis-symmetric CAF by assuming the annulus thickness is much smaller than the core radius.

All the above research has been focused on laminar-laminar CAF. The study of the instability problem of turbulent-laminar core-annular flow, to the best of the author's knowledge, has not been done with one exception: Náraigh et al. (2011) carried out a linear stability analysis with a turbulent base flow in a stratified two-phase channel configuration.

The wave characteristics in the turbulent region have been examined in various experimental studies. Oliemans et al. (1987) did experiments for horizontal oil-water pipe flow. They found that the wave length correlated with watercut and superficial oil velocity, and they obtained an empirical correlation for the wave length. De Castro et al. studied the wave shape for the stratified oil-water flow as a function of the two-phase Froude number. Al-Wahaibi & Angeli (2011) studied the wave characteristics for stratified oil-water pipeline flow. They found that the wave amplitude increased with superficial velocity and decreased with oil holdup, and that the wave length increased with oil/water superficial velocity difference. Barral & Angeli (2014) used a high-speed camera and a parallel wires conductivity probe to measure the instantaneous fluctuations of the interface. They obtained the power spectrum of the interface for stratified flow. A unique peak frequency for the interfacial wave is found, but the signal is less obvious downstream of the pipe. Tripathi et al. (2017) did experiments for horizontal CAF. They used a high-speed camera to capture the interface and correct the interface using a ray tracing method for the refraction effect. Dimensionless numbers showed that the surface tension and gravity play a minor role in the interface dynamics and the cross section is close to a circle. They found the dependence of interface height and interface length on the shear Reynolds number. Besides the mentioned experimental studies, Kim & Choi (2018) carried out detailed Direct Numerical Simulations (DNS) for vertical CAF. The 3D wave structure in both azimuthal and streamwise directions are studied. The energy spectrum shows that the dominant azimuthal wave length is about equal to the pipe circumference and the dominant streamwise wave length increases with increasing water holdup.

### 1.2.5 CFD simulations

CFD simulations can provide detailed information on the flow field, which will help to understand the physical mechanisms in detail. It is quite a challenge, however, to accurately simulate the complex multiphase and turbulent flow system. For example, there is a jump in the viscosity and in the velocity gradient across the interface, the turbulent flow in the water annulus will be damped towards the interface, and the flow may become fully laminar at streamwise locations where the thickness of the water annulus has decreased after the passage of the peak in the interface wave. However, with the growth of computer power and the development of CFD tools, more advanced simulations have become possible.

Li & Renardy (1999) used the Volume of Fluid (VOF) method to perform direct numerical simulations of the laminar-laminar 2D core-annular flow, and the instability problem and wave shape were studied. A similar numerical method was used by Ooms et al. (2013); 3D simulations for CAF at both higher and lower Reynolds numbers (Stokes region) were performed. Bai et al. (1996) simulated the interfacial wave shape, though Kang et al. (2006) argued that the obtained wave is too smooth. Instead, they used the level set method for the 2D axis-symmetric vertical core-annular flow to simulate the “bamboo wave” with sharper wave crest. The breaking and merging of the oil core is also simulated. Beerens et al. (2014) used the VOF method to simulate the 2D vertical laminar-laminar core-annular flow. The wave growth was studied for short pipe sections. Multiple wave lengths were found for longer pipe sections, though the averaged wave length is close to the wave length with the highest growth rate.

With respect to turbulent-laminar CAF simulations, relatively little literature is available. Huang et al. (1993) used the Reynolds-Averaged Navier-Stokes approach (RANS) with a low Reynolds number  $k-\varepsilon$  model to simulate the velocity profile of eccentric perfect core-annular flow. Ko et al. (2002) simulated the turbulent water annulus with  $k-\omega$ , while assuming the oil core to be solid; the solid “interface” was simulated using the same method as Bai et al. (1996). The results showed that wave length decreased with increasing Reynolds number and with decreasing water holdup. The secondary flow and pressure distribution along the interface at different Reynolds numbers were shown. Ingen Housz et al. (2017) performed 3D simulations for horizontal CAF; they used the VOF method for the interface capturing and the low Reynolds Launder–Sharma  $k-\varepsilon$  model for turbulence. For the considered conditions, it is found that the flow is laminar in the top layer water and turbulent in the bottom water layer. Shi et al. (2017a,b) simulated horizontal oil-water flow with matched density. The VOF method is used, and several flow patterns were simulated: CAF, oil plug/slug flow, and water emulsion flow. The SST  $k-\omega$  model was found to give the best results. The simulated flow patterns were sensitive to the contact angle. Gosh et al. (2010) simulated downward CAF using VOF and the  $k-\varepsilon$  method, but a rather coarse mesh was used. As was already mentioned Kim & Choi (2018) performed DNS using the level set method for CAF in a vertical pipe, and a detailed analysis was provided for the turbulent statistics.

## 1.3 About this thesis

In this thesis, various aspects of Core-Annular Flow are studied. In particular, 1D, 2D, and 3D RANS simulations are carried out for various conditions. Also, Large-Eddy Simulations (LES) and DNS are carried out. Furthermore, a limited number of lab experiments are carried out. The simulation results are compared with experiments, which enables one to get new insights in the flow physics that were not reported earlier.

The main purpose of this PhD work is to extend the knowledge of core-annular flow from the laminar-laminar state to the laminar-turbulent state, i.e. from a laminar annulus to a turbulent annulus.

Several aspects of the core-annular flow are considered in this thesis, all related to the formation and impact of interfacial waves in the presence of a turbulent annulus. This is related to the four key hydraulic quantities: pressure drop, total volumetric flow rate, watercut, and water holdup.

This PhD thesis includes five technical chapters, each of which reproduces a recent publication by the author in a peer-reviewed leading journal on multiphase flow (either already published, accepted for publication, or under review). There is also an appendix that contains a copy of a paper by the author that appeared in the proceedings of a multiphase flow conference.

- **Chapter 2. “1D/2D/3D RANS for CAF”.** Simulation of turbulent horizontal oil-water core-annular flow with a low-Reynolds number  $k-\epsilon$  model. (International Journal of Multiphase Flow 142, 103744, 2021; [10.1016/j.ijmultiphaseflow.2021.103744](https://doi.org/10.1016/j.ijmultiphaseflow.2021.103744)).
- **Chapter 3. “Friction factors for CAF”.** Simulation of a turbulent annulus with interfacial waves in core-annular pipe flow. (International Journal of Multiphase Flow 154, 104152, 2022; <https://doi.org/10.1016/j.ijmultiphaseflow.2022.104152>).
- **Chapter 4. “Interfacial wave growth”.** Interfacial wave growth for core-annular pipe flow with a turbulent annulus. (Submitted for journal publication, 2023).
- **Chapter 5. “Vertical CAF”.** Simulation of vertical core-annular flow with a turbulent annulus. (International Journal of Multiphase Flow, 167, 104551, 2023; <https://doi.org/10.1016/j.ijmultiphaseflow.2023.104551>).
- **Chapter 6. “RANS/LES/DNS for CAF”.** Comparison of RANS, LES, and DNS for core-annular flow with a turbulent annulus. (Submitted for journal publication, 2023).
- **Chapter 7** provides an overview of the main conclusions and recommendations for further research.
- **Appendix. “Flow envelope”.** Turbulence and waves in oil-water pipe flow. (Proceedings 20<sup>th</sup> Conference on Multiphase Production, 2023).

## References

- Al-Wahaibi, T., Angeli P., 2011. Experimental study on interfacial waves in stratified horizontal oil–water flow. *International Journal of Multiphase Flow* 37, 930–940.
- Arney, M.S., Bai, R., Guevara, E., Joseph, D.D., Liu, K., 1993. Friction factor and holdup studies for lubricated pipelining - 1. Experiments and correlations. *International Journal of Multiphase Flow* 19, 1061–1067.
- Bai, R., Chen, K., Joseph, D.D., 1992. Lubricated pipelining: stability of core-annular flow. Part 5. Experiments and comparison with theory. *Journal of Fluid Mechanics* 240, 97–132.
- Bai, R., Kelkar, K., Joseph, D.D., 1996. Direct simulation of interfacial waves in a high-viscosity-ratio and axisymmetric core–annular flow. *Journal of Fluid Mechanics* 327, 1–34.
- Bannwart, A.C., 2001a. Bubble analogy and stabilization of core–annular flow. *Journal of Energy Resources Technology ASME* 123, 127–132.
- Bannwart, A.C., 2001b. Modeling aspects of oil–water core-annular flows. *Petroleum Science and Engineering* 32, 127–143.
- Barral, A.H., Angeli, P. 2014. Spectral density analysis of the interface in stratified oil–water flows. *International Journal of Multiphase Flow* 65, 117–126.
- Beerens, J.C., 2013. Lubricated transport of heavy oil; Simulation of multiphase flow with OpenFOAM. Master Thesis, Delft University of Technology, Report Number MEAH-272.
- Beerens, J.C., Ooms, G., Pourquié, M.J.B.M., 2014. A comparison between numerical predictions and theoretical and experimental results for laminar core-annular flow. *AIChE Journal* 60, 3046–3056.
- Bentwich, M., Kelly, D.A.I., Epstein, N., 1970. Two-phase eccentric interface laminar pipeline flow. *ASME J. Basic Eng.* 92, pp. 32–36
- Boomkamp, P.A.M., Miesen, R.H.M. 1996. Classification of instabilities in parallel two-phase flow. *International Journal of Multiphase Flow* 22, 67–88.
- Brauner, N., 1991. Two-phase liquid-liquid annular flow. *International Journal of Multiphase Flow* 17, 59–76.
- Brauner, N., Maron, D.M. 1992. Flow pattern transitions in two-phase liquid-liquid flow in horizontal tubes. *International Journal of Multiphase Flow* 18, 123–140.
- Brauner, N., Maron, D.M. 1999. Classification of liquid–liquid two-phase flow systems and the prediction of flow pattern maps. *Second International Symposium on Two-Phase Flow Modeling and Experimentation–ISTP*, vol. 99.
- Charles, M.E., Govier, G.W., Hodgson, G.W., 1961. The horizontal pipeline flow of equal density oil-water mixtures. *Canadian Journal of Chemical engineering* 39, 27–36.
- Clark, A.F., Shapiro, A. 1949. Method of pumping viscous petroleum. US Patent No. 2533878.
- Clifton, E.G., Handley, L.R., 1958. Method and apparatus for lubricating pipelines, US patent No. 2821205.
- De Castro, M.S., Pereira, C., Dos Santos, J.N., Rodriguez, O.M.H., 2012. Geometrical and kinematic properties of interfacial waves in stratified oil–water flow in inclined pipe. *Experimental Thermal and Fluid Science* 37, 171–178.
- Ghosh, S., Mandal, T.K., Das, G., 2009. Review of oil water core annular flow. *Renewable and Sustainable Energy Reviews* 13, 1957–1965.
- Ghosh, S., Das, G., Das, P.K., 2010. Simulation of core annular downflow through CFD—A comprehensive study. *Chemical Engineering and Processing: Process Intensification* 49, 1222–1228.
- Hickox, C.E., 1971. Instability due to viscosity and density stratification in axisymmetric pipe flow. *Physics of Fluids* 14, 251–262.
- Huang, A., Christodoulou, C., Joseph, D.D., 1994. Friction factor and holdup studies for lubricated pipelining part. 2: Laminar and k–epsilon models of eccentric core flow. *International Journal of Multiphase Flow* 20, 481–491.
- Hu, H., Joseph, D.D., 1989. Lubricated pipelining: stability of core-annular flow. Part 2. *Journal of*



- Fluid Mechanics 205: 359-396.
- Hu, H., Lundgren, S., Joseph, D.D., 1990. Stability of core-annular flow with very small viscosity ratio. *Physics Fluids* 2:1945–1954.
- Hu, H., Jing, J., Tan, J., 2020. Flow patterns and pressure gradient correlation for oil–water core–annular flow in horizontal pipes. *Experimental and Computational Multiphase Flow* 2, 99-108.
- Ingen Housz, E., Ooms, G., Henkes, R.A.W.M., 2017. A comparison between numerical predictions and experimental results for horizontal core-annular flow with a turbulent annulus. *International Journal of Multiphase Flow* 95, 271-282.
- Joseph, D.D., Renardy, M., Renardy, Y., 1984. Instability of the flow of two immiscible liquids with different viscosities in a pipe. *Journal of Fluid Mechanics* 141, 309–317.
- Joseph, D.D., Bai, R., Chen, K.P., 1997. Core-annular flows. *Annual Review of Fluid Mechanics* 29, 65-90.
- Kang, M., Shim, H., Osher, S., 2007. Level set based simulations of two-phase oil–water flows in pipes. *Journal of Scientific Computing* 31, 153-184.
- Kim, K., Choi, H., 2018. Direct numerical simulation of a turbulent core-annular flow with water-lubricated high viscosity oil in a vertical pipe. *Journal of Fluid Mechanics* 849, 419-447.
- Ko, T., Choi, H.G., Bai, R., 2002. Finite element method simulation of turbulent wavy core–annular flows using a  $k-\omega$  turbulence model method. *International Journal of Multiphase Flow* 28, 1205-1222.
- Li, J., Renardy, Y., 1999. Direct simulation of unsteady axisymmetric core–annular flow with high viscosity ratio. *Journal of Fluid Mechanics* 391, 123-149.
- Miesen, R., Beijnon, G., Duijvestijn, P.E.M., 1992. Interfacial waves in core-annular flow. *Journal of Fluid Mechanics* 238, 97-117.
- Náraigh, L.Ó., Spelt, P.D.M., Matar, O.K., 2011. Interfacial instability in turbulent flow over a liquid film in a channel. *International Journal of Multiphase Flow* 37, 812-830.
- Oliemans, R.V.A., Ooms, G., 1986. Core-annular flow of oil and water. *Multiphase Science and Technology* 2, 1-4.
- Oliemans, R.V.A., Ooms, G., Wu, H.L., Duijvestijn, A. 1987. Core annular oil/water flow: the turbulent-lubricating–film model and measurements in a 5 cm pipe loop. *International Journal of Multiphase Flow* 13, 23-31.
- Ooms, G. 1971. Fluid-mechanical studies on core-annular flow. Doctor Thesis.
- Ooms, G., 1972. The hydrodynamic stability of core-annular flow of two ideal liquids. *Applied Scientific Research* 26, 147-158.
- Ooms, G., Beckers, H.L., 1972. The flow of a rigid core surrounded by an annular liquid layer through a horizontal tube. *Applied Scientific Research* 26, 321-334.
- Ooms, G., Segal A., Van der Wees, A.J., 1983. A theoretical model for core-annular flow of a very viscous oil core and a water annulus through a horizontal pipe. *International Journal of Multiphase Flow* 10, 41-60.
- Ooms, G., Poesio, P. 2003. Stationary core-annular flow through a horizontal pipe. *Physical Review E* 68, 066301.
- Ooms, G., Vuik, C., Poesio, P. 2007. Core-annular flow through a horizontal pipe: hydrodynamic counterbalancing of buoyancy force on core. *Physics of Fluids* 19, 092103.
- Ooms, G., Pourquié, M., Poesio, P. 2012. Numerical study of eccentric core-annular flow. *International Journal of Multiphase Flow* 42, 74-79.
- Ooms, G., Pourquié, M., Beerens, J. C., 2013. On the levitation force in horizontal core-annular flow with a large viscosity ratio and small density ratio. *Physics of Fluids* 25, 032102.
- Ooms, G., Poesio, P., 2014. Analytical study of slightly eccentric core–annular flow. *Journal of Engineering Mathematics* 85, 65-81.
- Papageorgiou, D.T., Maldarelli, C., Rumschitzki, D.S., 1990. Nonlinear interfacial stability of core-annular film flows. *Physics of Fluids A: Fluid Dynamics* 2, 340-352.
- Preziosi, L., Chen, K., Joseph, D.D., 1989. Lubricated pipelining: stability of core-annular flow. *Journal of Fluid Mechanics* 201, 323-356.

- Rodriguez O. M.H, Bannwart, A.C., 2008. Stability analysis of core-annular flow and neutral stability wave number. *AIChE journal* 54, 20-31.
- Russell, T.W.F, Charles, M.E., 1959. The effect of less viscous liquid in the laminar flow of two immiscible liquids. *Canadian Journal of Chemical Engineering* 37, 18–24.
- Shertok, J.T., 1976. Velocity profiles in core-annular flow using a laser Doppler velocimeter. PhD Thesis.
- Shi, J., Gourma, M., Yeung, H., 2017a. CFD simulation of horizontal oil-water flow with matched density and medium viscosity ratio in different flow regimes. *Journal of Petroleum Science and Engineering* 151, 373-383.
- Shi, J., Lao, L., Yeung, H., 2017b. Water-lubricated transport of high-viscosity oil in horizontal pipes: The water holdup and pressure gradient. *International Journal of Multiphase Flow* 96, 70-85.
- Sotgia, G., Tartarini, P., Stalio, E., 2008. Experimental analysis of flow regimes and pressure drop reduction in oil-water mixtures. *International Journal of Multiphase Flow* 34, 1161-1174.
- Tripathi, S., Tabor, R. F., Singh, R., 2017. Characterization of interfacial waves and pressure drop in horizontal oil-water core-annular flows. *Physics of Fluids* 29, 082109.
- Ullmann, A., Brauner, N., 2004. Closure relations for the shear stress in two-fluid models for core-annular flow. *Multiphase Science and Technology* 16, 4.



# 2

## 1D/2D/3D RANS for CAF

*1D, 2D and 3D numerical simulations were carried out with the Reynolds-Averaged Navier-Stokes equations (RANS) for horizontal oil-water core-annular flow in which the oil core stays laminar while the water layer is turbulent. The turbulence is described with the Launder-Sharma low-Reynolds number  $k - \epsilon$  model. The simulation results are compared with experiments carried out in our lab in a 21 mm diameter pipe using oil and water with a viscosity ratio of 1150 and a density ratio of 0.91. The 1D results represent perfect turbulent CAF (i.e. no gravity, no interfacial waves), the 2D results represent axi-symmetric CAF (i.e. no gravity, with interfacial waves), and the 3D results represent eccentric CAF (i.e. with gravity, with interfacial waves). The simulation results typically show a turbulent water annulus in which the structure of the (high-Reynolds number) inertial sublayer can be recognized. The pressure drop reduction factor (which is the ratio between the pressure drop for CAF and the pressure drop for single phase viscous oil flow) for the 2D and 3D results is about the same, but its value is about 35% higher than in the experiment. The holdup ratio in the 3D model is close to the experimental value, but the 2D prediction is slightly lower. The eccentricity predicted by the 3D simulations is much higher than in the experiment. Most likely, the observed differences between the simulations and the experiments are due to limitations of using a low-Reynolds number  $k - \epsilon$  model. In particular the water layer at the top in the 3D results shows a relaminarization, which might be absent in the experiment.*

## 2.1 Introduction

Oil-water core-annular flow (CAF) is a typical two-phase flow pattern in a pipe, in which there is a viscous oil core surrounded by a water annulus. The thin water annulus lubricates the pipe wall, which significantly decreases the pressure drop compared to single phase viscous oil transport. For example, this kind of flow pattern is applicable in transporting highly viscous oil in the petroleum industry. In addition to its application opportunities, core-annular flow is also of great interest from a more fundamental fluid mechanics perspective.

At relatively low flow rates, both the oil core and the water annulus will be laminar. But if the flow velocities become higher, the water annulus will become turbulent. Further increase of the flow rates will give dispersion of the oil as droplets in the water, with oil fouling of the pipe wall. At low flow rates in a horizontal pipe a stratified water-oil layer will be found. This core-annular flow is only a single flow regime within the flow pattern map. The occurrence of core-annular flow (and the characteristics of the core-annular flow) depend on a range of parameters, such as: the pipe inclination, the pipe diameter, the total flow rate, the fraction of water in the total flow rate (which is the watercut), the ratio of the oil viscosity and the water viscosity, the ratio of the oil density and the water density, and the interfacial tension between the oil and the water.

For given conditions, the key parameters are the pressure gradient and the water holdup fraction. Core-annular flow is characterized by waves at the interface. The presence of this interface will cause a stress in flow direction between the oil core and the water annulus. The resulting interfacial force will consist of a contribution due to the shear stress and due to form drag. The latter is the resultant of the pressure working on the wavy interface in main flow direction. This interfacial stress will give water accumulation, which means that the water holdup fraction is higher than the watercut.

Over the past decades much research has been devoted to CAF, for vertical upflow and, albeit to a lesser extent, also for horizontal flow. This includes the pioneering work of Daniel Joseph and his team; an overview is given by Joseph et al. (1997). Huang and Joseph (1995), Preziosi et al. (1993), and Chen et al. (1990) studied the stability of core-annular flow, showing bamboo-shaped waves in both their experimental and numerical results. Li and Renardy (1999) carried out a numerical study of vertical CAF with the linear and non-linear stability of interfacial waves. Recently, Song et al. (2019) determined the different linear and nonlinear instability mechanisms for a laminar vertical CAF by using a phase-field method to capture the deformation of the oil-water interface. For a horizontal pipe, as gravity is now acting perpendicular to the pipe axis, and as the density of the oil core is smaller than the density of the water annulus, eccentric CAF will occur. The presence of waves at the oil-water interface is crucial for the levitation mechanism, i.e. this will generate a downward force to counterbalance the upward buoyancy force. Ooms et al. (1984) developed a lubrication film model by assuming a sawtooth-shaped wave at the interface. Ooms et al. (2007, 2012, 2013) performed a numerical study in the laminar case for eccentric horizontal CAF with a low Reynolds number in the annulus layer. Based on lab experiments in vertical and horizontal pipes for CAF at various conditions (flow rates, watercut, oil/water viscosities and densities) various correlations were derived for the pressure drop and the holdup. See for example the work by Arney et al. (1993), who provided an empirical correlation for the holdup and who used a concentric cylindrical CAF model to find a correlation for the pressure drop that only depends on a single Reynolds number. An overview of available correlations is given by Ghosh et al. (2009). Also Bannwart (2001) gave an overview of modelling for CAF, and he concludes that “pressure drop in horizontal core-annular flow should take into account the turbulence in the annulus and waviness of the interface; these aspects lead to a correlation very different from the PCAF model (laminar-laminar flow with a smooth interface)”.

To illustrate the rich physics of the flow of two immiscible liquids, reference is made to the

experimental study by Hasson et al. (1970). They injected two liquids with almost the same viscosity, but with a slightly different density, in a 12.6 mm diameter horizontal pipe. Initially the lighter liquid was flowing in the core and the heavier liquid was flowing in an annulus, giving CAF with travelling interfacial waves. A flow visualization was made to assess whether the CAF could be maintained over the length of the pipeline. One instability mechanism (Rayleigh instability), being due to the interplay of interfacial tension and inertia, gave a growth of the interfacial wave into the core, such that the core structure was broken leading to slug flow. The CAF could also end due to the ascend of the lighter liquid core towards the pipe top, leading to the disruption of the annulus film. If only an incidental touch of the top wall by the lighter liquid did occur, the breakage of the annulus was also dependent on the wettability properties of the liquids. Quite recently, Roccon et al. (2019, 2021) carried out Direct Numerical Simulations (DNS) for two immiscible liquids in a channel. Another liquid type with a small flow rate was added to the bulk flow of the original type; the additional liquid amount was meant to give a lubrication effect with pressure reduction. Initially the two viscosities were taken equal. As the two liquids are immiscible (as indicated by the finite interfacial tension) an interface will be formed that leads to the replacement of the turbulent flow along the lubricated pipe wall by laminar flow, which in turn gives a lower pressure drop as compared to the case with single phase flow. Decreasing the viscosity of the lubricated fluid by a factor 4 will keep the flow in a turbulent state, but this still leads to a small pressure reduction as the presence of the interface mitigates the size of the eddies in the lubrication layer (as compared again to the case with single phase flow). In contrast to the work by Roccon et al., in our study, a high viscosity core fluid will be considered, but the relaminarization phenomenon (depending on the local shear-based Reynolds number) will turn out to remain very relevant.

The present study extends the conditions for horizontal CAF (with a highly viscous oil core) to a higher flow rate (or larger pressure drop), with a higher Reynolds number, in which a turbulent (instead of laminar) water flow in the annulus is found (while the viscous oil core is still laminar). Both lab experiments and numerical simulations will be presented. The numerical simulations are based on solving the unsteady Reynolds-Averaged Navier-Stokes (RANS) equations with the Launder & Sharma low-Reynolds number  $k - \epsilon$  model. The idea is that the wave formation at the interface is still captured by the unsteady terms with the RANS, but that the high-frequency, small scale turbulent structures are represented by the Reynolds stresses, which in turn are described by closure relations using the  $k - \epsilon$  model. The low-Reynolds number  $k - \epsilon$  model is expected to work well for the turbulent boundary layer (within the water annulus) along the pipe wall, but may show shortcomings in describing the recirculation zones that will be found in the interfacial wave troughs (as experienced by an observer travelling with the waves).

A few studies exist in which turbulence modelling has been used for CAF. Huang et al. (1994) have applied the Launder & Spalding low-Reynolds number  $k - \epsilon$  model to the eccentric water annulus in horizontal core-annular flow. The lift mechanism, which determines where the levitated core is located, is associated with interface deformations, but this has been neglected in that study. Instead, the eccentricity is prescribed in their model, and the oil core is represented by a solid cylinder without waves. Therefore only the single-phase, steady, 2D RANS equations had to be solved for the eccentric water annulus. Ko et al. (2002) have used the Shear Stress Transport (SST)  $k - \omega$  model in their steady, single-phase RANS simulations for the turbulent water annulus in concentric, axisymmetric CAF in a horizontal pipe. The axi-symmetric assumption means that gravity effects are not included. The steady equations are solved, in which the pipe wall has been given a velocity opposite to the wave velocity. The oil core is assumed to be solid. The wave pattern at the interface is obtained by the applying the Young-Laplace pressure jump that results from the interfacial tension at the curved interface. Shi et al. (2017, 2017) and Archibong-Eso et al. (2017) have used the Shear Stress Transport (SST)  $k - \omega$  model in their 3D RANS simulations in the Fluent CFD package for horizontal water-oil flow. The focus in their studies was on obtaining an overview of the different flow regimes that can occur (i.e. CAF, water droplets in oil, oil droplets in water, oil plugs in water),

with the corresponding pressure drop and water holdup fraction. The details of the waves and turbulence were not reported. Quite recently, Kim & Choi (2018) have carried out Direct Numerical Simulations (DNS) for vertical CAF with a laminar (very viscous) oil core and with a turbulent water annulus. Obviously, such simulations require a very fine numerical grid, and small numerical time steps, but have the advantage that the waves and turbulence are fully resolved. A method in between DNS and RANS is Large-Eddy Simulations (LES), but we are not aware of any examples where LES has been applied to CAF.

The simulation set up in the present study is based on CAF experiments that were recently carried out in our lab by Van Duin et al. (2019) and that have been extended to obtain interface data that will be used for comparison. The pipe is horizontal with a 21 mm diameter. The viscous oil core is laminar and the water annulus is turbulent. The viscosity ratio between the oil and water is 1150, and the density ratio is 0.91. Simulations are carried out for cases both without gravity (using 1D and 2D formulations) and with gravity (using a 3D formulation). In particular the velocity profile and the turbulent structure in the water annulus are studied. Furthermore, the eccentricity and the levitation mechanism of the oil core and the related interfacial waves are examined. A force balance is performed on the oil core and the levitation force is split into the reduced pressure force and the viscous force.

## 2.2 Experimental and numerical method

### 2.2.1 Lab experiments

Flow measurements (pressure drop and flow visualization) were carried out in the horizontal core-annular flow loop (with 21 mm internal diameter) of our lab. The same loop was used in a previous study (Van Duin et al., 2019), but for the present study additional measurements for the water annulus thickness were obtained. The flow loop is approximately 7.5 m long and is partly made of PVC. The measurement section is 3 m long and is made of plexiglas (PMMA) to give good optical access. Near the end of this measurement pipe there are two points (spaced 1 m apart) to measure the pressure drop. Between these two points is the optical box, made of PMMA and filled with water, where the visualisation takes place. Through using mirrors, a high speed camera can simultaneously record the water annulus at the top, bottom, left and right sides of the pipe.

Upstream of the inlet of the pipe there is a 60 litre oil tank. In the tank there is a copper coil for heating, which allows to change the oil viscosity. Water is taken from the tap. A pump is used to circulate the flow. The oil flow rate is measured through the calibrated pump frequency and the water flow rate is measured through a Biotech turbine meter. At the inlet of the pipe there is a divider, in which the oil is added through a concentric pipe and water is added in through an annulus, to create core-annular flow. At the end of the flow loop there is a three way valve that will either send the content of the flow loop to the rinsing tank or to the separation barrel. There also is an approximately 200 litre barrel where the oil-water mixture from the experiment is separated. Inside the barrel there is a floater that is attached to a small electrical gear pump, which pumps the oil back to the oil tank. At the bottom there is a drain valve which is used to dispose the excess water in the tank after the oil has been pumped back to the tank.

The main purpose of this experiment is to measure the water film thickness (in space and time). The camera used for this visualisation is a Phantom Vision VEO 640L. A LED panel is placed behind the optical box to illuminate the measurement section so that clear images are produced. To mitigate the amount of optical distortion, an optical box is attached to the measurement section. Since the thickness of the water film is small (order of a mm only), it is important to correct for any remaining distortion of the image. Thereto, the experiment was calibrated by using a test pipe section with a calibration

grid. In addition this was also verified by reconstructing the light paths with a ray-tracing calculation method. An example of the flow visualization and the wall correction is given in Figure 2.1.

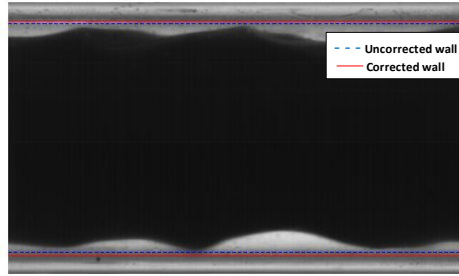


**Figure 2.1.** Snapshot of the flow visualization in the lab experiment, showing the wave structure (flow is from left to right).

### 2.2.2 Governing equations

The mass and momentum conservation equations for an incompressible, isothermal fluid are (in cartesian coordinates):

$$\frac{\partial u_i}{\partial x_i} = 0 \quad (2.1)$$

$$\frac{\partial \rho u_i}{\partial t} + \rho u_j \frac{\partial u_i}{\partial x_j} = \frac{\partial}{\partial x_j} \left( \rho (\nu + \nu_t) \left( \frac{\partial u_i}{\partial x_j} + \frac{\partial u_j}{\partial x_i} \right) \right) - \frac{\partial p}{\partial x_i} + \rho g_i + F_{\sigma,i} \quad (2.2)$$

These are the Reynolds-Averaged Navier-Stokes Equations (RANS). Here  $u_i$  is the velocity,  $\rho$  and  $\mu$  are the fluid density and viscosity,  $g_i$  is the gravitational acceleration,  $p$  is the pressure and  $F_{\sigma,i}$  is the interfacial tension force. For the pipe flow, we will use  $x_1 = x$  for the coordinate along the pipe axis,  $x_2 = y$  for the vertical coordinate, and  $x_3 = z$  for the pipe width coordinate; the velocity components are  $u$ ,  $v$ , and  $w$ , in the directions  $x$ ,  $y$ , and  $z$ , respectively. The gravity components are:  $g_1 = g_3 = 0$ , and  $g_2 = -g$ , where  $g$  is the gravitational acceleration.

The turbulent viscosity is modelled with the low-Reynolds number  $k - \epsilon$  model of Launder & Sharma (1974), which reads as follows:

$$\nu_t = C_\mu f_\mu \frac{k^2}{\epsilon} \quad (2.3)$$

$$\frac{\partial k}{\partial t} + u_j \frac{\partial k}{\partial x_j} = \frac{\partial}{\partial x_j} \left( \nu + \frac{\nu_t}{\sigma_k} \right) \frac{\partial k}{\partial x_j} + \nu_t \left( \frac{\partial u_j}{\partial x_j} \right)^2 - \tilde{\epsilon} - D \quad (2.4)$$

$$\frac{\partial \tilde{\epsilon}}{\partial t} + u_j \frac{\partial \tilde{\epsilon}}{\partial x_j} = \frac{\partial}{\partial x_j} \left( \nu + \frac{\nu_t}{\sigma_\epsilon} \right) \frac{\partial \tilde{\epsilon}}{\partial x_j} + C_1 f_1 \frac{\tilde{\epsilon}}{k} \nu_t \left( \frac{\partial u_j}{\partial x_j} \right)^2 - C_2 f_2 \frac{\tilde{\epsilon}^2}{k} + E \quad (2.5)$$

With  $D = 2\nu \frac{\partial \sqrt{k}}{\partial x_j} \frac{\partial \sqrt{k}}{\partial x_j}$  and  $E = 2\nu \nu_t \left( \frac{\partial u_j}{\partial x_j} \right)^2$ . The turbulent energy dissipation rate is  $\epsilon = \tilde{\epsilon} + D$ .

Furthermore,  $C_\mu = 0.09$ ,  $C_1 = 1.44$ ,  $C_2 = 1.92$ ,  $\sigma_k = 1.0$ ,  $\sigma_\epsilon = 1.3$ ,  $f_\mu = \exp\left(\frac{-3.4}{(1 + \frac{Re_t}{50})^2}\right)$ ,  $f_1 = 1$ ,  $f_2 = 1 -$

$0.3 \exp(-Re_t^2)$ ,  $Re_t = \frac{k^2}{\epsilon \nu}$ . The boundary conditions at the wall are:  $k=0$  and  $\tilde{\epsilon} = 0$ .

Quite a number of low-Reynolds number  $k - \epsilon$  formulations are available in the literature. A large advantage of the Launder-Sharma one is that the low-Reynolds number terms do not include the explicit distance to the closest wall. Instead the parameter  $Re_t$  is used to incorporate the effect of turbulence damping when a wall is approached. In the same way, the model will incorporate the possible damping of turbulence when the oil-water interface is approached in core-annular flow. The low-Reynolds number  $k - \epsilon$  model is used everywhere in the domain, also in the laminar oil core. Because of the presence of the low-Reynolds number terms the model automatically relaminarizes in

the viscous oil core (i.e. it gives zero turbulent viscosity).

### 2.2.3 Numerical method

We used the open-source package OpenFOAM to solve the RANS equations, applying the CLVOF method for the interface capturing. The CLSVOF solver, which was developed by Yamamoto et al. (2017), is based on the interFoam Volume of Fluid (VOF) solver in OpenFOAM. The level set function is used to calculate the interfacial tension force. Starting from the VOF method, the oil volume fraction  $\alpha$  is introduced to distinguish between the two fluid phases:  $\alpha = 0$  is the oil phase,  $\alpha = 1$  is the water phase, and  $0 < \alpha < 1$  denotes the oil-water interface. Then the fluid density and viscosity in the equations are:

$$\rho = (1 - \alpha)\rho_o + \alpha\rho_w \quad (2.6)$$

$$\mu = (1 - \alpha)\mu_o + \alpha\mu_w \quad (2.7)$$

The subscript “o” refers to oil, and the subscript “w” refers to water.  $\alpha$  is calculated from the following advection equation:

$$\frac{\partial \alpha}{\partial t} + \nabla \cdot (\alpha \vec{u}) + \nabla \cdot ((1 - \alpha)\alpha \vec{u}_r) = 0 \quad (2.8)$$

The third term on the left-hand side is the compressive term (with the divergence of compressive flux); here  $\vec{u}_r = \vec{u}_w - \vec{u}_o$ . The term is meant to control the sharpness of interface.

The level set function  $\Phi$  is defined as the distance from the interface, where the interface is the isoline with  $\Phi = 0$ . The initial value of the level set function  $\Phi_0$  is obtained from the initialized volume-of-fluid field, where the interface is defined at  $\alpha = 0.5$ :

$$\Phi_0 = (2\alpha - 1)\Gamma \quad (2.9)$$

$$\Gamma = 0.75\Delta X \quad (2.10)$$

Here  $\Delta X$  is the minimum mesh size near the interface. Thereafter the re-initialization equation is solved to turn the initial level set function into the distance from the interface:

$$\frac{\partial \Phi}{\partial \tau} = \text{sign}(\Phi_0)(1 - |\nabla \Phi|) \quad (2.11)$$

Here  $\tau = 0.1\Delta X$  is the iteration time step of  $\Phi$  and the sign function denotes:

$$\text{sign}(\Phi) = \begin{cases} 1 & \Phi > 0, \text{ water} \\ 0 & \Phi = 0, \text{ interface} \\ -1 & \Phi < 0, \text{ oil} \end{cases} \quad (2.12)$$

Then the interface tension force is calculated as:

$$\vec{F}_\sigma = \sigma \kappa(\Phi) \delta_\phi \nabla(\Phi) \quad (2.13)$$

Here  $\sigma$  is the interface tension and  $\delta_\phi$  is the smoothed delta function:

$$\delta_\phi = \begin{cases} \frac{1}{2\gamma} \left( 1 + \cos\left(\frac{\pi\Phi}{\gamma}\right) \right) & \text{for } |\Phi| < \gamma \\ 0 & \text{elsewhere} \end{cases} \quad (2.14)$$

The quantity  $\gamma$  is the interface thickness coefficient (see Yamamoto et al., 2017) and  $\kappa(\Phi)$  is the interface curvature:

$$\kappa(\Phi) = \nabla \cdot \vec{n}_c \quad (2.15)$$

$$\vec{n}_c = \frac{(\nabla \Phi)_f}{|(\nabla \Phi)_f|} \quad (2.16)$$

Here  $\vec{n}_c$  is the surface unit normal vector. The contact angle  $\theta$  between the interface and the pipe wall is defined as:

$$\cos(\theta) = \vec{n}_c \cdot \vec{n}_w \quad (2.17)$$

With  $\vec{n}_w$  being the unit normal vector at the wall. The contact angle is set to  $90^\circ$  in our simulations. This means that both the level set function  $\Phi$  and the volume fraction of the fluid  $\alpha$  satisfy the zero

gradient condition at the pipe wall boundary.

A perfect (laminar) core-annular flow (which means that the oil core is cylindrical and concentric) is set as an initial condition. An analytical (laminar) velocity profile is set for the whole flow domain:

$$u^*(r^*) = \begin{cases} (a^2 - r^{*2})/A & 1 \leq r^* \leq a \\ 1 - mr^{*2}/A & r^* < 1 \end{cases} \quad (2.18)$$

$$A = m + a^2 + 1$$

Where  $r^* = r/R_c$  is the dimensionless distance to the pipe centre,  $R_c$  is the oil core radius,  $a = R/R_c$  is the ratio of the pipe radius and the oil core radius,  $m = \mu_w / \mu_o$  is the ratio of the water viscosity and the oil viscosity.  $u^* = u/u_c$  is the dimensionless velocity in the main flow direction, where  $u_c$  is the centreline velocity. Note that this velocity profile is only used to start the simulation. Of interest is the oscillating solution obtained after some time, which is (supposed to be) independent of the start condition.

A pressure drop in the flow direction is added as an extra force term to the right-hand side of equation (2.2), with periodic boundary conditions on the left and right side of the pipe. The velocity profile will then develop over time under this pressure drop in the transient simulation until a stable state (with an eccentric oil core) is obtained. Therefore, the pressure that remains in the equations is periodic with respect to the left and right side of the computational pipe section.

A second-order backward implicit time discretization scheme is applied, with a very small time step (small Courant number). This gives a very accurate time integration. We use a second-order scheme for the advection terms in the momentum equations and in the interface equation (as used in the level set method), but a first-order upwind scheme for the advection in the equations for the turbulence quantities  $k$  and  $\varepsilon$ ; trying a second-order scheme for the latter gave numerical instabilities. Through successive mesh refinement, however, we have demonstrated (see the details later) that the simulation results are accurate (and not suffering from large numerical diffusion).

In all the simulations, periodic boundary conditions are applied on the left and right side of the pipe, which restricts the wavelengths in the axial direction to twice the domain length divided by an integer value. At the pipe wall, the no-slip condition is imposed. We have used the symmetric PBiCG solver for the velocity and for the turbulent quantities, the GAMG solver for the pressure, and the PIMPLE solver for the velocity-pressure coupling.

### 2.2.4 Considered base conditions

The simulation conditions were the same as in the lab experiment. The pipe radius is  $R=0.0105$  m (pipe diameter is 21 mm). The length of the pipe section is set to 0.0256 m (25.6 mm), which is twice the most dominant wavelength, as estimated from a linear instability analysis (albeit for laminar flow) by Beerens et al. (2014). The fluid properties are set as follows: the oil and water kinematic viscosity are  $\nu_o = 7.73 \times 10^{-4}$  m<sup>2</sup>/s and  $\nu_w = 6.7 \times 10^{-7}$  m<sup>2</sup>/s, the oil and water densities are  $\rho_o = 902$  kg/m<sup>3</sup> and  $\rho_w = 993$  kg/m<sup>3</sup>, and the interfacial tension between oil and water is  $\sigma = 0.016$  N/m (Shell Morlina S2 B 680 at 40 °C was used in the experiments). Note that the ratio between the kinematic viscosities of oil and water is 1150, and the density ratio between the oil and water is  $\rho_o/\rho_w = 0.91$ . The Reynolds number in wall units, i.e.  $Re_\tau = d^+ = u_\tau d/\nu_w$ , is about 150 (here  $u_\tau$  is the wall shear stress velocity and  $d$  is the average thickness of the water annulus). This is above the minimum value of about 90 which is needed to sustain turbulence in single phase channel flow (where  $d$  is half the channel width); this criterion was derived by Jimenez & Moin (1991), who applied DNS to channel flow. The occurrence of turbulence in the water annulus is confirmed in the present simulations, which show an inertial sublayer with a maximum turbulent viscosity ( $\nu_t/\nu_w$ ) of about 20.



### 2.2.5 Key parameters

Four important parameters are: the total flow rate, the pressure drop, the watercut, and the water holdup fraction. When two parameters are set as input (e.g. the total flow rate and the watercut in the experiments), the other two will follow as output.

The watercut is defined as the ratio of the water volumetric flow rate and the total volumetric flowrate:

$$WC = Q_w / (Q_o + Q_w) \quad (2.19)$$

where  $Q$  denotes the volumetric flow rate. The water holdup fraction is defined as the ratio of the in-situ water volume in the pipe and the total volume of oil and water:

$$\alpha_w = \frac{V_w}{V_w + V_o} \quad (2.20)$$

A related parameter is the so-called holdup ratio  $h$ , which is defined as:

$$h = \frac{Q_o/Q_w}{V_o/V_w} \quad (2.21)$$

This can also be rewritten as  $h = 1 + u_r/u_w$ . Here the velocity difference  $u_r = u_o - u_w$ , is the apparent (average) slip velocity between the oil core (having a bulk velocity  $u_o$ ) and the water annulus (having a bulk velocity  $u_w$ ). Note that  $h=1$  if there is no slip between the bulk oil and water velocities. The holdup ratio thus is a measure of the apparent slip between the oil core and the water annulus.

### 2.2.6 Verification of the simulations

To verify the implementation of the Launder& Sharma low-Reynolds number  $k - \epsilon$  model in the OpenFOAM CFD package, we have coded the same model in Matlab, though using the 1D equations. 1D means that perfect core-annular flow is considered, though allowing for a turbulent water annulus. “Perfect” means that the oil core is concentric (i.e. no gravity in a horizontal pipe) and that there are no waves on the water-oil interface. The 1D model also allowed to determine the required grid resolution close to the wall for the accurate representation of the turbulent profiles. Similar 1D simulations were carried out with OpenFOAM. There was excellent agreement between the results obtained with the two simulation models.

To verify the numerical accuracy of the mesh resolution in OpenFOAM, first the 2D axi-symmetric case is studied, because such a simulation requires far less computer time than a full 3D simulation. We imposed a constant total flow rate of  $4.3 \times 10^{-4} \text{ m}^3/\text{s}$  (which is the value applied in the lab experiment). To obtain a watercut of (about) 20% (being the same as in the experiment condition), the water holdup fraction in the simulation had to be set to 0.257. Therefore in these simulations the total flow rate and the water holdup fraction were used as boundary conditions, whereas the pressure drop and the watercut are obtained as output values.

For the mesh refinement, the following stretch function is used in the radial direction:

$$\frac{y_j}{y_{j\max}} = 1 + \frac{\tanh[\alpha_1(j/j\max - 1)/2]}{\tanh(\alpha_1/2)}, \quad j = 0, 1, \dots, j\max \quad (2.22)$$

Where  $j\max$  is the total number of mesh points and  $y_{j\max}$  is the coordinate of the  $j^{\text{th}}$  node. A proper value of  $\alpha_1$  is used to ensure that there are several grid points in the viscous sublayer along the pipe wall. The stretch function will make the mesh smooth (which improves the numerical accuracy and increases the simulation speed). The coefficient  $\alpha_1$  is found from the expression  $\alpha_2 = \alpha_1/\sinh(\alpha_1)$ , in which  $\alpha_2$  is close to zero. In the present simulations we took  $\alpha_2 = 0.26$ , in order to make sure that some grid points are located in the viscous sublayer along the pipe wall. A uniform mesh is used in the axial direction. In the 3D case, also a uniform mesh is used in the circumferential direction.

Table 2.1 summarizes the values of key quantities at successively refined meshes in the 2D



simulations (100x100, 200x200, and 400x400). The quantities shown in the table were obtained by analysing the temporal results at a fixed streamwise location in the simulated pipe section. It turns out that the wave velocity is practically independent of the local water annulus thickness (or the local wave height). This means that the temporal wave evolution can be converted to the spatial wave propagation through using this constant wave velocity (i.e. the Taylor hypothesis applies). The simulated section length of 25.6 mm shows precisely 2 waves; the wave length thus is 12.8 mm. The wave amplitude is defined as

$$A = \sqrt{2(\delta - \bar{\delta})^2} \quad (2.23)$$

Here an overbar denotes the time-averaged value (as determined at a fixed  $x$ -location in the pipe);  $\delta$  is the thickness of the water annulus. The amplitude is defined such that it gives the usual value of the amplitude for the case that the wave is a pure sinus (where the amplitude is half the difference between the maximum and the minimum value). Note that definition (23) for the amplitude is also meaningful for an irregular time dependence of the water annulus thickness (i.e. without a single frequency). Figure 2.2 gives an example of the simulated wavy interface.

Mesh refinement does not yet show the full asymptotic decay of the numerical error, but the differences between the various meshes are quite small. This is shown for the oscillating thickness of the water annulus in Figure 2.3. The table also confirms that some grid points are located in the viscous sublayer along the pipe wall ( $y^+ < 5$ ). This is important because here the turbulence is damped by the low-Reynolds number terms in the  $k - \epsilon$  model. Having sufficient grid points here is essential for obtaining an accurate numerical value for the wall shear stress, and thus for the pressure drop. As shown in the table, the pressure drop still shows some mesh dependence (from 814 Pa/m on the 100x100 mesh to 748 Pa/m for the 400x400 mesh). To verify the importance of having sufficient grid points very close to the wall, the simulation with 100x100 points was repeated with a different value of the stretching parameter in Equation 2.22, giving the first inner grid point at  $y^+ = 0.6$  instead of 3; this indeed improves the prediction of the pressure drop from 814 to 746 Pa/m (with the latter value being close to 748 Pa/m found on the very fine 400x400 mesh). There are also a significant number of grid points through the wavy interface. In the 2D simulations, considering the number of points in radial direction covering the wave between its crest and trough, we have about 25 points for the 100x100 mesh, 50 points for the 200x200 mesh, and 100 points for the 400x400 mesh.

**Table 2.1. Mesh verification in the 2D case.**

Quantity	Unit	100× 100	200× 200	400× 400
Imposed total flow rate	m <sup>3</sup> /s	0.00043	0.00043	0.00043
Imposed water holdup fraction		0.257	0.257	0.257
Watercut	%	21.4	21.9	22.2
Pressure drop	Pa/m	814	818	748
Water layer thickness	mm	1.53	1.51	1.49
Wave amplitude	mm	0.60	0.71	0.73
Wave velocity	m/s	1.23	1.24	1.25
Wave frequency	Hz	96.1	96.7	97.7
Wave length	mm	12.8	12.8	12.8
Maximum $v_t/v_w$		17.2	16.9	18.8
$y^+$ value at the first inner grid point		3	1	0.6

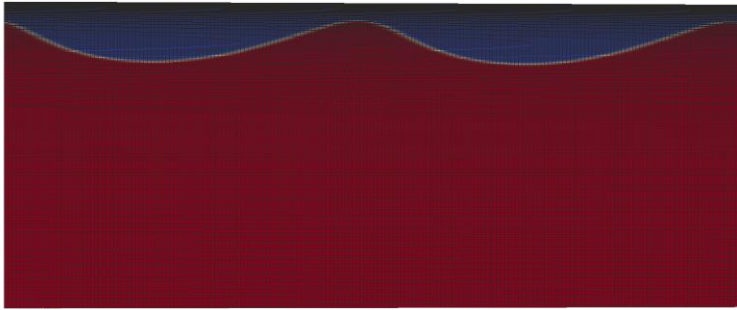


**Figure 2.2.** Snapshot of the 2D axis-symmetric simulation showing the oil-water interface together with the 200x200 mesh. The travelling waves at the interface move from left to right. The water layer is shown in blue, the oil core in red, and the interface is shown as a white line.

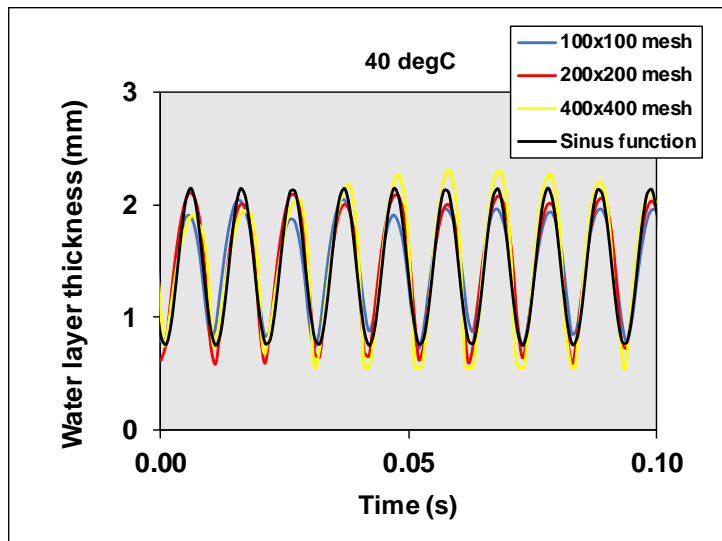


**Figure 2.3.** Mesh dependence of the oscillating thickness of the water annulus. For comparison, also a purely sinusoidal oscillation is included.

The applied mesh in the 3D simulations is as follows. Near the origin we use a pentagon area, which is covered with a structured O-grid. This area is part of the laminar oil core. Around this area there is a cylindrical area up to the pipe wall that applies an axis-symmetric grid. This covers the outer part of the oil core, the wavy oil-water interface and the water annulus. Here we use an axis-symmetric grid with a uniform distribution in azimuthal direction. The mesh stretching function in radial direction is the same as used in the 2D axisymmetric simulations. Based on the 2D mesh verification results, the mesh resolutions of  $100 \times 200 \times 80$  points and  $100 \times 200 \times 160$  points were used in axial, radial, and the circumferential direction, respectively, in the 3D simulations. In the verification of the 3D results the imposed pressure drop was 725 Pa/m and the imposed water holdup fraction was 0.257. It is found that the results, such as the total flow rate, are not very sensitive to the resolution in the circumferential direction; the total flow rate is  $4.8 \times 10^{-4} \text{ m}^3/\text{s}$  with 80 points in circumferential direction and  $4.7 \times 10^{-4} \text{ m}^3/\text{s}$  with 160 points in circumferential direction. However, there is more dispersion of oil droplets in the water annulus with the 80 points than with the 160 points. The mesh resolution with 160 points in circumferential direction is concluded to be adequate; the 3D results obtained with the  $100 \times 200 \times 160$  mesh resolution will be discussed in this chapter.

## 2.3 1D results

The base case conditions for the comparison between the simulation results and the lab experiments are the total flow rate of  $0.00043 \text{ m}^3/\text{s}$  and a watercut of 20%. The oil viscosity is  $\nu_o = 7.73 \times 10^{-4} \text{ m}^2/\text{s}$  (and the other oil and water properties are those specified in section 2.4). The corresponding average velocity (or the mixture velocity, being the ratio of the total flow rate and the cross section of the pipe) is  $1.24 \text{ m/s}$ .

The 1D model (which means that there is no gravity effect and no interfacial waves) gives a pressure drop of  $418 \text{ Pa/m}$  and a water holdup fraction of  $0.320$  (these results are fully grid-independent). This pressure drop is significantly higher than the value of only  $108 \text{ Pa/m}$  for laminar perfect CAF, which shows the effect of turbulence in the water annulus (but the water holdup fraction for laminar flow remains about the same at  $0.333$ ). The predicted pressure drop with the turbulent water annulus is significantly lower than the experimental value of (about)  $1100 \text{ Pa/m}$  and the water holdup fraction is significantly higher than the experimental value of (about)  $0.257$ . The difference is not surprising, as a flat interface (no waves) has been assumed in this model, being perfect turbulent CAF. However, the 1D model already gives a good impression of the turbulence in the water annulus. Thereto, Figure 2.4 shows the streamwise velocity profile and the turbulent viscosity. Here the distance to the wall is  $y=R-r$ . The velocity and distance are given in the familiar “plus” units (or wall units, using the wall shear velocity and the kinematic water viscosity). The turbulent viscosity is scaled with the kinematic water viscosity. The water annulus is driven by the combined effect of the pressure gradient and the oil core movement. This gives the Couette like velocity profile, which closely follows the logarithmic law-of-the-wall in the inertial sublayer (which is between about  $y^+$  is 10 and 100 in this simulation). Close to the interface, the water velocity shows a sharp increase to reach the oil core value.

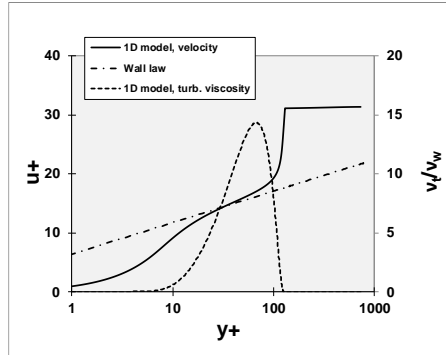


**Figure 2.4. 1D velocity and turbulent viscosity; total flow rate is  $0.00043 \text{ m}^3/\text{s}$ , watercut is 20% (oil viscosity is  $\nu_o = 7.73 \times 10^{-4} \text{ m}^2/\text{s}$ ). Distance to wall is  $y = R - r$ .**

It is convenient to use the 1D model to verify the scaling of the turbulent water annulus. The model runs very fast and fully grid-independent results can be obtained. Thereto the shear-based Reynolds number for the water layer was increased with a factor 10 and 100 with respect to its base value; see the results in Figure 2.5. As shown by Henkes (1998), the Launder & Sharma low-Reynolds number  $k - \epsilon$  model will give the following asymptotic behaviour in the inertial sublayer of wall-bounded turbulent flow:

$$u^+ = \frac{1}{\kappa} \ln y^+ + C, \quad v_t^+ = \kappa y^+, \quad k^+ = \frac{1}{\sqrt{C_\mu}}, \quad \epsilon^+ = \frac{1}{\kappa y^+} \quad (2.24)$$

With  $\kappa = 0.431$ ,  $C = 6.4$ ,  $C_\mu = 0.09$  (these parameters hold for the Launder & Sharma formulation).

The  $+$  superscript refers to quantities scaled with the kinematic water viscosity  $\nu_w$  and with the wall shear velocity  $u_\tau = \sqrt{\tau_w/\rho_w}$  (in which  $\tau_w$  is the wall shear stress):

$$u^+ = u/u_\tau, \quad v_t^+ = v_t/\nu_w, \quad k^+ = k/u_\tau^2, \quad \epsilon^+ = \epsilon \nu_w/u_\tau^4 \quad (2.25)$$

As shown in Figure 2.5, an increasing Reynolds number for the water annulus gives an increasing range of  $y^+$ , which gives converge to the asymptotic wall laws specified in Equation (2.24). The inertial subrange for the relatively low Reynolds number that corresponds with the experimental conditions that are the main focus of the present study is relatively small (namely from about  $y^+=10$  to 100). But despite this, the Reynolds number is already sufficiently high to give fully turbulent flow that is close to the asymptotic law-of-the-wall behaviour. When analysing the 2D and 3D results in the subsequent sections, the wall laws will again be shown for comparison.

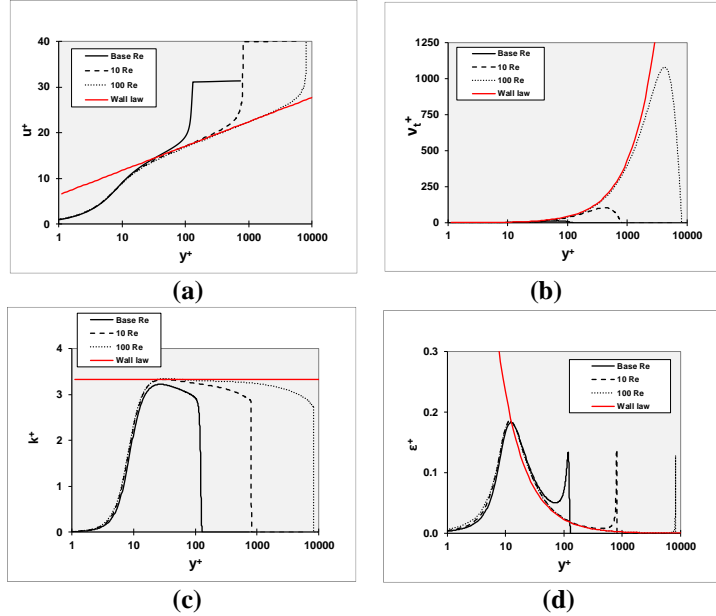


**Figure 2.5. Turbulent scaling in the inertial sublayer of the water annulus (applying the 1D model); (a) streamwise velocity,  $u^+ = u/u_\tau$ , (b) turbulent viscosity,  $\nu_t^+ = \nu_t/\nu_w$ , (c) turbulent kinetic energy,  $k^+ = k/u_\tau^2$ , (d) turbulent dissipation rate,  $\epsilon^+ = \tilde{\epsilon}\nu_w/u_\tau^4$ .**

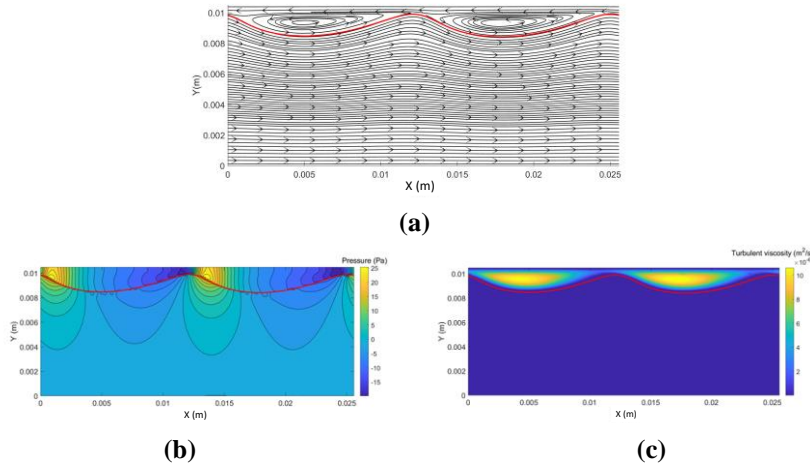
## 2.4 2D results

The prescribed conditions in the 2D simulations were a total flow rate of 0.00043 m<sup>3</sup>/s and a water holdup fraction of 0.257. This gives as output a watercut of 22% and a pressure drop of about 750 Pa/m (see Table 2.1). The water holdup fraction and watercut are in agreement with the experimental values (being 0.257 and 20%). The pressure drop is still significantly underpredicted (by about 30% compared to 1100 Pa/m), though this already means a large improvement compared to the 1D case. Also the 2D results for the water holdup / watercut in 2D are much better than for the 1D case. As expected, allowing for the presence of waves in the model is crucial for the prediction of the pressure drop in core annular flow.

The average oil velocity (being the ratio of oil flow rate and the oil holdup fraction) is 1.30 m/s, and the average water velocity (being the ratio of the water flow rate and the water holdup fraction) is 1.06 m/s. The mixture velocity is 1.24 m/s.

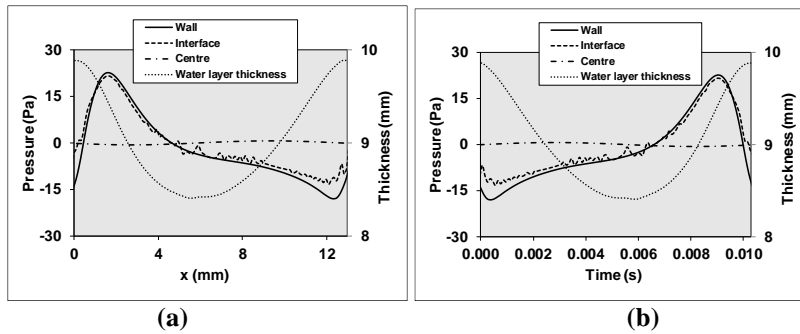
The waves in the 2D results move with a practically constant velocity of 1.24 m/s (independent of the local wave height, or of the local thickness of the water annulus); the wave velocity happens to be equal to the mixture velocity here (which is in between the average oil velocity and the average water velocity). This constant wave velocity means that an observer traveling with this wave velocity will experience a steady state flow (with the RANS approach). That flow as seen from a reference frame moving with the wave velocity is depicted in Figure 2.6 for the streamlines, pressure and turbulent

viscosity. When defining the waves with respect to the oil core, the wave crest is at the location where the water annulus is thinnest and the wave trough is at the location where the water annulus is thickest. With respect to the travelling wave, there is a recirculation zone of water in between the wave trough and crest locations. Turbulence is highest at the wave trough location (thickest water annulus, giving highest local shear-based Reynolds number) and lowest at the wave crest location (thinnest water annulus, giving lowest local shear-based Reynolds number). At a certain streamwise location, the pressure is almost constant across the thickness of the water annulus.



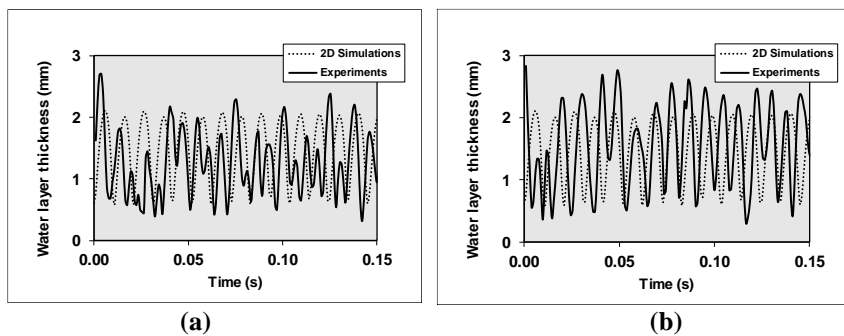
**Figure 2.6. 2D results with respect to observer that travels with the wave velocity of 1.24 m/s; (a) streamlines, (b) isobars, (c) turbulent viscosity.**

Figure 2.7 shows the pressure at the pipe wall and at the oil-water interface, along with the thickness of the water annulus. This is done both at a certain time in spatial direction (left graph) and at a certain streamwise location over time (right graph). The two graphs can be converted into one another by using the 1.24 m/s wave velocity. The figure confirms that the wall pressure and interface pressure are very close. The pressure is largest at the location where the dividing streamline of the recirculation zone reattaches at the interface (which can be seen as the windward side of the interface) and pressure is lowest at the location where the dividing streamline of the recirculation zone leaves the interface (which can be seen as the leeward side of the interface). Through integrating the pressure along the interface in  $x$ -direction the form drag working on the wave interface can be determined. The shear-stress force on the interface in  $x$ -direction can be determined from a force balance (using the wall shear stress force, the driving pressure force, and the form drag). It turns out that 68% of the interface force is due to pressure (form drag) and 32% due to shear stress. Figure 2.7 also shows that the pressure at the oil core centre is almost constant. As the pressure jump across the interface due to the interface tension is 4 Pa at most (at locations with the highest interface curvature), the fluctuations in the interface pressure (of about 20 Pa) are also felt in the oil core. This will lead to (small) secondary flow in the oil core.



**Figure 2.7.** 2D simulation results for the pressure distribution; (a) spatial (flow is from left to right), (b) temporal.

As shown in Figure 2.8, there is a very good agreement for the frequency and amplitude of the interfacial waves as obtained in the 2D simulations and in the lab experiments. This will be discussed further in the next sections, which will also include the 3D simulation results.



**Figure 2.8.** Comparison of 2D results with experiments for the thickness of the water annulus; (a) top layer, (b) bottom layer.

## 2.5 3D Results

### 2.5.1 Simulation set-up

3D simulations were carried out for cases without and with gravity. Without gravity, the oil core remains concentric in the pipe, but a symmetry breaking of the interface has appeared, as compared to the results obtained with the 2D axi-symmetric model (but the flow characteristics remain fairly close to the 2D results). When the gravity is added, the oil core becomes eccentric, with a water annulus that is thinner at the top than at the bottom. Some dispersion of oil droplets in the bottom water layer occurs; these oil droplets make up about 0.3% of the oil volume in the oil core.

In the 3D simulations with gravity a pressure drop of 725 Pa/m was prescribed, along with a water holdup fraction of 0.257, which gave a total volumetric flow rate of  $0.00047 \text{ m}^3/\text{s}$  and a watercut of 20% (which are close to the value set in the experiments, being  $0.00043 \text{ m}^3/\text{s}$  total flow rate and 20% watercut). The pressure drop and water holdup fraction were used as boundary conditions in the 3D simulations, as this is computationally much more convenient than prescribing the total flow rate and the watercut. Note that the 3D simulations (on a rather fine mesh) require a large computational time. It would have been better to iterate the conditions for the pressure drop to obtain a flow rate precisely equal to the experimental value (while maintaining the 20% watercut), but this was not done because of the available computer resource capacity.

Although the flow rate in the 3D simulation (with gravity) is slightly higher than in the experiments (by 9%), the pressure drop is still 34% lower (725 Pa/m instead of 1100 Pa/m). Thus, switching from 2D to 3D does not imply a pressure drop value closer to the experimental value.

### 2.5.2 Turbulence characteristics

The (spatially and temporally averaged) values of the turbulent viscosity (scaled with the water viscosity) over the cross section of the pipe are shown in Figure 2.9. Shown are the values obtained by averaging both in time and in streamwise spatial direction. Both the results with gravity and without gravity are depicted. Without gravity, the (time and space averaged) oil core is concentric and circular (i.e. axi-symmetric). The water annulus is turbulent (as  $\nu_t/\nu_w > 1$ ) and the oil core is laminar (almost zero turbulent viscosity). When gravity is added, the oil core rises giving a thinner water annulus at the top and a thicker water annulus at the bottom. As a consequence (compared to the concentric core without gravity), the turbulent viscosity decreases in the top layer and increases in the bottom layer.

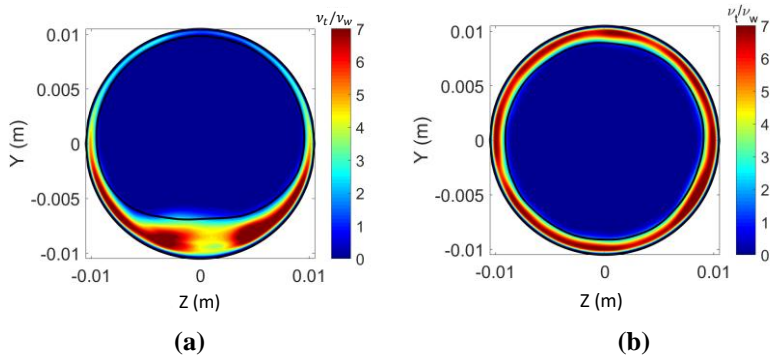


**Figure 2.9. Comparison of the turbulent viscosity (scaled with the water viscosity) for the 3D simulation; (a) with gravity, (b) without gravity. Values are averaged over time and along the main flow direction. The oil-water interface is indicated with a solid black line.**

What follows here is for the case with gravity. The relation between the turbulence and the water annulus thickness is also clear from the temporal fluctuations at a fixed streamwise location, as is shown in Figure 2.10. The frequency of the oscillation of the top layer is about double that of the bottom layer. The turbulence in the top layer is very low, whereas the bottom layer shows an oscillation between full turbulence at the wave trough and a tendency to relaminarization at the wave crest.

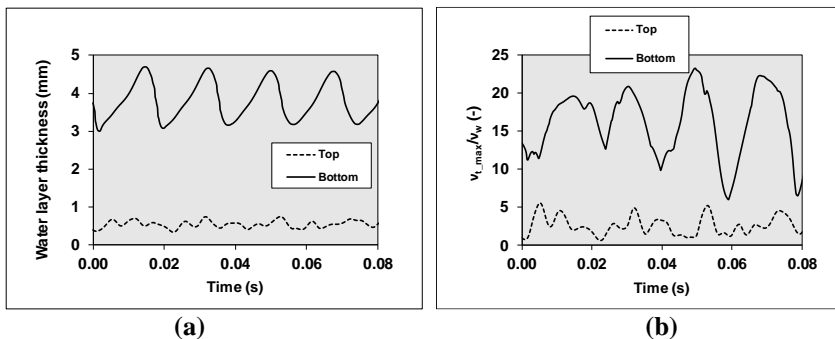


**Figure 2.10. Temporal fluctuation at fixed streamwise location in 3D simulation; (a) water layer thickness, (b) maximum in the turbulent viscosity.**



A snapshot of the turbulence profiles in the bottom layer at the location where the water annulus is thickest (wave trough) is shown in Figure 2.11. For comparison, also the 1D and 2D simulation results are included. All quantities are non-dimensionalized with the wall shear velocity  $u_\tau$  and the kinematic water viscosity  $\nu_w$ . Also the asymptotic wall layer layers (see section 3) are included. There is a close agreement between the scaled velocity profile as found in the 1D, 2D, and 3D simulations. Note the maximum value of  $u^+$  (which denotes the bulk oil core velocity) is different for the 1D, 2D, and 3D results; this is because of the difference in wall shear stress near the pipe wall. Very close to the wall, which is in the viscous sublayer, we have  $u^+ = y^+$ . In the inertial sublayer, i.e. between about 10 and 100 in these simulations, the turbulence profiles are fairly close to the law-of-wall curves, which demonstrates that full turbulence (i.e. vanishing effect of the low-Reynolds number terms in the  $k - \epsilon$  model) has been reached.

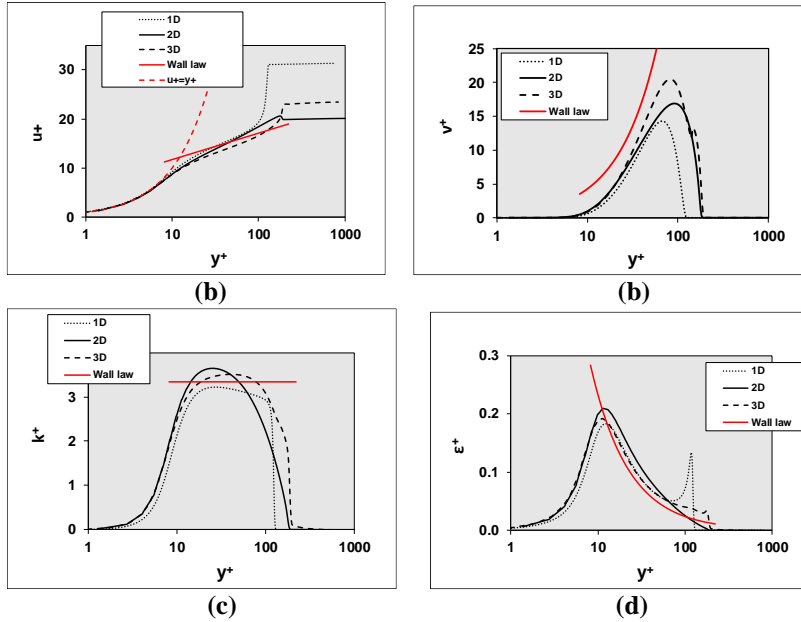


**Figure 2.11.** Instantaneous quantities as function of the scaled distance to the wall at the location of the thickest water annulus along the bottom (wave trough); (a) streamwise velocity,  $u^+ = u/u_\tau$ , (b) turbulent viscosity,  $\nu_t^+ = \nu_t/\nu_w$ , (c) turbulent kinetic energy,  $k^+ = k/u_\tau^2$ , (d) turbulent dissipation rate,  $\epsilon^+ = \epsilon \nu_w / u_\tau^4$ .

### 2.5.3 Levitation mechanism

The density difference between the water and oil, in the presence of gravity in horizontal CAF flow, will cause the oil core to move upward, giving an eccentricity. To study this levitation mechanism due to the presence of gravity, the forces acting on the oil core will be analysed. See the sketch with definitions in Figure 2.12. The index 2 denotes the wall location and  $S_2$  is the pipe wall. Furthermore,  $w$  represents water and  $o$  represents oil,  $\vec{n}$  is the surface normal vector,  $\rho$  is the density,  $g$  is the gravitational acceleration,  $V$  is the volume,  $p$  is pressure and  $\tau$  is shear stress.



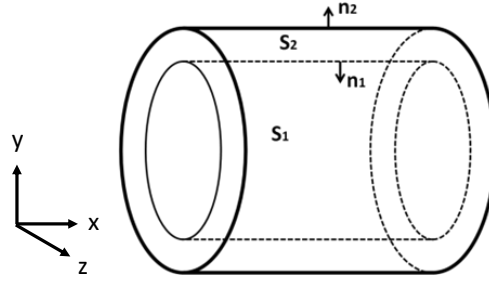


**Figure 2.12. Definition of the surfaces and the normal vectors.**

The total force on the oil core in our simulation can also be calculated as:

$$F_y^{core} = \frac{d}{dt} \int_{V_o} \rho_o v dV \quad (2.26)$$

This total force acting on the oil core, as derived from the 3D simulation results, is shown in Figure 2.13. In the first part of the transient simulation ( $t < 0.25$  s), which starts with a concentric oil core, the total force is positive, due to the upward buoyancy, and the oil core moves upward. Then, in the time interval  $0.13 \text{ s} < t < 0.25 \text{ s}$  (as indicated in the figure), the total force on the core is negative, acting downward. This is the stage during which the eccentric core is decelerated and its upward velocity is reduced. The downward force is related to waves which are created at the oil-water interface. After 1 s, when the levitation of the core has become stable, the total force acting on the oil core shows a small oscillation around zero.

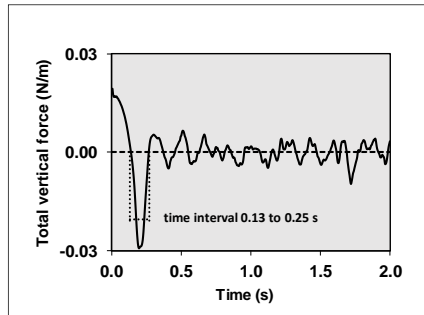


**Figure 2.13. Total upward force (per meter pipe length) acting on the oil core as a function of time.**

The levitation mechanism of CAF has been studied by several researchers (albeit in the presence of a laminar water annulus). By neglecting inertia, Ooms et al. (1984) developed the lubricated-film model, in which the viscous force acting on the core surface balances the buoyancy force. This model is applied with a saw tooth shaped interface. Bai et al. (1992) claimed that the lubrication force and the inertia force might coexist in core-annular flow. Under the effect of the inertia force, the wave shape will become more rounded. Clearly under the present conditions with a Reynolds number that gives turbulent flow in the water annulus, the inertia terms are important (as they lead to the Reynolds stresses in the RANS equations, as modelled by the  $k - \epsilon$  model). To study the wave forces, the reduced pressure is used in this study:  $\phi_2$  is defined as the hydrodynamic pressure without the hydrostatic contribution due to water:

$$\phi_2 = p_2 + \rho_w g y \quad (2.27)$$

Then the total resulting force (which gives the acceleration) acting on the oil core can be split as:

$$F_y^{core} = \underbrace{\int_{S_1} (\phi_2)_{S_1} n_{1,y} dS_1}_{\phi_y^{core}} + \underbrace{\int_{S_1} (-\tau_{2,yk}^{(v)}) n_{1,y} dS_1}_{\tau_y^{core}} + \underbrace{(\int_{S_1} (-\rho_w g y)_{S_1} n_{1,y} dS_1 - \rho_o g V_o)}_{B_y^{core}} \quad (2.28)$$

$S_1$  is the oil-water interface (which has  $\alpha = 0.5$ ),  $n_1$  is the normal vector at the oil-water interface, calculated from the volume fraction  $\alpha$ :

$$n_1 = \frac{\nabla \alpha_1}{|\nabla \alpha_1|} \quad (2.29)$$

The first and second terms on the right hand side of Equation 2.28 are the reduced pressure force  $\Phi_y^{core}$  and the viscous stress  $T_y^{core}$  acting on the core, respectively, and the third term is the buoyancy force for the core  $B_y^{core}$ .

The reduced pressure force, the viscous force, and the buoyancy force, all working on the oil core, are shown in Figure 2.14. Here the minus sign denotes that the force is acting downwards.

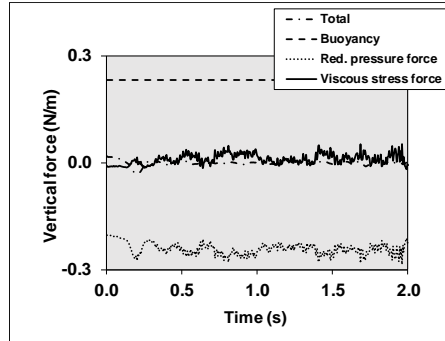


**Figure 2.14.** Reduced pressure force, shear stress force, buoyancy force, and resulting force for the oil core as a function of time; note that the vertical axis shows the force per meter pipe length.

Under the influence of gravity, a secondary flow will be induced by the flow dynamics. To obtain the main characteristics of the secondary flow, the velocity is averaged both in time and in streamwise spatial direction. In this way a 2D velocity field is obtained. When the oil core is moving upward in the time-dependent flow with traveling waves at the oil-water interface, a downflow of water will be induced in the water annulus at the left and right sides. Due to the wave motion the oil core will locally move continuously up and down over time. After averaging, non-zero values of the velocity in the 2D velocity field are found.

The resulting averaged streamlines are shown in Figure 2.15a, where the colour represents the velocity magnitude. Due to the averaging, a (nearly) symmetric flow pattern is obtained. The maximum in the (averaged) secondary flow velocity is 0.014 m/s, which is around 1% of the oil core velocity. The maximum is found in the water annuli at the left and right sides. The velocity magnitude in the top and bottom layer is small. Figure 2.15b shows the azimuthal velocity at various angles. As can be seen, a shear flow exists at the left and right hand side of the pipe. The water close to the pipe wall is flowing downward and the water close to the interface with the oil core flowing upward. In the bottom layer, two symmetric vortices, with opposite rotation direction, exist. The secondary flow velocity is also large near to these vortices. A higher turbulent viscosity exists in these recirculation zones. At the very bottom part, the streamlines show more recirculation zones but the velocity magnitude is small. This is where some dispersed oil droplets float in the water layer. Figure 2.15c shows the isobars for the reduced pressure. The reduced pressure is higher in the top water layer than in the bottom water layer. The pressure difference between the top and bottom compensates the buoyancy force on the oil core. This will be discussed in more detail in the next subsection.

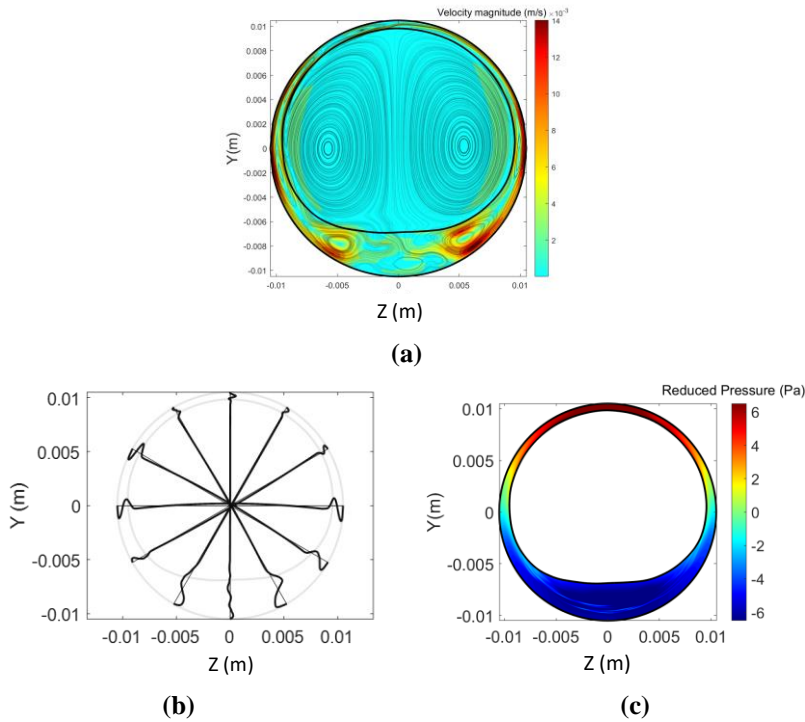


**Figure 2.15. Flow in 2D plane obtained after averaging; (a) streamlines, (b) azimuthal velocity distribution at different angle locations, (c) contours of the reduced pressure.**

### 2.5.4 Interfacial waves

As discussed in the previous subsection, the (reduced) pressure plays a major role in the levitation of the oil core. The build-up of the pressure is closely related to the waves at the oil-water interface. To determine the wave velocity from the 3D results, the time dependent oscillation of the thickness of the water annulus was monitored at two very close streamwise locations and the time shift was determined. The ratio of distance between the locations and the time shift gives the wave velocity. This wave velocity is determined at the 3, 6, 9, and 12 o'clock locations around the perimeter. At a certain location along the perimeter, the wave velocity is almost constant (i.e. independent of the local water layer thickness), which means that the spatial wave movement and the temporal wave oscillations can be converted into each other by this fixed wave velocity. This wave velocity is about 1.2 m/s for the top wave and about 1.43 m/s for the bottom wave; this is comparable to the average velocity of 1.33 m/s in the oil core.

Figure 2.16 shows the instantaneous fluctuation in the pressure along the interfacial wave in the mid plane. The fluctuation is obtained by subtracting the time averaged pressure from the instantaneous value. The secondary flow velocity (which is the velocity after subtraction of the mean oil core velocity) is shown as streaklines in the same figure. The figure shows that the pressure fluctuates most at the top interface. At the bottom interface, there is less fluctuation. The streaklines show that there is flow recirculation in the wave trough in the bottom layer.

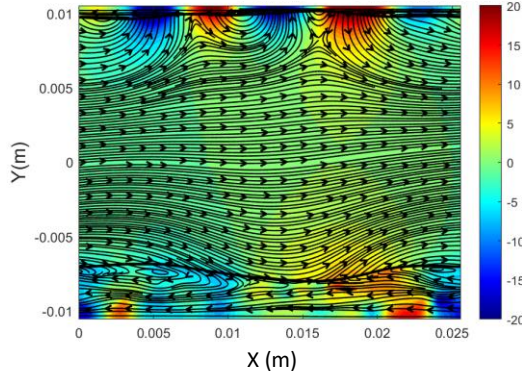


**Figure 2.16. Snap shot of the pressure fluctuation in the mid plane, as well as streak lines of the secondary flow. The oil-water interface is represented by a thick black line.**

Figure 2.17 shows the reduced pressure distribution along the top and bottom water annuli. Both the temporal and spatial dependence are shown. In fact the temporal result was mapped to the spatial distribution by using the fixed wave velocity; therefore, the spatial length in the figure is longer than the 25.6 mm used in the simulation.

As was already shown in Figure 2.10a for the 3D simulation results, the interfacial waves at the top have a wave length of about one-third (8.5 mm) of the waves at the bottom (25.6 mm). Due to the eccentricity, the average thickness of the water annulus at the top (0.6 mm) is much thinner than at the bottom (3.6 mm). As the water annulus is much thinner at the top, here the pressure reacts stronger on passing waves than at the bottom. This explains the difference in fluctuations in the reduced pressure, as shown in Figure 2.17. When comparing the pressure distribution with the location of the wave crests and troughs, it is seen again (similar to the 2D results) that the pressure is highest on the windward side of the interface and lowest at the leeward side of the interface. Through integrating the pressure along the interface in  $x$ -direction the form drag working on the wave interface can be determined. It turns out that 48% of the interface force is due to pressure (form drag) and 52% due to shear stress. This is the average for the total interface (i.e. all around the perimeter and along the length of the pipe section). The form drag strongly depends on the location at the interface: it is much smaller along the bottom interface (where the reduced pressure is fairly flat) compared to the top layer (where the reduced pressure shows a strong fluctuation).

From Figure 2.17 it is clear that the value of the reduced pressure in the top layer is almost always and everywhere higher than at the bottom layer. This gives a net downward force on the oil core, which counter balances the upward buoyancy force and prevents the oil from fouling the top wall. The figure also shows that the reduced pressure is fairly flat along the interface at the bottom layer, whereas it shows strong fluctuations along the top layer. This can be related to the amplitude of the waves along the bottom interface and along the top interface (see Figure 2.10): a thick water annulus with relatively large amplitude waves at the bottom and a thin water layer with small amplitude waves along the bottom. The amplitude of the waves at the bottom is so large that the water flow easily separates at almost the location of the wave crest, which gives almost parallel flow and thus almost no pressure change. This is in contrast to the top layer where the water flow follows the interface over a longer distance before it separates and reattaches, leading to the significant pressure fluctuations. The net effect is a “flying core flow” (as described by Joseph et al, 1997) with downward lift that counterbalances the upward buoyancy.

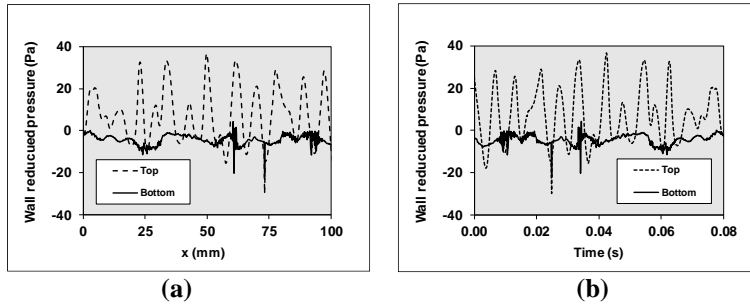


Figure 2.17. 3D simulation results for the reduced pressure distribution for the bottom and top layers; (a) spatial (flow is from left to right), (b) temporal.

## 2.6 Comparison of simulations with experiments

Table 2.2 compares the results from the CFD simulations with the experiments obtained in our lab. For the simulations, both the 2D and 3D results are considered. In the experiments the total flow rate and watercut were prescribed, and the output parameters pressure drop and water holdup fraction were obtained. In the 2D simulations (i.e. axi-symmetric, no gravity), the total flow rate and the water holdup fraction were prescribed, and the pressure drop and watercut followed as output. In the 3D simulations (with gravity) the pressure drop and water holdup fraction were prescribed, and the total flow rate and watercut followed as output. To make a most meaningful comparison, it is best to use scaled quantities to represent the flow rate and pressure drop on one hand, and the watercut and water holdup fraction on the other hand; chosen are the pressure drop reduction ratio ( $R_p$ ) and the holdup ratio ( $h$ ). The pressure reduction ratio is defined as the ratio between the pressure drop for single phase flow at the given oil flow rate and the water/oil pressure drop. The single phase oil flow will be laminar and has the well know pressure drop for Poiseuille flow:

$$-\frac{dP_{oil}}{dx} = \frac{128}{\pi} \frac{v_{oil} \rho_{oil} Q_o}{D^4} \quad (2.30)$$

The holdup ratio was already defined by Equation 2.21. The table shows that the pressure drop reduction factor for the 2D and 3D results is about the same, but its value is about 35% higher than in the experiment (or, at the same oil flow rate, the predicted pressure drop is about 35% lower than in the experiment).

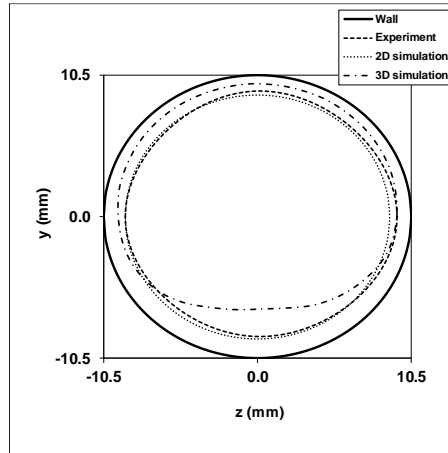
A holdup ratio larger than 1 corresponds to the relative accumulation of water (giving a lower bulk water velocity than the bulk oil velocity), which can be explained by the encapsulation of water in the troughs of the interfacial waves. Bai et al. (1992) performed an experimental study of vertical core-annular flow; it was found that in cases with high flow, for both upward and downward CAF, the holdup ratio is always equal to 1.39, independent of the oil and water flow rates. In the present study for horizontal CAF, the holdup ratio in the 3D model ( $h=1.38$ ) is close to the experimental value ( $h=1.41$ ), but the 2D prediction is slightly lower ( $h=1.23$ ). Therefore, the apparent slip between the oil and water (due to the interfacial stress) in the 3D simulation agrees with the experiment, but the 2D simulation gives a too low slip (or too much interfacial stress).

Table 2.2 . Comparison of the results.

		Experiment	2D simulation	3D simulation
Total flow rate	m <sup>3</sup> /s	0.00043	0.00043	0.00047
Water holdup fraction		0.26	0.257	0.257
Watercut	%	20	22	20
Pressure drop	Pa/m	1120	748	725
Holdup ratio (h)		1.41	1.23	1.38
Press. drop red. factor ( $R_p$ )		45	65	76
Eccentricity factor		0.014	0.000	0.145
Water layer thickness:				
Left	mm	1.48	1.49	1.22
Right	mm	0.96	1.49	1.04
Top	mm	1.24	1.49	0.57
Bottom	mm	1.53	1.49	3.62
Wave amplitude:				
Left	mm	0.83	0.73	0.48
Right	mm	1.09	0.73	0.46
Top	mm	0.78	0.73	0.19
Bottom	mm	1.13	0.73	0.65
Wave length:				
Left	mm	11.4	12.8	12.8
Right	mm	10.7	12.8	12.8
Top	mm	10.8	12.8	8.5
Bottom	mm	11.8	12.8	25.6
Wave velocity:				
Left	m/s	1.3	1.24	1.33
Right	m/s	1.37	1.24	1.33
Top	m/s	1.37	1.24	1.2
Bottom	m/s	1.21	1.24	1.43

It is also meaningful to compare the location of the oil core and the structure of the interfacial waves (wave amplitude, wave length, wave velocity). Figure 2.18 shows the average location of the water-oil interface, which also reveals the eccentricity of the oil core. The eccentricity factor is defined as the half the difference between thickness of the water annulus at the bottom and the top, scaled with the pipe radius. As shown in the figure (and in Table 2.2), there is only very little eccentricity in the experiment, whereas the 3D simulation gives much eccentricity (bottom water layer is much thicker than the top water layer). Comparison of the water layer thickness and the wave amplitude in Table 2.2 reveals a good agreement between the 2D predictions and the experiments, but larger deviations between the 3D predictions and the experiments. The 2D and 3D results for the wave velocity and

wave length (and for the wave frequency) are in good agreement with the experiments. An exception is the wave length in the bottom layer of the 3D results: this wave length is double the measured value.



**Figure 2.18.** Average location of the water-oil interface.

The comparison shows that there are remarkable differences between the simulations and the lab experiments: the predicted pressure drop reduction factor is significantly higher in the simulation than in the experiments and the eccentricity predicted by the 3D simulations is much higher than in the experiment. Due to the low eccentricity in the experiment, the 2D axi-symmetric simulation results (i.e. zero eccentricity) for the interfacial waves are in better agreement with the flow visualization in the experiments than the 3D results.

The observed differences can be due to limitations of using a low-Reynolds number  $k - \epsilon$  model. Such a model is expected to work well for attached wall-bounded flow, as the model parameters in the original model formulation have been tuned to properly describe the viscous sublayer and the intertial sublayer of such flows. The model will be less good in describing flow separation and the extent of recirculation zones, where using a differential stress model (within the RANS approach) instead of a two-parameter model like  $k - \epsilon$  should be used. A low-Reynolds number  $k - \epsilon$  model will also be less good in describing laminar-turbulent transition, such as in flows with relaminarization periods or zones. The considered water annulus in the present study has all three flow features: wall bounded flow along the pipe wall, flow separation with recirculation along the wave water-oil interface, relaminarization tendency if the water layer becomes too thin.

Using DNS for single phase channel flow, Jiménez & Moin (1991) (see also Rocco et al., 2019, 2021) have shown that a minimum value of about 90 is needed for  $Re_\tau = d^+ = u_\tau d / \nu_w$  to have sustained turbulent flow. Figure 2.19 shows  $Re_\tau$  and  $\nu_{t,max} / \nu_w$  for the current 1D, 2D, and 3D simulations. It shows that full turbulence has been reached in the 1D and 2D simulations, and in the bottom layer of the 3D simulation, but not in the top layer where a tendency to relaminarization is found. It is very well possible that the relaminarization in the top layer with sustained turbulent flow in the bottom layer is responsible for the relatively large eccentricity in the 3D simulation. Sustained turbulent flow in the top layer may lead to a reduced eccentricity, as found in the experiments.

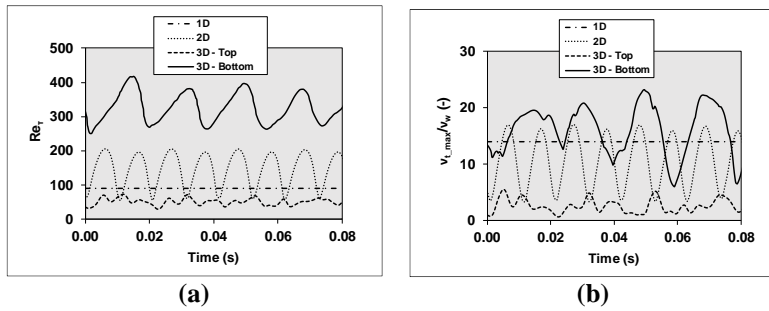


**Figure 2.19.** Comparison of simulation results; (a) shear-based Reynolds number ( $Re_\tau$ ), (b) scaled maximum turbulent viscosity ( $v_{\tau,max}^+ = v_{\tau,max}/v_w$ ).

## 2.7 Conclusions

1D, 2D, and 3D numerical simulations were performed for horizontal core-annular flow (CAF) with a turbulent water annulus. Thereto, the Reynolds-Averaged Navier-Stokes (RANS) equations were solved with the low-Reynolds number Launder & Sharma  $k - \varepsilon$  model for the turbulence. The base case is the flow in a 21 mm diameter pipe with oil and water that have a viscosity ratio of 1150 and a density ratio of 0.91. The flow is characterized by travelling waves at the oil-water interface. The oil core is laminar, and the water annulus is turbulent. The simulation results were compared with experiments (pressure drop measurements, flow visualization) obtained in our lab. To verify the good numerical accuracy of the simulation results, the simulations were repeated on successively refined meshes. Obviously, it is important to have a sufficient number of numerical grid points close to the wall in the viscous sublayer, as well as in the wavy interfacial zone.

The 1D results represent perfect turbulent CAF (i.e. no gravity, no interfacial waves), the 2D results represent axi-symmetric CAF (i.e. no gravity, with interfacial waves). And the 3D results represent eccentric CAF (i.e. with gravity, with interfacial waves). The simulation results typically show a turbulent water annulus in which the structure of the (high-Reynolds number) inertial sublayer can be recognized. The inertial sublayer scaling (using wall units) was demonstrated to be present for the streamwise velocity, for the turbulent viscosity, for the turbulent kinetic energy, and for the turbulent energy dissipation. However, as the shear-based Reynolds number is limited, also the extent of the inertial sublayer is limited.

The 2D and 3D results for the interfacial waves show that the waves are travelling with a practically constant wave velocity. This means that the temporal and spatial results can be converted into one another using this convective velocity. It also means that an observer traveling with the waves will see an almost steady flow. The turbulence is highest at the streamwise location where the water annulus is thickest (i.e. at the trough location of the wave) and lowest at the location where the water annulus is thinnest (i.e. at the crest location of the waves). With respect to the travelling waves, a water recirculation zone is found in between the successive crest locations. Monitoring the pressure along the interface, the pressure is largest at the location where the dividing streamline of the recirculation zone reattaches at the interface (which can be seen as the windward side of the interface) and pressure is lowest at the location where the dividing streamline of the recirculation zone leaves the interface (which can be seen as the leeward side of the interface). Through integrating the pressure along the interface in streamwise direction the form drag working on the wave interface can be determined. For the 2D results, 68% of the interface force is due to pressure (form drag) and 32% due to shear stress. For the 3D results we find 48% form drag and 52% shear stress force.

A force balance on the oil core was performed for the 3D results to determine the levitation in vertical direction. Thereto, the total force is split into a reduced pressure force, viscous force and buoyancy force. It is found that during the initial stage of the transient simulation (which starts with a concentric



oil core), the reduced pressure force and the viscous force at the oil-water interface are both acting in opposite direction to the buoyancy force; these two forces together grow larger than the buoyancy force, creating a downward resulting force on the oil core. The levitation mechanism is closely related to the shape of the interfacial waves. The amplitude of the waves at the bottom is such large that the water flow easily separates at almost the location of the wave crest, which gives almost parallel flow and thus almost no pressure change in streamwise direction. This is in contrast to the top layer where the water flow longer follows the interface before it separates and reattaches, leading to the significant pressure fluctuations. Almost everywhere the reduced pressure along the top interface is higher than at the bottom interface, which provides the downward force in line with the flying-core concept (downward lift) described by Joseph et al. (1997).

There are significant differences between the simulation results and the lab experiments. The pressure drop reduction factor (which is the ratio between the pressure drop for CAF and the pressure drop for single phase viscous oil flow) for the 2D and 3D results is about the same, but its value is about 35% higher than in the experiment (or, at the same oil flow rate, the predicted pressure drop is about 35% lower than in the experiment). The holdup ratio in the 3D model ( $h=1.38$ ) is close to the experimental value ( $h=1.41$ ), but the 2D prediction is slightly lower ( $h=1.23$ ). Therefore, the apparent slip between the oil and water (due to the interfacial stress) in the 3D simulation agrees with the experiment, but the 2D simulation gives a too low slip (or too much interfacial stress). The 2D and 3D results for the wave velocity and wave length (and for the wave frequency) are in good agreement with the experiments. An exception is the wave length in the bottom layer of the 3D results: this wave length is double the measured value. The eccentricity predicted by the 3D simulations is much higher than in the experiment. Due to the low eccentricity in the experiment, the 2D axi-symmetric simulation results (i.e. zero eccentricity) for the interfacial waves are in better agreement with the flow visualization in the experiments than the 3D results.

Most likely, the observed differences between the simulations and the experiments are due to limitations of using a low-Reynolds number  $k - \epsilon$  model. Such a model is suited for attached wall-bounded flow, but less good for flow separation with recirculation and for relaminarization. For fully turbulent flow a shear-based Reynolds number  $Re_\tau$  of at least about 90 is needed. Full turbulence has been reached in the 1D and 2D simulations, and in the bottom layer of the 3D simulation, but not in the top layer where a tendency to relaminarization is found. It might be that the relaminarization in the top layer with sustained turbulent flow in the bottom layer is responsible for the relatively large eccentricity in the 3D simulation. Additional experiments and simulations are needed to further verify this. With respect to the experiments one can think of more detailed measurements of the flow in the water annulus (e.g. using Particle-Image Velocimetry). Also using a larger pipe diameter (which gives a thicker, more turbulent water annulus) would be helpful. This increases the  $Re_\tau$  value in the experiments, which would probably make the conditions easier for simulation with a low-Reynolds number  $k - \epsilon$  model. Additional 3D simulations with a higher  $Re_\tau$  could be carried out to verify its effect on the eccentricity. Repeating the simulations for the current conditions with a LES approach, or even with a DNS approach, is also recommended.

## References

- Archibong-Eso, A., Shi, J., Baba, Y.D., Aliyu, A.M., Raji, Y.O., Heung, H., 2017. High viscous oil–water two–phase flow: experiments & numerical simulations. *Heat and Mass Transfer* 55, 755–767.
- Arney, M.S., Bai, R., Guevara, E., Joseph, D.D., Liu, K., 1993. Friction factor and holdup studies for lubricated pipelining-I. Experiments and correlations. *Int. J. Multiphase Flow* 19, 1061–1076.
- Bai, R., Chen, K., Joseph, D.D., 1992. Lubricated pipelining: stability of core-annular flow. part 5. experiments and comparison with theory. *J. Fluid Mechanics* 240, 97–132.
- Bannwart, A. A., 2001. Modeling aspects of oil-water core-annular flows. *J. Petrol. Sci. Engng* 32, 127–143.
- Beerens, J.C., Ooms, G., Pourquié, M.J.B.M., Westerweel, J., 2014. A comparison between numerical predictions and theoretical and experimental results for laminar core-annular flow. *AIChE Journal* 60.8, 3046–3056.
- Chen, K., Bai, R., Joseph, D.D., 1990. Lubricated pipelining. Part 3 Stability of core-annular flow in vertical pipes." *Journal of Fluid Mechanics* 214, 251–286.
- Ghosh, S., Mandal, T.K., Das, P.K., 2009. Review of oil water core annular flow." *Renewable and Sustainable Energy Rev.* 13, 1957–1965.
- Hasson, D., Mann, V., Nir, A., 1970. Annular flow of two immiscible liquids I. Mechanisms. *Can. J. Chem. Engng* 48, 514–520.
- Henkes, R.A.W.M., 1998. Scaling of the turbulent boundary layer along a flat plate according to different turbulence models. *Int. J. of heat and Fluid Flow* 19, 338–347.
- Huang, A., Christodoulou, C., Joseph, D.D., 1994. Friction factor and holdup studies for lubricated pipelining - II; laminar and  $k - \epsilon$  models of eccentric core flows. *Int. J. Multiphase Flow* 20, 481–491.
- Huang, A., D.D. Joseph., 1995. Stability of eccentric core–annular flow. *Journal of Fluid Mechanics* 282, 233–245.
- Jiménez, J., Moin, P., 1991. The minimal flow unit in near-wall turbulence. *J. Fluid Mechanics* 225, 213–240.
- Joseph, D.D., Bai, R., Chen, K.P., Renardy, Y.Y., 1997. Core-Annular Flows. *Annual Review of Fluid Mechanics* 29, 65–90.
- Kim, K., Choi, H., 2018. Direct numerical simulation of a turbulent core-annular flow with water-lubricated high viscosity oil in a vertical pipe. *J. Fluid Mech.* 849, 419–447.
- Ko, T., Choi, H.G., Bai, R., Joseph, D.D., 2002. Finite element method simulation of turbulent wavy core-annular flows using a  $k - \omega$  turbulence model method. *Int. J. Multiphase Flow* 29, 1205–1222.
- Launder, B.E., Sharma, B.T., 1974. Application of the energy dissipation model of turbulence to the calculation of flow near a spinning disc. *Lett. Heat and Mass Transfer* 1, 131–138.
- Li, J., Renardy, Y., 1999. Direct simulation of unsteady axisymmetric core–annular flow with high viscosity ratio. *Journal of Fluid Mechanics* 391, 123–149.
- Preziosi, L., Chen, K. and Joseph, D.D., 1989. Lubricated pipelining: stability of core-annular flow. *Journal of Fluid Mechanics* 201, 323–356.
- Ooms, G., Segal, A., Van der Wees, A.J., Meerhoff, R., Oliemans, R.V.A., 1984. A theoretical model for core-annular flow of a very viscous oil core and a water annulus through a horizontal pipe. *International Journal of Multiphase Flow* 10.1, 41–60.
- Ooms, G., Vuik, C., Poesio, P., 2007. Core-annular flow through a horizontal pipe: hydrodynamic counterbalancing of buoyancy force on core. *Physics of Fluids* 19.9, 092103.
- Ooms, G., Pourquié, M. J. B. M. , Poesio, P., 2012. Numerical study of eccentric core-annular flow. *Int. Journal of Multiphase Flow* 42, 74–79.
- Ooms, G., Pourquié, M. J. B. M. , Beerens, J.C., 2013. On the levitation force in horizontal core-annular flow with a large viscosity ratio and small density ratio. *Physics of Fluids* 25.3, 032102.

- Roccon, A., Zonta, F., Soldati, A., 2019. Turbulent drag reduction by compliant lubricating layer. *J. Fluid Mech.* 863, R1 (1-11).
- Roccon, A., Zonta, F., Soldati, A., 2021. Energy balance in lubricated drag reduced turbulent channel flow. *J. Fluid Mech.* 911, A37 (1-36).
- Shi, J., Gourma, M., Yeung, H., 2017. CFD simulation of horizontal oil-water flow with matched density and medium viscosity ratio in different flow regimes. *J. Petroleum Science and Engineering* 151, 373-383.
- Shi, J., Lao, L., Yeung, H., 2017. Water-lubricated transport of high-viscosity oil in horizontal pipes: The water holdup and pressure gradient. *Int. J. Multiphase Flow* 96, 70-85.
- Song, B., Plana, C., Lopez, J.M., Avila, M., 2019. Phase-field simulation of core-annular pipe flow. *Int. J. Multiphase Flow* 117, 14-24.
- Van Duin, E., Henkes, R.A.W.M., Ooms, G., 2019. Influence of oil viscosity on oil-water core-annular flow through a horizontal pipe. *Petroleum* 5.2, 199-205.
- Yamamoto, T., Okano, Y., Dost, S., 2017. Validation of the S-CLSVOF method with the density-scaled balanced continuum surface force model in multiphase systems coupled with thermocapillary flows. *Int. J. for Numerical Methods in Fluids* 83.3, 223-244.



# 3

## Friction factors for CAF

*Interfacial waves in core-annular pipe flow are studied through two-phase numerical simulations. Here the water annulus is turbulent, whereas the oil core stays laminar. The low-Reynolds number Launder & Sharma  $k - \epsilon$  model is applied. By extracting the moving wave shape from the two-phase results and imposing this as a solid boundary in a single-phase simulation for the water annulus gives single-phase results (for the pressure drop and holdup ratio) that are in close agreement with values obtained from the two-phase approach. The influence of wave amplitude and wave length on the pressure drop and holdup ratio is then studied by using the single-phase flow model. This gives insight in the appearance of core-annular flow, where the water-based Fanning wall-friction factor and the holdup ratio are selected as the most important quantities. The effect of watercut and eccentricity on these quantities is also investigated.*

### 3.1 Introduction

Core-annular flow is a typical flow regime for liquid-liquid transport in a pipeline. The flow consists of a viscous core liquid (e.g. oil) and a far less viscous annulus liquid (e.g. water). The water lubrication causes that the pressure drop required to transport the viscous oil is much less than what is needed for single-phase viscous oil transport. Over the past decades an extensive literature on core-annular flow has appeared. This is because of its industrial applications and its richness of fluid mechanics fundamentals (see e.g. Joseph et al., 1997, and Ghosh et al., 2009).

Due to the apparent slip effect between the two phases, interfacial waves will be formed. For a laminar water annulus, the dominant wave length can be predicted with stability theory (Chen et al. (1990), Bai et al. (1992)). Some experimental studies (like Rodriguez & Bannwart (2006), Tripathi et al. (2017)) succeeded in measuring the interfacial wave characteristics (incl. wave amplitude, wave length, and wave speed). The appearance of interfacial waves will make the flow characteristics (like the pressure drop and the holdup ratio), for given liquid-liquid flow rates, different from those found with a flat liquid-liquid interface (so-called Perfect Core-Annular flow). Bannwart (2001) and Ullmann & Brauner (2004) developed semi-empirical two-fluid models to predict the pressure drop and holdup ratio. The wall friction factor and the interfacial friction factors appear in the two-fluid model, and empirical correlations are used for the closure. A good understanding of the liquid-liquid interaction at the interface is thus important for the core-annular flow modelling.

Most studies have considered a laminar annulus flow, but the recent study will focus on core-annular flow with a turbulent annulus. The simulation of such flow is quite challenging because of the presence of both the turbulent water annulus and the interface with travelling waves. The interface capturing method (e.g. Volume of Fluid, Level Set method) has been applied in various studies, e.g. Ingen Housz et al. (2017) and Kim & Choi (2018). A very fine mesh, with large computational effort, is needed to obtain a sharp and accurate interface. Bai et al. (1996) assumed a sharp interface, and they simulated the 2D wave shape by iterating the force balance across the interface; the converged wave shape compared quite well with the experiments. In oil-water core-annular flow, the ratio of the oil and water viscosities is very high, causing that the oil core moves approximately as a solid body with a fixed wave pattern. Ooms et al. (2012) adopted the 2D wave shape from the results by Bai et al. (1996) in 3D eccentric simulations with a laminar water annulus. By assuming the oil core to behave as a solid body, a downward levitation force is found on the oil core at higher Reynolds number.

The present study builds on our previous work on core-annular flow (Li et al. 2021). The turbulence in the water annulus is represented by using the RANS approach (Reynolds-Averaged Navier-Stokes), applying the  $k - \epsilon$  model with the Launder-Sharma low-Reynolds number terms. A number of other studies have followed a similar approach (either with variants of the  $k - \epsilon$  model or of the  $k - \omega$  model; see Huang et al. (1994), Ko et al. (2002), Ingen Housz et al. (2017). Despite the shortcomings with RANS in modelling the complex water annulus flow, particularly due to the presence of a wavy interface, it can still be an attractive way of studying the flow structures as a function of the many parameters that play a role in core annular flow, such as: the watercut, the Reynolds number, the viscosity ratio, the density ratio, the pipe inclination, the liquid-liquid interfacial tension.

A number of studies was devoted to the pressure drop and holdup for core annular flow, either through experiments or through theoretical models and simulations. These studies include: Arney et al. (1993), Shi et al. (2017), Hu et al. (2020); these inspired us to focus our study on the behaviour of the dimensionless pressure drop relation and the holdup relation in core-annular flow. For the dimensionless pressure drop, the water-based Fanning friction factor will be used. This can answer how the pressure drop for core-annular flow compares to the case in which only water is flowing through the pipe. For the holdup, the so-called holdup ratio will be used. This describes the relative water accumulation compared to the watercut (which is an indicator of the relative slip between the

two liquid phases). As a first estimate, the wall friction factor for core-annular flow can be taken equal to the value for water-only flow (at the same flow rate as the corresponding combined water-oil flow rate for core-annular flow). But the presence of the viscous core will have an effect on the turbulence in the water annulus, which might thus be different from the turbulence found for single-phase water flow. The formation of waves at the interface will decrease the total water accumulation giving a smaller average thickness of the water annulus. This gives a higher average bulk water velocity, which increases the wall friction (and herewith the pressure drop and friction factor). But the larger oil core and thinner average water annulus may also hinder the turbulence in the annulus, which will tend to decrease the wall friction. What is the final balance for core-annular flow, i.e. between oil and water flow rates on the one hand versus pressure drop and holdup on the other hand?

To answer this, 2D two-phase simulations were carried out for different conditions. In addition also 2D and 3D single-phase simulations were carried out for only the water annulus, with imposed waves (with varying wave length and wave amplitude) at the location of the two-phase interface. In this way the effect of the wavy interface on the friction factor and on the holdup ratio can be systematically assessed. In particular also the effect of the watercut and the core eccentricity was simulated.

## 3.2 Modelling approach

### 3.2.1 Governing equations

The mass and momentum conservation equations for an incompressible, isothermal fluid are (in Cartesian coordinates):

$$\frac{\partial u_i}{\partial x_i} = 0 \quad (3.1)$$

$$\frac{\partial \rho u_i}{\partial t} + \rho u_j \frac{\partial u_i}{\partial x_j} = \frac{\partial}{\partial x_j} \left( \rho (\nu + \nu_t) \left( \frac{\partial u_i}{\partial x_j} + \frac{\partial u_j}{\partial x_i} \right) \right) - \frac{\partial p}{\partial x_i} + \rho g_i + F_{\sigma,i} \quad (3.2)$$

These are the Reynolds-Averaged Navier-Stokes Equations (RANS). Here  $u_i$  is the velocity,  $\rho$  and  $\mu$  are the fluid density and viscosity,  $g_i$  is the gravitational acceleration,  $p$  is the pressure and  $F_{\sigma,i}$  is the interfacial tension force. For the pipe flow, we will use  $x_1 = x$  for the coordinate along the horizontal pipe axis,  $x_2 = y$  for the vertical coordinate, and  $x_3 = z$  for the pipe width coordinate; the velocity components are  $u$ ,  $v$ , and  $w$ , in the directions  $x$ ,  $y$ , and  $z$ , respectively. The gravity components are:  $g_1 = g_3 = 0$ , and  $g_2 = -g$ , where  $g$  is the gravitational acceleration.

The turbulent viscosity is modelled with the low-Reynolds number  $k - \epsilon$  model of Launder & Sharma (1974), which reads as follows:

$$\nu_t = C_\mu f_\mu \frac{k^2}{\tilde{\epsilon}} \quad (3.3)$$

$$\frac{\partial k}{\partial t} + u_j \frac{\partial k}{\partial x_j} = \frac{\partial}{\partial x_j} \left( \nu + \frac{\nu_t}{\sigma_k} \right) \frac{\partial k}{\partial x_j} + \nu_t \left( \frac{\partial u_j}{\partial x_j} \right)^2 - \tilde{\epsilon} - D \quad (3.4)$$

$$\frac{\partial \tilde{\epsilon}}{\partial t} + u_j \frac{\partial \tilde{\epsilon}}{\partial x_j} = \frac{\partial}{\partial x_j} \left( \nu + \frac{\nu_t}{\sigma_\epsilon} \right) \frac{\partial \tilde{\epsilon}}{\partial x_j} + C_1 f_1 \frac{\tilde{\epsilon}}{k} \nu_t \left( \frac{\partial u_j}{\partial x_j} \right)^2 - C_2 f_2 \frac{\tilde{\epsilon}^2}{k} + E \quad (3.5)$$

With  $D = 2\nu \frac{\partial \sqrt{k}}{\partial x_j} \frac{\partial \sqrt{k}}{\partial x_j}$  and  $E = 2\nu \nu_t \left( \frac{\partial^2 u_j}{\partial x_j^2} \right)^2$ . The turbulent energy dissipation rate is  $\epsilon = \tilde{\epsilon} + D$ .

Furthermore,  $C_\mu = 0.09$ ,  $C_1 = 1.44$ ,  $C_2 = 1.92$ ,  $\sigma_k = 1.0$ ,  $\sigma_\epsilon = 1.3$ ,  $f_\mu = \exp\left(\frac{-3.4}{(1 + \frac{Re_t}{50})^2}\right)$ ,  $f_1 = 1$ ,  $f_2 = 1 -$

$0.3 \exp(-Re_t^2)$ ,  $Re_t = \frac{k^2}{\tilde{\epsilon} \nu}$ . The boundary conditions at the wall are:  $k=0$  and  $\tilde{\epsilon} = 0$ .

Quite a number of low-Reynolds number  $k - \epsilon$  formulations are available in the literature. A large advantage of the Launder-Sharma one is that the low-Reynolds number terms do not include the explicit distance to the closest wall. Instead the parameter  $Re_t$  is used to incorporate the effect of turbulence damping when a wall is approached. In the same way, the model will incorporate the possible damping of turbulence when the oil-water interface is approached in core-annular flow. The

low-Reynolds number  $k - \epsilon$  model is used everywhere in the domain, also in the laminar oil core. Because of the presence of the low-Reynolds number terms the model automatically relaminarizes in the viscous oil core (i.e. it gives zero turbulent viscosity).

### 3.2.2 Numerical method

We used the open-source package OpenFOAM to solve the RANS equations, applying the CLSVOF method for the interface capturing. The CLSVOF solver, which was developed by Yamamoto et al. (2017), is based on the interFoam Volume of Fluid (VOF) solver in OpenFOAM. The level set function is used to calculate the interfacial tension force. Starting from the VOF method, the oil volume fraction  $\alpha$  is introduced to distinguish between the two fluid phases:  $\alpha = 0$  is the oil phase,  $\alpha = 1$  is the water phase, and  $0 < \alpha < 1$  denotes the oil-water interface. Then the fluid density and viscosity in the equations are:

$$\rho = (1 - \alpha)\rho_o + \alpha\rho_w \quad (3.6)$$

$$\mu = (1 - \alpha)\mu_o + \alpha\mu_w \quad (3.7)$$

The subscript “o” refers to oil, and the subscript “w” refers to water.  $\alpha$  is calculated from the following advection equation:

$$\frac{\partial \alpha}{\partial t} + \nabla \cdot (\alpha \vec{u}) + \nabla \cdot ((1 - \alpha)\alpha \vec{u}_r) = 0 \quad (3.8)$$

The third term on the left-hand side is the compressive term (with the divergence of the compressive flux); here  $\vec{u}_r = \vec{u}_w - \vec{u}_o$ . This term is meant to control the sharpness of interface.

The level set function  $\Phi$  is defined as the distance from the interface, where the interface is the isoline with  $\Phi = 0$ . The initial value of the level set function  $\Phi_0$  is obtained from the initialized volume-of-fluid field, where the interface is defined at  $\alpha = 0.5$ :

$$\Phi_0 = (2\alpha - 1)\Gamma \quad (3.9)$$

$$\Gamma = 0.75\Delta X \quad (3.10)$$

Here  $\Delta X$  is the minimum mesh size near the interface. Thereafter the re-initialization equation is solved to turn the initial level set function into the distance from the interface:

$$\frac{\partial \Phi}{\partial \tau} = \text{sign}(\Phi_0)(1 - |\nabla \Phi|) \quad (3.11)$$

Here  $\tau = 0.1\Delta X$  is the iteration time step of  $\Phi$  and the sign function denotes:

$$\text{sign}(\Phi) = \begin{cases} 1 & \Phi > 0, \text{ water} \\ 0 & \Phi = 0, \text{ interface} \\ -1 & \Phi < 0, \text{ oil} \end{cases} \quad (3.12)$$

Then the interface tension force is calculated as:

$$\vec{F}_\sigma = \sigma \kappa(\Phi) \delta_\Phi \nabla(\Phi) \quad (3.13)$$

Here  $\sigma$  is the interface tension and  $\delta_\Phi$  is the smoothed delta function:

$$\delta_\Phi = \begin{cases} \frac{1}{2\gamma} \left( 1 + \cos\left(\frac{\pi\Phi}{\gamma}\right) \right) & \text{for } |\Phi| < \gamma \\ 0 & \text{elsewhere} \end{cases} \quad (3.14)$$

The quantity  $\gamma$  is the interface thickness coefficient (see Yamamoto et al., 2017) and  $\kappa(\Phi)$  is the interface curvature:

$$\kappa(\Phi) = \nabla \cdot \vec{n}_c \quad (3.15)$$

$$\vec{n}_c = \frac{(\nabla \Phi)_f}{|(\nabla \Phi)_f|} \quad (3.16)$$

Here  $\vec{n}_c$  is the surface unit normal vector. The contact angle  $\theta$  between the interface and the pipe wall is defined as:

$$\cos(\theta) = \vec{n}_c \cdot \vec{n}_w \quad (3.17)$$

With  $\vec{n}_w$  being the unit normal vector at the wall. The contact angle is set to  $90^\circ$  in our simulations.



This means that both the level set function  $\Phi$  and the volume fraction of the fluid  $\alpha$  satisfy the zero gradient condition at the pipe wall boundary.

A pressure drop in the flow direction is added as an extra force term to the right-hand side of Equation 3.2, with periodic boundary conditions on the left and right side of the pipe. Therefore, the pressure that remains in the equations is periodic with respect to the left and right side of the computational pipe section. The initially assumed velocity profile will then develop over time under this pressure drop in the transient simulation until a stable state is obtained.

A second-order backward implicit time discretization scheme is applied, with a very small time step (small Courant number). This gives a very accurate time integration. We use a second-order scheme for the advection terms in the momentum equations and in the interface equation (as used in the level set method), but a first-order upwind scheme for the advection in the equations for the turbulence quantities  $k$  and  $\varepsilon$ ; trying a second-order scheme for the latter gave numerical instabilities. Through successive mesh refinement, however, we have verified that the simulation results are accurate (and not suffering from large numerical diffusion).

In all the simulations, periodic boundary conditions are applied on the left and right side of the pipe, which restricts the wavelengths in the axial direction to the domain length divided by an integer value. At the pipe wall, the no-slip condition is imposed. We have used the symmetric PbiCG solver for the velocity and for the turbulent quantities, the GAMG solver for the pressure, and the PIMPLE solver for the velocity-pressure coupling.

### 3.2.3 Basic simulation set-up

In the simulations for the basic set-up, the following parameters were kept the same as in the experiments carried out in our lab. The pipe radius is  $R=0.0105$  m (pipe diameter is 21 mm). The length of the pipe section is set to 0.0256 m (25.6 mm), which is twice the most dominant wavelength, as estimated from a linear instability analysis (albeit for laminar flow) by Beerens et al. (2014). The section length was also varied to investigate its effect on the wave selection. The fluid properties are set as follows: the oil and water kinematic viscosity are  $\nu_o = 7.73 \times 10^{-4}$  m<sup>2</sup>/s and  $\nu_w = 6.7 \times 10^{-7}$  m<sup>2</sup>/s, the oil and water densities are  $\rho_o = 902$  kg/m<sup>3</sup> and  $\rho_w = 993$  kg/m<sup>3</sup>, and the interfacial tension between oil and water is  $\sigma = 0.016$  N/m (Shell Morlina S2 B 680 at 40 °C was used in the experiments). Note that the ratio between the kinematic viscosities of oil and water is 1150, and the density ratio between the oil and water is  $\rho_o/\rho_w = 0.91$ . The Reynolds number in wall units, i.e.  $Re_\tau = d^+ = u_\tau d/\nu_w$ , is about 150 (here  $u_\tau$  is the wall shear stress velocity and  $d$  is the average thickness of the water annulus). This is above the minimum value of about 90 which is needed to sustain turbulence in single-phase channel flow (where  $d$  is half the channel width); this criterion was derived by Jimenez & Moin (1991), who applied DNS (Direct Numerical Simulations) to channel flow. The occurrence of turbulence in the water annulus is confirmed in the present simulations, which shows an inertial sublayer with a maximum turbulent viscosity ( $\nu_t/\nu_w$ ) of about 20.

### 3.2.4 Key parameters

Four important parameters are: the total flow rate, the pressure drop, the watercut, and the water holdup fraction. When two parameters are set as input (e.g. the total flow rate and the watercut in the experiments), the other two will follow as output.

The watercut is defined as the ratio of the water volumetric flow rate and the total volumetric flowrate:

$$WC = Q_w / (Q_o + Q_w) \quad (3.18)$$

where  $Q$  denotes the volumetric flow rate. The water holdup fraction is defined as the ratio of the in-situ water volume in the pipe and the total volume of oil and water:

$$\alpha_w = \frac{V_w}{V_w + V_o} \quad (3.19)$$

A related parameter is the so-called holdup ratio  $h$ , which is defined as:

$$h = \frac{Q_o/Q_w}{V_o/V_w} \quad (3.20)$$

This can also be rewritten as  $h = 1 + u_r/u_w$ . Here the velocity difference  $u_r = u_o - u_w$ , is the apparent (average) slip velocity between the oil core (having a bulk velocity  $u_o$ ) and the water annulus (having a bulk velocity  $u_w$ ). Note that  $h=1$  if there is no slip between the bulk oil and water velocities. The holdup ratio thus is a measure of the apparent slip between the oil core and the water annulus. When waves appear at the liquid-liquid interface, the wave amplitude can be defined as

$$A = \sqrt{2(\delta - \bar{\delta})^2} \quad (3.21)$$

Here  $\delta$  is the instantaneous thickness of the annulus; an overbar denotes the averaged value (in space and time). The amplitude is defined such that it gives the usual value of the amplitude for the case that the wave is a pure sinus (where the amplitude is half the difference between the maximum and the minimum value).

### 3.2.5 Force balance

It will be helpful for the interpretation of the results to also consider the integral force balance for the flow (after averaging in space and time), using the quantities shown in Figure 3.1. Here  $x$  is the streamwise pipe coordinate, and  $r$  is the radial pipe coordinate. The pipe has radius  $R$ . The oil flow is represented by a concentric core with radius  $R_c$ , and the water flows in an annulus with thickness  $R - R_c$ . The flow is driven by the pressure gradient  $-dp/dx$ . The wall imposes a wall shear stress  $\tau_w$  on the water annulus (taken positive in upstream direction). The water annulus imposes an interfacial stress  $\tau_i$  on the oil core (taken positive in upstream direction). The oil core also imposes an interfacial stress on the water annulus, it has the same magnitude as  $\tau_i$ , but now taken positive in downstream direction. The water flows with an average velocity (bulk velocity)  $u_w$ , and the oil flow with an average velocity (bulk velocity)  $u_o$ . The bulk velocity follows from the superficial velocity as:  $u_w = u_{sw}/\alpha_w$  and  $u_o = u_{so}/\alpha_o$ , with  $u_{sw} = Q_w/A_p$  and  $u_{so} = Q_o/A_p$ . Here  $A_p = \pi R^2$  is the cross sectional area of the pipe.

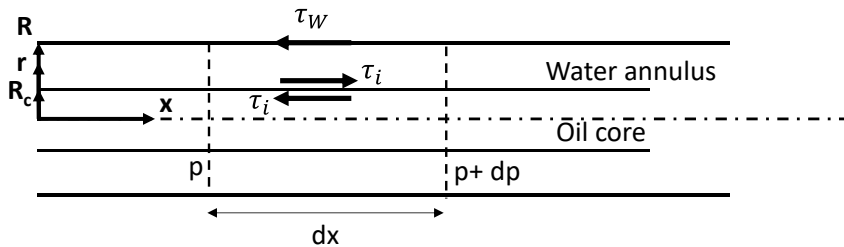


Figure 3.1. Stresses imposed on the core-annular flow

The force balance for the combined oil-water flow in a horizontal pipe reads:

$$-\frac{dp}{dx} A_p - \tau_w 2\pi R = 0 \quad (3.22)$$

The force balance for the oil core gives:

$$-\frac{dp}{dx} \alpha_o A_p - \tau_i 2\pi R_c = 0. \quad (3.23)$$

Here  $\alpha_o$  is the oil holdup fraction, with  $\alpha_o = (R_c/R)^2$ .

From force balances (22) and (23) it also follows that the wall shear stress and interfacial stress are related as  $\tau_i = \tau_w R_c/R$ . Note that the force balances (22) and (23) hold for the core-annular flow (with or without interfacial waves) after averaging in space and time.

Due to the considered high ratio of the oil and water viscosities, the oil core will be laminar. The

typical streamwise velocity profile is shown in Figure 3.2. As the oil viscosity is high, the oil velocity is almost constant throughout the core. Assuming parallel flow in the laminar oil core (i.e. neglecting non-parallel effects in the oil flow close to the wave interface), the flow here can be described by the force balance:

$$-\frac{dp}{dx}\pi r^2 - \mu_o \frac{du}{dr} 2\pi r = 0, \quad (3.24)$$

with the interface condition:  $\tau_i = -\mu_o \left(\frac{du}{dr}\right)_{r=R_c}$ .

Integration gives the following expression of the velocity at the interface:

$$u_i = -\frac{R_c}{4\mu_o} \tau_i + \frac{Q_o}{\pi R_c^2}, \quad (3.25)$$

in which  $Q_o$  is the oil flow rate. For all conditions considered in the present study, the first term on the right hand side is much smaller than the second term. This means that within the boundaries of validity of the shown force-balance approach with parallel core flow, the interfacial velocity is the same as the bulk oil velocity.

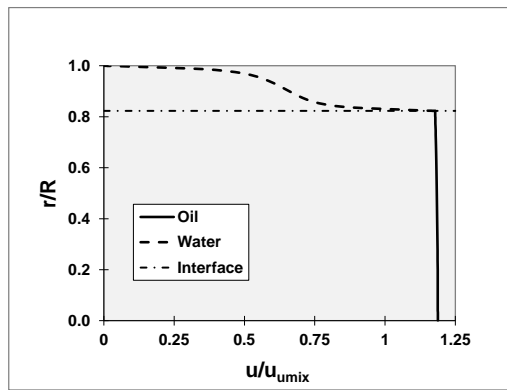


Figure 3.2. Typical streamwise velocity profile for core-annular flow.

### 3.2.6 Mechanistic models

The force balance method as discussed in the previous subsection can be used to determine a mechanistic model for core-annular flow. The most simple mechanistic modelling approach for core-annular flow is obtained by assuming that the frictional pressure drop (or the wall shear stress) is the same as found for a fully turbulent pipe flow that transports single-phase water, in which the water flow rate is taken the same as the total oil plus water flow rate for the corresponding core-annular flow. This seems to be a rough assumption, but the present study will show that it is in fact quite accurate. The Reynolds number for this flow is based on the water properties and on the mixture velocity. The wall shear stress  $\tau_w$  in the overall pipe flow balance (3.22) can be expressed as  $\tau_w = f_w \frac{1}{2} \rho_w u_m^2$ , in which  $f_w$  is the Fanning friction factor. Substitution into Equation 3.22 gives:

$$f_w = -\frac{dp}{dx} \frac{R}{\rho_w u_m^2} \quad (3.26)$$

The mixture velocity is defined as  $u_m = \frac{Q_w + Q_o}{A}$ . Different very accurate correlations exist in the literature to describe the Fanning friction factor for single-phase pipe flow. An accurate example is the Churchill correlation, which reads (for a smooth wall):

$$f_w = 2 \left[ \left( \frac{8}{Re_w} \right)^{12} + \frac{1}{(A^* + B^*)^{3/2}} \right]^{1/12} \quad (3.27)$$

$$A^* = \left\{ -2.457 \ln \left[ \left( \frac{7}{Re_w} \right)^{0.9} \right] \right\}^{16} \quad \text{and} \quad B^* = \left( \frac{37530}{Re_w} \right)^{16}$$

The Reynolds number is defined as:  $Re_w = \frac{\rho_w D u_m}{\mu_w}$ . As an alternative to the Churchill correlation also

the Blasius equation can be used:  $f_W = \frac{0.046}{Re_w^{0.2}}$ .

The Churchill correlation and the Blasius correlation give practically the same values in for turbulent single-phase flow; the correlations have been extensively validated against lab experiments and DNS, and are very accurate. Using the single-phase mechanistic modelling approach, the pressure drop for core-annular flow is independent of the water holdup fraction.

Ullmann & Brauner (2004) have proposed a more refined mechanistic model for core-annular flow in horizontal and inclined pipes. They propose the following empirical expressions for the wall shear stress and the interfacial stress, as appearing in the force balances (3.22) and (3.23):

$$\tau_w = \frac{1}{2} \rho_w f_w u_w^2, \text{ with } f_w = C_w / Re_{sw}^{n_w} \quad (3.28)$$

$$\tau_i = \frac{1}{2} \rho_o f_i u_o (u_o - C_i u_w), \text{ with } f_i = C_o F_i / Re_o^{n_o} \quad (3.29)$$

The Reynolds numbers in these expressions are defined as:

$$Re_{sw} = \frac{\rho_w u_{sw} 2R}{\mu_w} \quad \text{and} \quad Re_o = \frac{\rho_o u_o 2R_i}{\mu_o}$$

Note that the water Reynolds number is based on the superficial water velocity and the oil Reynolds number is based on the bulk oil velocity. Assuming a turbulent water annulus and a laminar oil core, Ullmann & Brauner use the following values for the different coefficients:  $n_w = 0.2$ ,  $C_w = 0.046$ ,  $n_o = 1$ ,  $C_o = 16$ ,  $F_i = 1.0$ . The value for  $C_i$  can be taken between 1.14 and 1.22; we have used  $C_i = 1.17$  in the present study.

After substitution of these correlations, it is straightforward to resolve the pressure drop and the holdup ratio from the two equations 3.22 and 3.23. For a high value of the ratio between the oil viscosity and the water viscosity, it turns out that  $h = C_i$ . We can also relate the pressure drop according to the Ullmann & Brauner model and the single-phase (water-based) model, by rewriting the Ullmann & Brauner expression for the wall shear stress as:

$$\tau_w = f \frac{1}{2} \rho_w u_m^2 \quad \text{with} \quad f = C^* \frac{0.046}{Re_w^{0.2}} \quad \text{and} \quad C^* = \frac{(1+WC(h-1))^2}{h^2 WC^{0.2}} \quad (3.30)$$

WC is the watercut (fraction) and  $h = C_i = 1.17$ . The Reynolds number is the same as defined for single-phase flow, i.e.  $Re_w = \frac{\rho_w D u_m}{\mu_w}$ . This shows that the Fanning friction factor is the same as for single-phase water flow (using the Blasius correlation), multiplied by a factor  $C^*$  that only depends on the watercut (see Figure 3.3); it should be noted (according to the authors' knowledge) that the way in which we have rewritten the model has enabled this insightful interpretation, has not been reported in the literature yet. This shows that the friction factor for core-annular flow in the Ullmann & Brauner model only depends on the water-based Reynolds number and on the watercut. For high watercut, the friction factor follows the single-phase value, whereas for smaller watercut (say below 25%), the friction factor is higher than the single-phase value. Or: for lower watercut the pressure drop for core-annular flow will be higher than what is found with assuming single-phase water flow (with the oil-water mixture velocity).

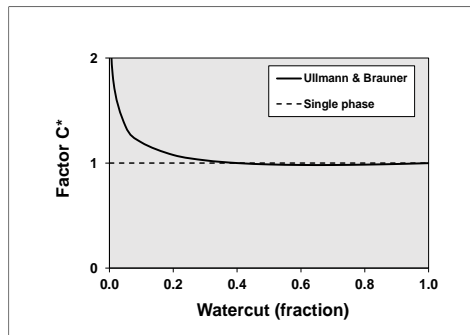


**Figure 3.3.** Ratio ( $=C^*$ ) between the pressure drop according to the Ullmann & Brauner model and single-phase water flow.

As described in our previous study (Li et al., 2021), sustaining a fully turbulent water annulus requires that the Reynolds number in wall units (the shear-based Reynolds), i.e.  $Re_\tau = d^+ = u_\tau d / \nu_w$ , is at least about 90. Here  $u_\tau$  is the wall shear velocity and  $d$  is the average thickness of the water annulus:  $u_\tau = \sqrt{\tau_w / \rho_w}$  and  $d/D = (1 - \sqrt{1 - \alpha_w})/2$ . Using the definition of the Fanning friction factor  $f_w$  and of the holdup ratio  $h$  it follows that:

$$Re_\tau = \sqrt{\frac{f_w}{8}} \left( 1 - \sqrt{\frac{1-WC}{1-WC+hWC}} \right) Re_w \quad (3.31)$$

Here WC is the watercut (fraction).

### 3.3 Pressure drop in various experiments

To better understand the structure of core-annular flow, we have reviewed different sets of experimental lab data as available in the literature. The relevant parameters as used in these studies are summarized in Table 3.1. All these experiments are for a horizontal pipe, except for the study by Vanegas Prada (1999), which was for a vertical pipe. But the density difference between the oil and water in the latter study is so low that the gravity effect can be neglected, and the results can be compared with those obtained in a horizontal pipe with negligible eccentricity. The considered experiments cover a pipe diameter range between 15.5 and 50 mm, an oil to water viscosity ratio range between 750 and 18000, a density difference range between 20 and 115 kg/m<sup>3</sup>, and a value for the water-based Reynolds number  $Re_w$  up to 146000. The experiments also cover a range of watercuts.

The measured values of the pressure drop are converted into a Fanning friction factor by using Equation 3.26. Figure 3.4 shows the ratio of the Fanning friction factors for the different sets of experiments. That ratio is either the experimental Fanning friction factor divided by the Fanning friction factor for single-phase water flow (using the oil-water mixture velocity; see Equation 3.27) or the experimental Fanning friction factor divided by Ullmann & Brauner Fanning friction factor (see Equation 3.30). The comparison shows that in general the experimental value of the Fanning friction factor (or the pressure drop) is (slightly) higher than the single-phase value. Using the Ullmann & Brauner model gives better agreement with the experiments than the single-phase approach. This improvement is fully due to the correction factor (see Figure 3.3) for the watercut. The improvement is particularly noticeable for the experiments by Oliemans et al. (1987).

All the considered experiments have the tendency to give a wall friction factor that is somewhat above the wall friction factor for single-phase water flow. The experiments by Grassi et al. (2008) and by Sotgia et al. (2008) give a wall friction factor that is almost the same as the value for single-phase water flow. This supports that the Fanning wall friction factor is an attractive quantity for the scaling of the pressure drop as measured in different core-annular flow configurations.

**Table 3.1. Overview of some core-annular flow experiments.**

Experiment	Pipe diameter	Kin. viscosity	Density diff.	max. $Re_w$
	mm	ratio	kg/m <sup>3</sup>	
Oliemans et al. (1987)	50	3000	20	146000
Vanegas Prada (1999)	27.5	18000	35	60000
Grassi et al. (2008)	21	700	115	38000
Sotgia et al. (2008)	26	1000	110	46000
Tripathi et al. (2017)	15.5	100	10	21000
Van Duin et al. (2019)	21	750 - 3000	90	25000

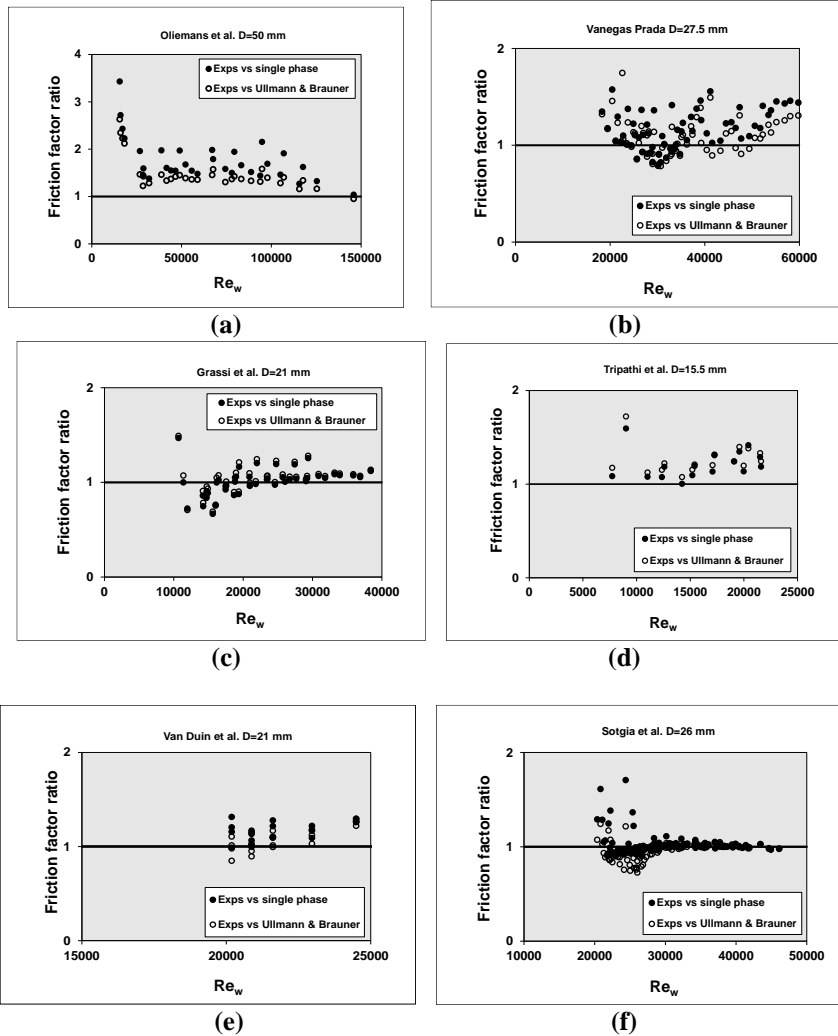


**Figure 3.4.** Overview of experimental results for the wall friction factor; experiments by (a) Oliemans et al., (b) Vanegas Prada, (c) Grassi et al., (d) Tripathi et al., (e) Van Duin et al., (f) Sotgia et al.

Next to the pressure drop, another quantity of interest is the relative water accumulation as expressed by the holdup ratio  $h$ . The asymptotic value is  $h = 1$  (i.e. no apparent slip between the oil core and the water annulus). The Ullmann & Brauner model applies  $h = 1.17$ . Bai et al. (1992) proposed  $h = 1.39$ , as derived from the video recordings of their lab experiments. Oliemans (1986) derived the following expression for the holdup ratio as based on photos of the accumulation:  $h = 1 + \frac{0.2(1-WC)^4}{1-0.2WC(1-WC)^4}$ . Here WC is the watercut (fraction). The value for  $h$  in this expression varies from 1.2 for small watercut to 1 for higher watercut.

The experiments mentioned above were taken for a range of watercuts. By determining the shear based-Reynolds number with Equation 3.31 for all these experiments (using the watercut, the measured pressure drop, and an estimated holdup ratio  $h = 1.39$ ) it is found that the measurements with a watercut of about 15% or lower have a water annulus that is expected to be laminar or not fully turbulent as  $Re_\tau$  is below 90. The measurement for a watercut of 20% or higher give an annulus that

is expected to be in the fully turbulent regime. As an example, Figure 3.5 shows that value of  $Re_\tau$  is as function of the watercut for the experiments by Sotgia et al. (2008) and by Van Duin et al. (2019).

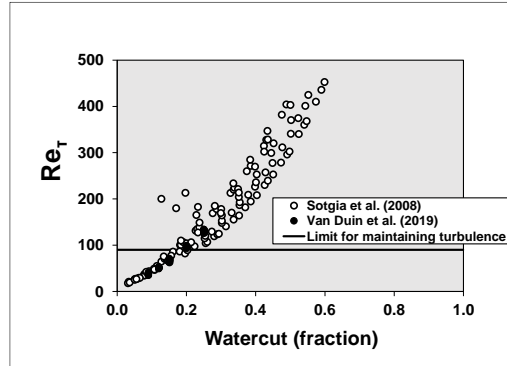


**Figure 3.5: Shear-based Reynolds for different watercuts for which core-annular flow experiments are available.**

Summary of findings in this section:

- A review of different sets of lab data for core-annular flow shows that the Fanning friction factor for the wall, which makes the pressure drop dimensionless with the dynamic pressure based on the water density and on the mixture velocity, is an attractive parameter.
- In the experiments, that friction factor is close to the value found for turbulent water-only flow, and almost independent of the watercut.

### 3.4 Effect of pipe section length

Simulations were carried out with the 2D axisymmetric model for the base case conditions (i.e. with 21 mm diameter, see Section 3.2.3) to determine the dependence of the dominant wave length on the chosen computational domain in streamwise direction. The imposed total flow rate is  $0.00043 \text{ m}^3/\text{s}$  (i.e. 1.24 m/s mixture velocity) and the imposed water holdup fraction is 0.2573. Periodic boundary conditions are imposed at the inlet and outlet of the section. A simulation example of the wave train is shown in Figure 3.6. The results for the dominant wave length, and its frequency, amplitude and velocity are shown in Figure 3.7. Note that the wave length  $\lambda$ , the wave frequency  $f$  and the wave velocity  $u_{\text{wave}}$  are related as  $u_{\text{wave}} = \lambda f$ . The wave length for the base case is  $L^* = 25.6 \text{ mm}$ , which gives two waves, having a wave length is  $L^*/2 = 12.8 \text{ mm}$ . The base case wave length was both increased in steps to  $L/L^* = 2$  and larger, and decreased to smaller values up to zero. For  $L/L^*$  above 1 the dominant wave length is between 9.6 and 12.8 mm. For  $L/L^*$  between 0.5 and 1 the dominant wave length is between 12.2 and 12.8 mm. For  $L/L^*$  below 0.5 the wave length is equal to the length of computational domain, until the waves disappear when the  $L/L^*$  falls below about 0.1. For wave lengths larger than  $L/L^* = 0.5$ , the wave frequency and the wave velocity are almost independent of the length of the computation domain. As shown in the Figure 3.8, this is also true for the resulting pressure drop and holdup ratio. When the waves disappear at small length of the computational domain, obviously the 1D values for the pressure drop and holdup ratio are retained (as presented in detail in Li et al., 2021).



**Figure 3.6. Example result showing the preferred wave length when the streamwise length of**

the considered pipe section is increased.

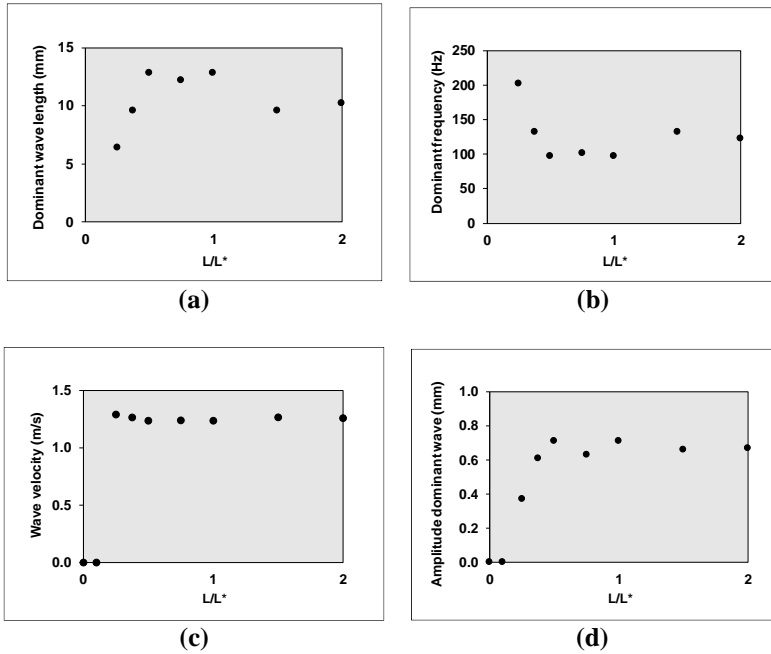


**Figure 3.7. Dependence of the dominant wave development on the considered pipe section length  $L/L^*$  (with  $L^* = 25.6$  mm); (a) wave length, (b) wave frequency, (c) wave velocity, (d) wave amplitude.**

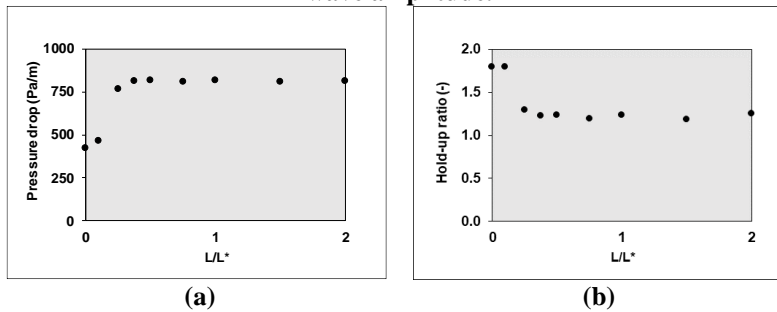


**Figure 3.8. Pressure drop and holdup ratio for different lengths of the computational domain (using a fixed imposed value of  $0.00043 \text{ m}^3/\text{s}$  for the total flow rate and of  $0.2573$  for the water holdup fraction).**

Summary of findings in this section:

- The predicted wave length, wave velocity, and wave frequency are almost independent of the length of the computational domain.
- Also the predictions of the pressure drop and the watercut (for given total flow rate and water holdup fraction) are almost independent of the section length.

### 3.5 Two-phase versus single-phase results

To better examine what happens close to the wavy oil-water interface we also made a comparison between two-phase simulations for the oil-water flow and single-phase simulations for the water annulus. Again the base case conditions are used. The imposed total flow rate is  $0.00043 \text{ m}^3/\text{s}$



(mixture velocity of 1.24 m/s) and the imposed water holdup fraction is 0.2573 (this will give a watercut of about 20%). The water-based Reynolds number is  $Re_w=39000$ . The shear-based Reynolds is about  $Re_\tau=140$ , which has a fully turbulent water annulus. First the relation between the two-phase and single-phase simulations will be demonstrated. Thereafter the single-phase approach will be used to determine the dependence of the interfacial stress on various parameters.

The two-phase simulations have shown that an almost single frequency wave is found at the interface that moves with an almost constant velocity. Therefore, observed from a reference frame that moves with that wave velocity one will see an (almost) steady flow. If so, it makes sense to change the simulation from an approach with a “fixed wall” as the frame of reference, to one in which there is a “moving wall” having an imposed velocity that is about equal to the velocity of the interfacial wave though in opposite direction. Mesh refinement was carried out for the moving wall approach for the 2D base case configuration, similarly as was done for a fixed wall as reported previously (Li et al. 2021). On the finest grid (400 points in radial direction and 200 points in streamwise direction using a domain with 12.8 mm length), there is good agreement for key output parameters like the pressure drop (both give 748 Pa/m), the holdup ratio  $h$  (1.21 for the fixed wall versus 1.22 for the moving wall) and the wave amplitude  $A$  (0.73 mm for the fixed wall versus 0.74 mm for the moving wall). As shown in Figure 3.9, on the considered relatively fine numerical grid, there is only a limited deviation between the interface radius and the turbulent viscosity; the maximum of the ratio of the turbulent viscosity and the kinematic water viscosity (taken over the full  $x, r$  domain) is 18.8 for the fixed wall approach versus 22.5 for the moving wall approach. The conclusion is that (as expected) both approaches converge to the same solution upon grid refinement. The moving wall approach has the advantage, in comparison to the fixed wall approach, that the grid convergence is faster and the required numerical time step can be larger (due to a smaller value of the maximum Courant number).

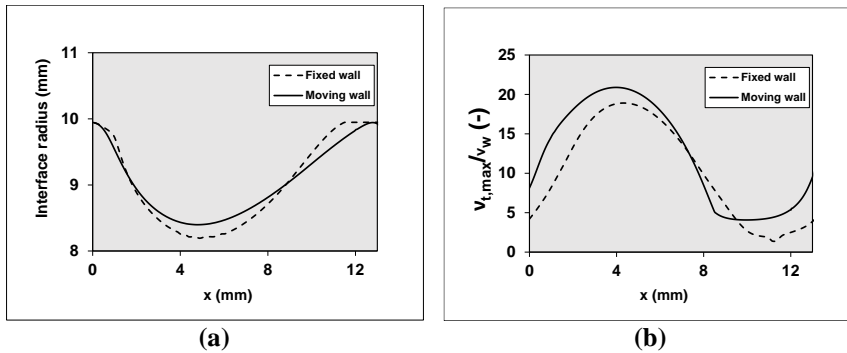


**Figure 3.9. Fixed wall approach versus the moving wall approach for the 2D base case configuration using 200 points in streamwise direction and 400 points in radial direction; (a) interface location, (b) maximum turbulent viscosity.**

The single-phase simulations for the water annulus apply the configuration as depicted in Figure 3.10. The pipe section has the length  $\lambda$  of a single interfacial wave. The wavy interface is fixed and the straight wall of the pipe moves with an imposed (negative) velocity as indicated in the figure. The inflow and outflow velocity profiles are equal, as periodic boundary conditions are imposed. The pressure drop is handled as a source term in the momentum equation. It is important to note that the numerical method is set up such that the relative water flow rate is varied for each time step until the overall streamwise force balance 3.22 is satisfied. Thus the pressure drop source satisfies:  $-dp/dx = 2\tau_w/R$  (where  $R$  is the pipe radius). The obtained water flow rate can be converted to a watercut by assuming a total flow rate (i.e. oil plus water) of  $0.00043 \text{ m}^3/\text{s}$  (or a mixture velocity of 1.24 m/s), which is the same total flow rate as applied in the two-phase simulation.

Figure 3.10 also indicates the averaged water annulus thickness  $d_w$  and the wave amplitude  $A$ . The

imposed interface used has either a pure sinusoidal shape or the shape as obtained from the two-phase simulation. Obviously, a clear difference between the two approaches is that the interface in the single-phase simulation is non-deforming (with no slip boundary conditions) and the interface in the two-phase simulation is flexible. In fact the single-phase approach assumes a solid wavy oil core (or oil with an infinitely large viscosity). Furthermore there can be a pressure change across the curved interface due to the oil-water interfacial tension in the two-phase approach, which does not play a role in the single-phase approach.

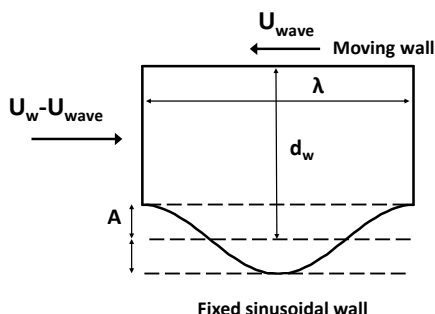


**Figure 3.10. Configuration for the single-phase simulations.**

For the base case conditions, the following simulation approaches were compared: (1) two-phase flow, (2) single-phase water flow in the annulus with a sinusoidal interface with an amplitude that is equal to the one obtained in the two-phase simulation, and (3) single-phase water flow in the annulus with an interface that has the same shape as obtained in the two-phase simulation. The imposed velocity at the moving wall in the single-phase simulations is 1.24 m/s (which is the wave velocity obtained in the two-phase simulation), and the imposed water holdup fraction is 0.2573. For all three approaches the number of grid cells was successfully refined (up to 200 cells in streamwise direction and 400 cells in radial direction) to verify that a good numerical accuracy was obtained.

The numerical values of selected output parameters are compared in Table 3.2. The pressure drops are quite close, albeit that the value for the single-phase simulation with sinusoidal interface is 12% lower than for the other two. The watercut found in the single-phase simulation with sinusoidal interface is slightly lower than the value found in the two-phase simulation, and it also has a higher value of the holdup ratio; the agreement with the two-phase result is better for the single-phase simulation with imposed two-phase interface. The table also shows the values (averaged along streamwise direction) for the wall shear stress and for the interfacial stress. The latter is also splitted in a pressure contribution and in a viscous stress (or shear stress) contribution. The pressure contribution at the interface can be found from integration of the pressure along the location of the interface in streamwise direction. This pressure contribution can also be described as “form drag”, and its percentage contribution to the total interfacial stress is included in the table as well. Obviously, the form drag will be zero in the absence of waves, but for the considered conditions most of the interfacial stress is due to form drag.

Some quantities as obtained with the three modelling approaches are compared in Figure 3.11, which shows the interface shape, the maximum turbulent viscosity, the interface pressure and the interface shear stress. When the two-phase interface is compared with the sinusoidal interface (Figure 3.11a), the two-phase result shows the typical saw-tooth shape. The predictions for the turbulent viscosity in the three approaches (Figure 3.11b) are quite close. There is also good agreement for the interface pressure (Figure 3.11c) although the peak in the single-phase simulation with sinusoidal interface is

slightly shifted, which is in line with the difference in interface shape.

As shown by the shear stress at the interface in Figure 3.11d, which includes zero crossings, there is a water recirculation zone along the wave interface. The shear stress for the two-phase simulation is omitted from the graph, as it is difficult to accurately deduce that profile from the simulation results. The recirculation zone is more clearly illustrated in Figure 3.12, which shows the streamlines. To understand the physics, one should realize that the bulk flow of water, when travelling with the wave, moves from right to left in the figure. The increasing annulus thickness (from right to left) causes the water layer to separate from the interface. In downstream direction (seen from the bulk water moving from right to left), where the thickness of the annulus converges again, the water layer reattaches, which closes the recirculation zone.

The Impingement of the bulk water layer on the Interface at the reattachment location causes a pressure peak (see Figure 3.11c) that gives a main contribution to the form drag (Table 3.2). The flow in the recirculation gives a shear stress contribution that is opposite to the direction of the pressure stress (form drag).

**Table 3.2. Comparison of single-phase and two-phase simulations for the base case conditions (using a fine 200x400 mesh).**

Quantity	Unit	Twophase	Single phase sinusoidal interface	Single phase interface same as twophase
Pressure drop	Pa/m	748	657	760
Watercut	%	22.1	20.0	21.4
Holdup ratio (h)		1.22	1.39	1.27
Wall shear stress	Pa	3.9	3.4	4.0
Total interface stress	Pa	3.4	3.0	3.4
Interface pressure stress	Pa	2.5	2.5	3.4
Interface viscous stress	Pa	0.9	0.5	0.0
Form drag at interface	%	73	84	100

Summary of findings in this section:

- The simulations with either a fixed frame of reference or with a moving-wall frame of reference give similar results.
- The single-phase simulation with sinusoidal interface gives a good agreement with the two-phase approach.
- Therefore the single phase model with imposed waviness can be used to study the effect of the wave structure on the annulus flow.

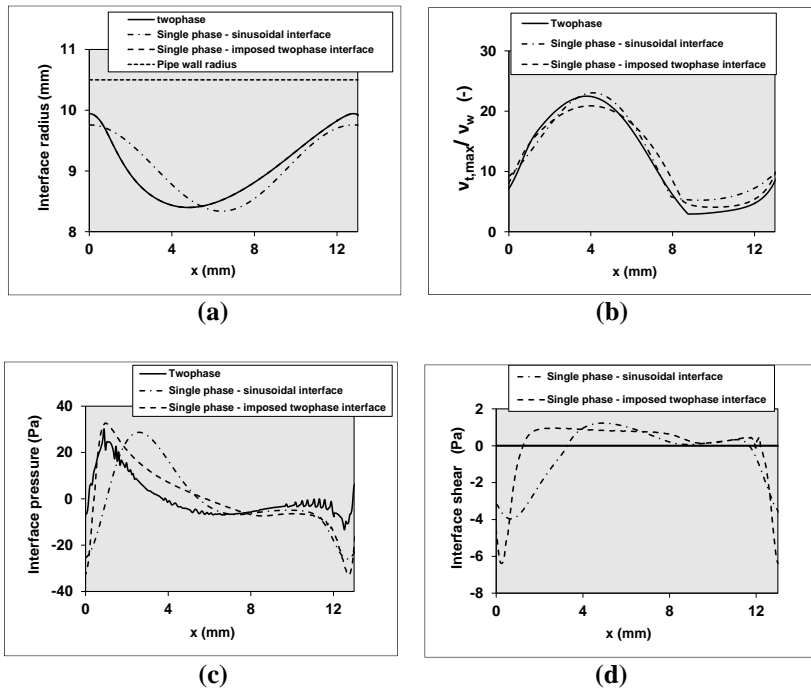


**Figure 3.11.** Comparison of single-phase and two-phase simulations for the base case conditions (using a fine 200x400 mesh); (a) interface location, (b) maximum turbulent viscosity, (c) interface pressure, (d) interfacial shear stress.

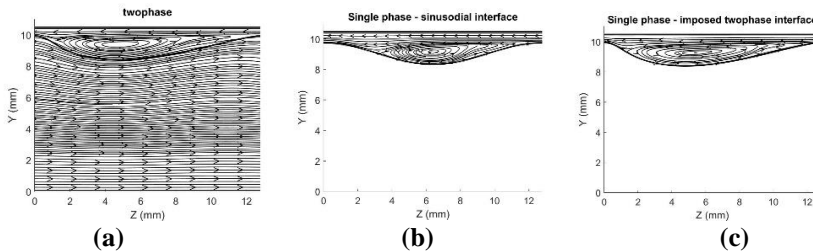


**Figure 3.12.** streamlines showing recirculation zone for single-phase and two-phase simulation for the base case conditions; (a) two-phase, (b) single-phase with sinusoidal interface, (c) single-phase with imposed two-phase interface.

### 3.6 Concentric single-phase results

In the previous section it was found that the single-phase simulation with sinusoidal interface gives a good agreement with the two-phase approach. Therefore, it is attractive to use the single-phase approach for a sensitivity study. We are particularly interested in the dependence of the pressure drop and the water holdup on the wave structure at the interface. The single-phase approach allows to carry out such a sensitivity assessment relatively quickly (i.e. at relatively low computational cost).

Single-phase simulations were carried out for the base case configuration, in which the wave length was varied as 25.6, 12.8, and 6.4 mm, and the wave amplitude was varied between zero and about 1 mm. A pure sinusoidal interface was prescribed in the moving wall simulations (see Figure 3.10). As

explained before, the resulting water flow rate in each simulation is such that the overall force balance for the pipe is satisfied with  $-dp/dx = \frac{2\tau_w}{R}$  (being Equation 3.22). To make a meaningful comparison, the watercut was fixed at 20% (based on a total flow rate, i.e. oil plus water) of 0.00043 m<sup>3</sup>/s, or a mixture velocity of 1.24 m/s). This requires to properly take the (implicit) presence of the oil flow in the core into account. This is done by using Equation 3.25 for the interface velocity, while neglecting the first term on the right hand side of the equation (which indeed can be verified to be very small for large values of the oil/water viscosity ratio). Basically this means that the oil core is predicted by a velocity profile that is everywhere equal to the average oil velocity, and also the interfacial wave velocity is equal to the average oil velocity. This all means that as part of the numerical iteration process, the water holdup fraction (i.e. the average interface location) has to be determined such that the 20% watercut is found. Note that the 20% watercut for a total flow rate of 0.00043 m<sup>3</sup>/s corresponds to a water flow rate of  $8.6 \times 10^{-5}$  m<sup>3</sup>/s.

The single-phase simulation results for the pressure drop, water holdup fraction and the maximum turbulent viscosity are shown in Figure 3.13. The concentric two-phase simulation results are also included, which are in good agreement with the single-phase predictions for a wave length of 12.8 mm. For amplitudes above about 0.9 mm, the water annulus becomes locally so thin that the turbulent viscosity drops due to relaminarization. For amplitudes between the about 0.6 mm and 0.9 mm the pressure drop reaches a maximum plateau level. The smallest considered wave length of 6.4 mm gives the lowest turbulence levels and herewith the lowest pressure drop.

The Increase In pressure drop (up to a plateau value) for increasing amplitude of the interfacial waves, with fixed total flow rate can be explained as follows. A larger wave amplitude gives an increased grip of the oil flow on the water flow. The increased interfacial stress gives an increased water bulk velocity (at fixed total flow rate with fixed watercut) in a thinner water annulus. The increased water bulk velocity gives a higher wall shear stress, and herewith a higher pressure drop.

The dimensionless pressure drop (being the Fanning friction factor at the wall) and the water holdup / watercut dependence (being the holdup fraction) are shown in Figure 3.14. The figure also includes the value for the friction factor for single-phase water flow; if the wave amplitude is sufficiently large (say between 0.6 mm and 0.9 mm) the friction factor for the core-annular flow is close to the water-only value. This is consistent with the reduced value of the holdup ratio for these relatively large value of the wave amplitude, where the large interfacial stress has reduced the water accumulation tendency.

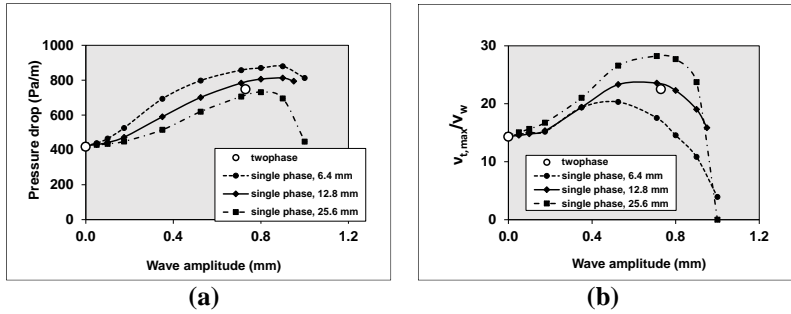
Figure 3.15a shows the interfacial friction factor  $f_i$ , which is defined through  $\tau_i = f_i \frac{1}{2} \rho_w (u_i - u_w)^2$ .

Here  $u_i$  is interface velocity and  $u_w$  is the bulk water velocity.

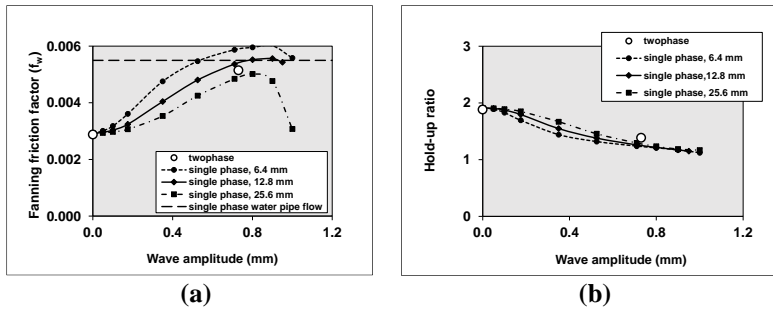
The interfacial friction is built up of a shear stress part and a form stress part, i.e.  $f_i = f_{shear} + f_{form}$ .

Figure 3.15b shows the dependence of the ratio  $f_{form}/f_i$  on the wave amplitude: the form drag becomes dominant at about 90% of the interfacial stress if the wave amplitude increases to about 0.9

mm in the base case configuration.



**Figure 3.13.** Single-phase simulations for the water annulus with sinusoidal wavy interface for the base case configuration with 20% watercut; dependence on the wave amplitude of (a) pressure drop, (b) maximum turbulent viscosity.



**Figure 3.14.** Single-phase simulations for the water annulus with sinusoidal wavy interface for the base case configuration with 20% watercut; dependence on the wave amplitude for (a) Fanning friction factor at the wall, (b) holdup ratio.

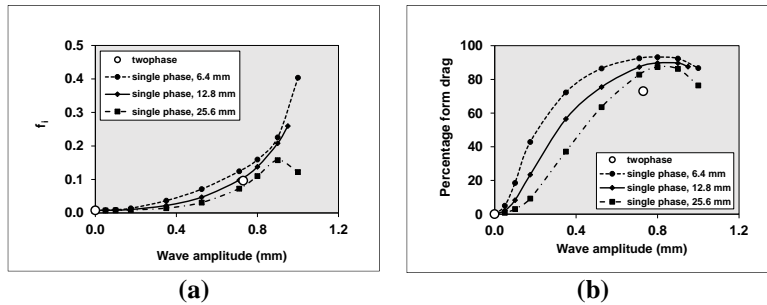


**Figure 3.15.** Single-phase simulations for the water annulus with sinusoidal wavy interface for the base case configuration with 20% watercut; dependence on the wave amplitude for (a) interface friction factor, (b) from drag contribution to interfacial stress.

It is also attractive to apply the single-phase approach to determine the effect of the watercut on the core-annular flow behaviour. Again the same procedure as described above was followed, albeit now for different watercuts. The prescribed total flow rate in the base case configuration is  $0.00043 \text{ m}^3/\text{s}$ , corresponding to a mixture velocity of  $1.24 \text{ m/s}$ . The results for the pressure drop and for the maximum turbulent viscosity, with various values of the wave amplitude, as simulated with the 2D model (i.e. concentric flow, without gravity) are shown in Figure 3.16. In fact the results for zero wave amplitude were obtained with the 1D two-phase model (see Li et al., 2021). The single-phase results with non-zero amplitude waves and the 1D two-phase results (i.e. zero wave amplitude) also compared with the 2D two-phase results. If the wave amplitude is sufficiently high (i.e. say above  $0.35 \text{ mm}$ ), giving sufficient interfacial stress, the pressure drop will become very close to the water only case (at the same fixed total flow rate). When for a given wave height, the watercut is increased to almost 100%, the results for the pressure drop and maximum turbulent viscosity will show a jump when the oil core becomes very small. This is because there is a discontinuity in the configuration: from one with a thin wave core to one where the core is totally absent. Though the jump in the values is not very large here.

The results can also be made dimensionless by using the following two Important quantities: the Fanning wall friction factor  $f_W$  and the holdup ratio  $h$ . As shown in Figure 3.17, the trends are as expected: an increasing wave amplitude gives an increasing friction factor (more wall friction) and a decreasing holdup ratio (less apparent slip between the water and oil flows). The friction factor and holdup ratio are not very strongly dependent on the watercut. The wave amplitude in the two-phase results increases with increasing watercut. The two-phase results for the friction factor, like the single-phase results for the larger wave amplitudes, are almost independent of the watercut. The holdup ratio gradually decreases with increasing watercut.

Figures 3.16 and 3.17 also include the “water equivalent” RANS results, as a function of the (apparent) watercut fraction. These water equivalent results are found from the simulation for water-only flow in the pipe; in the interpretation of these results, they are “artificially” splitted in a core and annulus (while the two thus have the same properties for the viscosity and density); see also Section 3.8. The pressure drop is  $750 \text{ Pa/m}$  and the Fanning friction factor is  $0.0052$ . The two-phase water-oil results for the holdup ratio are close to the water-equivalent results (giving  $h = 1.2$  for large watercut). The maximum turbulent viscosity for the two-phase results is lower than for the water-equivalent results. This shows that the presence of the oil core mitigates the turbulence in the water annulus.

Figures 3.16 and 3.17 also show that the two-phase prediction (with fixed total flow rate) has a minimum in the pressure drop (and also in the Fanning friction factor for the wall) when the watercut is decreased. This is due to the relaminarization of the water annulus. For very low watercut, the pressure drop (and also the Fanning friction factor) increases again. This is because now the (high viscous) oil core is so close to the wall that it imposes a high stress on the water annulus and herewith on the pipe wall, even though the flow is laminar. The minimum and the sharp increase for the pressure drop and Fanning friction factor at decreasing watercut is also clearly visible in the simulations without interfacial waves (zero wave amplitude).

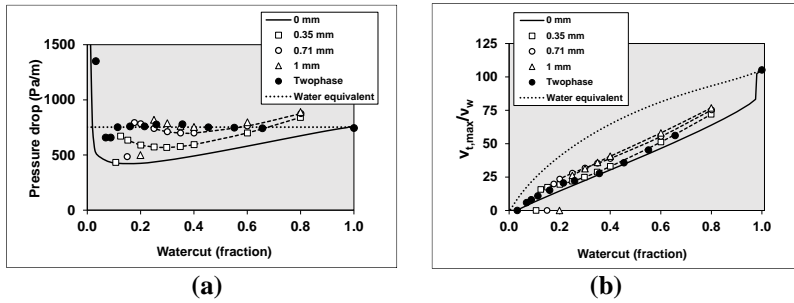


**Figure 3.16. Single-phase simulations for the water annulus with sinusoidal wavy interface for the base case configuration with fixed total flow rate; dependence on the watercut for (a) pressure drop, (b) maximum turbulent viscosity.**

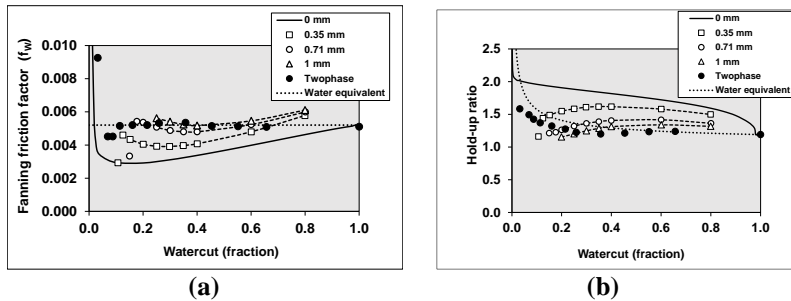


**Figure 3.17. Single-phase simulations for the water annulus with sinusoidal wavy interface for the base case configuration with fixed total flow rate; dependence on the watercut for (a) Fanning friction factor, (b) holdup ratio.**

Summary of findings in this section:

- The integral force balance for core annular flow includes the wall friction between the water annulus and the pipe wall and the interfacial stress between the oil core and the water annulus. The interfacial stress depends on the length and amplitude of the waves at the interface.
- The wall friction and interfacial stress can be determined from the RANS simulations.
- Unless the waves are absent or the imposed wave amplitude is very small, the travelling waves easily create sufficient stress on the water annulus, such that it is apparently felt by the pipe wall as a fully turbulent single-phase water flow.
- Most of the interfacial stress is due to form drag (with local water recirculation zones with respect to an observer travelling with the waves) and only a small part is due to shear stress.
- The water holdup fraction for the core-annular flow closely agrees with the value found for the so-called “water equivalent flow” (i.e. single phase water pipe flow, with an artificial split between a water core and a water annulus).
- A good estimate of the frictional pressure drop and the holdup ratio of core annular flow with a turbulent water annulus is to take the Fanning friction factor the same as the well-known value for water only pipe flow and the holdup ratio the same as for the equivalent water flow (i.e. about  $h = 1.2$ ).

### 3.7 Eccentric single-phase results

The single-phase RANS model was also used to investigate effect of an eccentric core. Thereto again the base case configuration was considered (as defined in Section 3.2.3). The total flow rates was fixed at 0.00043 m<sup>3</sup>/s, or a mixture velocity of 1.24 m/s, with 20% watercut. The interface has either



no waves or waves with a prescribed amplitude of 0.71 mm. The pipe section length was set to 12.8 mm.

To create an eccentric case in the single-phase simulation for the annulus, the imposed interface with waves was moved in the direction to the top of pipe. If the (average) water layer thickness at the top and bottom are denoted as  $d_{top}$  and  $d_{bottom}$ , respectively, the eccentricity is defined as  $e = \frac{d_{bottom} - d_{top}}{d_{bottom} + d_{top}}$ . Thus  $e = 0$  for a concentric oil core, and  $e = 1$  for a fully eccentric oil core. An eccentric core requires carrying out a 2D single-phase simulation when there are no waves (i.e. no 3D simulation is needed as the flow is the same in each cross sectional plane) and a 3D single-phase simulation when there is a finite-amplitude wave. The simulation results for the pressure drop and maximum turbulent viscosity are shown in Figure 3.18, and for the Fanning friction factor at the wall and the holdup ratio in Figure 3.19. As the top/bottom water annulus becomes thinner/thicker with increasing eccentricity, the turbulence level increases in the bottom layer and decreases in the top layer. If the eccentricity becomes too high the top water annulus relaminarizes. The effect of the eccentricity on the pressure drop, friction factor, and holdup ratio is small.

Assuming a horizontal pipe with gravity, Figure 3.20 shows the pressure force (corrected for water hydrostatic head) and the shear force on the oil core in vertical direction. These forces are scaled with the buoyancy force (which is known from the hold-up fraction and from the water and oil densities specified in Section 3.2.3). This shows that the eccentricity (i.e. oil core located in the direction of the pipe top) gives both downward directed pressure and shear forces. In this example, there is a force equilibrium at an eccentricity of about  $e=0.19$ . In the absence of waves the vertical pressure force (corrected for water hydrostatic head) is zero (as there is parallel flow), whereas the downward shear force turns out to be very small (being insufficient to compensate the buoyancy force). This thus confirms that waves are needed to prevent the oil core from touching the upper wall in horizontal core-annular flow.

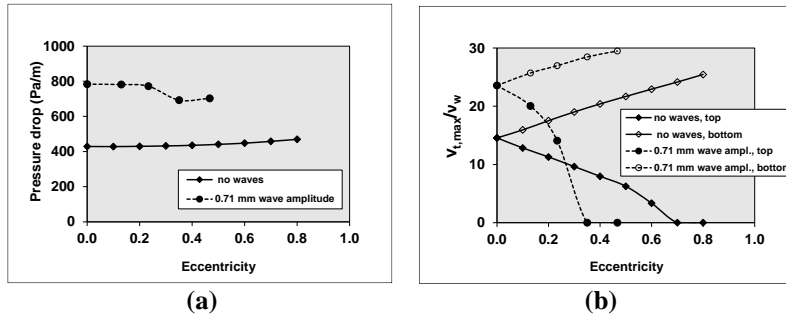


**Figure 3.18.** Single-phase simulations for the water annulus with sinusoidal wavy interface for the base case configuration with 20% watercut; dependence on the eccentricity for (a) pressure drop, (b) maximum turbulent viscosity.

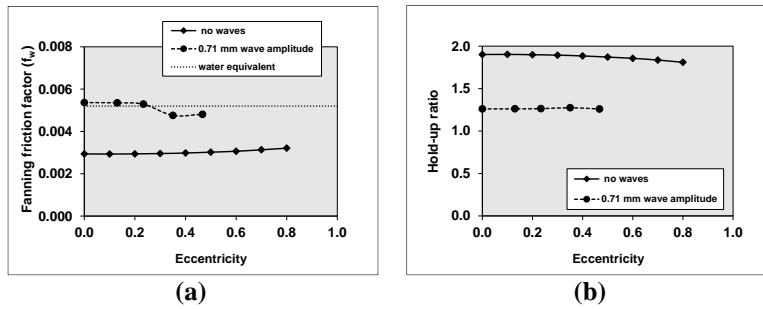


**Figure 3.19. Single-phase simulations for the water annulus with sinusoidal wavy interface for the base case configuration with 20% watercut; dependence on the eccentricity for (a) Fanning friction factor at the wall, (b) holdup ratio.**

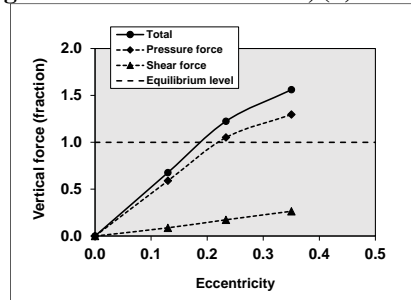


**Figure 3.20. Single-phase 3D simulations for the water annulus with sinusoidal wavy interface with 0.71 mm amplitude for the base case configuration with 20% watercut; vertical forces on the oil core.**

Summary of findings in this section:

- The dimensionless pressure drop (which is the Fanning friction factor for the wall) is almost independent of the eccentricity, and equal to the water-only value.
- There is also an eccentricity where the vertical force balance for the single phase annulus simulation is satisfied, with a downward directed pressure force and a downward directed shear force.
- Such a balance cannot be found in the RANS results for eccentric core-annular flow without interface waves. This supports the conjecture that waves are needed to enable stable horizontal core-annular flow.

### 3.8 Comparison with experiments and DNS

Figure 3.21 compares the concentric, two-phase RANS simulations with the experiments by Van Duin et al., (2019) and with the experiments by Sotgia et al. (2008). The “friction factor ratio” is shown, which is defined as the ratio of the Fanning friction factor at the given watercut and the Fanning friction factor for water only flow. In the sections above we have argued that the pressure drop for two-phase core annular flow is about the same as found for water only flow (at the same total flow

rate) for all watercuts, except for low watercuts. This is confirmed by the comparison in Figure 3.21.

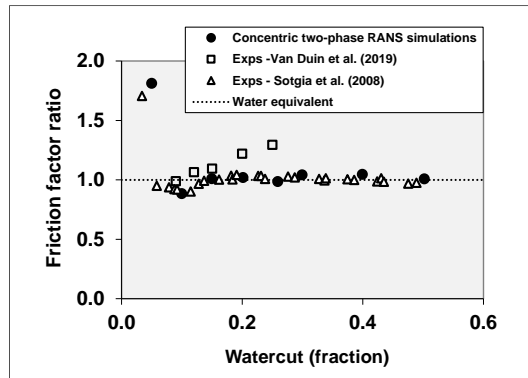


**Figure 3.21. Comparison between simulations and experiments; Fanning friction factor versus watercut.**

The single phase simulation for the water annulus in a horizontal pipe for the base case conditions at eccentricity  $e=0.19$  (which satisfies the vertical force balance as shown in Section 3.7) is compared with the water-oil interface obtained in the experiments by Duin et al. (2017). There is very good agreement; the experiment has only a slightly lower eccentricity of  $e=0.12$ . In fact, for both the single phase simulation and the experiment the eccentricity is very small (see also Figure 3.21). This is in contrast to the (eccentric) 3D two-phase simulation result, as presented in our earlier study (Haoyu et al., 2021), which gives a much larger eccentricity ( $e=0.7$ ) than the experiment. This is probably due to laminarization in the RANS model for the top water annulus, compared to a fully turbulent bottom layer. Work is ongoing to further investigate this (using the type of approach with single phase simulations and performing a vertical force balance as outlined in the present chapter).

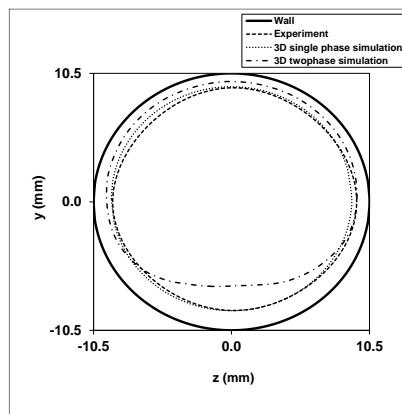


**Figure 3.22. Comparison between simulations and experiments; Average location of the water-oil interface.**

As accurate experimental results for the holdup ratio as a function of the watercut for core-annular flow seem to be missing in the literature, we have used the Direct Numerical Simulation results by Kim & Choi (2018) as a reference for validation of the RANS model and the different mechanistic models. They simulated 5 watercut conditions for the pipe flow that were also used in the experiments by Vanegas Prada (1999); see Table 3.1. The simulation results for the Fanning friction factor ( $f_W$ ), the friction factor ratio, and the holdup ratio ( $h$ ) for the five watercut conditions are shown in Figure 3.23. All simulations (i.e. RANS and DNS) have a fixed prescribed frictional pressure drop of 400

Pa/m.

3

For all 5 watercuts, except for the smallest value, for which DNS results are available, the Fanning friction factor is almost the same as for turbulent flow with only water (i.e. all oil is assumed to be replaced by water). As shown in Figure 3.23a, the lowest watercut in the DNS gives a higher value for the Fanning friction factor, which is because now the water annulus is so thin that it gives laminar flow instead of turbulent flow. Considering the 4 watercuts with the turbulent water annulus, the Fanning friction factor that is found from our RANS simulations is also almost independent of the watercut, but it is about 18% smaller than the DNS results, 17% smaller than the single-phase water value found with the Churchill correlation, and 11% smaller than the single-phase water value found with Launder & Sharma  $k - \epsilon$  model. As the Churchill correlation for the Fanning friction factor is almost exact for single-phase water flow, this also shows that the Launder & Sharma  $k - \epsilon$  model underpredicts single-phase turbulent pipe flow by  $(17-11)=6\%$ . For the 4 watercuts with the turbulent annulus, the Ullmann & Brauner model prediction for the Fanning friction factor is only about 3% higher than the DNS predictions.

The DNS and RANS predictions for the holdup ratio  $h$  are compared in Figure 3.23c. Also included are the expressions used by Oliemans, Bai et al., and Ullmann & Brauner (as referred to in Section 3.3). The DNS and RANS results show a slow decrease of the holdup ratio for increasing watercut; this means that the water accumulation effect (i.e.  $WC > \alpha_w$ ) decreases when the watercut becomes larger. For the 4 watercut values used in the DNS (with turbulent water annulus) the RANS prediction for the holdup ratio is about 12% above the DNS prediction. Thus the water accumulation effect is larger in RANS than in DNS.

Figure 3.23c also includes a curve denoted as the “water equivalent” holdup ratio. As already mentioned in Section 3.6, this curve is found by considering water-only flow, that is “artificially” splitted in a core and annulus (but the two thus have the same properties for the viscosity and density). The watercut and holdup ratio are now referring to the annulus part of the single-phase RANS results; here the watercut is determined by integrating the RANS velocity profile in the annulus to give the water flow rate in the annulus, and divide this by the total flow rate through the pipe. This shows that there is relatively much water accumulation close to the pipe wall for low watercut, where the water is slowed down due to the wall presence. For high watercut (i.e. vanishing core layer) the holdup ratio decreases to  $h = u_{centre}/u_{bulk}$  (i.e. the ratio of the water velocity at the pipe centre and the average water velocity over the pipe cross section). It is helpful to be aware of this natural accumulation effect when interpreting the holdup ratio for core-annular flow with a real difference in viscosity between the core liquid and the annulus liquid. In fact this means that the increase in holdup ratio found for decreasing watercut in the DNS and RANS for the configuration of Kim & Choi can (at least) partly be explained from this natural accumulation effect.

The largest three watercuts have a shear-based Reynolds number as  $Re_\tau$  that is above 90, which gives a turbulent water annulus. The lowest watercut of 7% has  $Re_\tau = 33$ , which gives a laminar water

annulus. A more detailed comparison of the RANS and DNS simulation results is given in Chapter 6.

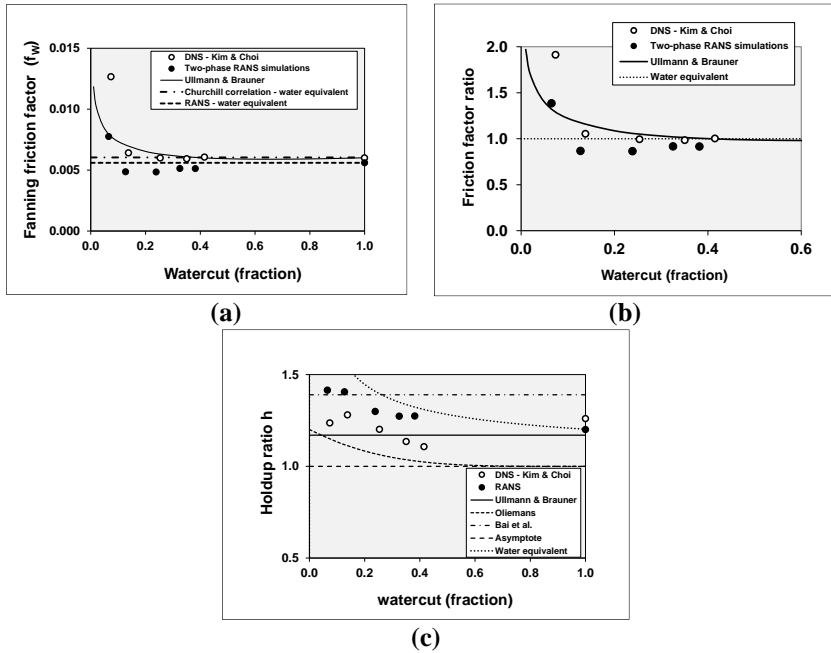


**Figure 3.23. Comparison of RANS and mechanistic models (or correlations) with the DNS results for different watercuts by Kim & Choi (2018) at a fixed frictional pressure drop is 400 Pa/m; (a) Fanning friction factor, (b) Friction factor ratio, (c) holdup ratio.**

Summary of findings in this section:

- The simulation results were validated by comparison with different sets of experimental data (particularly with those by Sotgia et al. and by Duin et al.) and with the Direct Numerical Simulations by Kim & Choi. The comparison supports the theoretical findings.
- More work is needed to understand the effect of gravity in horizontal core-annular flow (through different types of models, e.g. RANS, LES, DNS, and experiments).

### 3.9 Conclusions

1. Simulations were carried out for core-annular flow with a turbulent water annulus through solving the RANS two-phase equations with the Launder-Sharma low-Reynolds number  $k-\epsilon$  model. The flow is characterized by travelling waves at the oil-water interface. As expected, the simulations with either a fixed frame of reference or with a moving-wall frame of reference give similar results.
2. Unless the pipe section length in the simulation is chosen too short, the predicted wave length, wave velocity, and wave frequency are almost independent of the length of the computational domain. Also the predictions of the pressure drop and the watercut (for given total flow rate and water holdup fraction) are almost independent of the section length.
3. A review of different sets of lab data for core-annular flow shows that the Fanning friction factor for the wall, which makes the pressure drop dimensionless with the dynamic pressure based on the water density and on the mixture velocity, is an attractive parameter. In the experiments, that friction factor is close to the value found for turbulent water-only flow, and almost independent of the watercut.

4. A force balance for core annular flow was considered, which includes the wall friction between the water annulus and the pipe wall and the interfacial stress between the oil core and the water annulus. The wall friction and interfacial stress were determined from the RANS simulations. The interfacial stress will be dependent on the length and amplitude of the waves at the interface. Details could be simulated through considering a single phase RANS model for the water annulus with imposed waviness on a moving wall.
5. Unless the waves are absent or the imposed wave amplitude is very small, the travelling waves easily create sufficient stress on the water annulus, such that it is apparently felt by the pipe wall as a fully turbulent single-phase water flow. Most of the interfacial stress is due to form drag (with local water recirculation zones with respect to an observer travelling with the waves) and only a small part is due to shear stress.
6. The water holdup fraction for the core-annular flow, which is a second important quantity next to the Fanning wall friction factor, closely agrees with the value found for the so-called “water equivalent flow” (i.e. single phase water pipe flow, with an artificial split between a water core and a water annulus).
7. A good estimate of the frictional pressure drop and the holdup ratio of core annular flow with a turbulent water annulus is to take the Fanning friction factor the same as the well-known value for water only pipe flow and the holdup ratio the same as for the equivalent water flow (giving about  $h = 1.2$ ).
8. By re-writing the mechanistic model of Ullmann & Brauner, we found that this estimate is actually also hidden in that model. The RANS simulation show that a different behaviour is only found when the watercut is decreased to a very low value, where the water annulus becomes so thin that it relaminarizes. Here the near-wall presence of the moving oil core with the high imposed shear determines the wall friction.
9. Simulations were also carried out with the single phase RANS model for the water annulus for an eccentric rather than a concentric interface for horizontal pipe flow. Again, the dimensionless pressure drop (which is the Fanning friction factor for the wall) is almost independent of the eccentricity, and equal to the water-only value. There is also an eccentricity where the vertical force balance for the single phase annulus simulation is satisfied, with a downward directed pressure force and a downward directed shear force. These two forces balance the upward buoyancy force, and they physically make up the levitation mechanism that prevent that the oil core touches the top wall. Such a balance cannot be found in the RANS results for eccentric core-annular flow without interface waves. This 82 supports the conjecture that waves are needed to enable stable horizontal core-annular flow.
10. The simulation results were validated by comparison with different sets of experimental data (particularly with those by Sotgia et al. and by Duin et al.) and with the Direct Numerical Simulations by Kim & Choi. The comparison supports the theoretical findings.

## References

- Arney, M.S., Bai, R., Guevara, E., Joseph, D.D., Liu, K., 1993. Friction factor and holdup studies for lubricated pipelining-I. Experiments and correlations. *Int. J. Multiphase Flow* 19, 1061-1076.
- Bai, R., Chen, K., Joseph, D.D., 1992. Lubricated pipelining: stability of core-annular flow. Part 5. experiments and comparison with theory. *J. Fluid Mechanics* 240, 97-132.
- Bai, R., Kelkar, K., Joseph, D.D., 1996. Direct simulation of interfacial waves in a high-viscosity-ratio and axisymmetric core-annular flow. *Journal of Fluid Mechanics* 327: 1-34.
- Bannwart, A. A., 2001. Modeling aspects of oil-water core-annular flows. *J. Petrol. Sci. Engng* 32, 127-143.
- Beerens, J.C., Ooms, G., Pourquié, M.J.B.M., Westerweel, J., 2014. A comparison between numerical predictions and theoretical and experimental results for laminar core-annular flow. *AIChE Journal* 60.8, 3046-3056.
- Chen, K., Bai, R., Joseph, D.D., 1990. Lubricated pipelining. Part 3 Stability of core-annular flow in vertical pipes. *Journal of Fluid Mechanics* 214, 251-286.
- Ghosh, S., Mandal, T.K., Das, P.K., 2009. Review of oil water core annular flow. *Renewable and Sustainable Energy Rev.* 13, 1957-1965.
- Grassi, B., Strazza, D., Poesio, P., 2008. Experimental validation of theoretical models in two-phase high-viscosity ratio liquid-liquid flows in horizontal and slightly inclined pipes. *Int. J. Multiphase Flow* 34, 950-965.
- Hu, H., Jing, J., Tan, J., Yeoh, G.H., 2020. Flow patterns and pressure gradient correlation for oil-water core-annular flow in horizontal pipes. *Experimental and Computational Multiphase Flow* 2, 99-108.
- Huang, A., Christodoulou, C., Joseph, D.D., 1994. Friction factor and holdup studies for lubricated pipelining - II; laminar and  $k - \epsilon$  models of eccentric core flows. *Int. J. Multiphase Flow* 20, 481-491.
- Ingen Housz, E.M.R.M., Ooms, G., Henkes, R.A.W.M., Pourquié, M.J.B.M., Kidess, A., Radhakrishnan, R., 2017. A comparison between numerical predictions and experimental results for core-annular flow with a turbulent annulus, *Int. J. Multiphase Flow* 95, pp. 271-282.
- Jiménez, J., Moin, P., 1991. The minimal flow unit in near-wall turbulence. *J. Fluid Mechanics* 225, 213-240.
- Joseph, D.D., Bai, R., Chen, K.P., Renardy, Y.Y., 1997. Core-Annular Flows. *Annual Review of Fluid Mechanics* 29, 65-90.
- Kim, K., Choi, H., 2018. Direct numerical simulation of a turbulent core-annular flow with water-lubricated high viscosity oil in a vertical pipe. *J. Fluid Mech.* 849, 419-447.
- Ko, T., Choi, H.G., Bai, R., Joseph, D.D., 2002. Finite element method simulation of turbulent wavy core-annular flows using a  $k - \omega$  turbulence model method. *Int. J. Multiphase Flow* 29, 1205-1222.
- Launder, B.E., Sharma, B.T., 1974. Application of the energy dissipation model of turbulence to the calculation of flow near a spinning disc. *Lett. Heat and Mass Transfer* 1, 131-138.
- Li, H., Pourquié, M.J.B.M., Ooms, G., Henkes, R.A.W.M. 2021. Simulation of turbulent horizontal oil-water core-annular flow with a low-Reynolds number  $k - \epsilon$  model. *Int. J. Multiphase Flow* 142, 103744.
- Oliemans, R.V.A. 1986 The lubricating-film model for core-annular flow, PhD Thesis, Delft University of Technology.
- Oliemans, R.V.A., Ooms, G., Wu, H.L., Duijvestein, A., 1987. Core-annular oil/water flow: the turbulent-lubricating-film model and measurements in a 5 cm pipe loop. *Int. J. Multiphase Flow* 13, 23-31.
- Ooms, G., Pourquié, M. J. B. M. , Poesio, P., 2012. Numerical study of eccentric core-annular flow. *Int. Journal of Multiphase Flow* 42, 74-79.
- Rodriguez, O.M., Bannwart, A.C., 2006. Experimental study on interfacial waves in vertical core

- flow. *J. Petroleum Science and Engineering* 54, 140-148.
- Shi, J., Lao, L., Yeung, H., 2017. Water-lubricated transport of high-viscosity oil in horizontal pipes: The water holdup and pressure gradient. *Int. J. Multiphase Flow* 96, 70-85.
- Sotgia, G., Tartarini, P., Stalio, E., 2008. Experimental analysis of flow regimes and pressure drop reduction in oil–water mixtures. *Int. J. Multiphase Flow* 34, 1161-1174.
- Tripathi, S., Tabor, R.F., Singh, R., Bhattacharya, A., 2017. Characterization of interfacial waves and pressure drop in horizontal oil-water core-annular flows. *Physics of Fluids* 29, 082109.
- Ullmann, A., Brauner, N., 2004. Closure relations for the shear stress in two-fluid models for core-annular flow. *Multiphase Science and Technology* 16, 355-387.
- Van Duin, E., Henkes, R.A.W.M., Ooms, G., 2019. Influence of oil viscosity on oil-water core-annular flow through a horizontal pipe. *Petroleum* 5.2, 199-205.
- Vanegas Prada, J.W., 1999. Estudo experimental do escoamento anular óleo-água (“core flow”) na elevação de óleos ultraviscosos. Master Thesis, University of Campinas, Brazil.
- Yamamoto, T., Okano, Y., Dost, S., 2017. Validation of the S-CLSVOF method with the density-scaled balanced continuum surface force model in multiphase systems coupled with thermocapillary flows. *Int. J. for Numerical Methods in Fluids* 83.3, 223-244.



## 4

Interfacial wave  
growth

*Detailed numerical simulations were carried out for the wave initiation, growth, and saturation at the oil-water interface in core-annular flow. The focus is on conditions with a turbulent water annulus, but the laminar water annulus was considered as well. The simulation results were compared with lab measurements. The growth rate for the linear instability of different wave lengths in the case of a turbulent water annulus can be accurately obtained from 2D axisymmetric RANS simulations with the Launder-Sharma low-Reynolds number  $k - \varepsilon$  model. This also provides the most unstable wave length for the turbulent water annulus. The maximum wave growth rate for a turbulent water annulus is significantly higher than for a laminar water annulus. The most unstable wave length in the simulations is slightly smaller than in the experiments. There is a reasonably good agreement between the amplitudes of the different wave lengths as found in the experiments and in the simulations.*

## 4.1 Introduction

Under certain conditions for two-phase liquid-liquid flow in a pipe, the less viscous liquid (e.g. water) can migrate to the high shear region near to the pipe wall (forming an annulus flow), leaving the more viscous liquid (like oil) in the centre of the pipe (forming core flow). This flow pattern is referred to as core-annular flow (CAF); see the review by Joseph et al. (1997). In this way, the less viscous liquid functions as a lubrication layer, which greatly reduces the pressure drop compared to the case in which only the high viscous liquid is transported through the pipe. Oil-water core annular flow can be applied in the petroleum industry for effective transportation. This flow type is also of high interest for the understanding of physics of interfacial waves in fluid mechanics.

Core-annular flow with a completely flat liquid-liquid interface is called perfect core-annular flow (PCAF). That flow type is only possible in a vertical pipe in a small range of velocities, as visualized in the experiments by Chen et al. (1990) and Bai et al. (1992). Chen et al. (1990) considered the effect of gravity on the neutral stability curve, and found that PCAF in a vertical pipe can remain stable within a certain interval range of Reynolds numbers. The density ratio can be optimized to maximize the stable range of Reynolds numbers. In most practical cases, however, the flat interface cannot remain stable, and waves will develop leading to so-called wavy core-annular flow (WCAF). In horizontal pipes, the presence of interfacial waves is essential to provide a downward force to balance the upward buoyancy force; Ooms et al. (2013) have studied this levitation mechanism in the presence of a laminar water annulus. Depending on the flow conditions (such as the oil and water superficial velocities), the stability of CAF can also be lost to give transition to another flow regime, like stratified flow, oil slug flow, or oil flow with dispersed water droplets. Bai et al. (1992) provided a flow pattern map with six different flow patterns based on the oil and water superficial velocities. The largest reduction factor in pressure drop occurs with the CAF pattern. Within WCAF, there can be bamboo waves or cork-screw waves.

The formation of interfacial waves is caused by the instability of disturbances at the initially flat liquid-liquid interface of the flow. Over the years, the linear instability problem of laminar-laminar two-phase flow has been studied by various researchers. In the theoretical investigation of linear instability, the governing equations are linearized to describe a small disturbance with its growth rate. The solution is obtained by solving an eigenvalue problem for the linearized equation. The disturbance can be assumed to be a wave with a long, medium, or short length. Parameters that determine the linear instability include surface tension, viscosity, and gravity. Yih (1967) has shown that in 2D liquid-liquid channel flow, a long wave instability exists for all values of the Reynolds number, and the instability is due to the viscosity difference between the two fluids. Hooper (1985) studied instability for two-phase plane Couette flow and found that the flow is always unstable if the thickness of the layer with less viscous fluid is small. Hickox (1971) found that long waves are always unstable for an axisymmetric Poiseuille flow with the less viscous fluid in the core. Ooms (1971) analysed the stability of laminar-laminar core-annular flow, while ignoring the effect of viscosity on the flow stability and found two types of instability: one is the Kelvin-Helmholtz instability, which is due to the apparent difference in flow velocity near the interface, and the other is a capillary instability, induced by the surface tension. The considered disturbance is axisymmetric and has a wave length larger than the circumference of the oil core. Hooper & Boyd (1983) studied short-wave instability of two viscous fluids in unbounded Couette flow. The flow is always unstable when surface tension is neglected. The instability is of viscous nature and is created quickly close to the interface in the less viscous fluid part. Surface tension can stabilize this type of short-wave instability. Preziosi et al. (1989) found that surface tension stabilizes short waves in core annular flow. Long waves are destabilizing the flow and will lead to oil droplets in the water annulus. With increasing Reynolds number, the long wave capillary instability can be stabilized by shear. However, when the Reynolds is above a critical value, a second capillary instability causes emulsion of oil into water. Therefore, upper and lower branches of the critical Reynolds number exist in relation to the neutral stability curve. This

stabilization phenomenon agrees well with the experiment from Charles et al. (1961).

Hu & Joseph (1989) used the energy equation to study the linear instability mechanism. They found that three parameters are involved: surface tension, interface stress, and wave Reynolds stress. At small Reynolds numbers, surface tension can cause instability, while the other two sources stabilize the flow. At large Reynolds number, surface tension stabilizes the flow, and the other two sources destabilize the flow. For even higher Reynolds number, the wave Reynolds stress in the water is the main source of instability. The wavy core-annular flow pattern in the experiment by Charles et al. (1961) is regarded as a stable flow, where the destabilizing Reynolds stress and the stabilizing interface viscosity compensate each other. Bai et al. (1992) found a new flow pattern with bamboo waves in their vertical pipe flow experiment. Energy budgets show that the bamboo wave is induced by interfacial viscous friction, the surface tension is only slightly destabilizing, and the wave Reynolds stress stabilizes the flow. Miesen et al. (1992) focused their analysis on disturbances with an intermediate wave length. A rather good agreement is found when comparing the wave stability relationship with the experimental wave distribution. Boomkamp & Miesen (1996) found five instability types for two-phase parallel flow. They argue that stable core-annular flow, as found in the stability analyses by Preziosi et al. (1989), Hu & Joseph (1989) and Miesen et al. (1992), is due to the stabilizing effect of the presence of the jump in viscosity near the interface. When the wave amplitude becomes significant, non-linear effects can saturate the linear instability. Papageorgiou et al. (1990) studied the non-linear stability of CAF by assuming the annulus thickness is much smaller than the core radius.

Besides the linear and nonlinear theoretical analysis (using an eigenvalue approach), numerical simulations can also be used to study instability problems. Li & Renardy (1999) used the Volume-of-Fluid (VOF) method to determine the instability in 2D vertical core-annular flow. Both the linear and non-linear stages are studied, and the relevant flow patterns are shown. Beerens et al. (2014) also used the VOF numerical method, with which they verified the stable and unstable regions with the neutral curve in the theoretical analysis by Hu & Joseph (1989), and they also reproduced the linear growth rate found in the theoretical analysis by Li & Renardy (1999). The effect of gravity on the streamlines is considered and the wave distribution for longer pipe sections is shown.

All the stability analyses referred to above considered a laminar-laminar two-phase base flow. In many applications, however, the base flow pattern can be turbulent. The presence of turbulence makes the stability problem even more challenging. Kuru et al. (1995) and Náráigh et al. (2011) carried out a linear stability analysis with turbulent base flow in a stratified two-phase channel configuration. They made the quasi-static assumption, which means that the size of the turbulent fluctuations in space and time is much smaller than the magnitude of the mean velocity profile.

The present study will be focussed on the linear and non-linear wave growth in core-annular flow, with a laminar oil core and a turbulent water annulus. We will carry out a detailed numerical analysis to track the full process of wave initiation, wave growth, and wave saturation. The simulation results are compared with experiments obtained in our lab. The work builds on recent core-annular flow studies by the same authors (Li et al., 2021, 2022).

## 4.2 Modelling approach

### 4.2.1 Governing equations

The mass and momentum conservation equations for an incompressible, isothermal fluid read (in Cartesian coordinates):

$$\frac{\partial u_i}{\partial x_i} = 0 \quad (4.1)$$

$$\rho \frac{\partial u_i}{\partial t} + \rho u_j \frac{\partial u_i}{\partial x_j} = \frac{\partial}{\partial x_j} \left( \rho (\nu + \nu_t) \left( \frac{\partial u_i}{\partial x_j} + \frac{\partial u_j}{\partial x_i} \right) \right) - \frac{\partial p}{\partial x_i} + \rho g_i + F_{\sigma,i} \quad (4.2)$$

These are the Reynolds-Averaged Navier-Stokes Equations (RANS). Here  $u_i$  is the velocity,  $\rho$  and  $\mu$  are the fluid density and viscosity,  $g_i$  is the gravitational acceleration,  $p$  is the pressure and  $F_{\sigma,i}$  is the interfacial tension force. For the pipe flow, we will use  $x_1 = x$  for the coordinate along the pipe axis, and  $x_2 = y$  and  $x_3 = z$  for the coordinates in the cross-sectional plane; the velocity components are  $u$ ,  $v$ , and  $w$ , in the directions  $x$ ,  $y$ , and  $z$ , respectively. The gravity components are:  $g_1 = -g$ , and  $g_2 = g_3 = 0$ , where  $g$  is the gravitational acceleration. The actual simulations were carried out using 2D axisymmetric coordinates with the radius  $r = \sqrt{y^2 + z^2}$ .

The turbulent viscosity is modelled with the low-Reynolds number  $k - \epsilon$  model of Launder & Sharma (1974), which reads:

$$\nu_t = C_\mu f_\mu \frac{k^2}{\epsilon} \quad (4.3)$$

$$\frac{\partial k}{\partial t} + u_j \frac{\partial k}{\partial x_j} = \frac{\partial}{\partial x_j} \left( \nu + \frac{\nu_t}{\sigma_k} \right) \frac{\partial k}{\partial x_j} + \nu_t \left( \frac{\partial u_j}{\partial x_j} \right)^2 - \tilde{\epsilon} - D \quad (4.4)$$

$$\frac{\partial \tilde{\epsilon}}{\partial t} + u_j \frac{\partial \tilde{\epsilon}}{\partial x_j} = \frac{\partial}{\partial x_j} \left( \nu + \frac{\nu_t}{\sigma_\epsilon} \right) \frac{\partial \tilde{\epsilon}}{\partial x_j} + C_1 f_1 \frac{\tilde{\epsilon}}{k} \nu_t \left( \frac{\partial u_j}{\partial x_j} \right)^2 - C_2 f_2 \frac{\tilde{\epsilon}^2}{k} + E \quad (4.5)$$

With  $D = 2\nu \frac{\partial \sqrt{k}}{\partial x_j} \frac{\partial \sqrt{k}}{\partial x_j}$  and  $E = 2\nu \nu_t \left( \frac{\partial^2 u_j}{\partial x_j^2} \right)^2$ . The turbulent energy dissipation rate is  $\epsilon = \tilde{\epsilon} + D$ .

Furthermore,  $C_\mu = 0.09$ ,  $C_1 = 1.44$ ,  $C_2 = 1.92$ ,  $\sigma_k = 1.0$ ,  $\sigma_\epsilon = 1.3$ ,  $f_\mu = \exp\left(\frac{-3.4}{(1 + \frac{Re_t}{50})^2}\right)$ ,  $f_1 = 1$ ,  $f_2 = 1 - 0.3 \exp(-Re_t^2)$ ,  $Re_t = \frac{k^2}{\tilde{\epsilon} \nu}$ . The boundary conditions at the wall are:  $k=0$  and  $\tilde{\epsilon} = 0$ .

Quite a few low-Reynolds number  $k - \epsilon$  formulations are available in the literature. A large advantage of the Launder-Sharma one is that the low-Reynolds number terms do not include the explicit distance to the closest wall. Instead, the parameter  $Re_t$  is used to incorporate the effect of turbulence damping when a wall is approached. In the same way, the model will incorporate the possible damping of turbulence when the oil-water interface is approached in core-annular flow. The low-Reynolds number  $k - \epsilon$  model is used everywhere in the domain, also in the laminar oil core. Because of the presence of the low-Reynolds number terms the model automatically relaminarizes in the viscous oil core (i.e. it gives zero turbulent viscosity).

#### 4.2.2 Numerical method

We used the open-source package OpenFOAM to solve the RANS equations, applying the CLSVOF method for the interface capturing. The CLSVOF solver, which was developed by Yamamoto et al. (2017), is based on the interFoam Volume of Fluid (VOF) solver in OpenFOAM. In the CLSVOF solver the level set function is used to calculate the interfacial tension force. Starting from the VOF method, the volume fraction  $\alpha$  is introduced to distinguish between the two fluid phases:  $\alpha = 0$  is the oil phase,  $\alpha = 1$  is the water phase, and  $0 < \alpha < 1$  denotes the oil-water interface. Then the fluid density and viscosity in the equations are:

$$\rho = (1 - \alpha)\rho_o + \alpha\rho_w \quad (4.6)$$

$$\mu = (1 - \alpha)\mu_o + \alpha\mu_w \quad (4.7)$$

The subscript “o” refers to oil, and the subscript “w” refers to water.  $\alpha$  is calculated from the following advection equation:

$$\frac{\partial \alpha}{\partial t} + \nabla \cdot (\alpha \vec{u}) + \nabla \cdot ((1 - \alpha)\alpha \vec{u}_r) = 0 \quad (4.8)$$

The third term on the left-hand side is the compressive term (with the divergence of the compressive flux); here  $\vec{u}_r = \vec{u}_w - \vec{u}_o$ . This term is meant to control the sharpness of interface.

The level set function  $\Phi$  is defined as the distance from the interface, where the interface is the isoline with  $\Phi = 0$ . The initial value of the level set function  $\Phi_o$  is obtained from the initialized volume-of-

fluid field, where the interface is defined at  $\alpha = 0.5$ :

$$\Phi_0 = (2\alpha - 1)\Gamma \quad (4.9)$$

$$\Gamma = 0.75\Delta X \quad (4.10)$$

Here  $\Delta X$  is the minimum mesh size near the interface. Thereafter the re-initialization equation is solved to turn the initial level set function into the distance from the interface:

$$\frac{\partial \Phi}{\partial \tau} = \text{sign}(\Phi_0)(1 - |\nabla \Phi|) \quad (4.11)$$

Here  $\tau = 0.1\Delta X$  is the iteration time step of  $\Phi$  and the sign function denotes:

$$\text{sign}(\Phi) = \begin{cases} 1 & \Phi > 0, \text{water} \\ 0 & \Phi = 0, \text{interface} \\ -1 & \Phi < 0, \text{oil} \end{cases} \quad (4.12)$$

Then the interface tension force is calculated as:

$$\vec{F}_\sigma = \sigma \kappa(\Phi) \delta_\phi \nabla(\Phi) \quad (4.13)$$

Here  $\sigma$  is the interface tension and  $\delta_\phi$  is the smoothed delta function:

$$\delta_\phi = \begin{cases} \frac{1}{2\gamma} \left( 1 + \cos\left(\frac{\pi\Phi}{\gamma}\right) \right) & \text{for } |\Phi| < \gamma \\ 0 & \text{elsewhere} \end{cases} \quad (4.14)$$

The quantity  $\gamma$  is the interface thickness coefficient (see Yamamoto et al., 2017) and  $\kappa(\Phi)$  is the interface curvature:

$$\kappa(\Phi) = \nabla \cdot \vec{n}_c \quad (4.15)$$

$$\vec{n}_c = \frac{(\nabla \Phi)_f}{|(\nabla \Phi)_f|} \quad (4.16)$$

Here  $\vec{n}_c$  is the surface unit normal vector. The contact angle  $\theta$  between the interface and the pipe wall is defined as:

$$\cos(\theta) = \vec{n}_c \cdot \vec{n}_w \quad (4.17)$$

With  $\vec{n}_w$  being the unit normal vector at the wall. The contact angle is set to  $90^\circ$  in our simulations. This means that both the level set function  $\Phi$  and the volume fraction of the fluid  $\alpha$  satisfy the zero-gradient condition at the pipe wall boundary.

A pressure drop in the flow direction is added as an extra force term to the right-hand side of Equation 4.2, with periodic boundary conditions on the left and right side of the pipe. Therefore, the pressure that remains in the equations is periodic with respect to the left and right side of the computational pipe section. The initially assumed velocity profile will then develop over time under this pressure drop in the transient simulation until a stable state is obtained.

A second-order backward implicit time discretization scheme is applied, with a very small time step (small Courant number). This gives a very accurate time integration. We use a second-order scheme for the advection terms in the momentum equations and in the interface equation (as used in the level set method for re-initialization), but a first-order upwind scheme for the advection in the equations for the turbulence quantities  $k$  and  $\varepsilon$ ; trying a second-order scheme for the latter gave numerical instabilities. Through successive mesh refinement, however, we have verified that the simulation results are accurate (and not suffering from large numerical diffusion).

In all the simulations, periodic boundary conditions are applied on the left and right side of the pipe, which restricts the wavelengths in the axial direction to the domain length divided by an integer value. At the pipe wall, the no-slip condition is imposed. We have used the symmetric PBiCG solver for the velocity and for the turbulent quantities, the GAMG solver for the pressure, and the PIMPLE solver for the velocity-pressure coupling.

### 4.2.3 Parameters

Following Li & Renardi (1999), six dimensionless groups are involved in the present study:

Viscosity ratio:  $m = \frac{\mu_w}{\mu_o}$ ;

Radius ratio:  $a = \frac{R}{R_c}$ ;

Density ratio:  $\xi = \frac{\rho_w}{\rho_o}$ ;

Driving force ratio:  $K = \frac{f^* + \rho_o g \sin(\vartheta)}{f^* + \rho_w g \sin(\vartheta)}$ ;

Interfacial tension parameter:  $J = \frac{\rho_o \sigma R_c}{\mu_o^2}$

Oil-based Reynolds-number:  $Re_o = \frac{\rho_o U_c R_c}{\mu_o}$ .

The subscript “o” refers to oil in the core and “w” to water in the annulus;  $R$  is the pipe radius, and  $R_c$  is the oil core radius;  $\vartheta$  is the pipe inclination ( $\vartheta = 0$  for a horizontal pipe, and  $\vartheta = 90$  deg. for a vertical pipe with upflow);  $\sigma$  is the interfacial tension;  $f^* = dp/dx$  (i.e., streamwise pressure gradient);  $U_c$  is the centre line velocity.

Also, four hydraulic parameters can be considered: the total flow rate, the pressure drop, the watercut, and the water holdup fraction. The watercut is defined as the ratio of the water volumetric flow rate and the total volumetric flowrate:

$$WC = Q_w / (Q_w + Q_o) \quad (4.18)$$

where  $Q$  denotes the volumetric flow rate. The water holdup fraction is defined as the ratio of the in-situ water volume in the pipe and the total volume of oil and water:

$$\alpha_w = \frac{V_w}{V_w + V_o} \quad (4.19)$$

For a given configuration, when two out of the four parameters are set as input, the other two will follow as output. In experiments, the total flow rate and the watercut are set as input, leading to the pressure drop and water holdup fraction as output. In our numerical simulations, the total flow rate and water holdup fraction are used as input, giving a pressure drop and watercut as output.

A related parameter is the so-called holdup ratio  $h$ , which is defined as:

$$h = \frac{Q_o / Q_w}{V_o / V_w} \quad (4.20)$$

The holdup ratio thus is a measure of the apparent slip between the oil core and the water annulus.

## 4.3 Wave stability curves

### 4.3.1 Vertical laminar-laminar core-annular flow

Li & Renardy (1999) have considered the linear and nonlinear stability of laminar-laminar upward going core-annular flow. They have numerically solved the eigenvalue problem of the linearized Navier-Stokes equations (which is in fact the Orr-Sommerfeld equation) to determine the most unstable linear modes. Li & Renardy refer to that solution as the one with “theoretical linear growth rate”. In addition, they have numerically solved the Navier-Stokes equations to obtain both the linear and nonlinear wave growth. Thereto the Volume of Fluid (VOF) numerical method was applied to the vertical laminar-laminar core-annular flow. When imposing a small initial disturbance on the flat liquid-liquid interface, the linear instability gives an exponential growth of the wave amplitude over time:

$$A^*(t^*) = A^*(0) \exp(k^* t^*) \quad (4.21)$$

Where  $A^*$  is the wave amplitude, made dimensionless with the radius of the oil core (i.e.  $A^* = A/R_c$ ),  $t^*$  is the time, made dimensionless with the centreline velocity and the oil core radius (i.e.,  $t^* = t R_c / U_c$ ), and  $k^*$  is the (dimensionless) growth rate.

To verify our numerical method, one of the laminar-laminar cases from Li & Renardy (1999) for

vertically upward going flow ( $\vartheta = 90$  deg.) was considered. The wave number is defined as  $\gamma^* = 2\pi/\lambda^*$ , with dimensionless wave length  $\lambda^* = \lambda/R_c$ . We applied a  $256 \times 256$  mesh in streamwise and axial direction (which is the same as used by Li & Renardi). Only the axisymmetric modes are simulated. The initial velocity distribution is set according to the following analytical expression of PCAF:

The core velocity (i.e., for  $r^* < 1$ ) is:

$$u^*(r^*) = 1 - \frac{mr^{*2}K}{\tilde{A}} \quad (4.22)$$

The annulus velocity (i.e., for  $1 \leq r^* \leq a$ )

$$u^*(r^*) = \frac{a^2 - r^{*2} - 2(K-1)\ln(r^*/a)}{\tilde{A}} \quad (4.23)$$

With  $\tilde{A} = mK + a^2 - 1 + 2(K-1)\ln a$

The \*-superscript means non-dimensionalization with the length scale  $R_c$  and the velocity scale  $U_c$  (i.e.,  $r^* = r/R_c$  and  $u^* = u/U_c$ ). The centre velocity can be expressed as:

$$U_c = -(f^* + \rho_w g \sin(\vartheta)) \frac{R_c^2 \tilde{A}}{4\mu_w} \quad (4.24)$$

In the considered case from Li & Renardy (1999), the six parameters are: viscosity ratio  $m=0.00166$ , radius ratio  $a=1.28$ , density ratio  $\xi=1.1$ , driving force ratio  $K=-0.4552$ , surface tension parameter  $J=0.0795$ , and oil-based Reynolds number  $Re_o=0.93$ .

Figure 4.1 compares our results from the 2D axisymmetric simulation with the theoretical linear values obtained by Li & Renardy. Figure 4.1a shows a very good agreement for the wave stability curve (i.e. growth rate versus wave number), in which the wave number  $\gamma^* = 2$  marks the most unstable wave length. The numerical simulations shown in the figure were obtained with periodic boundary conditions in a pipe section with a length set equal to the considered wave length. The growth rate was derived from the simulation results by assuming exponential growth in the time interval  $t^*$  between 1.5 and 3. The numerical values of the growth rate are quite close to the theoretical values. As shown in Figure 4.1b, the wave number  $\gamma^* = 2$  initially gives a growth rate of  $k^*=0.20$  in the numerical simulations, which is close to the theoretical value of  $k^*=0.1940$ , reported by Li & Renardy.

Because we only disturb the interface at time zero, while the velocity and pressure field will experience the disturbance once the effect of the wave growth has propagated, the flow system takes a short time to enter the linear growth region; this could explain the small plateau near time zero. The linear growth is clearly visible until  $t^*$  is 10, after which, due to non-linear effects, the growth levels off and reaches a saturation. The similar numerical procedure will be applied to cases with laminar-turbulent CAF, as will be discussed in the next section.

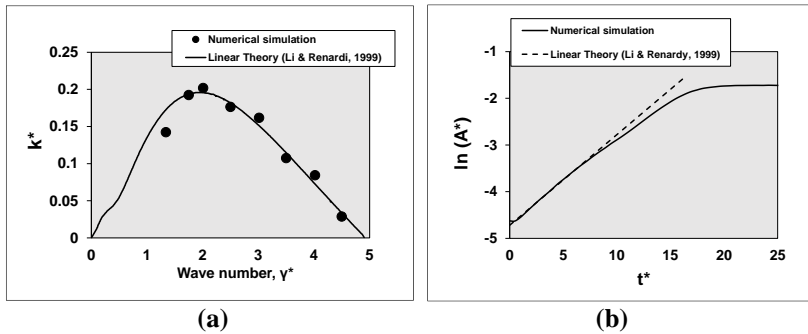


**Figure 4.1. Verification of numerical method against theoretical linear values from Li & Renardy for the instability of laminar-laminar core annular flow; (a) wave stability curve, showing the dimensionless growth rate  $k^*$  as function of the wave number  $\gamma^*$ , (b) growth of the dimensionless wave amplitude  $A^*$  for wave number  $\gamma^* = 2$ .**



### 4.3.2 Laminar-turbulent core-annular flow

To study the instability of laminar-turbulent core-annular flow, we first perform a mesh sensitivity study for the growth rate. The selected conditions are those used in our lab experiments for core-annular flow. The pipe radius is 10.5 mm, the oil density is  $\rho_o = 902 \text{ kg/m}^3$ , the water density is  $\rho_w = 993 \text{ kg/m}^3$ , the dynamic oil viscosity is  $\mu_o = 0.697 \text{ Pas}$ , the dynamic water viscosity is  $\mu_w = 6.65 \times 10^{-4} \text{ Pa s}$ , and the interfacial tension is 0.016 N/m. The imposed total flow rate is  $0.00043 \text{ m}^3/\text{s}$  (i.e. 1.24 m/s mixture velocity) and the imposed water holdup fraction is 0.26. The corresponding parameters are:  $a=1.16$ ,  $m=0.00096$ ,  $K=1$ ,  $J=0.268$ ,  $Re_o=14.5$ . In the determination of  $Re_o$ , we have replaced the centre velocity  $U_c$  by the mixture velocity  $U_{mix}$ ; this is because  $U_c$  is not a-priori known from the imposed conditions, whereas  $U_{mix}$  is known by taking the ratio of the imposed total flow rate and the pipe cross sectional area. The pipe used for the experiments was horizontal, which gave core-annular flow with only small eccentricity. Therefore, we have omitted gravity in the stability simulations, which gives  $K=1$ .

To initialize the flow, fully developed perfect core-annular flow (i.e. no interfacial waves), though with a turbulent water annulus, is first simulated in a pipe with very small streamwise section length. A strongly non-equidistant mesh was used in radial direction, giving a high concentration of points close to the pipe wall. The following stretch function was used:

$$\frac{r_j}{r_{jmax}} = 1 + \frac{\tanh[\alpha_1(j/jmax-1)/2]}{\tanh(\alpha_1/2)}, \quad j = 0, 1, \dots, jmax \quad (4.25)$$

Where  $jmax$  is the total number of mesh points and  $r_j$  is the coordinate of the  $j^{\text{th}}$  node. A proper value of  $\alpha_1$  is used to ensure that sufficient grid points are in the viscous sublayer ( $y^+ < 5$ ) both near the pipe wall and near the interface. Here  $y^+ = yU_\tau/\nu_w$ ; in which  $y$  is the distance to the wall and  $U_\tau$  is the wall shear velocity, i.e.  $U_\tau = \sqrt{\tau_w/\rho_w}$ , with the wall shear stress  $\tau_w$ .

This gives 1D profiles, that only depend on the radial coordinate; the resulting mean velocity profile and the turbulent viscosity profile are shown in Figure 4.2. The locations of the oil-water interface and of the pipe wall are shown as dashed lines. In the Launder-Sharma  $k - \varepsilon$  model, the low-Reynolds terms dampen the turbulence near the interface and near the pipe wall. In the water annulus, the 'S' shaped velocity profile is found; the viscous sublayer, the buffer layer and the logarithmic layer can be distinguished from the mean velocity profile both near the wall and near the interface. This is analogous to plane Couette flow, with the only difference being that the shear stress near the wall is higher than near the interface because of the axisymmetry. In the oil core, the flow is highly viscous, and the velocity is almost constant in the radial direction. Due to the difference in the oil and water viscosity, there is a jump in the velocity gradient at the interface. This will cause a large shear near the interface which may initiate instability. The maximum turbulent viscosity is around 11 times the water molecular kinematic viscosity.



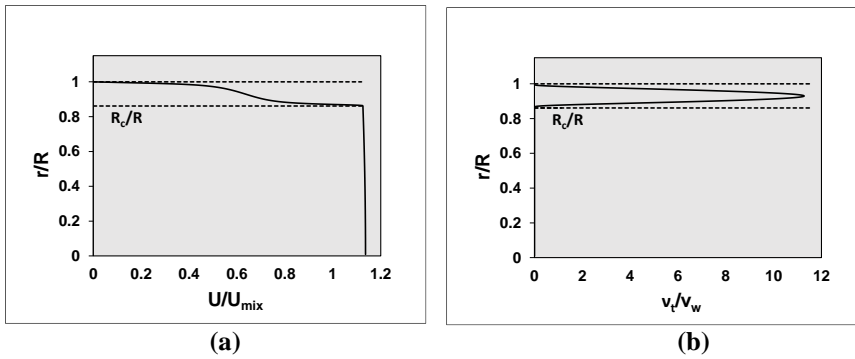


**Figure 4.2. Initial 1D profiles for laminar-turbulent CAF; (a) streamwise dimensionless velocity, (b) turbulent viscosity ratio.**

After the 1D fully developed flow has been obtained, the 1D result is mapped into a 2D domain with a certain length of the pipe section. In streamwise direction, the radial location of the interface is slightly disturbed with a sinusoidal shape with a wave length equal to the length of the pipe section to trigger the possible wave growth over time. In this simulation example for CAF with a turbulent water annulus, the length of the pipe section is set to 9.6 mm, which corresponds to the dimensionless wave length  $\lambda^* = 1.06$  (being about the most unstable wave, as will be shown later). The simulations are repeated at successively refined grids:  $75 \times 200$ ,  $150 \times 400$  and  $300 \times 800$  points in the streamwise  $\times$  radial directions.

The simulation results are shown in Figure 4.3a. Like for the laminar-laminar case, also for this laminar-turbulent case, there is an initial linear phase with exponential growth of the wave amplitude over time. The results are almost mesh independent, with a linear growth rate close to  $k^* = 0.65$ , which is significantly higher than the value of 0.20 found for the laminar-laminar case in the previous section.

It also found that after inserting the initial disturbance at time zero, the linear instability range is obtained faster if the mesh is refined (i.e. the initial plateau is longer for the coarser mesh). The  $150 \times 400$  mesh resolution is used for the further analysis of the nonlinear wave instability. The  $75 \times 200$  mesh is used for a sensitivity study for the fully developed saturated waves.

The “quasi-laminar assumption” (as described by Náráigh et al., 2011) was also tested. This means that the 1D turbulent mean velocity profile (Figure 4.2) is used as the initial condition, but that the 2D laminar Navier-Stokes equations are solved when monitoring the wave growth. As shown in Figure 4.3b, this is done both for a condition in which the turbulent viscosity is set to zero in the dynamic simulation and for a condition in which the turbulent viscosity remained fixed at its initial value. The figure shows that the simulation results for the three approaches initially give the same amplitude growth. Thereafter, the simulation with the quasi-laminar assumption gives a slower growth rate than the simulation that uses RANS with the  $k - \varepsilon$  model for the turbulence in the water annulus over time. The agreement for small time and the deviation for larger time is due to the shape of the mean velocity profile in the annulus (Figure 4.2a) and the corresponding turbulence level (Figure 4.2b): close to the interface the velocity profile is linear with vanishing turbulence (i.e. laminar like), where the quasi-laminar assumption applies, whereas it has an “S” shape with higher turbulence farther away from the location of the initial interface.

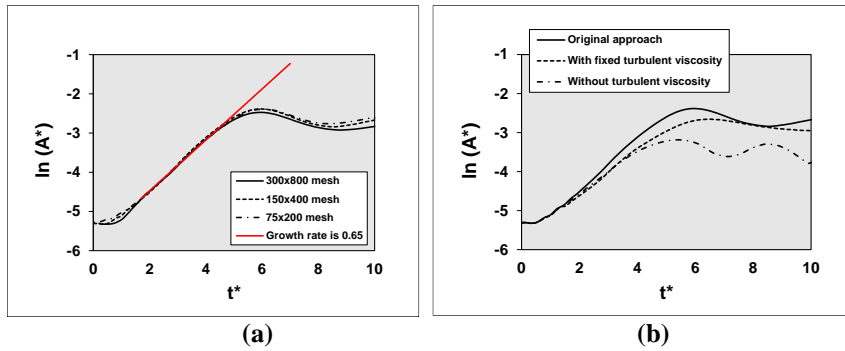


**Figure 4.3.** Growth of the dimensionless wave amplitude  $A^*$  over dimensionless time  $t^*$  for the case with laminar-turbulent core-annular flow; (a) mesh sensitivity, (b) comparison of three approaches on a  $150 \times 400$  mesh.

The wave growth simulations carried out for different lengths of the pipe section, with periodic boundary conditions (using the turbulence model). This provides the wave stability curve for the laminar-turbulent case (upper curve) that is shown in Figure 4.4 (Note: the figure also includes the curve for the laminar-laminar case with the same water holdup fraction, which will be discussed later in this chapter). The imposed water holdup fraction of 0.26 gives a watercut of 15% in the 1D initial flow (i.e. without waves). For large wave numbers (or small wave lengths), no wave growth is found. For small wave numbers (or large wave lengths), two instead of one unstable wave is found. Figure 4.4 only shows the simulations results with nonzero wave growth when a single wave is found.

Figure 4.5 shows the wave stability curves for different values of imposed water holdup fraction, while the imposed mixture velocity remained fixed at 1.24 m/s. The water annulus is turbulent for the water holdups fractions of 26%, 19%, and 14%, but a laminar water annulus is found if the water holdup fraction is decreased to 7%. All wave stability curves show a maximum, but the curves are quite flat. This means that the unstable waves (for a given water holdup fraction) have about the same growth rate. The most unstable wave lengths (or wave numbers) are summarized in Table 1. A decrease in water holdup fraction gives a slight decrease in the most unstable wave length (or increase in the most unstable wave number). When the water annulus becomes laminar (at 7% water holdup fraction), the most unstable wave length decreases, and its growth rate is significantly smaller than for the turbulent water annulus (found at higher water holdup fractions).

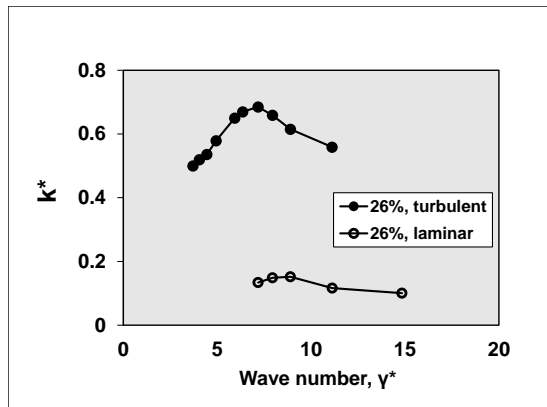


**Figure 4.4.** Dimensionless linear wave growth rate  $k^*$  as function of the wave number  $\gamma^*$  at 26% water holdup fraction for turbulent and laminar water annulus.

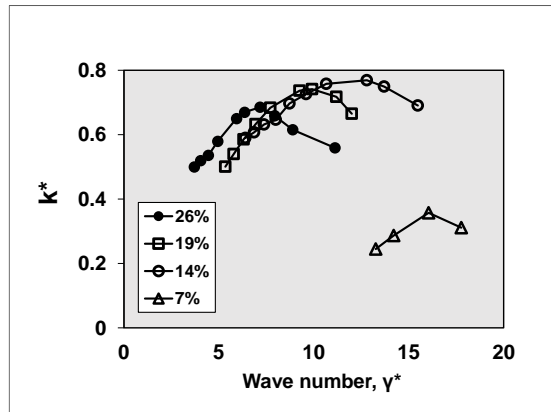


**Figure 4.5.** Dimensionless linear wave growth rate  $k^*$  as function of the wave number  $\gamma^*$  for laminar-turbulent core-annular flow for different values of the imposed water holdup fraction (shown in the legend).

**Table 4.1.** Most unstable wave for core-annular flow for different values of the water holdup fraction; wave length ( $\lambda, \lambda^*$ ), wave number ( $\gamma^*$ ), and wave growth rate ( $k^*$ ).

Water holdup %	$\lambda$ mm	$\lambda^*$	$\gamma^*$	$k^*$
26	7.9	0.88	7.2	0.69
19	6	0.63	9.9	0.74
14	4.8	0.49	13	0.77
7	4	0.39	16	0.36

The decrease in growth rate when going from a turbulent water annulus to a laminar water annulus is also observed when the water annulus at 26% water holdup fraction is relaminarized through increasing the water viscosity with a factor 5. See the lower curve in Figure 4.4: the growth for the most unstable decreases from 0.69 to 0.15.

## 4.4 Wave growth behaviour

### 4.4.1 Energy budget for the linear instability

To identify the physical mechanism of the linear instability, Hooper & Boyd (1982) have analysed the stability problem through the energy equation. This method has also been used by several other researchers; for example, Boomkamp & Miesen et al. (1996) used this for two-phase channel flow, Bai et al. (1992) for axisymmetric laminar-laminar core-annular flow, and Náráigh et al. (2011) for turbulent-laminar channel flow. Since previous stability studies for core-annular flow have only focused on laminar-laminar conditions, the laminar-turbulent CAF case will be analyzed in this section and compared with laminar-laminar CAF.

To obtain the energy equation for the disturbed flow, we first determine the disturbance  $u'$  by subtracting the initial undisturbed flow field  $u_0$  from the actual flow field  $u$ , i.e.:

$$u' = u - u_0 \quad (4.26)$$

We take the inner product of  $u'$  and the momentum Equation 4.2 to obtain:

$$u'_i \frac{\partial \rho u_i}{\partial t} = -\rho u'_i u_j \frac{\partial u_i}{\partial x_j} + u'_i \frac{\partial}{\partial x_j} \left( \rho(v + v_t) \left( \frac{\partial u_i}{\partial x_j} + \frac{\partial u_j}{\partial x_i} \right) \right) - u'_i \frac{\partial p}{\partial x_i} + u'_i F_{\sigma,i} \quad (4.27)$$

Gravity has been neglected. When the Navier-Stokes equation is linearized, the advection term

obtains the form  $-\rho u_i' u_j' \frac{\partial u_i}{\partial x_j}$ , being the first term on the right hand side of Equation 4.27; this is called the wave-induced Reynolds stress in the disturbed flow and it represents the energy transfer rate from the mean flow to the disturbed flow (Boomkamp & Miesen, 1996). The inner product with the velocity disturbance shows how each momentum term affects the disturbed flow, providing either amplification or damping. A positive value will amplify the energy for instability and a negative value will decrease the energy and stabilize the flow.

Integration of the energy Equation 4.27 over the volume of the pipe section gives an energy balance for the flow disturbances that consists of the following terms, having the unit of power (W):

$$\text{KIN} = \text{REY} + \text{DIF} + \text{TAN} + \text{HYD} + \text{TEN} \quad (4.28)$$

The different terms have the following meaning:

- KIN (kinetic energy) is the total power in the velocity disturbances, which results from the source terms on the right-hand side of Equation 4.27.
- REY (Reynolds stress) has resulted from the first term on the right-hand side of Equation 4.27; it shows the destabilizing effect of the advection term. This is different from the Reynolds stress in turbulent flow, as the turbulent Reynolds stress in the applied  $k - \epsilon$  model is already modelled with a turbulent viscosity.
- DIF (diffusion) stems from the viscous stress represented by the right-hand side of equation (4.27); a separate contribution is due to the oil core and water annulus, respectively. The interface region is excluded (but will be covered by the TAN term instead). The turbulent viscosity is included in the water annulus.
- TAN is the viscous stress tensor term integrated near the interface region (Hooper, 1985). This represents the amount of energy supplied by the shear stress near the two-phase interface. The interface is defined as the part where the local water volume fraction is between 0 and 1.
- HYD (hydrodynamic pressure) is due to the pressure term in Equation 4.27, while excluding gravity. The pressure has two components: the hydrodynamic pressure and the imposed pressure gradient. Both give values that are very small compared to the other terms in Equation 4.28.
- TEN (interface tension) represents the effect of the interface tension on the disturbed flow. Since the effect of interface tension appears as a body force in the interface region, we can still obtain a volume integral in the thin surface region when integrating Equation 4.27. The streamwise component of the interfacial tension force can stabilize the flow, while the normal component can destabilize the flow and generate capillary waves. In our case, however, this term is very small, as the value of the interfacial tension between the oil and water is small (namely  $\sigma=0.016$  N/m).

The results for the energy budgets for the unstable wave length  $\lambda = 9.6$  mm ( $\lambda^* = 1.06$ ) at 26% water holdup fraction (with 1.24 m/s mixture velocity) are shown in Figure 4.6. The considered wave length is slightly larger than the most unstable length of 7.9 mm ( $\lambda^* = 0.88$ ) given in Table 4.1. The energy rate (=power) is first divided by the volume content  $\lambda\pi R^2$  and thereafter made dimensionless with  $\rho U^3 L^2$ . Time is made dimensionless with  $L/U$ . Here  $U = U_{mix}$  and  $L = R_c$ . Since the focus is on the linear instability with small wave amplitude, only a short time interval is shown during which the wave amplitude is still below 10% of the water layer thickness. After introducing a very small disturbance the fastest growing wave will be formed (being equal to the section length) which shows up with a single exponential rate. The exponential growth rate of the total kinetic energy is about twice the growth rate of the wave amplitude, which agrees with the theory.

The main source of unstable energy stems from the REY term, which represents the energy in the wave-induced Reynolds stress. This has a large value in the water layer and on the interface, while it is almost zero in the oil layer. The viscous stress tensor and turbulent Reynolds stress tensor in the water layer give almost zero energy; therefore, this is omitted in Figure 4.6. The viscous stress in the

oil layer gives the main contribution (DIF in Figure 4.6) in stabilizing the flow. The TAN term, which was shown in a few studies to be the main source of energy in laminar-laminar flow, turns out to be less important in our case.

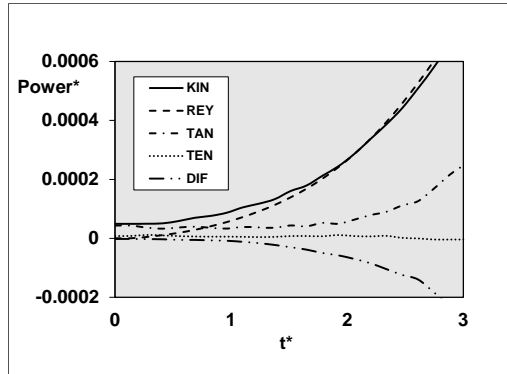


**Figure 4.6. Dimensionless power as a function of dimensionless time during the linear growth stage for the case with laminar-turbulent CAF (26% water holdup fraction, wave length is 9.6 mm,  $\lambda^* = 1.06$ ).**

To compare the different instability mechanisms in laminar-turbulent CAF and laminar-laminar CAF, we increased the water layer viscosity by a factor of 5 to make the water layer laminar. By doing this, the most unstable wave length becomes slightly shorter than in the turbulent case (6.4 mm instead of 7.9 mm, or  $\lambda^*$  is 0.71 instead of 0.88), and the highest growth rate is also much lower (0.15 versus 0.69). The energy budget during the linearly unstable stage is shown in Figure 4.7. As can be seen, the total energy rate (power) is smaller than in Figure 4.6 which corresponds to the smaller growth rate. The contribution of viscous diffusion (DIF) cannot be ignored anymore, since the water viscosity has become higher. The viscous stresses near the interface (TAN) form now the dominant source of energy, while the wave-induced Reynolds stress (REY) has become less important.

Therefore, the instability in the turbulent case is inertia-induced, whereas the instability in the laminar case is viscosity-induced.

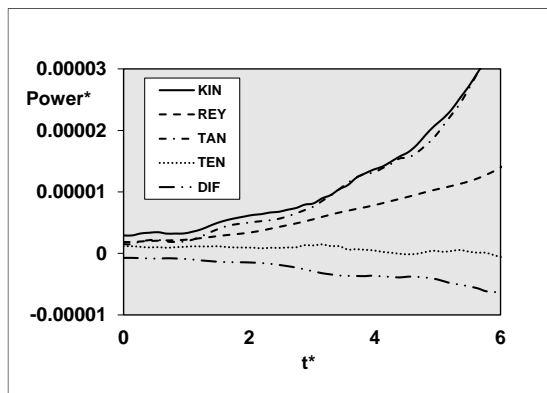


**Figure 4.7. Dimensionless power as a function of dimensionless time during the linear growth stage for the case with laminar-laminar CAF (26% water holdup fraction, wave length is 6.4 mm,  $\lambda^* = 0.71$ ).**

#### 4.4.2 Flow pattern during unstable stage

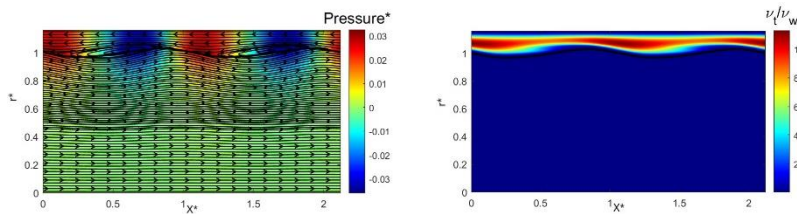
We have already shown that the initial formation of interfacial waves is due to a linear instability. Once the wave amplitude has become sufficiently large, non-linear effects saturate the growth until a stable wavy core-annular flow (WCAF) is obtained. Figure 4.8 shows the evolution from PCAF to

WCAF for 26% imposed water holdup fraction, and 1.24 m/s imposed mixture velocity, with a section length (or wave length) of 9.6 mm ( $\lambda^* = 1.06$ ). To better see the flow structure, two periodic waves are shown at different time levels. Shown are the isobars with streamlines in the left graphs, and the turbulent viscosity level in the rights graphs. The streamlines are shown with respect to a reference frame that moves with the wave velocity. Figure 4.9 shows the wall pressure at different time levels. Figure 4.10 shows the evolution of the dimensionless pressure drop (the Fanning friction factor), the turbulent viscosity, and the watercut. The Fanning friction factor is defined as the ratio of the pressure drop and  $\rho_w U_{mix}^2/R$ .

During the linearly unstable stage (which takes up to about  $t^*=4$ ), the pressure drop (or Fanning friction factor), the maximum turbulent viscosity, and watercut (as shown in Figure 4.10) change only little over time, although the wave amplitude (as can be observed in Figure 4.8) grows exponentially. A relatively long non-linear stage (between about  $t^*=4$  and 20) is found after the linear stage, after which the saturated long-term stage is reached. In particular, the pressure drop increases from 425 Pa/m to 790 Pa/m (or the Fanning friction factor from 0.00293 to 0.0054), the watercut from 15% to 22%, and the maximum turbulent viscosity ( $\nu_t/\nu_w$ ) from 10.8 to 16.7. Since the water holdup stays constant at 26%, the corresponding holdup ratio decreases from 1.8 to 1.24.

Based on the streamlines, pressure level and turbulent viscosity level, several phenomena can be observed. During the time interval in the linear stage, the wave amplitude grows exponentially, while the wave shape remains smooth and an increasing recirculation zone develops behind the wave crest. After the linear stage, the wave amplitude continues to increase and the recirculation region becomes larger and larger. The vorticity in the recirculation zone is so large that the pressure in the vortex centre decreases dramatically, corresponding to the large pressure fluctuation along the pipe. At the top of the vortex, the streamwise velocity decreases, because of the high negative relative velocity in the reference frame of the interface. This causes some local laminar flow (see the right graph in Figure 4.8(b)). The wave shape still stays smoothly rounded, and no noticeable difference between the wave crest and wave trough is found. The turbulent viscosity shows only a slight increase. The pressure drop is almost the same as in the 1D initial state. The very low pressure behind the wave crest produces a negative pressure force (form drag) to decelerate the oil core and accelerate the water layer. As shown in Figure 4.10c, the watercut also increases during this stage.

After about  $t^*=7$ , under the effect of pressure, the interfacial wave changes its shape into one with a rather flat profile at the trough and a sharp profile at the crest. The vortex has gradually dissipated, which is in line with the smaller absolute value of the pressure, as shown in Figure 4.9. The recirculation zone also started to move to the left. During the dissipation of the vortex, the water layer becomes more turbulent, as shown from the sharp increase in the turbulent viscosity in Figure 4.10b. Then pressure drop also increases rapidly. The turbulent viscosity decreases continuously after  $t^*=8$ . The final state is reached at about  $t^*=40$ .



(a)  $t^*=3.4$

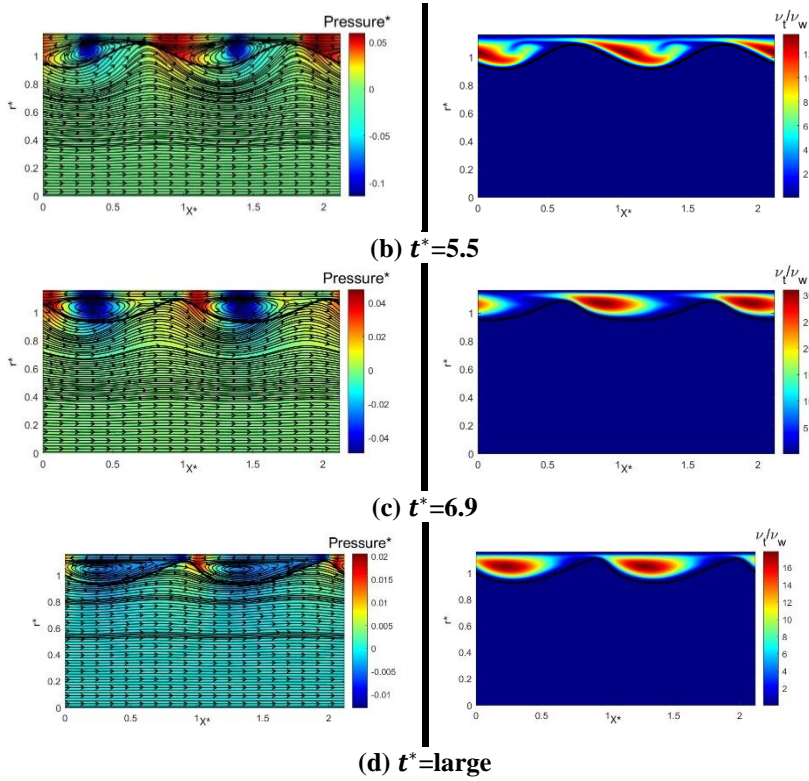


**Figure 4.8.** Flow pattern during the unstable stage at different time levels (26% water holdup fraction, 1.24 m/s mixture velocity, 9.6 mm wave length,  $\lambda^* = 1.06$ ); (left) isobars with streamlines, and (right) turbulent viscosity ratio level.

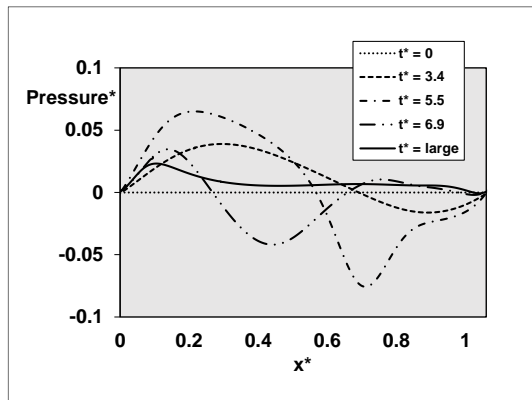


**Figure 4.9.** Distribution of the dimensionless wall pressure in the streamwise direction during the unstable stage (26% water holdup fraction, 1.24 m/s mixture velocity, 9.6 mm wave length,  $\lambda^* = 1.06$ ).

In the fully developed state, the wave crest is sharp, and the wave trough is flatter. This type of wave form, so-called bamboo wave, was first reported to occur in the experiment by Bai et al. (1992). The wave form is smooth at the beginning, and the change in wave form happened during the non-linear stage. A clear difference can be found when we compare Figure 4.8d with Figures 4.8a or 8b: the streamline pattern in Figure 4.8d is already close to the fully developed state, while the flow is still unstable, and will only slowly approach the fully developed state.



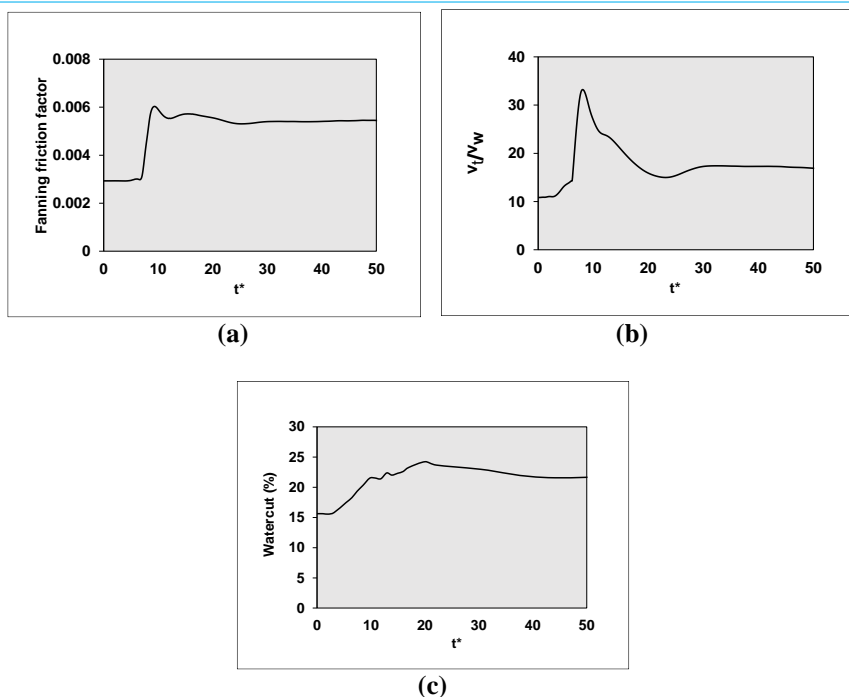


**Figure 4.10.** Hydraulic parameters during the unstable stage (26% water holdup fraction, 1.24 m/s mixture velocity, 9.6 mm wave length,  $\lambda^* = 1.06$ ); (a) Fanning friction factor, (b) maximum in the turbulent viscosity ratio, (c) watercut.

#### 4.4.3 Comparison with experiment

Experiments were carried out in our lab for various watercuts with core-annular flow in a horizontal pipe with 21 mm diameter. The base condition is a total flow rate of  $0.00043 \text{ m}^3/\text{s}$  (mixture velocity of 1.24 m/s) with 20% watercut. This gives a water holdup fraction of 0.26. Other watercuts were obtained by keeping the oil flow rate fixed at  $0.00034 \text{ m}^3/\text{s}$  (or superficial oil velocity of  $0.8 \times 1.24 \text{ m/s}$ ), and adding water until the watercut is 15% or 10%. The measured water holdup fractions for the latter are 0.21 and 0.16, respectively.

From the experiments, the interfacial waves were captured by a high-speed camera as shown in Figure 4.11. The ray tracing method is used to calibrate the recorded frames, to exclude the reflection effect of the pipe wall material. When extracting the wave lengths, we exclude wave lengths shorter than 1 mm, because these can be easily influenced by the noise in the frames.

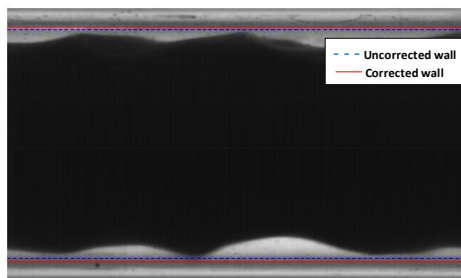


**Figure 4.11.** Snapshot of the flow visualization in the lab experiment, showing the wave structure (flow is from left to right).



Developed flow in the experiments is monitored over a time duration of 3 s, in which multiple wave lengths are captured by the camera. Figure 4.12 shows part of the time period with the measured water layer thickness, both at the top and bottom of the pipe. The duration of a wave is taken as the time between two subsequent maxima in the time signal. By using the measured wave velocity (which is about 1.37 m/s for the top layer and 1.21 m/s for the bottom layer, for the 26% water holdup fraction case, or 20% watercut case), the measured time period is converted to the wave length. Figure 4.13 shows the wave length distribution derived from the experiments. Thereto, all the detected wave lengths with their duration are distributed among wave length intervals (10 equal intervals were used up to the maximum wave length found). Thereafter the total duration time of the waves that ended up in each interval is compared: this gives the pdf (probability density function) of the wave length. The pdf is scaled such that the area under the curve showing the pdf versus the wave length is equal to one. The wave length distribution is rather broad; the spread in waves at the top is smaller than at the bottom. The maximum denotes the most dominant wave length. Almost the same value for this is found at the bottom and top (slightly longer at the bottom). Since a horizontal pipe is used in the experiment, gravity causes some eccentricity of the oil core with a thicker water annulus at the top than at the bottom. The thicker bottom water layer allows the waves to become longer with a larger amplitude.

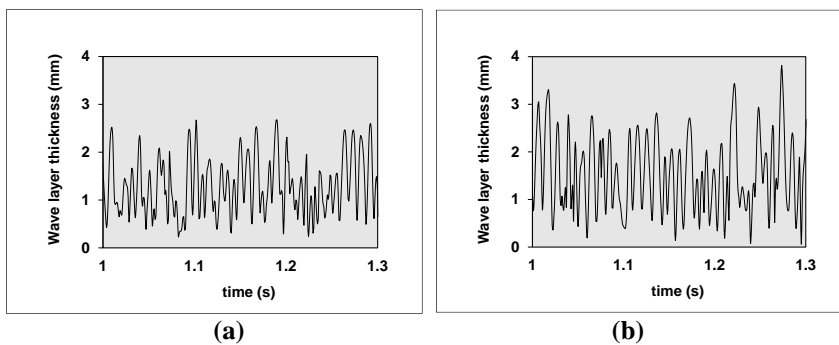


**Figure 4.12.** Measured water layer thickness at fixed location in the pipeline for 26% water holdup fraction; (a) top layer, (b) bottom layer.

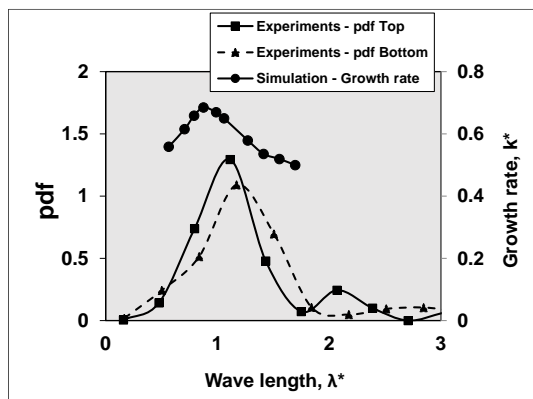


**Figure 4.13.** Comparison of numerical wave stability relationship (dimensionless growth rate  $k^*$  versus dimensionless wave length  $\lambda^*$ ) with the experimental wave distribution (pdf for  $\lambda^*$ ) for 26% water holdup fraction.

The wave length distribution is compared with the wave stability curve obtained from the 2D (i.e. concentric) numerical simulations with a turbulent water annulus. This follows a suggestion by Miesen et al. (1992) that the saturated wave distribution is correlated with the linear wave stability curve. They have carried out core-annular flow experiments in a horizontal pipe with 2-inch diameter

and determined the growth rate through solving the Orr-Sommerfeld equation for the laminar velocity profile in perfect core-annular flow. They mention: “*The idea that the measured wavelength distribution is in some way proportional to the growth rate can only be defended with ‘hand-waving’ arguments, and as kind of extension of the idea in hydrodynamics that the mode with the largest growth rate will be the dominant one.*”

Figure 4.13 shows that the wave length with the fastest growth rate in the simulations compares well with the dominant wave length in the experiment. With increasing water holdup fraction, the dominant wave length becomes longer. For the smaller water holdup fractions (14%, 19%) the most frequent wave length is around 0.6 times the oil core radius ( $\lambda^*=0.6$ ), whereas for the larger water holdup fraction (26%), the most frequent wave length is almost equal to the oil core radius ( $\lambda^*=1$ ).

However, the limitation of the numerical simulations is that we cannot construct the complete wave stability curve that starts and ends at zero growth rate. For a too long simulation domain, we noticed multiple waves to appear even while only one wave was initially disturbed. The growth rate for a very short wave length can neither be obtained, because the linear growth is difficult to derive from the transient simulation, or there even is no growth at all.

The numerical values of the different quantities are compared in Table 4.2. The smallest possible wave in the simulations does not compare well with the experiment: in the experiment, we can observe even very small waves. It should be noted that in the experiment, the oil core is somewhat eccentric towards the pipe top, whereas in the numerical simulations, the flow is assumed to be 2D axisymmetric, giving a concentric oil core. This difference can affect the stability behaviour. Therefore, only a part of the wave stability relationship could be obtained in the simulations, but the predicted 2D axisymmetric linear instability growth rate agrees well with the distribution of the longer wave lengths observed in the experiments.

Miesen et al. (1992) presented a model to predict the minimum cut-off unstable wave length through neglecting the viscosity ratio in the Orr-Sommerfeld solution, which gives:

$$\lambda_{min}^* = 7.44 \frac{d}{R_c} \left( \frac{\sigma^3}{\rho_w^2 U_c^5 d_w^2 \mu_w} \right)^{1/7} \quad (4.29)$$

They also presented a model to predict the maximum cut-off unstable wave length though neglecting the interface tension in the Orr-Sommerfeld solution, which gives:

$$\lambda_{max}^* = 15.36 \frac{d}{R_c} \left( \frac{\mu_o}{\rho_w U_c d_w} \right)^{\frac{1}{2}} \quad (4.30)$$

Here  $d$  is the thickness of the water annulus. Table 4.2 compares the wave statistics as obtained from the model, numerical simulation, and experiment. As can be seen, both the model and the numerical results are in good agreement with the experimental data. Indeed, the eccentricity in the experiments for the three cases is very small.

Note that Table 4.2 also includes the eccentricity of the oil core in the measurements. The eccentricity is defined as  $e = \frac{d_{bottom} - d_{top}}{d_{bottom} + d_{top}}$ . Thus  $e = 0$  for a concentric oil core, and  $e = 1$  for a fully eccentric oil core. As the simulation was axisymmetric, its eccentricity is zero.

**Table 4.2: Minimum, maximum, and the most dominant dimensionless wave length  $\lambda^*$  for the three considered cases.**

Water holdup fraction	Wave length $\lambda^*$	Miesen et al. model (1992)	Numerical simulation	Experiment top layer	Experiment bottom layer
26%	Minimum	0.4	0.5	0.2	0.3
	Maximum	1.5	1.8	1.9	2.2
	Dominant	-	0.9	1.1	1.2
	Eccentricity	-	0	0.03	
19%	Minimum	0.3	0.4	0.2	0.2
	Maximum	1.3	1.2	1.9	2.2
	Dominant	-	0.6	0.8	1.1
	Eccentricity	-	0	0.05	
14%	Minimum	0.3	0.4	0.2	0.2
	Maximum	1	1	1.9	2.2
	Dominant	-	0.6	0.7	0.9
	Eccentricity	-	0	0.03	

#### 4.4.4 Fully developed waves

##### 4.4.4.1 Effect of wave length

As a range of wave lengths is observed in the experiment, the effect of the wave length on the mean flow will be studied. Various pipe section lengths  $L$  are simulated sufficiently long over time until the flow has become fully developed. For the smaller section lengths, the wave length is equal to the section length, i.e.  $\lambda^* = L^*$ . When the section length in the simulation length is taken longer than a certain value, multiple waves appear along the interface length in the simulation. Furthermore, because the simulation applies periodic boundary conditions, only an integer number of waves is possible. The results for this were reported in detail by Li et al. (2021). The pressure drop and watercut (for the given total flow rate and water holdup fraction) are almost independent of the section length (or of the wave length), except for a very small section length where the waves are damped and a smooth interface is found (perfect core-annular flow with turbulent water annulus).

At a fully developed state, the oil core is balanced by pressure drop and two surface forces on the oil core: form drag and viscous shear force. In PCAF, the form drag in the axial direction is zero and the viscous force is the only surface force. When waves have appeared at the interface, the pressure is redistributed on the oil core surface, creating a net force acting opposite to the streamwise direction. This force is so-called form drag, which can be calculated by integrating the pressure component in the streamwise direction along the interface. The magnitude of the form drag is related to the form of the wave. With increased wave length, the form drag becomes more important in balancing the pressure drop. Besides, the shear stress force decreases slightly due to the larger and larger flow separation region near the interface.

To show the effect of the different wave lengths on the flow field, we probe the flow field at one fixed streamwise location. Figure 4.14 shows the interface location, wall pressure, maximum turbulent viscosity and wall shear stress, as function of time. As the pressure gradient across the thickness of the water annulus is very small, the wall pressure also gives a very accurate representation of the pressure distribution near the interface. As can be seen, the saturated wave amplitude has increased with increasing wave length. The wave amplitude increases quickly when  $L^*$  is increased to 1.06, and only slightly increases when  $L^*$  is increased further to 1.41. The flow field variation corresponds well with the wave amplitude. There is lower pressure at the back of the wave crest, and higher pressure in front of the wave crest. At the wave trough, the pressure curve is rather flat. The wall shear stress increases significantly from PCAF to WCAF. Near the wave crest, the wall shear stress behaves

similar to the pressure, but in the wave trough, there is another peak value, which corresponds to the flow separation point in front of the wave crest. For small waves, when the wave length is  $\lambda^*=0.71$ , both the pressure curve and the wall shear stress are more symmetric before and after the wave crest, which indicates a less tilted wave form. For  $L^*=0.29$  no waves occur, and PCAF does persist.

With increased wave amplitude, the peak value for the maximum turbulent viscosity increased slightly, while its lowest value decreased significantly for the cases with  $L^*=1.06$  and  $L^*=1.41$ . When there is a wave crest passing by, the flow is locally laminar. For the case  $L^*=0.71$ , the maximum turbulent viscosity is fluctuating always at a relatively higher level. The wave speed is 1.29 m/s for the case  $L^*=0.71$ , which is slightly higher than is 1.26 m/s for  $L^*=1.06$ , and 1.24 m/s for  $L^*=1.41$ .

The streamlines in the reference frame moving with the wave speed are shown for these three cases in Figure 4.15: the recirculation zone increases with increasing wave length.

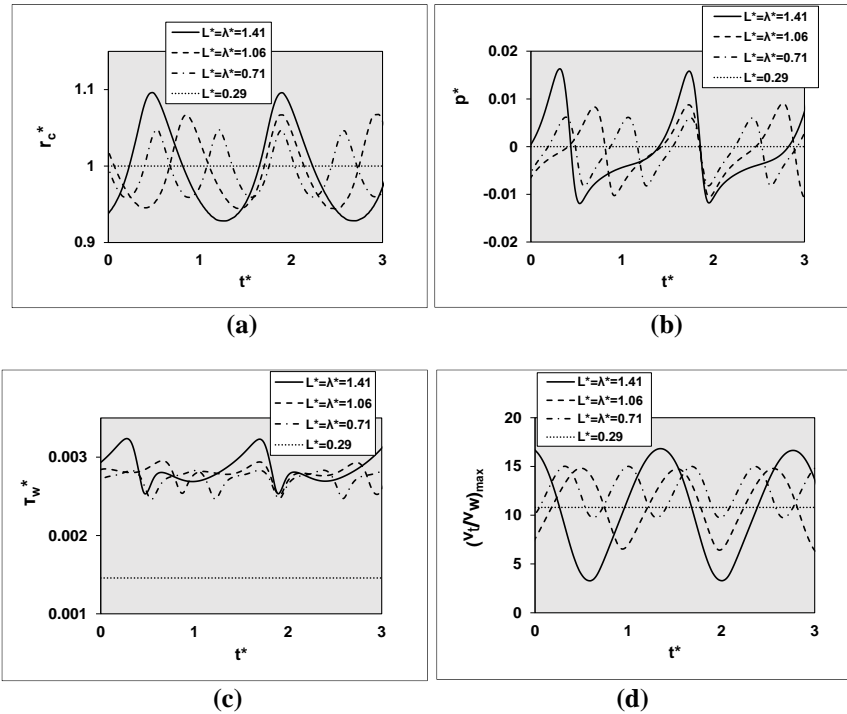


**Figure 4.14.** Flow characteristics at fully developed flow for different pipe section lengths  $L^*$  in the simulations; (a) dimensionless wave location, (b) dimensionless wall pressure, (c) dimensionless wall shear stress, (d) maximum in the turbulent viscosity ratio.

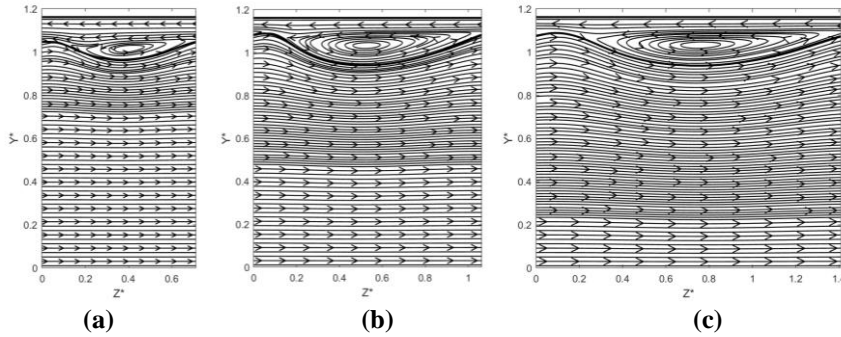


**Figure 4.15.** Streamlines in a reference frame moving with the wave velocity; (a)  $\lambda^*=0.7$ , (b)  $\lambda^*=1.1$ , (c)  $\lambda^*=1.4$ .

#### 4.4.4.2 Wave form

Figure 4.16 compares the wave amplitudes found for the different wave lengths in the numerical simulations and in the experiments. In each simulation a single wave length was simulated, and the wave amplitude was determined as being equal to half the difference between the maximum and minimum thickness of the water annulus. In the experiments, the amplitude was determined as the average of the amplitudes of the waves that ended up in the 10 intervals to determine the pdf of the wave length distribution, as explained in Section 4.4.3. Both in the simulations and in the experiments, the wave amplitude increases with increasing wave length, up to a certain maximum level for the longest waves. As shown in Figure 4.16, for the same wave length in the experiments, the amplitude is larger in the bottom layer than in the top layer. This is related to the eccentricity of the oil core in the experiments, which gives a thicker water annulus at the bottom than at the top. There is also a reasonably good agreement between the simulated wave amplitude and the measured amplitude. As the simulation assumed axisymmetric flow, there is no difference between top and bottom.

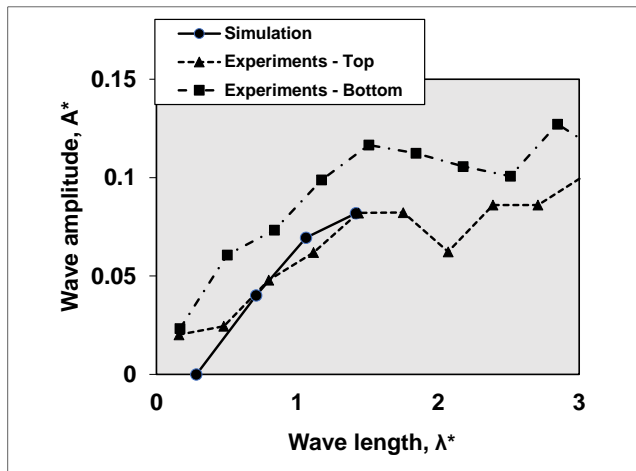


**Figure 4.16.** Dimensionless wave amplitude ( $A^*$ ) versus dimensionless wave length ( $\lambda^*$ ) as found in the simulations and experiments for 26% water holdup fraction.

The instantaneous wave form is shown in Figure 4.17. The experimental wave and the numerical wave have a similar shape, in which the wave is slightly tilted, i.e. the wave slope in front of the wave crest is higher than behind the wave crest. This wave shape corresponds to the flying core model

proposed by Bai et al. (1996), where the inertia effect is dominant. This is as expected since the flow in the water annulus is turbulent.

To compare the wave forms for turbulent and laminar flow conditions, the water viscosity has been increased by a factor 10 in the simulation to replace the turbulent water annulus by a laminar one. The laminar waves are also included in Figure 4.17. The wave form for the laminar condition is quite different from what was found for the turbulent condition; the wave in laminar flow is much shorter with a smaller amplitude, while the wave trough is flatter and the wave crest is more pointed. When the water viscosity is increased even further, the wave is broken and the wavy core-annular flow pattern is not stable anymore. Ooms et al. (2013) have presented a case for horizontal pipe flow, in which the water viscosity is so high that the flow is in the Stokes flow region. The top wave has a different shape than in our laminar case in Figure 4.17: the wave slope in front of the wave crest is lower than behind the wave crest. The wave form in the Stokes flow region corresponds to the lubricated film model proposed by Ooms et al. (1984).

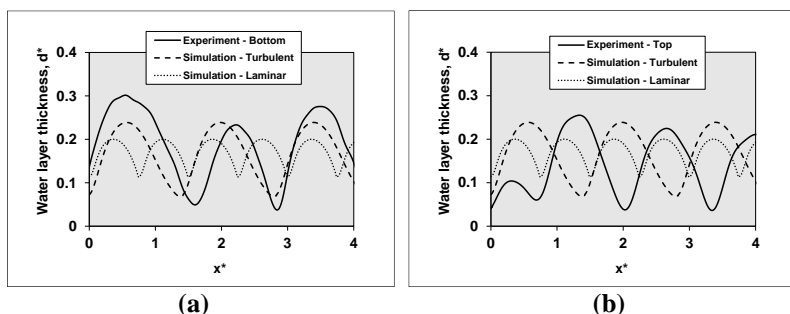


**Figure 4.17.** Instantaneous wave form (for the dimensionless water layer thickness,  $d^*$ ) in the experiments and simulations for a water holdup fraction of 26%; (a) top layer, (b) bottom layer.

## 4.5 Conclusions

Detailed numerical simulations were carried out for the wave initiation, growth, and saturation at the oil-water interface in core-annular flow. The focus was on conditions with a turbulent water annulus, but the laminar water annulus was considered as well. The simulation results were compared with lab measurements. The main conclusions are the following:

- The simulated growth rates for the laminar-laminar case are in very good agreement with values obtained in the linear stability analysis by Li & Renardy (1999).
- The growth rate for the linear instability of different wave lengths (i.e. the wave stability curve) in the case of a turbulent water annulus can be accurately obtained from 2D axi-symmetric RANS

- simulations with the Launder-Sharma low-Reynolds number  $k - \varepsilon$  model. This also provides the most unstable wave length for the turbulent water annulus.
- The maximum wave growth rate for a turbulent water annulus is significantly higher than for a laminar water annulus.
  - Both in the simulations and in the experiments, the most unstable wave length decreases with decreasing water holdup fraction (or decreasing watercut). The most unstable wave length in the simulations is slightly smaller than in the experiments.
  - If a relatively long pipe section is used in the simulations (i.e. longer than the most unstable wave length) multiple waves with the same wave length are predicted (with a length close to the most unstable one).
  - A range of waves is found in the experiment, albeit with a clear dominant wave length. The experiments could be used to construct the probability density function of the wave length distribution.
  - Applying the energy balance to the simulation results shows that linear wave instability at the interface is due to inertia in the turbulent case, and due to viscous effects in the laminar case.
  - The linear instability with exponential increase of the wave amplitude is followed by a nonlinear phase that ends in saturated waves in fully developed flow. The linear stage takes about 4 time units, and the nonlinear stage 16 time units (in which a time unit is the actual time non-dimensionalized with the oil core radius and the mixture velocity).
  - Both in the simulations and in the experiments, the wave amplitude increases with increasing wave length, up to a certain maximum level for the longest waves. There is a reasonably good agreement between the amplitudes of the different wave lengths as found in the experiments and in the simulations.

## References

- Bai, R., Chen, K., Joseph, D.D., 1992. Lubricated pipelining: stability of core-annular flow. Part 5. Experiments and comparison with theory. *Journal of Fluid Mechanics* 240, 97-132.
- Bai, R., Kelkar, K., Joseph, D.D., 1996. Direct simulation of interfacial waves in a high-viscosity-ratio and axisymmetric core-annular flow. *Journal of Fluid Mechanics* 327, 1-34.
- Beerens, J.C., Ooms, G., Pourquié, M.J.B.M., Westerweel, J., 2014. A comparison between numerical predictions and theoretical and experimental results for laminar core-annular flow. *AIChE Journal* 60.8, 3046-3056.
- Boomkamp, P.A.M., Miesen, R.H.M., 1996. Classification of instabilities in parallel two-phase flow. *International Journal of Multiphase Flow* 22, 67-88.
- Charles, M.E., Govier, G.W., Hodgson, G.W., 1961. The horizontal pipeline flow of equal density oil-water mixtures. *Canadian Journal of Chemical engineering* 39, 27-36.
- Chen, K., Bai, R., Joseph, D.D., 1990. Lubricated pipelining. Part 3 Stability of core-annular flow in vertical pipes. *Journal of Fluid Mechanics* 214, 251-286.
- Hickox, C.E., 1971. Instability due to viscosity and density stratification in axisymmetric pipe flow. *Physics of Fluids* 14, 251-262.
- Hooper, A.P., 1985. Long-wave instability at the interface between two viscous fluids: thin layer effects. *Physics of Fluids* 28, 1613-1618.
- Hu, H.H., Joseph, D.D., 1989. Lubricated pipelining: stability of core-annular flow. Part 2. *Journal of Fluid Mechanics* 205, 359-396.
- Hooper, A.P., Boyd, W.G.C., 1983 Shear-flow instability at the interface between two viscous fluids. *Journal of Fluid Mechanics* 128, 507-528.
- Joseph, D.D., Bai, R., Chen, K.P., Renardy, Y.Y., 1997. Core-annular flows. *Annual Review of Fluid Mechanics* 29, 65-90.
- Kuru, W.C., Sangalli, M., Uphold, D.D., McCreedy, M.J., 1995. Linear stability of stratified channel flow. *International Journal of Multiphase Flow* 21, 733-753.

- Launder, B.E., Sharma, B.T., 1974. Application of the energy dissipation model of turbulence to the calculation of flow near a spinning disc. *Letters in Heat and Mass Transfer* 1, 131-138.
- Li, H., Pourquié, M.J.B.M., Ooms, G., Henkes, R.A.W.M. 2021. Simulation of turbulent horizontal oil-water core-annular flow with a low-Reynolds number  $k - \epsilon$  model. *International Journal of Multiphase Flow* 142, 103744.
- Li, H., Pourquié, M.J.B.M., Ooms, G., Henkes, R.A.W.M. 2022. Simulation of turbulent annulus with interfacial waves in core-annular pipe flow. *International Journal of Multiphase Flow* 154, 104152.
- Li, J., Renardy, Y., 1999. Direct simulation of unsteady axisymmetric core-annular flow with high viscosity ratio. *Journal of Fluid Mechanics* 391, 123-149.
- Miesen, R., Beijnon, G., Duijvestijn, P.E.M., 1992. Interfacial waves in core-annular flow. *Journal of Fluid Mechanics* 238, 97-117.
- Náráigh, L.Ó., Spelt, P.D.M., Matar, O.K., Zaki, T.A., 2011. Interfacial instability in turbulent flow over a liquid film in a channel. *International Journal of Multiphase Flow* 37, 812-830.
- Ooms, G., 1971. Fluid-mechanical studies on core-annular flow. PhD Thesis, Delft University of Technology.
- Ooms, G., Pourquié, M.J.B.M., Beerens, J. C., 2013. On the levitation force in horizontal core-annular flow with a large viscosity ratio and small density ratio. *Physics of Fluids*, 25, 032102.
- Ooms, G., Segal, A., Van der Wees, A.J., Meerhoff, R., Oliemans, R.V.A., 1984. A theoretical model for core-annular flow of a very viscous oil core and a water annulus through a horizontal pipe. *International Journal of Multiphase Flow* 10, 41-60.
- Papageorgiou, D.T., Maldarelli, C., Rumschitzki, D.S., 1990. Nonlinear interfacial stability of core-annular film flows. *Physics of Fluids A: Fluid Dynamics* 2, 340-352.
- Preziosi, L., Chen, K., Joseph, D.D., 1989. Lubricated pipelining: stability of core-annular flow. *Journal of Fluid Mechanics* 201, 323-356.
- Yamamoto, T., Okano, Y., Dost, S., 2017. Validation of the S-CLSVOF method with the density-scaled balanced continuum surface force model in multiphase systems coupled with thermocapillary flows. *International Journal for Numerical Methods in Fluids* 83.3, 223-244.
- Yih, C S., 1967. Instability due to viscosity stratification. *Journal of Fluid Mechanics* 27, 337-352.



# 5

## Vertical CAF

*The Reynolds-Averaged Navier Stokes (RANS) with the Launder & Sharma low-Reynolds number  $k - \varepsilon$  model was used to simulate core-annular flow in the same configuration with vertical upflow as considered by Kim & Choi (2018), who carried out Direct Numerical Simulations (DNS), and by Vanegas Prada (1999), who performed experiments. The DNS are numerically very accurate and can thus be used for benchmarking of the RANS turbulence model. There is a large ratio between the oil and water viscosities, and the density difference between the water and oil is only small. The frictional pressure drop was fixed and the water holdup fraction was varied. Differences between the RANS and DNS predictions, e.g. in the wave structure and in the Reynolds stresses, are discussed. Despite the shortcomings of the considered Launder & Sharma low-Reynolds number  $k - \varepsilon$  model in RANS, in comparison to DNS, the RANS approach properly describes the main flow structures for upward moving core-annular flow in a vertical pipe, like the travelling interfacial waves in combination with a turbulent water annulus. The Fanning friction factor with RANS is 18% lower than with DNS, and the holdup ratio with RANS is only slightly higher than with DNS (i.e. it has a slightly larger tendency to accumulate water in RANS than in DNS).*

## 5.1 Introduction

For the transport of two-phase flow of immiscible fluids (like gas-liquid flow or liquid-liquid flow) through a horizontal or inclined pipe, different flow patterns can be distinguished. The prevailing flow pattern depends on a number of parameters, such as the pipe diameter and inclination, the flow rates of the two phases, and thermodynamic parameters of the phases, namely density, viscosity, and interfacial tension. When a very viscous liquid (like heavy oil) is combined with the flow of a certain amount of less-viscous liquid (like water), the so-called core-annular flow regime can occur. Here the oil is flowing in the centre of the pipe (“core flow”), and the water is flowing as a lubricating film (“annular flow”) along the wall of the pipe. In this way the high pressure drop that would be found if only the viscous oil was flowing through the pipe is significantly reduced, as now not the oil viscosity but the water viscosity determines the pressure drop. This makes core-annular flow an attractive technology for viscous oil transport. In addition, core-annular flow is also of high interest from a fundamental fluid mechanics view point. An overview of core-annular flow has been given by Joseph et al. (1997) and Ghosh et al. (2009).

Over the past decades quite some studies were devoted to core-annular flow. This included small scale lab experiments in horizontal pipe flow or in a vertically upward going flow, and theoretical studies to determine the wave growth at the liquid-liquid interface. Most of the studies considered a laminar annulus flow (in addition to the laminar core flow). However, if the annulus-based Reynolds number is increased, the flow in the lubricating film will become turbulent. This will add complexity due to the interaction between the turbulence in the lubricating annulus and the travelling waves at the liquid-liquid interface. Some authors have applied a Reynolds-Averaged Navier-Stokes (RANS) approach, with a  $k - \varepsilon$  model or a  $k - \omega$  model for turbulence. See e.g. Ghosh et al. (2010), Shi et al. (2017), Ingen Housz et al. (2017), and Li et al. (2021, 2022).

Recently a first very detailed study was published by Kim & Choi (2018), who have carried out Direct Numerical Simulations (DNS) for vertical upflow in the core-annular flow regime with a laminar oil core and a turbulent annulus flow. The pipe diameter is 27.6 mm. The dynamic viscosity ratio between the two liquids was large (17600), but the density difference between the two liquids was only small (35 kg/m<sup>3</sup>). Due to the small density difference, gravity almost does not play a role (note that there is no difference in flow in a horizontal or vertical pipe if the density of the two liquids is the same). Different values of the water holdup fraction in the pipe were simulated (i.e. different thicknesses of the annulus). Experiments for this configuration were carried out by Vanegas Prada (1999) and Vanegas Prada & Bannwart (2001). Due to the availability of DNS and experiments, this configuration can serve as an attractive case for benchmarking of turbulence models. Through grid refinement the DNS were shown to be very accurate, and they thus form the most accurate representation of the physics, as described by the Navier-Stokes equations. As the RANS approach contains closures for the turbulence (and DNS not), the RANS solution under transitional or turbulent flow conditions will be less accurate than DNS.

In the present study we have used RANS in the OpenFOAM CFD package, with the Launder & Sharma low-Reynolds number  $k - \varepsilon$  model, to simulate core-annular flow in the same vertical pipe configuration as considered by Kim & Choi (DNS) and by Vanegas Prada (experiments). We have recently also used the same RANS approach for core-annular flow in some different configurations (see Li et al, 2021, 2022). We have paid quite some attention to verifying that the RANS results are numerically accurate (through successive mesh refinement). As the RANS results will be axisymmetric, 2D unsteady simulations were made. This will reveal the travelling waves at the oil-water interface with the turbulent water annulus. The RANS results will be compared with the DNS and experiments. Some remarkable differences in the results will be discussed.

## 5.2 Modelling approach

### 5.2.1 Governing equations

The mass and momentum conservation equations for an incompressible, isothermal fluid are (in Cartesian coordinates):

$$\frac{\partial u_i}{\partial x_i} = 0 \quad (5.1)$$

$$\frac{\partial \rho u_i}{\partial t} + \rho u_j \frac{\partial u_i}{\partial x_j} = \frac{\partial}{\partial x_j} \left( \rho (\nu + \nu_t) \left( \frac{\partial u_i}{\partial x_j} + \frac{\partial u_j}{\partial x_i} \right) \right) - \frac{\partial p}{\partial x_i} + \rho g_i + F_{\sigma,i} \quad (5.2)$$

These are the Reynolds-Averaged Navier-Stokes Equations (RANS). Here  $u_i$  is the velocity,  $\rho$  and  $\mu$  are the fluid density and viscosity,  $g_i$  is the gravitational acceleration,  $p$  is the pressure and  $F_{\sigma,i}$  is the interfacial tension force. For the pipe flow, we will use  $x_1 = x$  for the coordinate along the pipe axis, and  $x_2 = y$  and  $x_3 = z$  for the coordinates in the cross sectional plane; the velocity components are  $u$ ,  $v$ , and  $w$ , in the directions  $x$ ,  $y$ , and  $z$ , respectively. The gravity components are:  $g_1 = -g$ , and  $g_2 = g_3 = 0$ , where  $g$  is the gravitational acceleration. The actual simulations were carried out using 2D axi-symmetric coordinates with the radius  $r = \sqrt{y^2 + z^2}$ .

The turbulent viscosity is modelled with the low-Reynolds number  $k - \epsilon$  model of Launder & Sharma (1974), which reads as follows:

$$\nu_t = C_\mu f_\mu \frac{k^2}{\epsilon} \quad (5.3)$$

$$\frac{\partial k}{\partial t} + u_j \frac{\partial k}{\partial x_j} = \frac{\partial}{\partial x_j} \left( \nu + \frac{\nu_t}{\sigma_k} \right) \frac{\partial k}{\partial x_j} + \nu_t \left( \frac{\partial u_j}{\partial x_j} \right)^2 - \epsilon - D \quad (5.4)$$

$$\frac{\partial \epsilon}{\partial t} + u_j \frac{\partial \epsilon}{\partial x_j} = \frac{\partial}{\partial x_j} \left( \nu + \frac{\nu_t}{\sigma_\epsilon} \right) \frac{\partial \epsilon}{\partial x_j} + C_1 f_1 \frac{\epsilon}{k} \nu_t \left( \frac{\partial u_j}{\partial x_j} \right)^2 - C_2 f_2 \frac{\epsilon^2}{k} + E \quad (5.5)$$

With  $D = 2\nu \frac{\partial \sqrt{k}}{\partial x_j} \frac{\partial \sqrt{k}}{\partial x_j}$  and  $E = 2\nu \nu_t \left( \frac{\partial^2 u_j}{\partial x_j^2} \right)^2$ . The turbulent energy dissipation rate is  $\epsilon = \tilde{\epsilon} + D$ .

Furthermore,  $C_\mu = 0.09$ ,  $C_1 = 1.44$ ,  $C_2 = 1.92$ ,  $\sigma_k = 1.0$ ,  $\sigma_\epsilon = 1.3$ ,  $f_\mu = \exp\left(\frac{-3.4}{(1 + \frac{Re_t}{50})^2}\right)$ ,  $f_1 = 1$ ,  $f_2 = 1 -$

$0.3 \exp(-Re_t^2)$ ,  $Re_t = \frac{k^2}{\tilde{\epsilon} \nu}$ . The boundary conditions at the wall are:  $k=0$  and  $\tilde{\epsilon} = 0$ .

Quite a number of low-Reynolds number  $k - \epsilon$  formulations are available in the literature. A large advantage of the Launder-Sharma one is that the low-Reynolds number terms do not include the explicit distance to the closest wall. Instead the parameter  $Re_t$  is used to incorporate the effect of turbulence damping when a wall is approached. In the same way, the model will incorporate the possible damping of turbulence when the oil-water interface is approached in core-annular flow. The low-Reynolds number  $k - \epsilon$  model is used everywhere in the domain, also in the laminar oil core. Because of the presence of the low-Reynolds number terms the model automatically relaminarizes in the viscous oil core (i.e. it gives zero turbulent viscosity).

### 5.2.2 Numerical method

We used the open-source package OpenFOAM to solve the RANS equations, applying the CLSVOF method for the interface capturing. The CLSVOF solver, which was developed by Yamamoto et al. (2017), is based on the interFoam Volume of Fluid (VOF) solver in OpenFOAM. The level set function is used to calculate the interfacial tension force. Starting from the VOF method, the volume fraction  $\alpha$  is introduced to distinguish between the two fluid phases:  $\alpha = 0$  is the oil phase,  $\alpha = 1$  is the water phase, and  $0 < \alpha < 1$  denotes the oil-water interface. Then the fluid density and viscosity in the equations are:

$$\rho = (1 - \alpha)\rho_o + \alpha\rho_w \quad (5.6)$$

$$\mu = (1 - \alpha)\mu_o + \alpha\mu_w \quad (5.7)$$

The subscript “o” refers to oil, and the subscript “w” refers to water.  $\alpha$  is calculated from the following

advection equation:

$$\frac{\partial \alpha}{\partial t} + \nabla \cdot (\alpha \vec{u}) + \nabla \cdot ((1 - \alpha) \alpha \vec{u}_r) = 0 \quad (5.8)$$

The third term on the left-hand side is the compressive term (with the divergence of the compressive flux); here  $\vec{u}_r = \vec{u}_w - \vec{u}_o$ . This term is meant to control the sharpness of interface.

The level set function  $\Phi$  is defined as the distance from the interface, where the interface is the isoline with  $\Phi = 0$ . The initial value of the level set function  $\Phi_0$  is obtained from the initialized volume-of-fluid field, where the interface is defined at  $\alpha = 0.5$ :

$$\Phi_0 = (2\alpha - 1)\Gamma \quad (5.9)$$

$$\Gamma = 0.75\Delta X \quad (5.10)$$

Here  $\Delta X$  is the minimum mesh size near the interface. Thereafter the re-initialization equation is solved to turn the initial level set function into the distance from the interface:

$$\frac{\partial \Phi}{\partial \tau} = \text{sign}(\Phi_0)(1 - |\nabla \Phi|) \quad (5.11)$$

Here  $\tau = 0.1\Delta X$  is the iteration time step of  $\Phi$  and the sign function denotes:

$$\text{sign}(\Phi) = \begin{cases} 1 & \Phi > 0, \text{water} \\ 0 & \Phi = 0, \text{interface} \\ -1 & \Phi < 0, \text{oil} \end{cases} \quad (5.12)$$

Then the interface tension force is calculated as:

$$\vec{F}_\sigma = \sigma \kappa(\Phi) \delta_\phi \nabla(\Phi) \quad (5.13)$$

Here  $\sigma$  is the interface tension and  $\delta_\phi$  is the smoothed delta function:

$$\delta_\phi = \begin{cases} \frac{1}{2\gamma} \left( 1 + \cos\left(\frac{\pi\Phi}{\gamma}\right) \right) & \text{for } |\Phi| < \gamma \\ 0 & \text{elsewhere} \end{cases} \quad (5.14)$$

The quantity  $\gamma$  is the interface thickness coefficient (see Yamamoto et al., 2017) and  $\kappa(\Phi)$  is the interface curvature:

$$\kappa(\Phi) = \nabla \cdot \vec{n}_c \quad (5.15)$$

$$\vec{n}_c = \frac{(\nabla \Phi)_f}{|(\nabla \Phi)_f|} \quad (5.16)$$

Here  $\vec{n}_c$  is the surface unit normal vector. The contact angle  $\theta$  between the interface and the pipe wall is defined as:

$$\cos(\theta) = \vec{n}_c \cdot \vec{n}_w \quad (5.17)$$

With  $\vec{n}_w$  being the unit normal vector at the wall. The contact angle is set to  $90^\circ$  in our simulations. This means that both the level set function  $\Phi$  and the volume fraction of the fluid  $\alpha$  satisfy the zero gradient condition at the pipe wall boundary.

A pressure drop in the flow direction is added as an extra force term to the right-hand side of Equation 5.2, with periodic boundary conditions on the left and right side of the pipe. Therefore, the pressure that remains in the equations is periodic with respect to the left and right side of the computational pipe section. The initially assumed velocity profile will then develop over time under this pressure drop in the transient simulation until a stable state is obtained.

A second-order backward implicit time discretization scheme is applied, with a very small time step (small Courant number). This gives a very accurate time integration. We use a second-order scheme for the advection terms in the momentum equations and in the interface equation (as used in the level set method), but a first-order upwind scheme for the advection in the equations for the turbulence quantities  $k$  and  $\varepsilon$ ; trying a second-order scheme for the latter gave numerical instabilities. Through successive mesh refinement, however, we have verified that the simulation results are accurate (and not suffering from large numerical diffusion).

In all the simulations, periodic boundary conditions are applied on the left and right side of the pipe, which restricts the wavelengths in the axial direction to the domain length divided by an integer value. At the pipe wall, the no-slip condition is imposed. We have used the symmetric PBiCG solver for the velocity and for the turbulent quantities, the GAMG solver for the pressure, and the PIMPLE solver for the velocity-pressure coupling.

### 5.2.3 Key parameters

Four important parameters are: the total flow rate, the pressure drop, the watercut, and the water holdup fraction. When two parameters are set as input (e.g. the total flow rate and the watercut in the experiments), the other two will follow as output.

The watercut is defined as the ratio of the water volumetric flow rate and the total volumetric flowrate:

$$WC = Q_w / (Q_o + Q_w) \quad (5.18)$$

where  $Q$  denotes the volumetric flow rate. The water holdup fraction is defined as the ratio of the in-situ water volume in the pipe and the total volume of oil and water:

$$\alpha_w = \frac{V_w}{V_w + V_o} \quad (5.19)$$

A related parameter is the so-called holdup ratio  $h$ , which is defined as:

$$h = \frac{Q_o / Q_w}{V_o / V_w} \quad (5.20)$$

This can also be rewritten as  $h = 1 + u_r / u_w$ . Here the velocity difference  $u_r = u_o - u_w$ , is the apparent (average) slip velocity between the oil core (having a bulk velocity  $u_o$ ) and the water annulus (having a bulk velocity  $u_w$ ). Note that  $h=1$  if there is no slip between the bulk oil and water velocities. The holdup ratio thus is a measure of the apparent slip between the oil core and the water annulus.

### 5.2.4 Basic simulation set-up

The base conditions for the considered configuration are the same as those used in the lab experiments described by Vanegas Prada (1999) and Vanegas Prada & Bannwart (2001). The vertical pipe has a diameter of 27.6 mm. The oil and water densities are  $\rho_o=963 \text{ kg/m}^3$  and  $\rho_w=998 \text{ kg/m}^3$ , and the oil and water viscosities are  $\mu_o=17.6 \text{ Pa s}$  and  $\mu_w=0.001 \text{ Pa s}$ . Therefore the oil dynamic viscosity is 17600 times higher than the water value. The interfacial tension between oil and water is  $\sigma=0.03 \text{ N/m}$ . In the DNS simulation by Kim & Choi different values of the water holdup fraction are used:  $\alpha_w=0.09, 0.17, 0.29, 0.38$ , and  $0.44$ . The imposed pressure drop in the simulations is such that the resulting wall shear stress corresponds to  $Re_\tau = u_\tau R / \nu = 720$ , which in fact means that the frictional pressure drop is equal to  $400 \text{ Pa/m}$ . The imposed full pressure drop is found by adding the hydrostatic head, which is  $(\rho_w \alpha_w + \rho_o \alpha_o)g \text{ [Pa/m]}$ .

The experiments are described in detail in the Master Thesis by Vanegas Prada (1999), which also includes tables with the experimental results. The key measurements are the pressure drop as function of the oil and water flow rates. Through the measured oil and water flow rates also the watercut is known. The water holdup fraction is  $\alpha_w$  was not measured, though a value for it is included in the tables. It looks like a holdup ratio of about  $h=1.1$  has been assumed. The measurement points with a frictional pressure drop of (about)  $400 \text{ Pa/m}$  have been selected by Kim & Choi (2018) for their validation of the DNS. The same set of experiments will be used in the present study as well.

Time-dependent, 2D, axisymmetric RANS simulations were carried out for a pipe section with a length of 16.6 mm. Sensitivity simulations were made to investigate the effect of the chosen section length. Periodic boundary conditions are imposed between the start and end of the section. The pressure gradient is prescribed. The water holdup  $\alpha_w$  is imposed as initial condition, and the total water holdup fraction is conserved over time. The oil and water flow rates follow as output quantities. The simulation is started with a flat oil-water interface. Waves develop at the interface in the transient

simulation. The simulation is continued over a sufficient long time such that fully developed flow with travelling interfacial waves has developed. Grid refinement was applied to verify that the simulation results are sufficiently numerically accurate. Thereto an equidistant grid was applied in streamwise direction (i.e.  $x$ -coordinate) and a non-equidistant grid in the radial direction (i.e.  $r$ -coordinate). The latter has a strong refinement close to the boundary layer along the pipe wall, where there are large radial gradients in the velocity profile.

It should be note that the difference in density between the oil and water is quite small, namely 35 kg/m<sup>3</sup>, which is 3.5% of the water density. Therefore the effect of the density difference on the core-annular flow will be very small, which was verified by the RANS simulations. This means that in fact, with good accuracy, gravity could have been omitted in the simulations.

### 5.2.5 Force balance

An integral force balance for the flow (after averaging in space and time) can be derived, using the quantities shown in Figure 1. Here  $x$  is the streamwise pipe coordinate, and  $r$  is the radial pipe coordinate. The pipe has radius  $R$ . The oil flow is represented by a concentric core with radius  $R_c$ , and the water flows in an annulus with thickness  $R - R_c$ . The flow is driven by the pressure gradient  $-dp/dx$ . The wall imposes a wall shear stress  $\tau_w$  on the water annulus (taken positive in upstream direction). The water annulus imposes an interfacial stress  $\tau_i$  on the oil core (taken positive in upstream direction). The oil core also imposes an interfacial stress on the water annulus, which has the same magnitude as  $\tau_i$ , but now taken positive in downstream direction. The water flows with an average velocity (bulk velocity)  $u_w$ , and the oil flow with an average velocity (bulk velocity)  $u_o$ . The bulk velocity follows from the superficial velocity as:  $u_w = u_{sw}/\alpha_w$  and  $u_o = u_{so}/\alpha_o$ , with  $u_{sw} = Q_w/A$  and  $u_{so} = Q_o/A$ . Here  $A = \pi R^2$  is the cross sectional area of the pipe. The bulk oil viscosity  $u_o$  can also be denoted as the core velocity  $u_{core}$ . The mixture velocity is defined as  $u_m = u_{sw} + u_{so} = (Q_w + Q_o)/A$ .

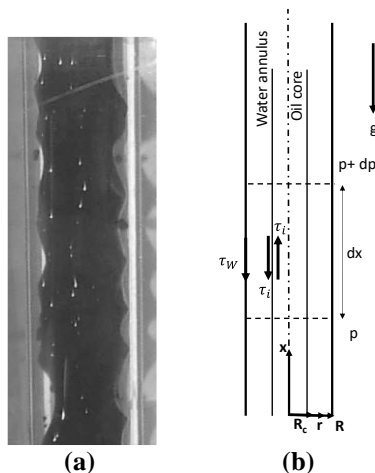


**Figure 5.1. Vertical core-annular flow; (a) snapshot from experiments (taken from Bannwart et al. , 2000) , (b) sketch of the forces.**

The force balance for the combined oil-water flow in a horizontal pipe reads:

$$-\frac{dp}{dx}A - \tau_w 2\pi R - (\rho_w \alpha_w + \rho_o \alpha_o)gA = 0 \quad (5.21)$$

The force balance for the oil core gives:

$$-\frac{dp}{dx}\alpha_o A - \tau_i 2\pi R_c - \rho_o g \alpha_o A = 0. \quad (5.22)$$

Here  $\alpha_o$  is the oil holdup fraction, with  $\alpha_o = (R_c/R)^2$ .

From force balances (5.21) and (5.22) it also follows that the wall shear stress and interfacial stress

are related as  $\tau_i = \tau_w \left( \frac{R_c}{R} \right) \left( 1 - \frac{1}{2} \left( 1 - \left( \frac{R_c}{R} \right)^2 \right) (\rho_w - \rho_{wo}) g R \right)$ . Note that the force balances (5.21) and (5.22) hold for the core-annular flow (with or without interfacial waves) after averaging in space and time.

Due to the considered high ratio of the oil and water viscosities, the oil core will be laminar. Assuming parallel flow in the laminar oil core (i.e. neglecting non-parallel effects in the oil flow close to the wave interface), the core flow can be described by the force balance:

$$-\frac{dp}{dx} \pi r^2 - \mu_o \frac{du}{dr} 2\pi r - \rho_o g \pi r^2 = 0, \quad (5.23)$$

with the interface condition:  $\tau_i = -\mu_o \left( \frac{du}{dr} \right)_{r=R_c}$ .

Integration gives the following expression of the velocity at the interface:

$$u_i = -\frac{R_c}{4\mu_o} \tau_i + \frac{Q_o}{\pi R_c^2}, \quad (5.24)$$

in which  $Q_o$  is the oil flow rate. For all conditions considered in the present study, the first term on the right hand side is much smaller than the second term. This means that within the boundaries of validity of the shown force-balance approach with parallel core flow, the interfacial velocity is the same as the bulk oil velocity.

## 5.3 RANS results

### 5.3.1 Water-only pipe flow

Various authors have carried out DNS for single-phase turbulent pipe flow up to high Reynolds numbers, such as Eggels et. al. (1998), Wu & Moin (2008), Wu et. al. (2012) and Pirozzoli et al. (2021). Accurate turbulent pipe experiments have been carried out by Den Toonder & Nieuwstadt (1997), for moderate Reynolds numbers, and by Zaragoza & Smits (1998), using the Princeton Superpipe up to very high Reynolds numbers. Predictions for the Fanning friction factor as function of the Reynolds number as obtained with the RANS model with the Launder & Sharma low-Reynolds number  $k - \varepsilon$  model are compared with the DNS and experiments in Figure 2 (the Reynolds number is based on the pipe diameter, bulk velocity, and kinematic fluid viscosity, i.e.  $Re = uD/\nu$ ). The Fanning friction factor is defined as  $f_w = -\left( \frac{dp}{dx} \right) \frac{R}{\rho u^2}$ . The values in the DNS and experiments are very close to each other. RANS slightly underpredicts the friction factor, though the deviation becomes less for increasing Reynolds number. At about  $Re=27000$ , which is the (mixture) Reynolds number in the core-annular flow DNS by Kim & Choi, the RANS value of the friction factor is 0.0056, which is about 7% lower than the DNS and experimental value of 0.006.

Figure 5.3 compares various quantities in turbulent pipe flow at  $Re=24580$  as obtained from our RANS simulations and with the DNS by Wu & Moin (2008) and Wu et al. (2012). The DNS have a corresponding  $Re_\tau = u_\tau R/\nu = 685$ . The shown quantities (velocity, turbulent kinetic energy, Reynolds stress, and turbulent viscosity) have a plus superscript to indicate that they are non-dimensionalized with the wall shear velocity  $u_\tau$  and the kinematic viscosity  $\nu$ . The wall shear velocity  $u_\tau$  is defined as  $u_\tau = \sqrt{\tau_w/\rho_w}$ , in which the wall shear stress is related to the frictional pressure drop as  $\tau_w = -(dp/dx) R/2$ . Figure 5.3 shows that RANS and DNS for the velocity and Reynolds stress are in fairly close agreement, but the peak for the kinetic energy with RANS ( $k^+=3.2$ ) is significantly below the DNS value  $k^+=4.7$ . The level of the turbulent viscosity  $\nu_t^+$  away from the wall is about 40 for the DNS and 60 for the RANS simulations.

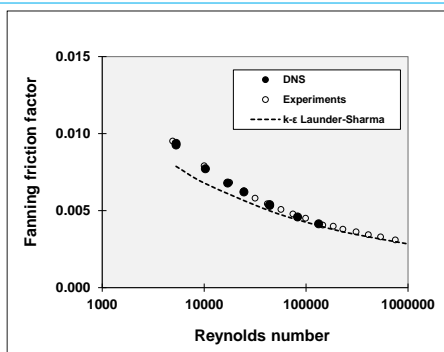


Figure 5.2. Comparison of RANS, DNS, and experiments; Fanning friction factor as function of the Reynolds number for single-phase turbulent pipe flow.

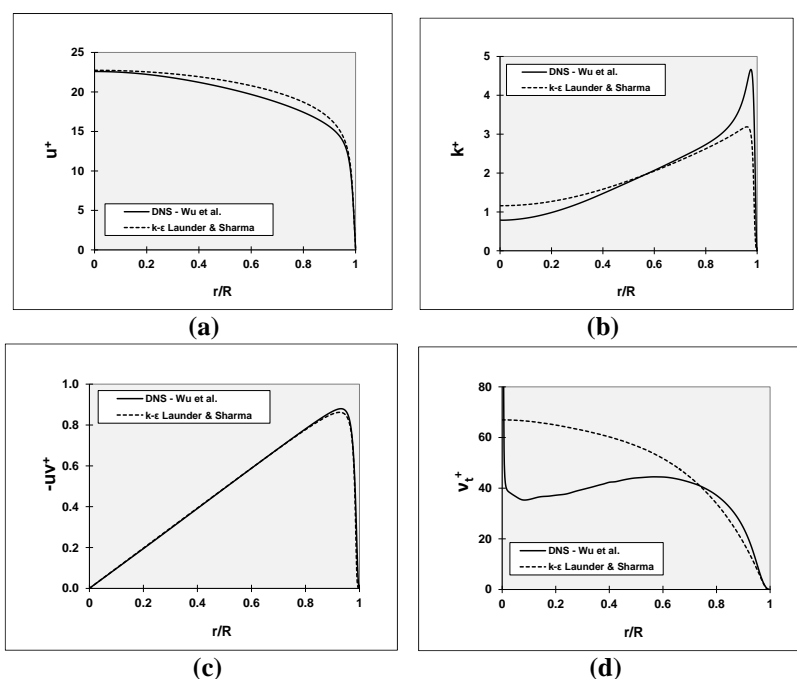


Figure 5.3. RANS versus DNS for single phase turbulent pipe flow at  $Re=24600$ ; (a) streamwise velocity, (b) turbulent kinetic energy, (c) Reynolds stress, (d) turbulent viscosity.

### 5.3.2 Two-phase flow

#### 5.3.2.1 Numerical accuracy and dependence on oil viscosity

The two-phase RANS simulations were carried out in a moving frame of reference, in which the wall has been given a velocity of 1 m/s, which is close to the velocity of the interface waves. As a result, the waves in the moving frame of reference are almost stagnant, which helps to improve the numerical stability. Despite this, numerical instabilities remained if the oil viscosity was set to  $\mu_o=17.6$  Pa s, which is the same value as used in the lab experiments by Vanegas Prada (1999) and in the DNS by Kim & Choi (2018). Numerically stable and accurate solutions could be obtained if the oil viscosity was reduced to a value of the order 1 Pa s. This is significantly lower than the target value, though



still very much higher (by a factor 1000) than the water viscosity of 0.001 Pa s.

An example of the good numerical accuracy is given in Figure 5.4 for  $\mu_o=0.75$  Pa s, which shows snapshots of the annulus thickness and the maximum turbulent viscosity. Numerical values are listed in Table 5.1 (which also includes the results for  $\mu_o=0.46$  and 1.5 Pa s. The length of the pipe section is set to 16.6 mm and a water holdup fraction of 0.29 was used. The imposed frictional pressure drop is 400 Pa/m. The good accuracy of the numerical simulations is shown through comparing the results on a coarser 100x200 grid (i.e. 100 points in streamwise direction, and 200 points in radial direction) and on a refined 200x400 grid.

For  $\mu_o=0.75$  Pa s on the finer grid, the resulting mixture velocity is 1.07 m/s, and the watercut is 24%. The corresponding core velocity is 1.15 m/s. The wave velocity is slightly lower than the core velocity, namely 1.11 m/s. The wave frequency is 67 Hz (being equal to the ratio of the wave velocity and the section length). As shown in Figure 5.4 for an oil viscosity  $\mu_o=0.75$  Pa s, the oscillation of the thickness of the water annulus and in the maximum turbulent viscosity in the water annulus on the 200x400 grid is very close to the results on the coarser 100x200 grid. Figure 5.5 shows (using the finer 400x200 grid) that the oscillation only slightly depends on the oil viscosity. Therefore, it makes good sense to compare the present RANS results with the DNS of Kim & Choi with the experiments by Vanegas Prada (1999), despite the latter two were obtained for an even higher oil viscosity.

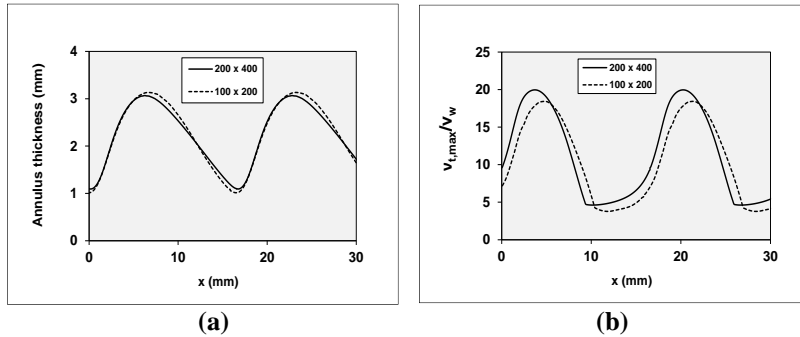


**Figure 5.4. RANS results for (a) annulus thickness, and (b) maximum turbulent viscosity (oil viscosity = 0.75 Pa s, water holdup fraction = 0.29, section length = 16.6 mm, frictional pressure drop = 400 Pa/m).**

**Table 5.1. RANS results for different oil viscosities on different numerical grids (water holdup fraction = 0.29, section length = 16.6 mm, frictional pressure drop 400 Pa/m).**

Dyn. oil viscosity Pa s	Grid	Mixture vel. m/s	Watercut %	Wave length mm	Wave velocity m/s	Wave frequency Hz
0.46	100x200	1.07	23	16.6	1.05	63
0.46	200x400	1.09	22	16.6	1.08	65
0.75	100x200	1.07	24	16.6	1.08	65
0.75	200x400	1.07	24	16.6	1.11	67
1.5	100x200	1.05	24	16.6	1.11	67
1.5	200x400	1	24	16.6	1.04	63

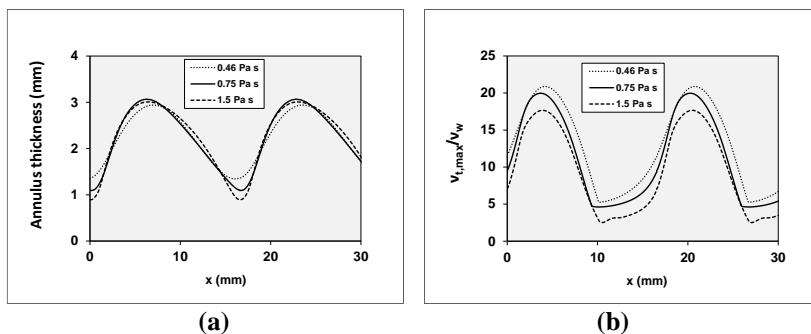


**Figure 5.5. RANS results with different oil viscosities for (a) annulus thickness, and (b) maximum turbulent viscosity; water holdup fraction = 0.29, section length = 16.6 mm, frictional pressure drop = 400 Pa/m.**

### 5.3.2.2 Dependence on pipe section length

The base section length in the RANS simulations is  $L=16.6$  mm. The effect of the section length on the interfacial waves was investigated by also simulating a section length of  $2L$  and  $3L$ . The numerical accuracy was verified by using both the 100x200 grid and the refined 200x400 grid. The considered conditions are: oil viscosity  $\mu_o=0.75$  Pa s, water holdup fraction  $\alpha_w=0.29$ , frictional pressure drop is 400 Pa/m. The different pipe sections all give a same mixture velocity of 1.07 m/s, and a watercut of 24% (corresponding to an average oil core velocity of 1.15 m/s). The wave velocity is between 1.05 and 1.11 m/s.

A snapshot of the thickness of the water annulus and of the maximum turbulent viscosity through the annulus thickness, as function of the streamwise pipe coordinate  $x$ , is shown in Figure 5.6. A single wave length of 16.6 mm is found when choosing the base section length  $L=16.6$  mm. When the section length is increased, the oscillation becomes more irregular, but the averaged wave length is still close to 16.6 mm, namely about 18 mm for  $2L$  and 13 mm for  $3L$ . The figure also shows that the turbulent viscosity is largest/smallest at the location where the thickness of the water annulus is (almost) largest/smallest.

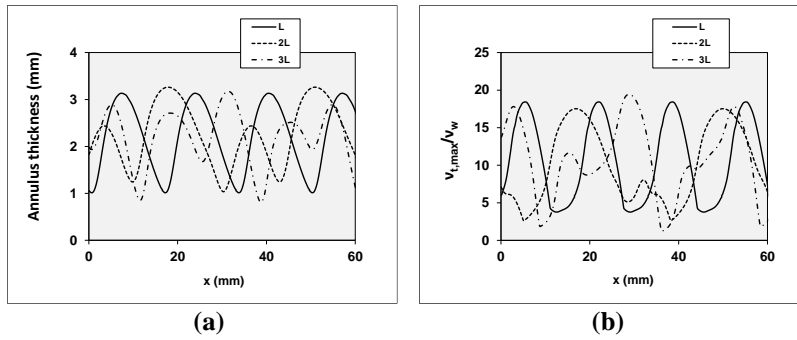


**Figure 5.6.** RANS results with different pipe section lengths (values shown in legend,  $L=16.6$  mm) for (a) annulus thickness, and (b) maximum turbulent viscosity; water holdup fraction  $\alpha_w=0.29$ , oil viscosity is  $\mu_o=0.75$  Pa s, frictional pressure drop is 400 Pa/m.

### 5.3.2.3 Dependence on the water holdup fraction

Various RANS simulations were carried out to determine the effect of the water holdup fraction  $\alpha_w$ . The considered conditions are: pipe section length is 16.6 mm, oil viscosity  $\mu_o=0.75$  Pa s, frictional pressure drop is 400 Pa/m. The simulated thickness of the water annulus and the maximum turbulent viscosity are shown in Figure 5.7. As expected, the amplitude of interfacial waves increases when the water holdup fraction is increased from 0.09 to 0.44. The wave length seen in the thickness of the water annulus is  $L=16.6$  mm for the higher values of the water holdup fraction (0.29, 0.38, and 0.44) though becomes half that value, i.e.  $L/2=8.4$  mm, for the lower fraction (0.17, 0.09). The maximum turbulent viscosity decreases with decreasing water holdup fraction, which means that the presence of a (thicker) oil core suppresses the turbulence. The value of the maximum turbulent viscosity is highest for water-only flow (i.e.  $\alpha_w=1$ ), namely  $v_{t,max}/v_w=67$ . For the smallest simulated value of the water holdup fraction ( $\alpha_w=0.09$ ), the thickness of the water annulus is so small that the layer fully relaminarizes (i.e.  $v_{t,max}/v_w=0$ ).

Figure 5.8 shows a snapshot of the streaklines with respect to an observer that moves with about the wave velocity at the interface. In the next section, the RANS results for various values of the water holdup fraction will also be used for comparison with the DNS of Kim & Choi (2018).

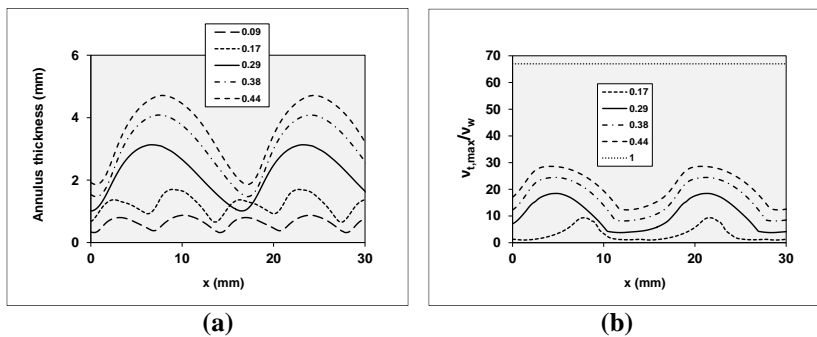


**Figure 5.7.** RANS results with different water holdup fraction (values shown in legend) for (a) annulus thickness, and (b) maximum turbulent viscosity; oil viscosity is  $\mu_o=0.75$  Pa s, section length  $L=16.6$  mm, frictional pressure drop is 400 Pa/m.

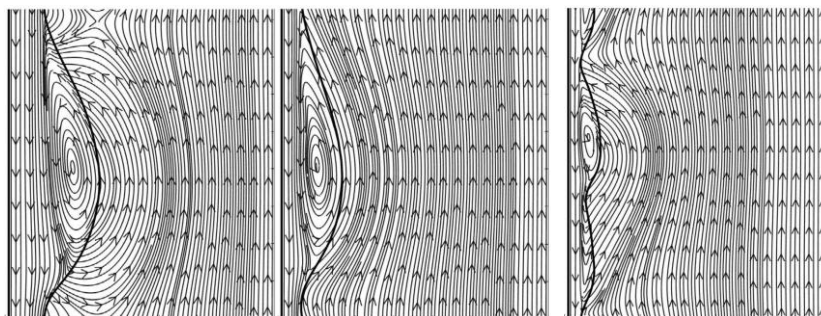


**Figure 5.8.** Snapshots of streamlines with respect to an observer moving with about the interface wave velocity; from left to right, water holdup fraction  $\alpha_w$  is 0.44, 0.29, and 0.17.

#### 5.3.2.4 Dependence on gravity

The density difference between the water and oil is so small (only 35 kg/m<sup>3</sup> compared to a water density of 998 kg/m<sup>3</sup>) that its effect on the vertical core annular flow is negligibly small. This is demonstrated for the RANS simulations (with oil viscosity  $\mu_o = 0.75$  Pa s) in Figure 5.9. The simulations without and with gravity give almost the same results for the oscillation of the thickness of the water annulus and of the maximum turbulent viscosity. Results without and with gravity are also practically the same when the length of the pipe section is increased to  $2L$  and  $3L$  (i.e. results without gravity are almost the same as those with gravity in Figure 5.6).

The DNS by Kim & Choi were only carried out with gravity. But it is very likely that also the DNS without gravity would be very close to the results with gravity. Thus this test case is actually one with a difference in liquid viscosity, though with a negligible difference in density. In fact this means that the results will be independent of the pipe inclination (vertical upflow is the same as horizontal flow, for an imposed frictional pressure drop of 400 Pa/m).

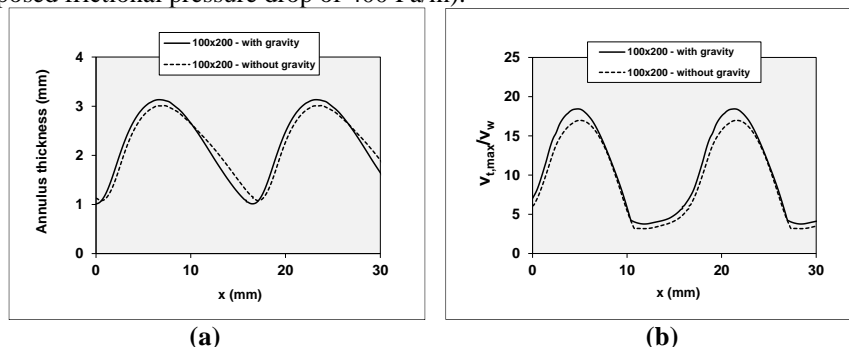


**Figure 5.9.** RANS results with and without gravity for (a) annulus thickness, and (b) maximum turbulent viscosity; water holdup fraction  $\alpha_w = 0.29$ , oil viscosity is  $\mu_o = 0.75$  Pa s, section length  $L = 16.6$  mm, frictional pressure drop is 400 Pa/m.

## 5.4 Comparison of RANS results with experiments and DNS

The RANS simulations used in this section for comparison were obtained with a pipe section length  $L = 16.6$  mm, an oil viscosity of  $\mu_o = 0.75$  Pa s, and an imposed frictional pressure drop of 400 Pa/m. The prescribed water holdup rate was varied. Figure 5.10 compares the resulting mixture velocity and watercut with the DNS simulations of Kim & Choi. For the mixture velocity we also compare with the experimental values by Vanegas Prada. RANS predictions for the mixture velocity are about 10% higher than the DNS results. For example at  $\alpha_w = 0.29$ , RANS gives a mixture velocity of 1.07 m/s, and DNS of 0.96 m/s. For the same water holdup fraction, the RANS value for the watercut is close

to the DNS value; in fact the RANS watercut is slightly lower than the DNS value. For example at  $\alpha_w = 0.29$ , RANS gives a watercut of 23.9% and DNS of 25.4%. This also implies that at the same watercut, RANS will give a higher water holdup fraction (i.e. more water accumulation) than DNS.

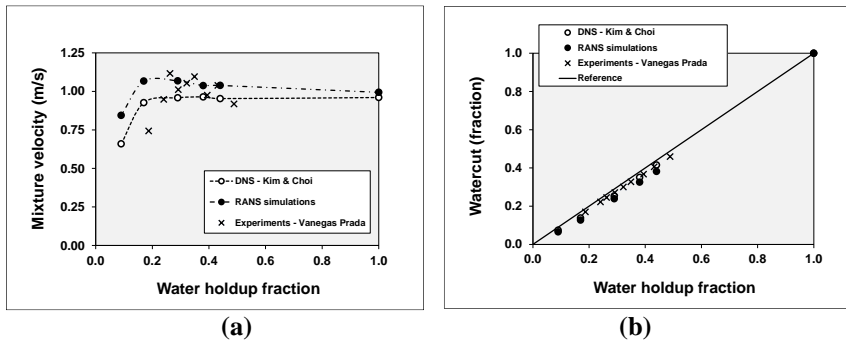


Figure 5.10. Comparison of (a) mixture velocity, and (b) watercut, as obtained from RANS, DNS, and experiments; fixed frictional pressure drop of 400 Pa/m and variation of water holdup fraction. The reference line in (b) denotes equal fractions for watercut and water holdup.

#### 5.4.1 Fanning friction factor

The Fanning friction factor is a dimensionless presentation of the (frictional) pressure drop:  $f_w = -\left(\frac{dp}{dx}\right)_{fric} \frac{R}{\rho_w u_m^2}$ . Figure 5.11a shows the Fanning friction factor for different watercuts, as obtained with RANS and DNS for a fixed frictional pressure drop of 400 Pa/m. From the experiments by Vanegas Prada, those points were selected that have a frictional pressure drop of (about) 400 Pa/m. The RANS predictions for the Fanning friction factor are typically about 18% lower than the DNS values (for watercut fractions in the range 0.1 to 0.5). This means that the same pressure drop (like 400 Pa/m) gives about 18/2=9% higher mixture velocity with RANS than with DNS.

There is a fair agreement for the predicted Fanning friction factor and the measurements by Vanegas Prada. When dividing the Fanning friction factor by its value found with water only flow (at the same 400 Pa/m frictional pressure drop), which defines the friction factor ratio as shown in Figure 5.11b, it turns out that this ratio is almost equal to 1 for all watercuts (except for the lowest values where the water annulus relaminarizes). This is particularly true for the DNS results.

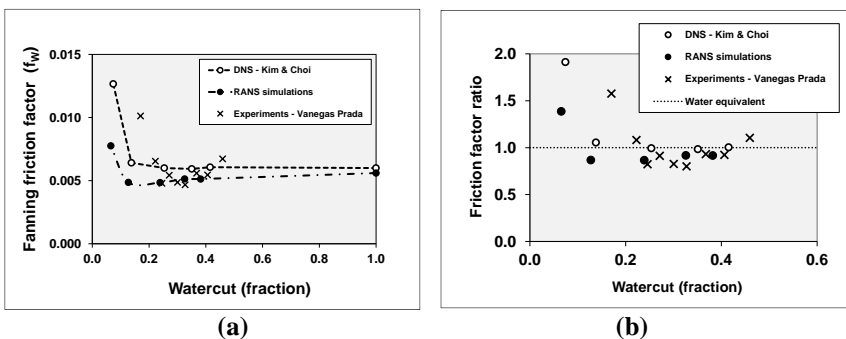
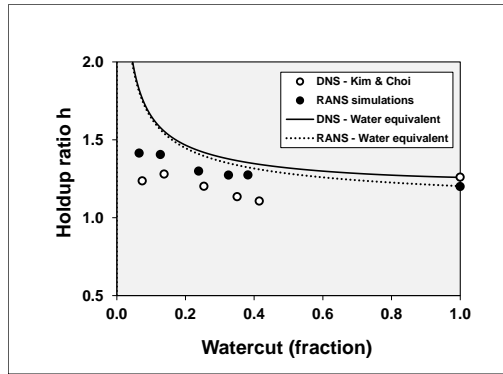


Figure 5.11. Comparison of friction factor with RANS, experiments and DNS as function of the watercut for a fixed frictional pressure drop of 400 Pa/m; (a) Fanning friction factor, (b) friction factor ratio.

#### 5.4.2 Holdup ratio

The holdup ratio  $h$  shown in Figure 5.12 is a measure of the relative water accumulation or of the

apparent slip between the oil and water (difference in bulk oil and water velocities). For the 4 higher watercut values used in the DNS (with turbulent water annulus) the RANS prediction for the holdup ratio is about 12% higher than the DNS prediction. Thus the water accumulation effect is larger in RANS than in the DNS, or: there is more apparent slip between the oil and water in the RANS simulations than in the DNS. The figure also includes a DNS curve and a RANS curve denoted as the “water equivalent” holdup ratio. This curve is found by considering water-only pipe flow, that is “artificially” splitted in a core and annulus (while they still have same properties for viscosity and density). The watercut and holdup ratio are now referring to the annulus part of the single-phase RANS results; here the watercut is determined by integrating the DNS or RANS velocity profile in the annulus to give the water flow rate in the annulus, and divide this by the total flow rate through the pipe. This shows that there is relatively much water accumulation (or more apparent slip) close to the pipe wall for low watercut, where water is slowed down due to the wall presence. In fact this means that the increase in holdup ratio found for decreasing watercut in the DNS and RANS for the configuration of Kim & Choi can (at least) partly be explained from this natural accumulation effect.



**Figure 5.12.** Comparison of the holdup ratio obtained with RANS and DNS as function of the watercut for fixed frictional pressure drop of 400 Pa/m.

### 5.4.3 Water annulus

The values of the temporally and spatially averaged streamwise water velocity in the annulus, as obtained with DNS and RANS, are compared in Figure 5.13. The average velocity is made dimensionless with the shear stress velocity  $u_\tau$ , and the distance to the pipe wall is made dimensionless with  $v_w/u_\tau$ . The profile in Figure 5.13a shows the averaged water velocity ( $u_{w,av}$ ), whereas Figure 5.13b shows the average water velocity multiplied with the average local water holdup fraction (this product is denoted by  $u_{w,av}^*$ ):

$$u_{w,av}^* = \frac{\iiint u(x,r,t) \alpha_w(x,r,t) dxdt}{\iiint dxdt} = \frac{\iiint u(x,r,t) \alpha_w(x,r,t) dxdt}{\iiint \alpha_w(x,r,t) dxdt} \cdot \frac{\iiint \alpha_w(x,r,t) dxdt}{\iiint dxdt} = u_{w,av} \cdot \alpha_{w,av} \quad (5.25)$$

The higher peak for the water velocity for RANS compared to DNS is consistent with the about 10% higher total flow rate (with about the same watercut, namely 23.9% versus 25.4%) found in RANS than in DNS (using an imposed frictional pressure drop of 400 Pa/m and an imposed water holdup fraction of 0.29).

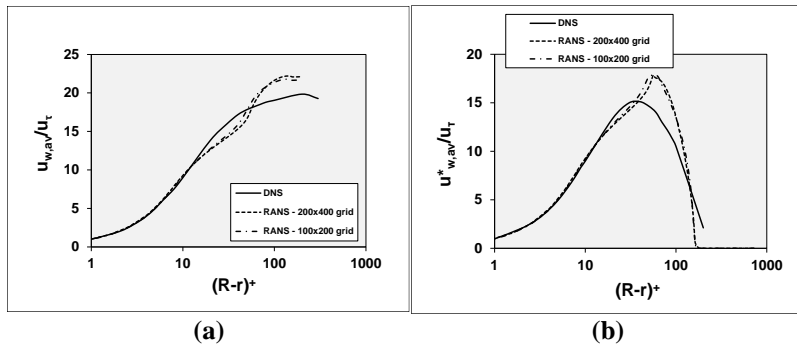


**Figure 5.13.** Average water velocity versus distance from the pipe wall in + units as obtained with DNS and RANS for a water holdup fraction  $\alpha_w = 0.29$  and a frictional pressure drop of 400 Pa/m; (a) average water velocity, (b) average of water velocity multiplied with local water holdup fraction.

Figure 5.14a shows the temporally- and spatially averaged value of the local water holdup fraction, as function of the radial coordinate in the pipe. The imposed overall water holdup fraction is 0.29. Shown are the results with DNS and RANS. For the latter, both the 2D axisymmetric as the 1D results are given. The 1D results are obtained by choosing a very short pipe section, such that all waves are suppressed. Due to the absence of waves the local water holdup fraction abruptly changes from 0 to 1, when the local radius  $r$  (scaled with the pipe radius  $R$ ) becomes larger than  $\sqrt{(1 - 0.29)} = 0.84$ . Due to the interface waves, DNS and 2D RANS give a more gradual profile of the water holdup fraction. It is also clear from Figure 5.14a that the interface waves can reach a higher amplitude in the DNS than in the RANS simulations.

The regularity of the interface waves can be quantified through determining the probability density function (PDF) of the thickness of the water annulus; see Figure 5.14b. RANS (for the base pipe section length  $L=16.6$ ) mm gives a pdf that corresponds to a fully periodic function. DNS has a pdf that corresponds to a spectrum of waves. Increasing the pipe section in the RANS simulations, e.g. to  $3L$  (see also Section 5.3.2.2), breaks the single wave appearance, and a broader PDF is found, that in Figure 5.14b looks more like the pdf found with DNS. The average annulus thickness is 2.17 mm (for both DNS and RANS), which corresponds to the imposed water holdup fraction of 0.29. The standard deviation in the water annulus thickness that can be derived from the PDF in the figure is 1.16 mm for the DNS, 0.70 mm for RANS with the base section length  $L=16.6$  mm, and 0.67 mm for RANS with  $3L$  pipe section length. This can be converted to an effective amplitude of the oscillation though multiplying the standard deviation with the factor  $\sqrt{2}$ ; this gives an average wave amplitude of 1.64 mm for the DNS, 1 mm for RANS with section length  $L$ , and 0.95 mm for RANS with section length  $3L$ . The amplitude of 1 mm for RANS with section length  $L$  is also clearly visible in the results shown in Figure 5.4a. The average amplitude of the oscillations in the water thickness (or in the interfacial waves) is thus significantly larger for DNS than for RANS (1.64 mm versus 1 mm). The amplitude in the RANS results is almost independent of the applied section length.

The PDF of the thickness as shown in Figure 5.14 only gives information on the wave amplitude, but not on the wave length. With respect to the latter, Kim & Choi (2018) also present graphs of the energy in the wave numbers (or wave length), and of the convective wave velocity for the wave numbers. For a water holdup fraction  $\alpha_w = 0.29$  the wave velocity is about 1.0 m/s in the DNS, versus 1.11 m/s in the RANS results. The spectra in the DNS show that there is energy in the wave numbers in the range of about  $1/R$  to  $10/R$ , corresponding to wave lengths between 8 mm and 80 mm (this range of wave lengths is also visible in the DNS snapshot of the structure of the oil-water interface shown in Figure 5.12 in the paper by Kim & Choi). RANS gives a single wave length of 16.6 mm when the applied section length is 16.6 mm, and an average wave length of about 13 mm to 18 mm if



larger pipe sections are used.

The remarkable difference in the wave spectra between DNS and RANS was also noted by Kim & Choi (2018) when analysing their DNS: “The phase interface amplitude has broadband spectra, which is very different from the observation of the one-wave number peak in laminar core annular flows (Bai et al. 1996, Li & Renardi 1999) and of smooth waves from RANS simulations of turbulent core-annular flows (Ghosh et al. 2010, Ingen Housz et al. 2017, Shi et al. 2017).” The present RANS study shows that choosing the length of pipe section about equal to the most unstable wave length (within the RANS model) will give a travelling wave at the oil-water interface with a single wave length. Increasing the length of the pipe section breaks the single wave appearance, though still gives a dominant with about the length of the originally chosen pipe section (16.6 mm). DNS gives a larger spread of wave lengths, up to sizes of 80 mm which is larger than what is found with RANS. Consistent with the larger waves found in DNS than in RANS, the average amplitude of the waves (1.64 mm) is larger than the RANS prediction (1 mm). The difference in wave spectrum may be due to the possibility of azimuthal symmetry breaking in DNS, which is not included in the 2D, axisymmetric RANS.

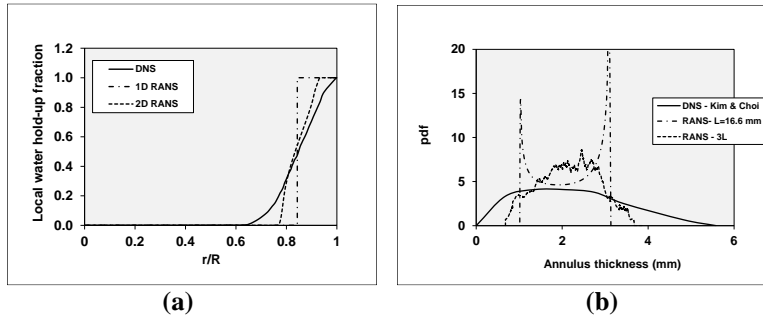


**Figure 5.14.** DNS versus RANS simulation and in DNS for a water holdup fraction  $\alpha_w = 0.29$  and an imposed frictional pressure drop of 400 Pa/m; (a) local water holdup fraction, (b) PDF for the location of the oil-water interface

#### 5.4.4 Stresses

The simulation results are averaged in time and space to obtain the dependence of the stresses on the radial pipe coordinate. The figures in this section present the stresses after normalization with  $\rho_w u_\tau^2$ . The averaged total shear stress (as function of the radial coordinate) balances the streamwise pressure force and the gravity force according to:

$$\bar{\tau} = \overline{\rho u_x u_r} - \mu \left( \frac{\partial u_x}{\partial r} + \frac{\partial u_r}{\partial x} \right) = \frac{r}{2} \left( -\frac{dp}{dx} \right) - \frac{1}{r} \int_0^r \bar{\rho} g r dr \quad (5.26)$$

The force due to interfacial tension has been neglected. This formulation is the same as equation (3.5) in Kim & Choi (2018). The overbar means averaging in the main stream direction and in time. The stress consists of the sum of the viscous stress and the Reynolds stress. In the averaging of the RANS results, the Reynolds stress can be split in a contribution that is due to the Reynolds closure in the  $k - \varepsilon$  model and a contribution due to the interfacial wave movement. Figure 5.15 shows the DNS and RANS results for the total stress (and for the split-up in a viscous stress and Reynolds stress). For RANS, both the results from the 1D simulation (i.e. no interfacial waves) and the 2D simulation (i.e. with waves) are included. The total stress in Figure 5.15a can be easily obtained from the two terms on the right hand side of Equation 5.26: the first term is the prescribed pressure drop (with 400 Pa/m frictional pressure drop), and the second term follows from integrating the radial profile of the averaged water holdup fraction shown in Figure 5.14a (with a prescribed total average value  $\alpha_w = 0.29$ ). As expected, due to the prescribed pressure drop and water holdup fraction, there is very good



agreement in the radial profile of the total stress for DNS and RANS. There is also good agreement between DNS and RANS for the viscous stress in the oil core (Figure 5.15b), which is the only contribution to the total stress in the oil core, but differences are larger in the water annulus. The latter is related to the significantly lower Reynolds stress in the turbulent water annulus (Figure 5.15c) according to DNS as compared to the RANS results. Figure 5.16 shows the split between the turbulent Reynolds stress and the wave contribution to the Reynolds stress, as derived from the RANS results: the wave contribution is much smaller than the turbulent contribution.

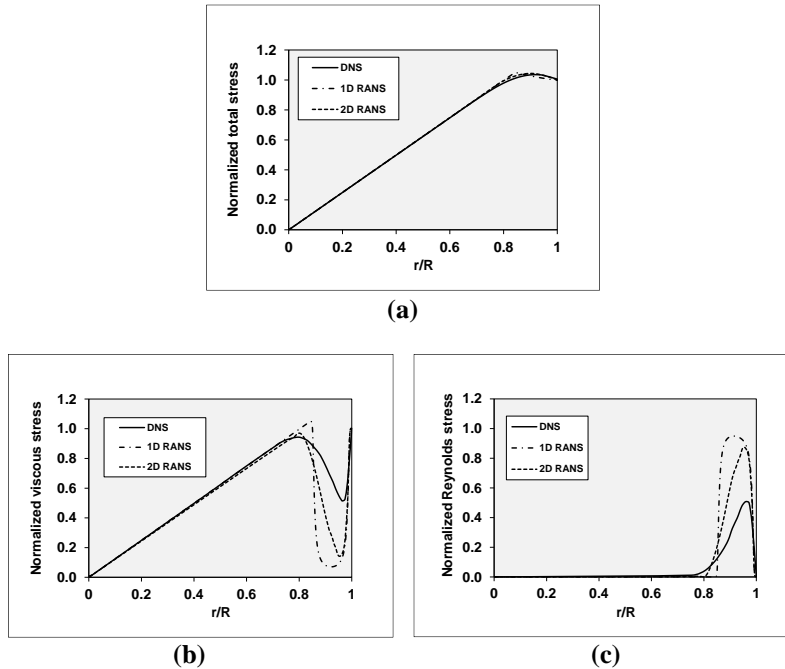


**Figure 5.15.** Profile for the water holdup fraction and stresses in the RANS simulation and in the DNS for a water holdup fraction is  $\alpha_w = 0.29$  and an imposed frictional pressure drop of 400 Pa/m; (a) total shear stress, (b) viscous stress, (c) Reynolds stress.

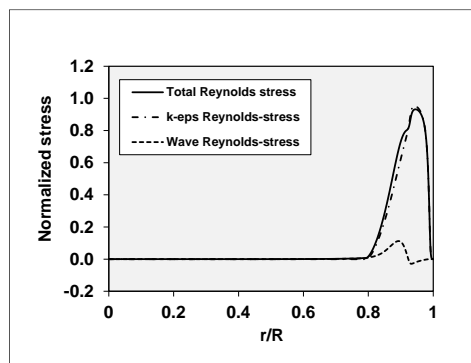


**Figure 5.16.** Radial profile of the composition of the Reynolds stress in the RANS simulation for a water holdup fraction  $\alpha_w = 0.29$  and an imposed frictional pressure drop of 400 Pa/m.

To further study the difference in Reynolds stress between DNS and RANS, Figure 5.17 gives the comparison for a range of water holdup fractions between 0.17 and 1. The predictions of the total stress are close (Figure 5.17a), but the Reynolds stress is significantly lower with DNS than with RANS (Figure 5.17b). The latter is true for all considered water holdup fractions, except for the

water-only pipe flow ( $\alpha_w = 1$ ), for which there is close agreement. It is illustrative to show the maximum Reynolds stress as function of the shear-based Reynolds number  $Re_\tau$  (see Figure 5.18), which is defined now as  $Re_\tau = d^+ = u_\tau d / \nu_w$ . Here  $u_\tau$  is the wall shear velocity and  $d$  is the average thickness of the water annulus:  $u_\tau = \sqrt{\tau_w / \rho_w}$  and  $\frac{d}{D} = \frac{1 - \sqrt{1 - \alpha_w}}{2}$ . Note that here  $Re_\tau$  is based on  $d$ , whereas earlier it was based on the pipe radius  $R$ . The maximum simulated value is  $Re_\tau = 720$ . According to Jimenez & Moin (1991), who applied DNS to channel flow, a minimum value of about  $Re_\tau = 90$  is needed to sustain turbulence in single-phase channel flow (where  $d$  is half the channel width). A decreasing water holdup ratio  $\alpha_w$  (i.e. decreasing average thickness of the water annulus  $d$ ) decreases  $Re_\tau$ , which will thus give turbulence damping if its value drops below the critical value of 90. As shown in Figure 5.17, some of the conditions have a value of  $Re_\tau$  that is close to, or even below, 90. This will give transitional or fully laminar flow. The low-Reynolds number  $k - \varepsilon$  model may be less accurate under transitional conditions. This can explain that the  $k - \varepsilon$  model in RANS gives more turbulence damping than DNS; the latter will be able (on sufficiently fine numerical grids) to accurately represent both transitional and fully turbulent flow conditions.

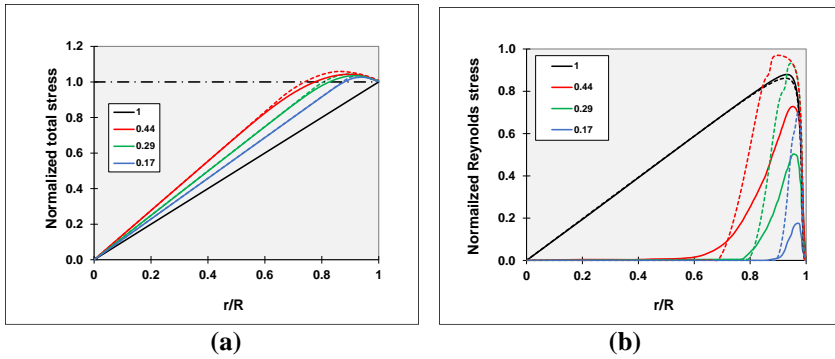


**Figure 5.17.** Radial profile of (a) the total stress, and (b) the (total) Reynolds stress for different values of the water holdup fraction (values in the legend) and an imposed frictional pressure drop of 400 Pa/m; solid lines denote DNS and dashed lines denote RANS results.

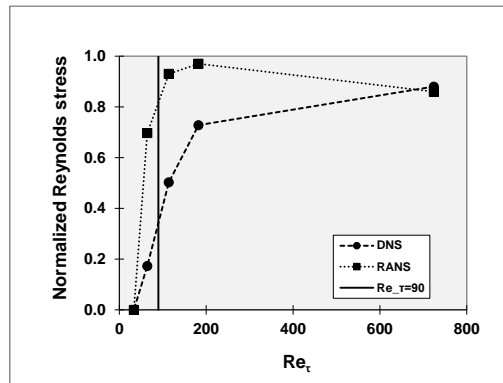


**Figure 5.18.** DNS versus RANS for the maximum Reynolds stress (normalized with  $\rho_w u_\tau^2$ ) as function of the shear-based Reynolds number  $Re_\tau$ .

## 5.5 Conclusions

RANS with the Launder & Sharma low-Reynolds number  $k - \varepsilon$  model was used to simulate core-annular flow in the same configuration as was considered by Kim & Choi (DNS) and by Vanegas

Prada (experiments). The DNS by Kim & Choi are numerically very accurate and can be used for benchmarking of the RANS turbulence model. The vertical pipe has a diameter of 27.6 mm there is a large ratio between the oil and water viscosities, and the density difference between the water and oil is only small. The frictional pressure drop was fixed at 400 Pa/m and the water holdup fraction was varied.

- The 2D axisymmetric RANS results were shown to be numerically accurate through grid refinement from 100x200 to 200x400 points. The high viscosity ratio used in the DNS and experiments led to the numerical instability in the RANS simulations, and therefore a lower ratio had to be used. Through sensitivity simulations (in which the viscosity ratio was changed) it was shown that the simulation results are not significantly dependent on the viscosity ratio.
- The mixture velocity with RANS is about 10% higher than DNS, and the Fanning friction factor (which is a normalized pressure drop) is about 18% lower. The watercut is only slightly lower with RANS than with DNS, which means that RANS tends to accumulate slightly more water (i.e. same watercut gives more water holdup); the holdup ratio with RANS is 12% higher than with DNS.
- Most RANS simulations were carried out with a pipe section of 16.6 mm which gives a single travelling wave at the oil-water interface with a wave length equal to the pipe section. Increasing the pipe section in RANS gives more irregular wave movement, though the dominant wave is still about 13 to 18 mm. DNS gives a broader spectrum of waves with wave lengths in the range of 8 mm to 80 mm.
- Both RANS and DNS give an almost constant velocity of the interface waves; for example, for a water holdup fraction  $\alpha_w = 0.29$ , the wave velocity is about 1.11 m/s with RANS and 1.0 m/s in DNS.
- Consistent with the shorter waves found with RANS than in DNS, the average amplitude of the waves with RANS is smaller than in DNS. For example, for a water holdup fraction  $\alpha_w = 0.29$ , the average amplitude of the waves is 1 mm in RANS versus 1.64 mm in DNS. The smaller wave amplitude in RANS will also give a smaller interfacial stress and herewith more water accumulation (i.e. higher holdup-ratio) than with DNS.
- In the RANS results, the Reynolds stress due to the interfacial waves is much smaller than the turbulent Reynolds stress.
- Decreasing the water holdup fraction (i.e. smaller average thickness of the water annulus) gives significantly less damping of the turbulence in RANS than in DNS (this means that the normalized maximum Reynolds stress in RANS is larger than in DNS). This is due to the complexity of transitional flow and relaminarization that occurs when the shear-based Reynolds is reduced below a critical value of about 90.

Despite the shortcomings of the considered Launder & Sharma low-Reynolds number  $k - \varepsilon$  model in RANS, in comparison to DNS, the RANS approach properly describes the main flow structures for upward moving core-annular flow in a vertical pipe, like the travelling interfacial waves in combination with a turbulent water annulus. The Fanning friction factor is predicted fairly well and the prediction of the holdup ratio is quite good.

## References

- Bai, R., Kelkar, K., Joseph, D.D., 1996. Direct simulation of interfacial waves in a high-viscosity-ratio and axisymmetric core-annular flow. *Journal of Fluid Mechanics* 327, 1-34.
- Bannwart, A. A., 2001. Modeling aspects of oil-water core-annular flows. *J. Petrol. Sci. Engng* 32, 127-143.
- Bannwart, A.C., Rodriguez, O.M.H., Carvalho, C.H.M., Wang, I.S., Vara, R.M.O., 2000. Flow patterns in heavy crude oil –water core annular flow. *Proceedings of the Engineering Technology Conference of Energy—ETCE 2001, CR-ROM, Feb. 5 – 7, Houston, Texas.*
- Den Toonder, J.M.J., Nieuwstadt, F.T.M., 1997. Reynolds number effects in a turbulent pipe flow for low to moderate  $Re$ . *Physics of Fluids* 9, 3398-3409.
- Eggels, J.G.M., Unger, F., Weiss, M.H., Westerweel, J., Adrian, R.J., Friedrich, R., Nieuwstadt, F.T.M., 1994. Fully developed turbulent pipe flow: a comparison between direct numerical simulation and experiment. *J. Fluid Mech.* 268, 175–210.
- Ghosh, S., Mandal, T.K., Das, P.K., 2009. Review of oil water core annular flow.” *Renewable and Sustainable Energy Rev.* 13, 1957-1965.
- Ghosh, S., Das, G., Das, P.K., 2010. Simulation of core annular downflow through CFD – a comprehensive study. *Chem. Engng Process.* 49, 1222-1228.
- Ingen Housz, E.M.R.M., Ooms, G., Henkes, R.A.W.M., Pourquié, M.J.B.M., Kidess, A., Radhakrishnan, R., 2017. A comparison between numerical predictions and experimental results for core-annular flow with a turbulent annulus, *Int. J. Multiphase Flow* 95, pp. 271-282.
- Jiménez, J., Moin, P., 1991. The minimal flow unit in near-wall turbulence. *J. Fluid Mechanics* 225, 213-240.
- Joseph, D.D., Bai, R., Chen, K.P., Renardy, Y.Y., 1997. Core-Annular Flows. *Annular Review of Fluid Mechanics* 29, 65-90.
- Kim, K., Choi, H., 2018. Direct numerical simulation of a turbulent core-annular flow with water-lubricated high viscosity oil in a vertical pipe. *J. Fluid Mech.* 849, 419-447.
- Launder, B.E., Sharma, B.T., 1974. Application of the energy dissipation model of turbulence to the calculation of flow near a spinning disc. *Lett. Heat and Mass Transfer* 1, 131-138.
- Li, H., Pourquié, M.J.B.M., Ooms, G., Henkes, R.A.W.M. 2021. Simulation of turbulent horizontal oil-water core-annular flow with a low-Reynolds number  $k - \epsilon$  model. *Int. J. Multiphase Flow* 142, 103744.
- Li, J., Renardy, Y., 1999. Direct simulation of unsteady axisymmetric core–annular flow with high viscosity ratio. *Journal of Fluid Mechanics* 391, 123-149.
- Pirozzoli, S., Romero, J., Fatica, M., Verzicco, R., Orlandi, P., 2021. One point statistics for turbulent pipe flow up to  $Re_\tau \approx 6000$ . *J. Fluid Mech.* 926, 355-377.
- Rodriguez, O.M., Bannwart, A.C., 2006. Experimental study on interfacial waves in vertical core flow. *J. Petroleum Science and Engineering* 54, 140-148.
- Shi, J., Lao, L., Yeung, H., 2017. Water-lubricated transport of high-viscosity oil in horizontal pipes: The water holdup and pressure gradient. *Int. J. Multiphase Flow* 96, 70-85.
- Shi, J., Gourma, M., Yeung, H., 2017. CFD simulation of horizontal oil-water flow with matched density and medium viscosity ratio in different flow regimes. *J. Petroleum Science and Engineering* 151, 373-383.
- Sotgia, G., Tartarini, P., Stalio, E., 2008. Experimental analysis of flow regimes and pressure drop reduction in oil–water mixtures. *Int. J. Multiphase Flow* 34, 1161-1174.
- Van Duin, E., Henkes, R.A.W.M., Ooms, G., 2019. Influence of oil viscosity on oil-water core-annular flow through a horizontal pipe. *Petroleum* 5.2, 199-205.
- Vanegas Prada, J.W., 1999. Estudo experimental do escoamento anular óleo-água (“core flow”) na elevação de óleos ultraviscosos. Master Thesis, University of Campinas, Brazil.
- Vanegas Prada, J.W., Bannwart, A.C. 2001. Modeling of vertical core-annular flows and application to heavy oil production. *Transaction ASME* 123, 194-199.

- Wu, X., Moin, K., 2008. A direct numerical simulation study on the mean velocity characteristics in turbulent pipe flow. *J. Fluid Mech.* 608, 81-112.
- Wu, X., Baltzer, J.R., Adrian, R.J., 2012. Direct numerical simulation of a 30R long turbulent pipe flow at  $R^+ = 685$ ; large- and very large-scale motions. *J. Fluid Mechanics* 698, 235-281.
- Zaragola, M.V., Smits, A.J., 1998 Mean flow scaling in turbulent pipe flow. *J. Fluid Mech.* 373, 33–79.



# 6

## RANS/LES/DNS for CAF

*DNS, LES, and RANS simulations were carried out for core-annular flow in a horizontal pipe and results were compared with experiments carried out with water and oil in our lab. In contrast to the various existing studies for core-annular flow available in the literature, the flow annulus is not laminar but turbulent. This makes the simulations more challenging. As DNS does not contain any closure correlations, this approach should give the best representation of the flow (provided a sufficiently accurate numerical mesh and numerical method is used). Various flow configurations were considered, such as without gravity (to enforce an on average concentric oil core) and with gravity (to allow for eccentricity in the oil core location). Both single-phase and two-phase conditions were considered; single-phase flow refers to the water annulus with imposed wavy wall, whereas two-phase flow includes the determination of the wavy interface. Mesh refinement was carried out to assess the numerical accuracy of the simulation results.*

## 6.1 Introduction

Oil-water core-annular flow (CAF) is a typical two-phase liquid-liquid flow pattern in a pipeline system. In this flow pattern, a viscous liquid core is surrounded by a less viscous annulus; for example the flow of oil and water. The thin water annulus can lubricate the pipe wall, which significantly decreases the pressure drop compared to viscous oil transport. Therefore, this kind of flow pattern is applicable in transporting highly viscous oil in the petroleum industry. In addition to its application opportunities, core-annular flow is also of great interest from a more fundamental fluid mechanics perspective.

Over the past decades, much research was devoted to core-annular flow. Research topics included: stability of CAF, interfacial waves, prediction of pressure drop and hold up ratio, and the levitation mechanism in horizontal pipe flow. Joseph et al. (1997) and Ghosh et al. (2009) have provided reviews. In addition to lab experiments, CFD simulations can provide a detailed description of the flow phenomena. The complexity of the multiphase flow, with its liquid-liquid interface and possibly turbulent water annulus, make the numerical simulations challenging. As the oil has a much higher viscosity than water, there is a jump in viscosity and velocity gradient across the interface, and the interface may dampen the turbulence in the water annulus. Besides, the apparent slip between the oil and water can cause flow instability, where waves will develop at the interface and these waves will interact with the turbulent flow field.

Li & Renardy (1999) used the Volume of Fluid (VOF) method to perform a direct numerical simulation of the laminar-laminar 2D core-annular flow, in which the instability problem and wave shape were studied. A similar numerical method was used by Ooms et al. (2013) for 3D laminar-laminar CAF with both higher and lower Reynolds numbers (Stokes region). Kang et al. (2006) used the level set method for 2D axisymmetric vertical core-annular flow; they managed to simulate the “bamboo wave” with a sharp wave crest. The breaking and merging of the oil core was also simulated. Beerens et al. (2014) used the VOF method to simulate 2D vertical core-annular flow. The linear wave growth was studied for shorter pipe section lengths, and multiple wave lengths were shown to appear in their long pipe simulation results. For the CAF simulation with a turbulent water annulus, Huang et al. (1993) used the low Reynolds number  $k - \varepsilon$  model to simulate the velocity profile of eccentric core-annular flow. Ko et al. (2002) simulated the turbulent water annulus assuming the oil core to be solid; the solid “interface” was simulated with a similar method as applied by Bai et al. (1996). They found the SST  $k - \omega$  model to perform better than the standard  $k - \omega$  model. The wave length, pressure drop and secondary flow for different Reynolds numbers were simulated. Ingen Housz et al. (2017) performed 3D simulations for horizontal CAF, using the VOF method for the interface capturing and the low Reynolds Launder–Sharma  $k - \varepsilon$  model for turbulence. It is found that the water is laminar in the top layer and turbulent in the bottom water layer. When comparing the simulation results with experiments, the pressure drop and the top wave amplitude in the simulation were both lower than in the experiments. Shi et al. (2017) simulated horizontal oil-water flow in which both liquids had the same density. The VOF method is used and various flow patterns were simulated. The SST  $k - \omega$  model was found to give the best results. Gosh et al. (2010) simulated downward CAF using VOF and the  $k - \varepsilon$  method, but a rather coarse mesh was used. Kim & Choi (2018) performed high-resolution DNS using the level set method for vertical core annular flow with a turbulent water annulus, and detailed flow statistics were provided. We have recently also used the the RANS approach for core-annular flow in different configurations (see Li et al. 2021, 2022, 2023a,b). We have paid quite some attention to verifying that the RANS results are numerically accurate (through successive mesh refinement). From the literature review, it becomes clear that DNS for horizontal CAF with a turbulent annulus are lacking.



Very accurate results from DNS are available for single phase pipe flow, such as Eggels et al. 1994, Wu & Moin 2008, and Pirozzoli et al. 2021. These studies provide a good reference to validate the performance of our current DNS. The interaction of the turbulent water annulus with the oil-water interface is an interesting phenomenon in core-annular flow, which has not been simulated very often so far. Sullivan et al. (2000) and Buckley et al. (2016) studied the interaction of turbulent air flow with an idealized water wave; here the wave-correlated velocity, and the critical layer of the turbulent momentum flux are studied for different wave speeds. The three contributions to the total stress (i.e. the turbulent stress, wave-induced stress, and viscous stress) are discussed separately by Youse et al. (2020). They found a wave-induced transfer of energy between the waves and the turbulent annulus flow and between the mean flow and the wave motion.

The main purpose of the present chapter is to perform DNS for horizontal oil-water core-annular flow, and compare the results with RANS results. Also a comparison is made with some Large-Eddy Simulations (LES). From the DNS, detailed flow characteristics can be shown. The comparison between DNS and RANS is first performed for single phase pipe flow. Then, the single-phase annulus flow is simulated to show the effect of waves on the turbulent annulus flow. Finally, DNS are performed for the two-phase CAF both with and without gravity. The DNS results are compared with the RANS simulation results and with lab experiments.

## 6.2 Method

### 6.2.1 Governing equations

The mass and momentum conservation equations for an incompressible, isothermal fluid are (in Cartesian coordinates):

$$\frac{\partial u_i}{\partial x_i} = 0 \quad (6.1)$$

$$\frac{\partial \rho u_i}{\partial t} + \rho u_j \frac{\partial u_i}{\partial x_j} = \frac{\partial}{\partial x_j} \left( \rho(\nu + \nu_t) \left( \frac{\partial u_i}{\partial x_j} + \frac{\partial u_j}{\partial x_i} \right) \right) - \frac{\partial p}{\partial x_i} + \rho g_i + F_{\sigma,i} \quad (6.2)$$

Here  $u_i$  is the velocity,  $\rho$  and  $\mu$  are the fluid density and viscosity,  $g_i$  is the gravitational acceleration,  $p$  is the pressure and  $F_{\sigma,i}$  is the interfacial tension force. For the pipe flow, we will use  $x_1 = x$  for the coordinate along the horizontal pipe axis,  $x_2 = y$  for the vertical coordinate, and  $x_3 = z$  for the pipe width coordinate; the velocity components are  $u$ ,  $v$ , and  $w$ , in the directions  $x$ ,  $y$ , and  $z$ , respectively. The gravity components are:  $g_1 = g_3 = 0$ , and  $g_2 = -g$ , where  $g$  is the gravitational acceleration. Some simulations were carried out using 2D axi-symmetric coordinates with the radius  $r = \sqrt{y^2 + z^2}$ .

For the RANS simulations, eq. (2) is the Reynolds-Averaged Navier-Stokes Equation, in which the turbulent viscosity  $\nu_t$  is modeled using the low-Reynolds number  $k - \varepsilon$  model of Launder & Sharma (1974):

$$\nu_t = C_\mu f_\mu \frac{k^2}{\varepsilon} \quad (6.3)$$

$$\frac{\partial k}{\partial t} + u_j \frac{\partial k}{\partial x_j} = \frac{\partial}{\partial x_j} \left( \nu + \frac{\nu_t}{\sigma_k} \right) \frac{\partial k}{\partial x_j} + \nu_t \left( \frac{\partial u_j}{\partial x_j} \right)^2 - \varepsilon - D \quad (6.4)$$

$$\frac{\partial \varepsilon}{\partial t} + u_j \frac{\partial \varepsilon}{\partial x_j} = \frac{\partial}{\partial x_j} \left( \nu + \frac{\nu_t}{\sigma_\varepsilon} \right) \frac{\partial \varepsilon}{\partial x_j} + C_1 f_1 \frac{\varepsilon}{k} \nu_t \left( \frac{\partial u_j}{\partial x_j} \right)^2 - C_2 f_2 \frac{\varepsilon^2}{k} + E \quad (6.5)$$

With  $D = 2\nu \frac{\partial \sqrt{k}}{\partial x_j} \frac{\partial \sqrt{k}}{\partial x_j}$  and  $E = 2\nu \nu_t \left( \frac{\partial^2 u_j}{\partial x_j^2} \right)^2$ . The turbulent energy dissipation rate is  $\varepsilon = \tilde{\varepsilon} + D$ .

Furthermore,  $C_\mu = 0.09$ ,  $C_1 = 1.44$ ,  $C_2 = 1.92$ ,  $\sigma_k = 1.0$ ,  $\sigma_\varepsilon = 1.3$ ,  $f_\mu = \exp\left(\frac{-3.4}{(1 + \frac{Re_t}{50})^2}\right)$ ,  $f_1 = 1$ ,  $f_2 = 1 -$

$0.3 \exp(-Re_t^2)$ ,  $Re_t = \frac{k^2}{\varepsilon \nu}$ . The boundary conditions at the wall are:  $k=0$  and  $\varepsilon = 0$ .

When using Large-Eddy Simulation (LES), the large scales of turbulence are directly simulated, and scales smaller than the grid size are modeled. The turbulent viscosity  $\nu_t$  appears in the subgrid scale tensor that is represented with the so-called SGS model. Therefore, a rather coarse mesh can be used. In our study the WALE model is used for the subgrid turbulent viscosity. According to Nicoud & Ducros (1999), the WALE model is able to simulate laminar-turbulent transitional flow, and has the advantage of accurate near-wall scaling of the subgrid viscosity without the need for wall damping. Within DNS,  $\nu_t$  will be removed from equation (6.2), and all scales of turbulence flow are directly simulated.

## 6.2.2 Numerical method

The open-source package OpenFOAM is used for solving the governing equations, in which the CLSVOF method is used for interface capturing. The CLSVOF solver, which was developed by Yamamoto et al. (2017), is based on the interFOAM Volume of Fluid (VOF) solver in OpenFOAM. The level set function is used to calculate the interfacial tension force. Starting from the VOF method, the volume fraction  $\alpha$  is introduced to distinguish between the two fluid phases:  $\alpha = 0$  is the oil phase,  $\alpha = 1$  is the water phase, and  $0 < \alpha < 1$  denotes the oil-water interface. Then the fluid density and viscosity in the equations are:

$$\rho = (1 - \alpha)\rho_o + \alpha\rho_w \quad (6.6)$$

$$\mu = (1 - \alpha)\mu_o + \alpha\mu_w \quad (6.7)$$

The subscript “o” refers to oil, and the subscript “w” refers to water.  $\alpha$  is calculated from the following advection equation:

$$\frac{\partial \alpha}{\partial t} + \nabla \cdot (\alpha \vec{u}) + \nabla \cdot ((1 - \alpha)\alpha \vec{u}_r) = 0 \quad (6.8)$$

The third term on the left-hand side is the compressive term (with the divergence of the compressive flux); here  $\vec{u}_r = \vec{u}_w - \vec{u}_o$ . This term controls the sharpness of interface.

The level set function  $\Phi$  is defined as the signed distance from the interface, where the interface is the isoline with  $\Phi = 0$ . The initial value of the level set function  $\Phi_0$  is obtained from the initialized volume-of-fluid field, where the interface is defined at  $\alpha = 0.5$ :

$$\Phi_0 = (2\alpha - 1)\Gamma \quad (6.9)$$

$$\Gamma = 0.75\Delta X \quad (6.10)$$

Here  $\Delta X$  is the minimum mesh size near the interface. Thereafter the re-initialization equation is solved to turn the initial level set function into the distance from the interface:

$$\frac{\partial \Phi}{\partial \tau} = \text{sign}(\Phi_0)(1 - |\nabla \Phi|) \quad (6.11)$$

Here  $\tau = 0.1\Delta X$  is the iteration time step of  $\Phi$  and the sign function denotes:

$$\text{sign}(\Phi) = \begin{cases} 1 & \Phi > 0, \text{ water} \\ 0 & \Phi = 0, \text{ interface} \\ -1 & \Phi < 0, \text{ oil} \end{cases} \quad (6.12)$$

Then the interface tension force is calculated as:

$$\vec{F}_\sigma = \sigma \kappa(\Phi) \delta_\phi \nabla(\Phi) \quad (6.13)$$

Here  $\sigma$  is the interface tension and  $\delta_\phi$  is the smoothed delta function:

$$\delta_\phi = \begin{cases} \frac{1}{2\gamma} \left( 1 + \cos\left(\frac{\pi\Phi}{\gamma}\right) \right) & \text{for } |\Phi| < \gamma \\ 0 & \text{elsewhere} \end{cases} \quad (6.14)$$

The quantity  $\gamma$  is the interface thickness coefficient (see Yamamoto et al., 2017) and  $\kappa(\Phi)$  is the interface curvature:

$$\kappa(\Phi) = \nabla \cdot \vec{n}_c \quad (6.15)$$

$$\vec{n}_c = \frac{(\nabla\Phi)_f}{|(\nabla\Phi)_f|} \quad (6.16)$$

Here  $\vec{n}_c$  is the surface unit normal vector. The contact angle  $\theta$  between the interface and the pipe wall is defined as:

$$\cos(\theta) = \vec{n}_c \cdot \vec{n}_w \quad (6.17)$$

With  $\vec{n}_w$  being the unit normal vector at the wall. The contact angle is set to  $90^\circ$  in our simulations. This means that both the level set function  $\Phi$  and the volume fraction of the fluid  $\alpha$  satisfy the zero-gradient condition at the pipe wall boundary.

A pressure drop in the flow direction is added as an extra force term to the right-hand side of equation (6.2), while using periodic boundary conditions on the left and right side of the pipe. Therefore, the pressure that remains in the equations is periodic with respect to the left and right side of the computational pipe section. The initially assumed velocity profile will then develop over time in the transient simulation under this pressure drop until a stable state is obtained. For DNS and LES simulation, the initial velocity is disturbed with given energy spectrum, the built-in utility “Boxturb” in OpenFOAM is used.

A second-order backward implicit time discretization scheme is applied, with a very small time step (small Courant number). This gives a very accurate time integration. For the advection terms in the Navier-Stokes equations we use second order central differences for LES and DNS and limited linear for RANS. For the turbulence model equations, second-order upwind is used for the advection terms. For the interface advection equation the OpenFOAM MULES scheme is used. In all the simulations, periodic boundary conditions are applied on the left and right side of the pipe, which restricts the wave lengths in the axial direction to the domain length divided by an integer value. At the pipe wall, the no-slip condition is imposed. We have used the symmetric PBiCG solver for the velocity and for the turbulent quantities, the GAMG solver for the pressure, and the PIMPLE solver for the velocity-pressure coupling.

### 6.2.3 Considered base conditions

The simulation conditions for two-phase CAF were the same as in the experiments carried out in our lab. The pipe radius is  $R=0.0105$  m (pipe diameter is  $D=21$  mm). The length of the pipe section is set to  $0.0256$  m (25.6 mm), which is twice the most dominant wave length, as estimated from a linear instability analysis (albeit for laminar flow) by Beerens et al. (2014). The fluid properties are set as follows: the oil and water kinematic viscosity are  $\nu_o = 7.73 \times 10^{-4}$  m<sup>2</sup>/s and  $\nu_w = 6.7 \times 10^{-7}$  m<sup>2</sup>/s, the oil and water densities are  $\rho_o = 902$  kg/m<sup>3</sup> and  $\rho_w = 993$  kg/m<sup>3</sup>, and the interfacial tension between oil and water is  $\sigma = 0.016$  N/m (Shell Morlina S2 B 680 at 40 °C was used in the experiments). Note that the ratio between the kinematic viscosities of oil and water is 1150, and the density ratio between the oil and water is  $\rho_o/\rho_w = 0.91$ . The Reynolds number in wall units, i.e.  $Re_\tau = d^+ = u_\tau d/\nu_w$ , is about 150 (here  $u_\tau$  is the wall shear stress velocity and  $d$  is the average thickness of the water annulus). This is above the minimum value of about 90 which is needed to sustain turbulence in single phase channel flow (where  $d$  is half the channel width); this criterion was derived by Jimenez & Moin (1991), who applied DNS to channel flow. The occurrence of turbulence in the water annulus is confirmed in our previous RANS simulations (Li et al. 2020, 2021), which show an inertial sublayer with a maximum turbulent viscosity ( $\nu_t/\nu_w$ ) of about 20.

### 6.2.4 Key parameters

Four important parameters are: the total flow rate, the pressure drop, the watercut, and the water holdup fraction. When two parameters are set as input (e.g. the total flow rate and the watercut in the experiments), the other two will follow as output.

The watercut is defined as the ratio of the water volumetric flow rate and the total volumetric flowrate:

$$WC = Q_w / (Q_o + Q_w) \quad (6.18)$$

where  $Q$  denotes the volumetric flow rate. The water holdup fraction is defined as the ratio of the in-situ water volume in the pipe and the total volume of oil and water:

$$\alpha_w = \frac{V_w}{V_w + V_o} \quad (6.19)$$

A related parameter is the so-called holdup ratio  $h$ , which is defined as:

$$h = \frac{Q_o/Q_w}{V_o/V_w} \quad (6.20)$$

This can also be rewritten as  $h = 1 + u_r/u_w$ . Here the velocity difference  $u_r = u_o - u_w$ , is the apparent (average) slip velocity between the oil core (having a bulk velocity  $u_o$ ) and the water annulus (having a bulk velocity  $u_w$ ). Note that  $h = 1$  if there is no slip between the bulk oil and water velocities. The holdup ratio thus is a measure of the apparent slip between the oil core and the water annulus.

The (total) mixture velocity is defined as:

$$U_{mix} = \frac{Q_w + Q_o}{A_{cross}} \quad (6.21)$$

Here  $A_{cross}$  is the cross-sectional area of the pipe, being equal to  $\pi R^2$  (in which  $R$  is the pipe radius). When waves appear at the liquid-liquid interface, the wave amplitude can be defined as

$$A = \sqrt{2(\delta - \bar{\delta})^2} \quad (6.22)$$

Here  $\delta$  is the instantaneous thickness of the annulus; an overbar denotes the averaged value (in space and time). The amplitude is defined such that it gives the usual value of the amplitude for the case that the wave is a pure sinus (where the amplitude is half the difference between the maximum and the minimum value).

### 6.2.5 Averaging

The first order and second order statistics of the RANS and DNS results will be determined by averaging in the main streamwise direction (i.e. the pipe direction  $x$ ) and in time. This is done as follows.

*(Total) water holdup fraction*

$$\alpha_w = \frac{\iint \alpha \, dxdt}{\iint dxdt} \quad (6.23)$$

Here  $\alpha$  is the local water holdup fraction. Note that the total water holdup fraction  $\alpha_w$  is the same quantity as defined in eq. (6.19).

*(Total) oil holdup fraction*

$$\alpha_o = 1 - \alpha_w = \frac{\iint (1-\alpha) \, dxdt}{\iint dxdt} \quad (6.24)$$

*Mixture velocity*

$$U_m = \frac{\iint u \, dxdt}{\iint dxdt} \quad (6.25)$$

*Superficial water velocity*

$$U_{sw} = \frac{\iint \alpha u \, dxdt}{\iint dxdt} \quad (6.26)$$

*Superficial oil velocity*

$$U_{so} = \frac{\iint (1-\alpha) u \, dxdt}{\iint dxdt} \quad (6.27)$$

*Turbulent kinetic energy*

$$k^+ = \frac{1}{\rho_w u_\tau^2} \left[ \langle \rho \frac{1}{2} (u^2 + v^2 + w^2) \rangle - \langle \rho \rangle \frac{1}{2} (\langle u \rangle^2 + \langle v \rangle^2 + \langle w \rangle^2) \right] \quad (6.28)$$

Here the brackets  $\langle \quad \rangle$  refer to averaging according to:

$$\langle \chi \rangle = \frac{\iint \chi \, dx dt}{\iint dx dt} \quad (6.29)$$

The wall shear velocity  $u_\tau$  appearing in the plus scaling of the turbulent kinetic energy follows from:

$$\rho_w u_\tau^2 = \tau_w = -\frac{R}{2} \frac{dp}{dx} \quad (6.30)$$

Here  $-dp/dx$  is the imposed pressure gradient, and  $\tau_w$  is the corresponding wall shear stress.

Reynolds shear stress

$$\overline{u'_i u'_j}^+ = \frac{1}{\rho_w u_\tau^2} [\langle \rho u_i u_j \rangle - \langle \rho \rangle \langle u_i \rangle \langle u_j \rangle] \quad (6.31)$$

The expressions above apply averaging with respect to the streamwise coordinate  $x$  and the time  $t$ . For simulations without gravity these average quantities will be axi-symmetric, i.e. only dependent on the radial coordinate  $r$ . Therefore for results obtained without gravity, the averaging is also done in azimuthal direction (in addition to averaging over  $x$  and  $t$ ), as this will give a faster convergence of the statistics.

When a turbulence model is used, like the Launder & Sharma low-Reynolds-number  $k - \varepsilon$  model within RANS in the presented study, part of the contribution to the turbulent kinetic energy and to the Reynolds stress is already covered by the closure relations used in the model. However, there is also a part due to the waves moving at the interface. In the presentation of the average RANS results the modeled part and the wave part will be added to give a single value for the (total) turbulent kinetic energy and the (total) Reynolds stress.

## 6.3 RANS and DNS for single phase pipe flow

Both RANS simulations, LES, and DNS were carried out for single-phase water flow through a pipe.

### 6.3.1 DNS at $Re_D=5300$

To validate the performance of OpenFOAM for direct numerical simulation of turbulent flows, first single-phase water pipe flow was tested. The same flow conditions as used by Eggels et al. (1994) are considered. In their case,  $Re_\tau=180$  was simulated, in which the shear-based Reynolds number is defined as  $Re_\tau = u_\tau R / \nu$  (here the wall shear velocity can be expressed as  $u_\tau = \sqrt{\tau_w / \rho}$ , where  $\tau_w$  is the wall shear stress). Eggels et al. used a staggered grid in a pipe section with a length equal to 5 times the pipe diameter. In our simulation, we are using a collocated grid with a pipe section length of 6 times the pipe diameter.  $Re_\tau = 180$  corresponds to a  $Re_D$  value of about 5300. Here  $Re_D = U_m D / \nu$  (in which  $U_m$  is the mean velocity,  $D$  is the pipe diameter, and  $\nu$  is the kinematic fluid viscosity).

To resolve the small-scale turbulent structures in pipe flow, the mesh size needs to be sufficiently small enough. The smallest scale is the Kolmogorov length scale:  $\eta = D \cdot Re_D^{-3/4}$ . For DNS, it is important to solve the turbulent dissipation, in which the energy of the macro structures is cascaded to micro structures. According to Pope (1994), the peak value of the dissipation spectrum is not at  $\eta$  but at  $10 \eta$ , and most of the energy is dissipated at  $3 \eta$ . According to Moin & Mahesh (1998), the required mesh size is also dependent on the numerical method. We have carried out simulations at successively refined meshes and found almost mesh-independent results when using  $\Delta r^+ = 1.3$ ,  $R\Delta\theta^+ = 3.5$ , and  $\Delta x^+ = 4.5$ , as shown in Table 1 (+ values denote  $\nu$  non-dimensionalized with  $\nu$  and  $u_\tau$ ). For the verification of the simulation accuracy, we consider the Fanning friction factor, which is the non-dimensionalized pressure gradient according to:

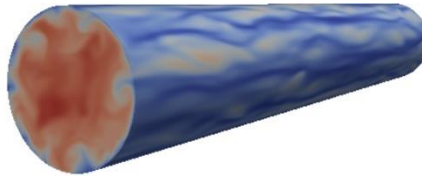
$$f = -\frac{dp}{dx} \frac{R}{\rho u_m^2} \quad (6.32)$$

Table 6.1 shows that the Fanning friction factor as obtained with the present DNS on the finest mesh

is close to the DNS predictions by Eggels et al. (1994), Wu & Moin (2008), and Pirozzoli et al. (2021). The value of  $\Delta r^+$  in the table is the averaged grid cell size in radial direction; in the actual simulation a non-equidistant grid is used which gives its first grid cell even closer to the wall than that value, i.e. well within the viscous sublayer.

A snapshot of the instantaneous streamwise velocity is shown in Figure 6.1. The outer cylindrical plane is close to the wall, and has a dimensionless distance  $(R - r)^+$  of about 7. Low speed streaks can be seen in this plane. In the cross section, according to Eggels et al. (1994), the velocity field is similar to a jet flow hitting the wall, which is due to the “impingent effect”: high-speed fluid from the centre hits the wall, and energy is transferred to the azimuthal and streamwise directions.

Besides the DNS, also LES on coarser mesh and on a fine mesh for the  $Re_\tau=180$  case are done, and the results are also included in Table 1. When using the coarser mesh, the maximum subgrid turbulent viscosity is around 3 times the molecular viscosity. The predicted Fanning friction factor is about 10% lower than the DNS value. Refining the mesh for LES gives the same value of the Fanning friction factor as found with DNS. This is not surprising as LES at a fine mesh gives an almost zero subgrid viscosity.



**Figure 6.1. DNS result for instantaneous streamwise velocity in single phase pipe flow at  $Re_\tau = 180$ .**

**Table 6.1. Fanning friction factor obtained with DNS/LES with different mesh resolutions for single phase pipe flow at  $Re_\tau = 180$ .**

Method	Mesh ( $x, r, \theta$ )	$\Delta x^+$	$\Delta r^+$	$R\Delta\theta^+$	Fanning friction factor
LES – present	80x50x80	27	3.6	14	0.0083
LES – present	240x60x160	9	2.6	7	0.0090
DNS – present	240x60x160	9	2.6	7	0.0091
DNS – present	480x120x320	4.5	1.3	3.5	0.0092
DNS – Eggels et al. (1994)	256x96x128	7	1.9	9	0.0092
DNS – Wu & Moin (2008)	512x256x512	5.3	0.7	2.2	0.0094
DNS – Pirozzoli et al. (2021)	256x67x256	10.5	2.7	4.4	0.0093

Figure 6.2 compares the present DNS results with literature values for the average streamwise velocity (non-dimensionalized with  $u_\tau$ ), the turbulent kinetic energy, and the Reynolds stress. There is very good agreement between the current and existing DNS predictions.

The comparison demonstrates that OpenFOAM code is able to perform rather accurate DNS once a sufficiently fine mesh is used. The LES, when using a coarser grid mesh that captures some subgrid turbulence, a 10% underprediction of the friction factor is found. As this deviation is relatively large, LES will not be used any further for the other (two-phase flow) conditions studied here.

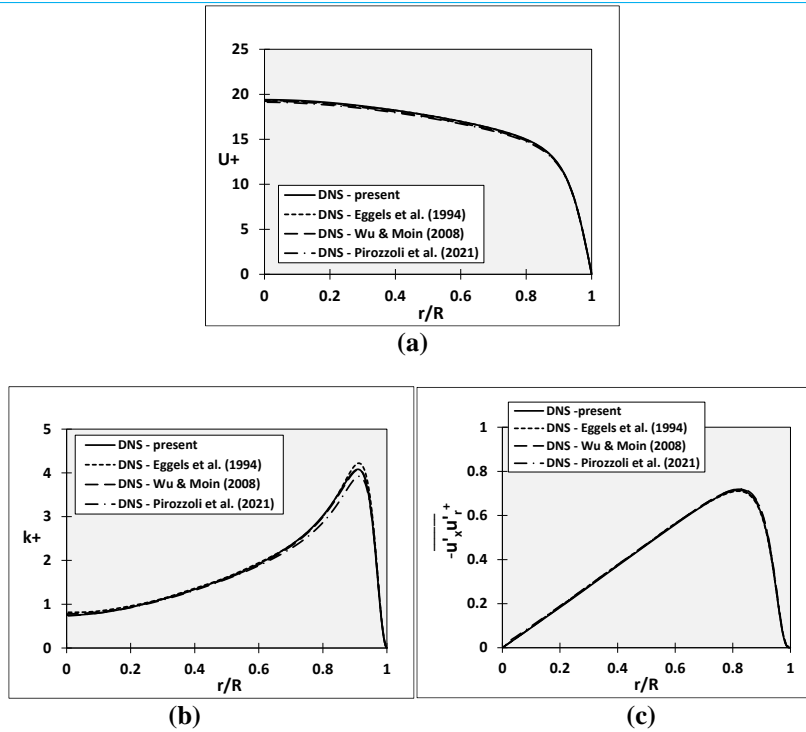


**Figure 6.2.** DNS for single-phase pipe flow at  $Re_\tau = 180$ ; (a) average streamwise velocity, (b) turbulent kinetic energy, (c) Reynolds shear stress.

### 6.3.2 Comparison between DNS/ RANS for single phase pipe flow

RANS with the Launder & Sharma low-Reynolds number  $k - \varepsilon$  model was used to simulate single phase pipe flow at  $Re_\tau = 180$  and 1140, corresponding to  $Re_D$  of about 5300 and 44000, respectively. The RANS results were obtained by solving the 1D axi-symmetric equations on a very fine grid (giving mesh independent results).

The profiles for the average streamwise, the turbulent kinetic energy, and the Reynolds shear stress are compared in Figure 6.3. Note that the DNS at  $Re_\tau = 1140$  were not obtained in the present study but are due to Pirozzoli et al. (2021). Compared to the DNS, RANS significantly underpredicts the turbulent kinetic energy in the boundary layer along the pipe wall, whereas the Reynolds shear stress is in good agreement. At the higher Reynolds number  $Re_\tau = 1140$ , the RANS prediction of the averaged streamwise velocity, non-dimensionalized with the wall shear stress  $u_\tau$ , is close to the DNS profile. For the lower Reynolds number of  $Re_\tau = 180$ , the RANS velocity profile is somewhat above the DNS profile. This is consistent with the lower value of the Fanning friction factor with RANS compared to DNS, as is shown in Figure 6.4. The friction factor with DNS (taken from the literature) is very close to the experiments (also taken from the literature), in a range of Reynolds numbers up to  $Re_D$  of one million. RANS (with Launder & Sharma low-Re  $k - \varepsilon$ ) gives an underprediction of the Fanning friction factor in the lower Reynolds number range. For example, the RANS value for the Fanning friction factor is 0.0078 at  $Re_D = 5300$  versus 0.0092 with DNS (i.e. 15% lower), and 0.0050 at  $Re_D = 44000$  versus 0.0053 with DNS (i.e. 6% lower).

This RANS/DNS comparison for single phase turbulent pipe flow is relevant for understanding core-annular flow with a turbulent annulus, as will be shown in the subsequent paragraphs of this chapter.

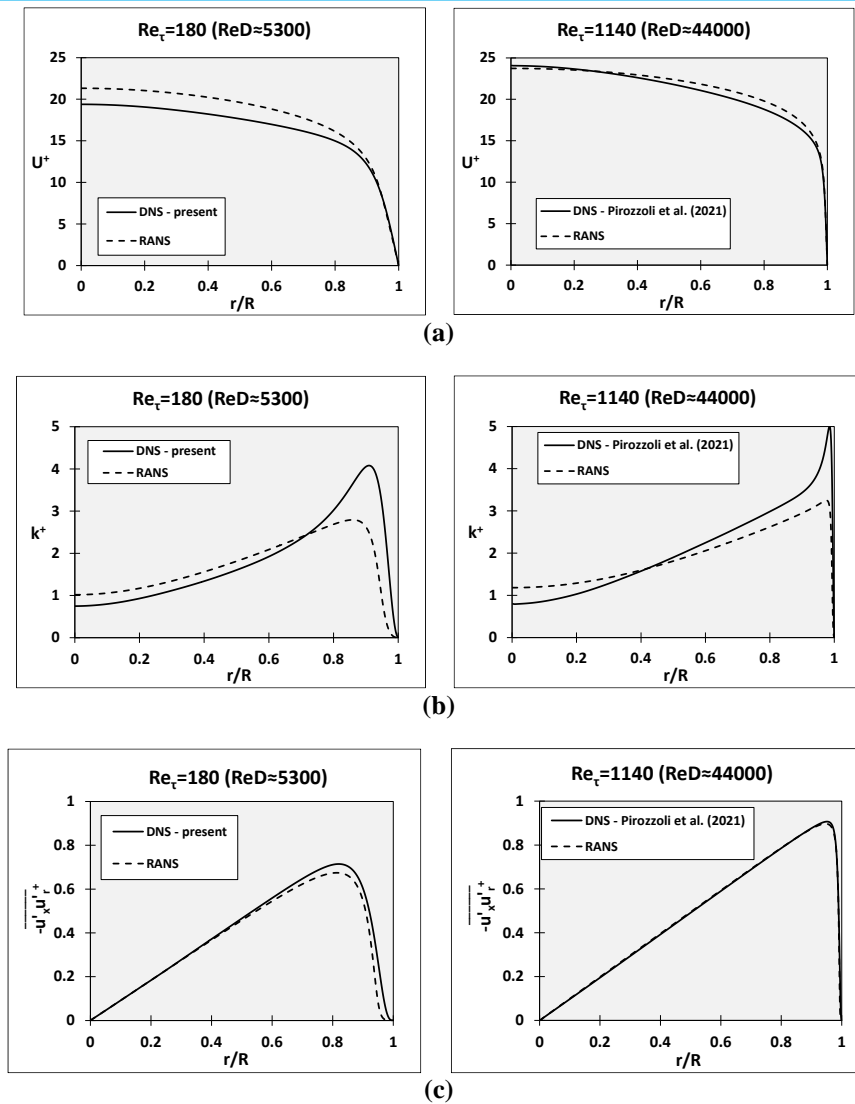


**Figure 6.3.** Comparison between DNS and RANS for single phase pipe flow at  $ReD \approx 5300$  (left graphs) and  $ReD \approx 44000$  (right graphs); (a) average streamwise velocity, (b) turbulent kinetic energy, (c) Reynolds shear stress.



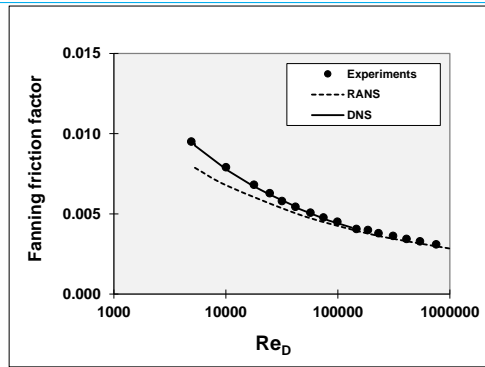


Figure 6.4. Comparison of the Fanning friction factor for single-phase pipe flow.

## 6.4 RANS and DNS for annulus flow with fixed wavy interface

In core-annular flow, interfacial waves appear due to the apparent slip effect between the oil and water. The interfacial waves are important for the oil levitation in a horizontal pipe. To study the interaction of the interface waves and the turbulent annulus, single phase simulations are carried out for the water annulus. This is done by assuming that the oil core moves as a solid body in which the interface appears as a travelling solid wavy wall. The assumption is based on the fact that the oil is around 1000 times more viscous than water.

To perform the single-phase simulation that represents a two-phase problem, a pressure drop term is added to the right-hand side of Eq. 6.2. The pressure drop is calculated at each iteration step in the numerical solver, by balancing the wall shear stress with the pressure drop acting on the whole pipe volume section, i.e. the combination of the simulated turbulent water annulus and the solid oil core. This numerical method has been verified for the RANS model by Li et al. (2021). In this section, the same procedure has been used for DNS in the annulus. The average values obtained with the DNS are compared with the RANS results. Note that gravity effects are ignored which gives concentric average profiles. This approach has the great benefit that only single-phase DNS have to be performed, which is much cheaper than multiphase DNS while it still gives insight in the behaviour of two-phase flow.

### 6.4.1 Geometry and mesh

The geometry for the annulus flow is shown in Figure 6.5; considered is a pipe section in a reference frame that is moving with the oil velocity that is set to 1.3 m/s. This means that the pipe wall in the reference frame is moving with a velocity of -1.3 m/s. The water holdup fraction of the annulus (i.e. the ratio of the annulus area and the pipe cross sectional area) is set to 0.257. A wavy sinusoidal-shaped core is imposed as the inner wall of the annulus. The wavelength and wave amplitude are taken from our previous 2D two-phase RANS simulation results (Li et al., 2022), namely a wave length of 12.8 mm and a wave amplitude  $A=0.71$  mm. The total flow rate is  $0.00043 \text{ m}^3/\text{s}$ , with a 20% watercut. With the pipe radius being the same as our experimental pipe, namely 10.5 mm, this gives a corresponding mixture velocity of 1.24 m/s. With the holdup fraction of 0.257 and the watercut of 20%, the corresponding holdup ratio  $h$  is equal to 1.39. A uniform mesh is applied in the radial, streamwise, and azimuthal directions. Note that because of the curvature of the interface, the radial mesh size is varying along the wave.

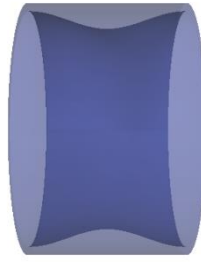


**Figure 6.5. Geometry for the annulus flow with a fixed wavy inner wall.**

To validate the numerical accuracy, several mesh resolutions are simulated. The results for LES, DNS, and RANS on the different meshes are summarized in Table 6.2. Gravity is not included, which means that it suffices to carry out a 2D axisymmetric simulations with RANS. Of course, 3D simulations are required for LES and DNS. Upon mesh refinement, both DNS and RANS give almost mesh independent results, in which the Fanning friction factor with RANS is about 15% lower than with DNS. LES also gives an about 15% lower Fanning friction factor than DNS, unless a very fine mesh is used which gives almost zero subgrid energy and therefore actually is similar to DNS.

The mixture-based Reynolds number,  $Re_D = U_{mix}D/\nu_w$ , for the considered condition is 39000. Single-phase pipe flow at this Reynolds number has a Fanning friction factor of 0.0055, when interpolating within both the DNS and experiments (taken from the literature), shown in Figure 4. For example, the DNS value for the Fanning friction factor for the slightly higher Reynolds number of 44000 is 0.0054 according to both Wu & Moin (2008) and Pirozzoli et al. (2021). The RANS value of single-phase pipe flow at  $Re_D = 39000$  is 0.0052. As shown in Table 2, the DNS value of 0.0055 for water-only pipe flow at  $Re_D = 39000$  is very close to the RANS value of 0.0052 for the annulus and slightly lower than the DNS value of 0.0062 for the annulus.

**Table 6.2: Mesh dependence for single-phase annulus simulations.**

	Mesh (x,r,θ)	Fanning friction factor
LES	75x50x225	0.0047
LES	100x67x300	0.0051
LES	150x100x450	0.0057
DNS	150x100x450	0.0057
DNS	225x150x675	0.0062
DNS	300x200x900	0.0062
RANS	50x100	0.0059
RANS	100x200	0.0054
RANS	200x400	0.0052

### 6.4.2 Averaged flow

Within the moving frame of reference, the 3D unsteady DNS results are averaged in time and in the azimuthal spatial directions to obtain the profiles at the x-coordinates along the wave. The averaged streamwise velocity, turbulent kinetic energy, and Reynolds shear stress are shown in Figure 6.8, both at the x locations where the annulus thickness is minimum and maximum. In addition, also the profiles after streamwise averaging are shown. As expected, the turbulent kinetic energy and Reynolds stress are largest in the thickest part of the water annulus. A good indication of the turbulence level is provided by the local value of the shear-based Reynolds number  $Re_\tau = d^+ = u_\tau d_w / \nu_w$ , in which  $d_w$  is the local water annulus thickness;  $Re_\tau = 66$  at the location where the water annulus is thinnest and 212 at the location where the water annulus is thickest. The higher the value of  $Re_\tau$ , the more turbulent the wall layer will be.

Figure 6.6 also includes the streamwise averaged DNS profiles, using the definitions given in section 6.2.5. The profiles in the annulus close to the pipe wall are in very good agreement with DNS for the single-phase pipe flow as obtained by Pirozzoli et al. (2021) for a slightly higher Reynolds number ( $Re_D = 44000$  instead of 39000)

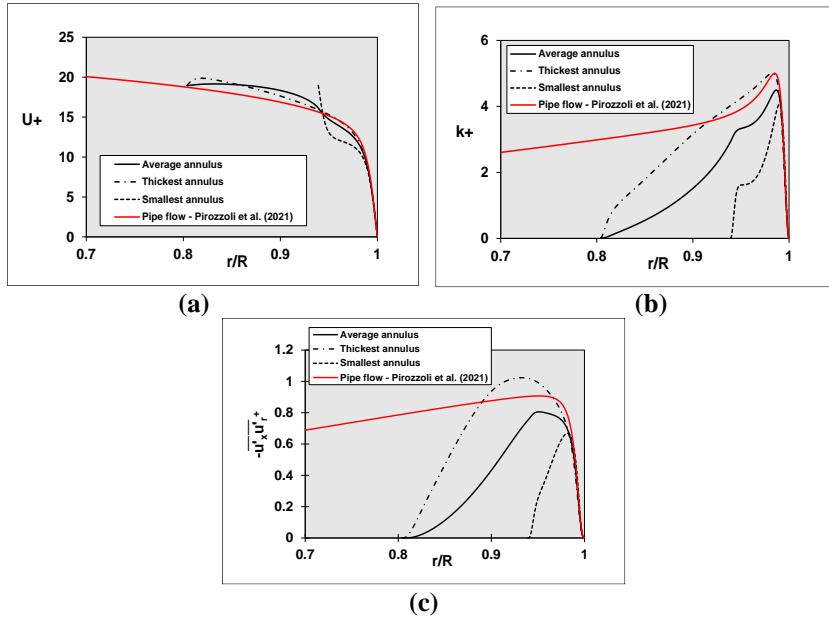


**Figure 6.6.** Single-phase DNS for annulus flow; (a) streamwise velocity, (b) turbulent kinetic energy, (c) Reynolds stress.

The steady state RANS results in the annulus, with respect to the moving frame of reference results, are compared with the average DNS results in Figure 6.7 for the streamlines and in Figure 6.8 for the turbulent kinetic energy. The recirculation zone along the wavy interface is slightly larger in RANS than in DNS, whereas the turbulence level is slightly smaller in RANS than in DNS.

The differences between RANS and DNS can also be examined through considering the streamwise averaged profiles (using the definitions from section 6.2.5). Shown in Figure 6.9 are (DNS as solid line, RANS as dashed line): the superficial velocities, the turbulent kinetic energy, and the Reynolds shear stress. As the wave pattern along the interface is fixed in these simulations, there is a zero wave-induced contribution to the turbulent kinetic energy and to the Reynolds shear stress. RANS and DNS for the superficial velocities almost coincide. The turbulent kinetic energy in RANS is slightly smaller than in the DNS, whereas the Reynolds shear stress is slightly larger.



**Figure 6.7.** Streamlines in averaged results with respect to moving wavy interface in simulations for the annulus; (a) RANS, (b) DNS.

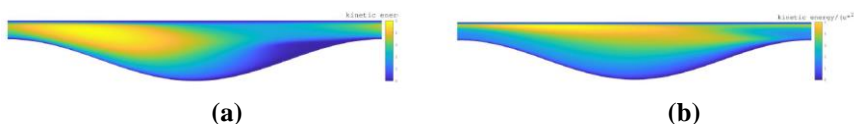
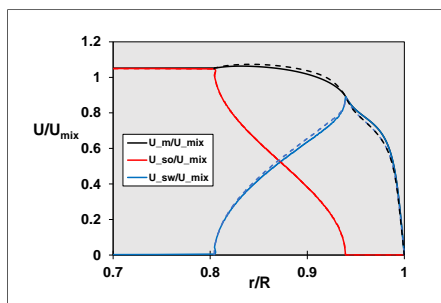
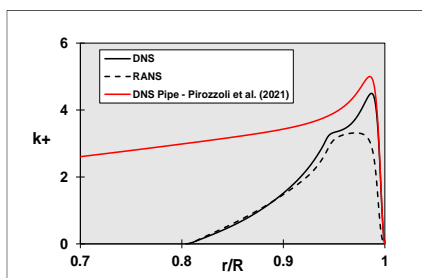


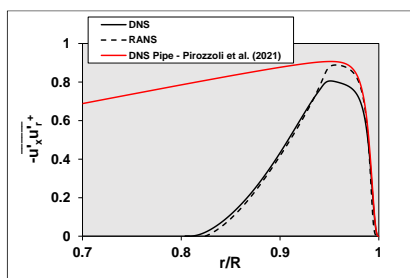
Figure 6.8. Turbulent kinetic energy  $k^+$  with respect to moving wavy interface in simulations for the annulus; (a) RANS, (b) DNS.



(a)



(b)



(c)

Figure 6.11. Comparison of DNS and RANS for single-phase annulus flow; (a) streamwise superficial velocity, (b) turbulent kinetic energy, (c) Reynolds shear stress.

## 6.5 RANS and DNS for two-phase CAF without gravity

3D DNS and 2D axisymmetric RANS simulations are performed for two-phase core-annulus flow. The conditions are the same as in the annulus simulation from the previous section: 12.8 mm pipe section length, 21 mm pipe diameter, 1.24 m/s mixture velocity, 0.257 total water holdup fraction. Gravity was not included yet. The ratio of the length of the water annulus and the averaged thickness of the annulus is about 9, which is expected to be sufficient for the turbulent structures to develop. The mesh resolution in the DNS is  $150 \times 300 \times 450$  in streamwise, radial, and azimuthal direction, respectively. A structured mesh is used in the whole domain. In the pipe centre, the mesh is built in a pentagon shape to avoid a singular mesh. Since only laminar oil goes through this region, the mesh size and shape are of less importance here. In total, 21 million structured grid cells are used in this DNS.

For both RANS and DNS, the resulting values for the Fanning friction factor, the holdup ratio  $h$ , and the wave amplitude  $A$  are given in Table 6.3. The RANS value of 0.0051 for the Fanning friction factor is very close to the value of 0.0052 found for the single-phase annulus flow simulation. The DNS value of 0.0053 value for the Fanning friction factor is smaller than the value of 0.0062 found for the single-phase annulus flow DNS on the finer grids, though it is only relatively little smaller than the value of 0.0057 found on the coarser grid in the single-phase annulus simulation. It is thus quite possible that the finite mesh dependence for the two-phase DNS gives an underprediction of the Fanning friction factor. RANS and DNS values for the holdup ratio and wave amplitude are close.

**Table 6.3. Two-phase core-annular flow without gravity.**

	Mesh (x,r,θ)	Fanning friction factor	h	Wave amplitude A (mm)
<b>DNS</b>	<b>150x300x450</b>	<b>0.0053</b>	<b>1.27</b>	<b>0.78</b>
<b>RANS</b>	<b>200x400</b>	<b>0.0051</b>	<b>1.22</b>	<b>0.73</b>

The averaged DNS and RANS profiles for the two-phase core-annular flow without gravity are compared in Figure 6.10. There is a slight deviation between the two approaches for the superficial velocity. As also found for the single-phase annulus simulations and for the single-phase pipe flow simulations, the RANS prediction for the turbulent kinetic energy is smaller than the DNS prediction. Note that the turbulent kinetic energy and Reynolds stress in RANS now also include a contribution induced by the fluctuating interface wave motion. The Reynolds stress profile in RANS is close to the DNS prediction. The DNS profiles close to the wall in the water annulus are in good agreement with the DNS simulations for the turbulent single-phase pipe flow by Pirozzoli et al. (2021).

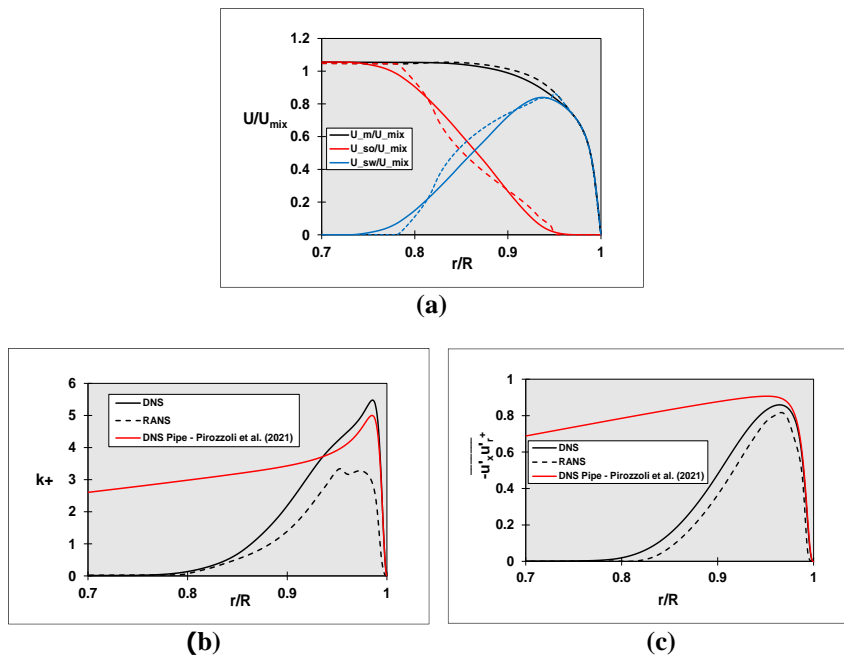


**Figure 6.10. Comparison of DNS and RANS for two-phase core-annular flow without gravity; (a) streamwise superficial velocity, (b) turbulent kinetic energy, (c) Reynolds shear stress.**

The DNS results for the single-phase annulus with imposed wavy interface and for the two-phase core annular flow without gravity are compared in Figure 6.11. Shown are: the water holdup fraction, the superficial velocity, the turbulent kinetic energy, and the Reynolds shear stress. The agreement between the two approaches is very good. Only the turbulent kinetic energy in the two-phase DNS is higher than in the single-phase DNS.

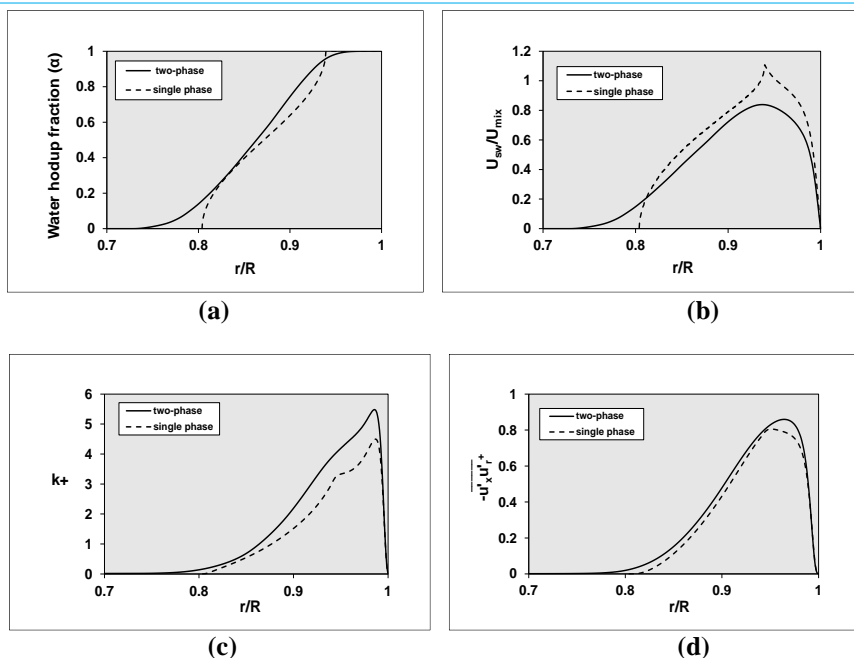


**Figure 6.11. Comparison of single phase and two-phase DNS (without gravity); (a) water holdup fraction, (b) streamwise superficial water velocity, (c) turbulent kinetic energy, (d) Reynolds shear stress.**

The lab experiments for the horizontal core annular flow show a rather concentric flow (i.e. only a small eccentricity due to the density difference between the oil and water). Therefore, it makes sense to compare the oscillations in the thickness of the water annulus at a certain streamwise location, as simulated with the DNS and RANS approach, with the experiments; see Figure 6.12 for the comparison with the experiments in the top and bottom water annulus. The simulated frequency in both DNS and RANS is close to the experimental value. Also the wave amplitude in the simulations (0.78 mm for DNS and 0.73 mm for RANS) is close to the measured value (0.78 mm in the top layer and 1.13 mm in the bottom layer).

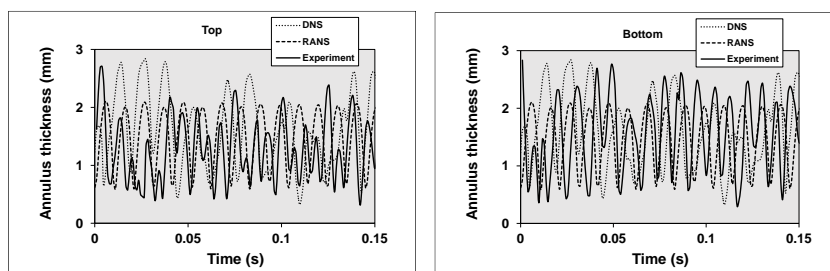


**Figure 6.12. comparison of time dependent thickness of the water annulus for DNS (without gravity), RANS (without gravity), and experiments; (a) top layer, (b) bottom layer.**

## 6.6 RANS, DNS, and experiments for two-phase horizontal CAF with gravity

3D RANS simulations and 3D DNS for two-phase core annular flow were carried out for the same conditions as in the previous sections, but now with inclusion of gravity for the horizontal pipe. The section used in RANS is twice the DNS length (25.6 mm versus 12.8 mm). Due to the difference in

density between the oil and the water (902 versus 993 kg/m<sup>3</sup>) there will be buoyancy to bring the oil core into an eccentric position in the direction of the upper pipe wall. A compensating pressure force will develop along the wavy oil-water interface such that the net upward force at the interface is equal to the downward gravity force of the oil core. In core annular flow an equilibrium will be found at an eccentric location where the top of the oil core still does not wet the upper pipe wall.

The mesh used in DNS is the same as used for the two-phase case without gravity, as presented in the previous section, i.e. 150×300×450 points in streamwise, radial, and azimuthal direction. For the RANS, 100×200×160 points are used. The resulting values for the Fanning friction factor, holdup ratio  $h$ , and the eccentricity  $e$  are summarized in Table 4. The eccentricity is defined as:

$$e = \frac{d_{bottom} - d_{top}}{d_{bottom} + d_{top}} \quad (6.33)$$

Here  $d$  is the averaged thickness of the water annulus. The DNS and RANS results are also compared with experiments obtained for the same conditions in the oil-water flow loop in our lab. The observations are as follows:

- The Fanning friction factor and holdup fraction in the DNS with gravity are very close to the DNS results without gravity (compare Tables 6.3 and 6.4; 0.0052 versus 0.0051). However, DNS with gravity has some eccentricity.
- RANS with gravity has a significantly lower Fanning friction factor than RANS without gravity (0.0042 versus 0.0051)
- The experimental Fanning friction factor is significantly above the DNS and RANS predictions. The experimental flow is much more concentric than the DNS and RANS predictions, though DNS is more concentric (and thus closer to the experiment) than RANS.

**Table 6.4. Fanning friction factor for two-phase core-annular flow with gravity.**

	Mesh ( $x, r, \theta$ )	Fanning friction factor	$h$	Eccentricity
Experiment		0.0077	1.41	0.12
DNS	150×300×450	0.0052	1.29	0.47
RANS	100×200×160	0.0042	1.38	0.73

The superficial velocities in the top annulus, bottom, and side annulus as obtained with RANS and DNS are compared in Figure 6.13. Results are close in the top and side layer, but the deviation is larger in the bottom layer. As shown in Figure 6.14, the same is true for the turbulent kinetic energy in the top and side layer, but a larger deviation is found in the bottom layer. In fact there is a large suppression of the kinetic energy and Reynolds stress for RANS in the bottom layer. The difference seems to be due to the occurrence of oil droplet dispersion in the bottom water annulus, as found for RANS, whereas no dispersion occurs in the DNS. The oil-in-water dispersion in the bottom layer is shown in Figure 6.15. Even though the dispersed oil droplets take a very small amount of volume, the highly viscous droplets cause a suppression of the turbulence and even a locally relaminarized flow. This also explains the reduction in the Fanning friction factor for RANS in the two-phase flow with gravity (as compared to DNS for the same configuration, and as compared to RANS in two-phase flow without gravity).

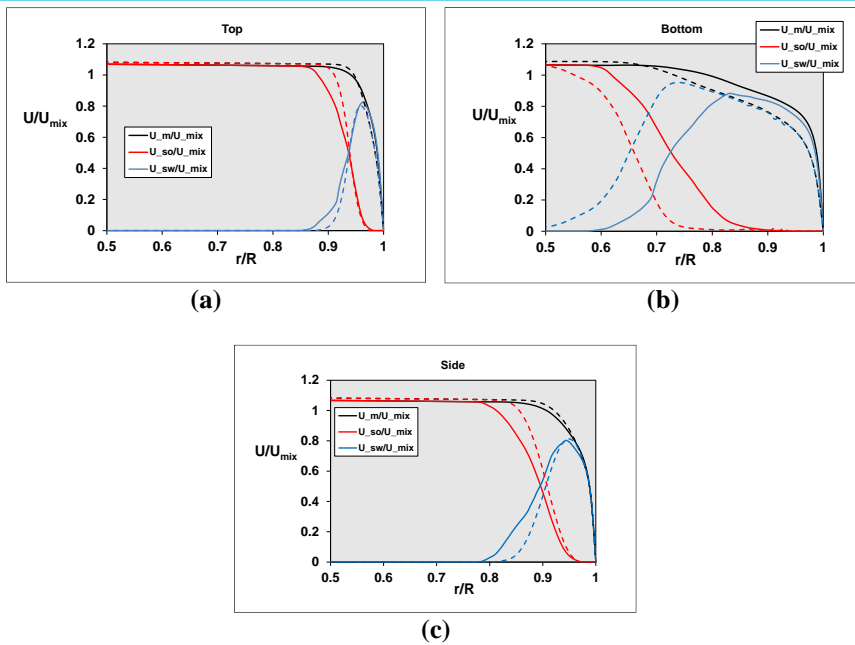


Figure 6.13. Streamwise superficial velocity for two-phase horizontal core-annular flow with gravity (DNS/ solid line and RANS/dashed line); (a) top, (b) bottom, (c) side.

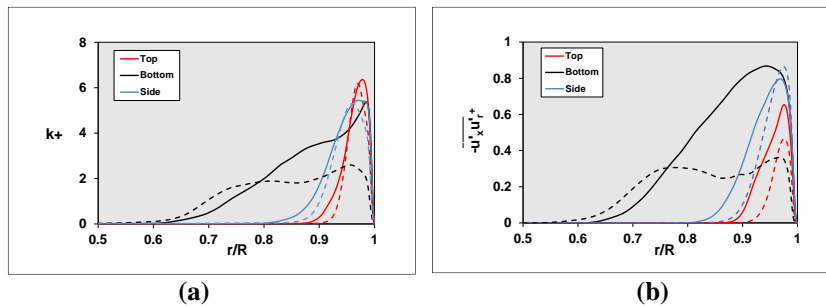


Figure 6.14. (a) Turbulent kinetic energy, and (b) Reynolds shear stress for two-phase horizontal core-annular flow with gravity; DNS/ solid line and RANS/dashed line.

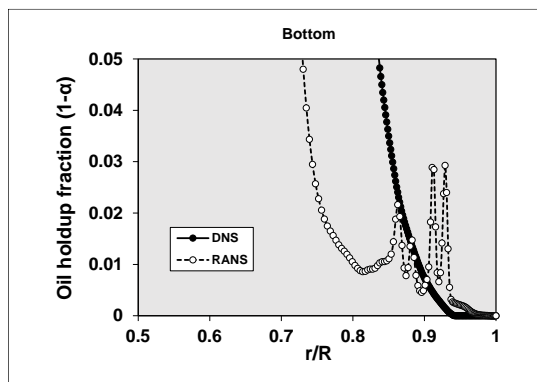
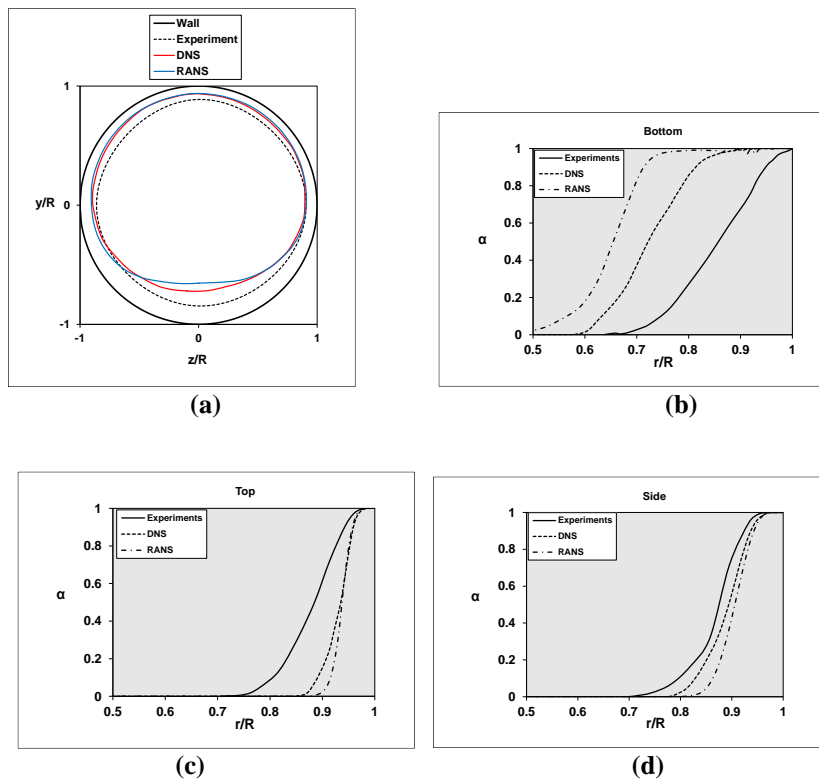


Figure 6.15. Oil holdup fraction in bottom layer for two-phase horizontal core-annular flow with gravity; DNS versus RANS.



Details on the core eccentricity are given in Figure 6.16. Here Figure 6.18a shows the average location of the oil-water interface in the cross-sectional plane (averaging is done in streamwise direction and over time). Figures 6.16b,c,d, show the average water holdup fraction in the cross-sectional plane along a vertical line to the top, vertical line to the bottom, and along a horizontal line to the side, respectively. The RANS and DNS results are relatively close to each other, but there is a significant deviation with the experimental values. Albeit that the DNS values are somewhat closer to the experiments than the RANS values. The deviation between the DNS and experiments is unexpected, as DNS does not contain any closer correlations. There can be a shortcoming in the obtained DNS, in the obtained experiments (or in both). The applied numerical grid may still be insufficient and the experiment may have suffered from insufficient flow control (like a remaining effect of the bend in the pipe upstream of the pipe section). There may also be an effect of the still relatively low turbulence level in the water annulus, giving transitional flow rather than fully developed flow. The higher Fanning friction factor in the experiments than in the simulations can be due to a higher turbulence level in the experiment, which can in turn have an effect on the core position. The tendency of laminarization in the simulations may enhance the difference in flow in the top and bottom annuli, leading to an increase in eccentricity.



**Figure 6.16. Interface location and water holdup fraction ( $\alpha$ ) for two-phase horizontal core-annular flow with gravity; (a) interface location, (b) water holdup fraction in bottom layer, (c) water holdup fraction in top layer, (d) water holdup fraction in side layer.**

Finally, Figure 6.17 compares the time evolution of the thickness of the water annulus at the top and bottom (at a fixed streamwise location), comparing the simulations (RANS and DNS) with the experiments. In fact the agreement for the fluctuating annulus thickness between the simulations and experiments is less good for the simulations with gravity (i.e. with eccentricity, shown in Figure 6.17) than for the simulations without gravity (i.e. concentric, shown in Figure 6.12).

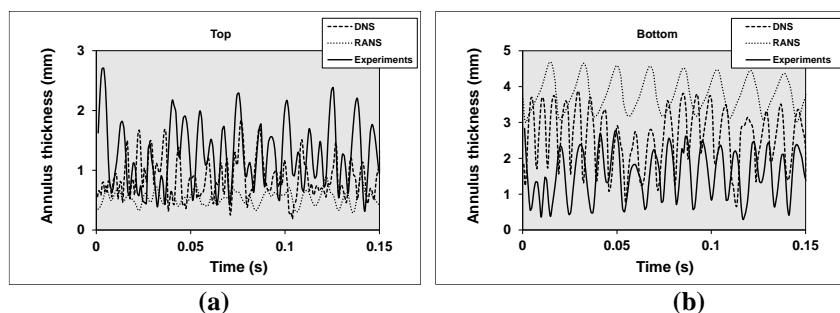


**Figure 6.17. Time-dependent annulus thickness for two-phase horizontal core-annular flow with gravity; (a) top layer, (b) bottom layer.**

## 6.7 Conclusions

DNS, LES, and RANS simulations were carried out for core-annular flow in a horizontal pipe and results were compared with experiments carried out with water and oil in our lab. The main conclusions are the following:

- Very good agreement of the present DNS for single-phase pipe flow with benchmark values available in the literature. LES on a coarse mesh with some finite subgrid energy gives a 10% lower value of the friction factor than DNS, and is therefore not a very attractive method for turbulent pipe flow modelling. Compared to DNS and experiments, RANS (with Launder & Sharma low- $Re$   $k - \varepsilon$ ) gives an underprediction of the Fanning friction factor by 6% at  $Re_D = 44000$ . Compared to the DNS, RANS significantly underpredicts the turbulent kinetic energy in the boundary layer along the pipe wall, whereas the Reynolds shear stress is in good agreement.
- Simulating the single-phase water annulus with an imposed wavy interface is an attractive method to get insight into core-annular flow, without the need to carry out two-phase simulations. In this way very accurate 2D RANS and 3D DNS results could be obtained. The considered mixture-based Reynolds is  $Re_D = 39000$ . The DNS value of 0.0055 for water-only pipe flow at this Reynolds number is very close to the RANS value of 0.0052 for the annulus and slightly lower than the DNS value of 0.0062 for the annulus. The recirculation zone along the wavy interface is slightly larger in RANS than in DNS, whereas the turbulence level is slightly smaller in RANS than in DNS. As the wave pattern along the interface is fixed in these simulations, there is a zero wave-induced contribution to the turbulent kinetic energy and to the Reynolds shear stress. RANS and DNS for the superficial velocities almost coincide. The turbulent kinetic energy in RANS is slightly smaller than in the DNS, whereas the Reynolds shear stress is slightly larger.
- 3D DNS and 2D axisymmetric RANS simulations were performed for two-phase core-annular flow without gravity (i.e. with a concentric oil core). The DNS value of 0.0053 value for the Fanning friction factor is smaller than the value of 0.0062 found for the single-phase annulus flow DNS on the finer grids, though it is only relatively little smaller than the value of 0.0057 found on the coarser grid in the single-phase annulus simulation. It is thus quite possible that the finite mesh dependence for the two-phase DNS gives an underprediction of the Fanning friction factor. There is a slight deviation between RANS and DNS for the superficial velocity. As also found for the single-phase annulus simulations and for the single-phase pipe flow simulations, the RANS prediction for the turbulent kinetic energy is smaller than the DNS prediction. The Reynolds stress profile in RANS is close to the DNS prediction. There is close agreement

- between the averaged velocity and turbulence profiles obtained in the two-phase (core-annulus) and the single-phase (annulus) approaches.
- 3D DNS and 3D RANS simulations were performed for two-phase core-annular flow in a horizontal pipe with gravity (i.e. with an eccentric oil core). The Fanning friction factor for the DNS with and without gravity are very close (0.0052 versus 0.0051), but RANS with gravity gives a significantly lower value than found without gravity (0.0042 versus 0.0051). The difference seems to be due to the occurrence of oil droplet dispersion in the bottom water annulus, as found for RANS, whereas no dispersion occurs in the DNS. The highly viscous droplets cause a suppression of the turbulence and even local relaminarization.
  - The experimental Fanning friction factor is significantly above the DNS and RANS predictions (0.0077 in the experiments versus 0.0052 in the DNS). The experimental flow is much more concentric than the DNS and RANS predictions, though DNS is more concentric (and thus closer to the experiment) than RANS. The cause for the differences between simulations and experiments is not clear yet. It might be due to the still relatively low turbulence level in the water annulus, giving transitional flow rather than fully developed flow. The higher Fanning friction factor in the experiments than in the simulations can be due to a higher turbulence level in the experiment, which can in turn have an effect on the core position.

## References

- Bai, R., Kelkar, K., Joseph, D.D., 1996. Direct simulation of interfacial waves in a high-viscosity-ratio and axisymmetric core-annular flow. *J. Fluid Mechanics* 327, 1-34.
- Beerens, J.C., Ooms, G., Pourquié, M.J.B.M., 2014. A comparison between numerical predictions and theoretical and experimental results for laminar core-annular flow. *AIChE Journal* 60, 3046-3056.
- Buckley, M.P., Veron, F., 2016. Structure of the airflow above surface waves. *Journal of Physical Oceanography* 46, 1377-1397.
- Eggels, J.G.M., Unger, F., Weiss, M.H., Westerweel, J., Adrian, R.J., Friedrich, R., Nieuwstadt, F.T.M., 1994. Fully developed turbulent pipe flow: a comparison between direct numerical simulation and experiment. *J. Fluid Mech.* 268, 175-210.
- Ghosh, S., Das, G., Das, P.K., 2010. Simulation of core annular downflow through CFD – a comprehensive study. *Chem. Engng Process.* 49, 1222-1228.
- Ghosh, S., Mandal, T.K., Das, P.K., 2009. Review of oil water core annular flow.” *Renewable and Sustainable Energy Rev.* 13, 1957-1965.
- Huang, A., Christodoulou, C., Joseph, D.D., 1994. Friction factor and hold up studies for lubricated pipelining part. 2: Laminar and k-epsilon models of eccentric core flow. *Int. J. Multiphase Flow* 20, 481-491.
- Ingen Housz, E.M.R.M., Ooms, G., Henkes, R.A.W.M., Pourquie, M.J.B.M., Kidess, A., Radhakrishnan, R., 2017. A comparison between numerical predictions and experimental results for core-annular flow with a turbulent annulus, *Int. J. Multiphase Flow* 95, pp. 271-282.
- Jiménez, J., Moin, P., 1991. The minimal flow unit in near-wall turbulence. *J. Fluid Mechanics* 225, 213-240.
- Joseph, D.D., Bai, R., Chen, K.P., Renardy, Y.Y., 1997. Core-Annular Flows. *Annual Review of Fluid Mechanics* 29, 65-90.
- Kang, M., Shim, H., Osher, S., 2007. Level set-based simulations of two-phase oil–water flows in pipes. *Journal of Scientific Computing* 31, 153-184.
- Kim, K., Choi, H., 2018. Direct numerical simulation of a turbulent core-annular flow with water-lubricated high viscosity oil in a vertical pipe. *J. Fluid Mech.* 849, 419-447.
- Ko, T., Choi, H.G., Bai, R., 2002. Finite element method simulation of turbulent wavy core–annular flows using a k-omega turbulence model method. *Int. J. Multiphase Flow* 28, 1205-1222.
- Launder, B.E., Sharma, B.T., 1974. Application of the energy dissipation model of turbulence to the calculation of flow near a spinning disc. *Lett. Heat and Mass Transfer* 1, 131-138.
- Li, H., Pourquié, M.J.B.M., Ooms, G., Henkes, R.A.W.M. 2021. Simulation of turbulent horizontal oil-water core-annular flow with a low-Reynolds number  $k - \epsilon$  model. *Int. J. Multiphase Flow* 142, 103744.
- Li, H., Pourquié, M.J.B.M., Ooms, G., Henkes, R.A.W.M. 2022. Simulation of turbulent annulus with interfacial waves in core-annular pipe flow. *Int. J. Multiphase Flow* 154, 104152.
- Li, H., Pourquié, M.J.B.M., Ooms, G., Henkes, R.A.W.M. 2023a. Simulation of vertical core-annular flow with a turbulent annulus. *Int. J. Multiphase Flow* 167, 104551.
- Li, H., Pourquié, M.J.B.M., Ooms, G., Henkes, R.A.W.M. 2023b. Interfacial wave growth for core-annular pipe flow with a turbulent annulus. Submitted for publication.
- Li, J., Renardy, Y., 1999. Direct simulation of unsteady axisymmetric core–annular flow with high viscosity ratio. *J. Fluid Mechanics* 391, 123-149.
- Moin, P., Mahesh, K., 1998. Direct numerical simulation: a tool in turbulence research. *Annual Review of Fluid Mechanics* 30, 539-578.
- Nicoud, F., Ducros, F., 1999. Subgrid-scale stress modelling based on the square of the velocity gradient tensor. *Flow, Turbulence and Combustion* 62, 183-200.
- Ooms, G., Pourquié, M., Beerens, J. C., 2013. On the levitation force in horizontal core-annular flow with a large viscosity ratio and small density ratio. *Physics of Fluids* 25, 032102.
- Pirozzoli, S., Romero, J., Fatica, M., Verzicco, R., Orlandi, P., 2021. One-point statistics for turbulent pipe flow up to  $Re_\tau \approx 6000$ . *J. Fluid Mech.* 926, 355-377.

- Pope, S.B., 2000. *Turbulent Flows*. Cambridge University Press.
- Wu, X., Moin, K., 2008. A direct numerical simulation study on the mean velocity characteristics in turbulent pipe flow. *J. Fluid Mech.* 608, 81-112.



# 7

## Conclusions and recommendations

## 7.1 Conclusions

The main purpose of this thesis is to use CFD tools to understand the physics of the multiphase liquid-liquid laminar-turbulent flow in a pipeline, known as Core-Annular Flow (CAF). That means finding the correlations between the major hydraulic parameters: pressure drop, holdup ratio, watercut and total flow rate. Also, assessing the performance of using RANS or DNS for the turbulent annulus flow. The simulation results were compared with both the existing literature and new experiments carried out in the Delft lab. The RANS approach applied the Launder & Sharma low-Reynolds number  $k-\epsilon$  model. OpenFOAM was used for the CFD simulations with RANS and DNS. In addition also a dedicated MATLAB model was used for 1D RANS.

For horizontal pipe flow, the base case configuration as used in the lab experiment was also used in most of the simulations, that is: pipe diameter of 21 mm, kinematic oil viscosity of  $7.744 \times 10^{-4} \text{ m}^2/\text{s}$ , oil density of  $901.49 \text{ m}^3/\text{s}$ , kinematic water viscosity of  $6.738 \times 10^{-7} \text{ m}^2/\text{s}$ , water density of  $993.15 \text{ m}^3/\text{s}$ , total flow rate of  $4.3 \times 10^{-4} \text{ m}^3/\text{s}$  and watercut of 20%. In the considered base case, the oil core is laminar and the water annulus is turbulent. In addition to the base case, also parameter variations were carried out. Various kinds of simulations were done: 1D/2D/3D two-phase RANS, 3D DNS for two-phase core-annular flow with and without gravity, 2D/3D single-phase RANS for the annulus flow, and 3D single-phase DNS for the annulus flow. For vertical pipe flow, the conditions of Kim & Choi (2018) were used, that is: pipe diameter of 27.6 mm, oil density of  $963 \text{ m}^3/\text{s}$ , oil dynamic viscosity of  $17.6 \text{ Pa.s}$ , water density of  $998 \text{ m}^3/\text{s}$  and dynamic water viscosity of  $0.001 \text{ Pa.s}$ .

The coupled level set and volume of fluid method (LSVOF) was used to capture the interface. The level set method (LS) can keep the interface sharpness, but can give volume loss. The volume of fluid method (VOF) conserves the volume well but tends to smear out the interface and causes heavy oil dispersion. The LSVOF method is able to combine the advantages of both methods: sharpening the interface while at the same time conserving the volume of each of the phases. The mesh was refined in steps to guarantee numerical accuracy. The velocity profile in streamwise direction shows the logarithmic law in the annulus flow near the pipe wall. The turbulence is damped towards the interface, and the flow becomes laminar in the oil core. In the simulations, regular traveling waves were observed. The wave velocity was found to be close to the mixture velocity. Within the reference frame linked to the travelling waves at the interface, the streamlines and turbulent statistics become almost steady. A flow recirculation was found near the wave trough. A certain amount of annulus liquid is encapsulated near the wave trough, and this travels with about the velocity of the oil core. Therefore, compared to a flat interface or an interface with a very small amplitude wave, the presence of interface waves will decrease the water holdup (or the holdup ratio), which gives less apparent slip between the oil and water flows. The resulting higher water velocity gives a higher pressure drop (or higher friction factor) for a wavy interface than found for perfect CAF.

The 1D results represent perfect turbulent CAF (i.e. no gravity, no interfacial waves), the 2D results represent axi-symmetric CAF (i.e. no gravity, with interfacial waves), and the 3D results represent eccentric CAF (i.e. with gravity, with interfacial waves). The simulation results typically show a turbulent water annulus in which the structure of the (high-Reynolds number) inertial sublayer can be recognized. The inertial sublayer scaling (using wall units) was demonstrated to be present for the streamwise velocity, for the turbulent viscosity, for the turbulent kinetic energy, and for the turbulent energy dissipation. However, as the shear-based Reynolds number is limited, also the extent of the inertial sublayer is limited. The 2D and 3D RANS results for the interfacial waves show that the waves are travelling with a practically constant wave velocity. This means that the temporal and spatial results can be converted into one another using this convective velocity. It also means that an observer traveling with the waves will see an almost steady flow. The turbulence is highest at the streamwise location where the water annulus is thickest (i.e. at the trough location of the wave) and



lowest at the location where the water annulus is thinnest (i.e. at the crest location of the waves). With respect to the travelling waves, a water recirculation zone is found in between the successive crest locations.

A review of different sets of lab data for core-annular flow shows that the Fanning friction factor for the wall, which makes the pressure drop dimensionless with the dynamic pressure based on water density and mixture velocity, is an attractive parameter. In the experiments available for CAF in the literature, that friction factor is close to the value found for turbulent water-only pipe flow, and almost independent of the watercut. Our simulations have shown that unless the waves are absent or the imposed wave amplitude is very small, travelling waves easily create sufficient stress on the water annulus, such that it is apparently felt by the pipe wall as a fully turbulent single-phase water flow. A force balance for core annular flow was considered, which includes the wall friction between the water annulus and pipe wall and the interfacial stress between the oil core and water annulus. The wall friction and interfacial stress were determined from the RANS simulations. The interfacial stress will be dependent on length and amplitude of the waves at the interface. Details could be simulated through considering a single-phase RANS model for the water annulus with imposed waviness on a moving wall. Most of the interfacial stress is due to form drag (with local water recirculation zones with respect to an observer travelling with the waves) and only a small part is due to shear stress. The water holdup fraction for core-annular flow closely agrees with the value found for the so-called “water equivalent flow” (i.e. single-phase water pipe flow, with an artificial split between a water core and a water annulus). A good estimate of the frictional pressure drop and holdup ratio of core annular flow with a turbulent water annulus is to take the Fanning friction factor the same as the well-known value for water only pipe flow and the holdup ratio the same as for the equivalent water flow.

Detailed numerical simulations were carried out for the wave initiation, growth, and saturation at the oil-water interface in core-annular flow. The simulated growth rates for the laminar-laminar case are in very good agreement with values obtained in the linear stability analysis by Li & Renardy (1999). The maximum wave growth rate for a turbulent water annulus is significantly higher than for a laminar water annulus. A range of waves is found in the experiment, albeit with a clear dominant wave length. Applying the energy balance to the simulation results shows that linear wave instability at the interface is due to inertia in the turbulent case, and due to viscous effects in the laminar case. Both in the simulations and in the experiments, the most unstable wave length decreases with decreasing water holdup fraction (or decreasing watercut). The most unstable wave length in the simulations is slightly smaller than in the experiments. The experiments could be used to construct the probability density function of the wave length distribution. Both in the simulations and in the experiments, the wave amplitude increases with increasing wave length, up to a certain maximum level for the longest waves. There is a reasonably good agreement between the amplitudes of the different wave lengths as found in the experiments and in the simulations.

The DNS by Kim & Choi for vertical core-annular flow are numerically very accurate and can be used for benchmarking of the RANS turbulence model. The high viscosity ratio used in the DNS and experiments led to the numerical instability in the RANS simulations, and therefore a lower ratio had to be used. Through sensitivity simulations (in which the viscosity ratio was changed) it was shown that the simulation results are not significantly dependent on the viscosity ratio. The Fanning friction factor with RANS is 18% lower than with DNS, whereas the holdup ratio with RANS is only slightly higher than with DNS (i.e. it has a slightly larger tendency to accumulate water in RANS than in DNS). The waves found with RANS are more regular and shorter than in DNS; RANS gives a dominant wave, whereas DNS show a spectrum of waves. Also, the average amplitude of the waves with RANS is smaller than in DNS. In a range of water holdup fractions, the Reynolds stress is significantly lower with DNS than with RANS. Despite the shortcomings of the considered Launder

& Sharma low-Reynolds number  $k$ - $\epsilon$  model in RANS, in comparison to DNS, the RANS approach properly describes the main flow structures for upward moving core-annular flow in a vertical pipe.

3D DNS and 2D RANS were carried out for the base case configuration from the Delft lab, though firstly without inclusion of gravity (i.e. concentric oil core). Both single-phase flow simulations were carried out for only the water annulus (with imposed interface) and two-phase flow simulations for the oil core with water annulus. The RANS prediction for the Fanning friction factor following from the single-phase annulus simulation is 16% lower than the DNS value. The RANS prediction for the turbulent kinetic energy is smaller than the DNS prediction. The Reynolds stress profile in RANS is close to the DNS prediction. There is close agreement between the averaged velocity and turbulence profiles obtained in the two-phase (core-annulus) and the single-phase (annulus) approaches.

Finally, 3D DNS and 3D RANS simulations were performed for two-phase core-annular flow in a horizontal pipe with gravity (i.e. with an eccentric oil core), using the base case conditions from the Delft experiment. The Fanning friction factor for the two-phase DNS with and without gravity are very close (0.0052 versus 0.0051), but RANS with gravity gives a significantly lower value than found without gravity (0.0042 versus 0.0051). The difference seems to be due to the occurrence of oil droplet dispersion in the bottom water annulus, as found for RANS, whereas no dispersion occurs in the DNS. The highly viscous droplets cause a suppression of the turbulence and even local relaminarization. The experimental Fanning friction factor is significantly above the DNS and RANS predictions (0.0077 in the experiments versus 0.0052 in the DNS; i.e. 30% higher experimental value). The experimental flow is much more concentric than the DNS and RANS predictions, though DNS is more concentric (and thus closer to the experiment) than RANS. The cause for the differences between simulations and experiments is not clear yet. It might be due to the still relatively low turbulence level in the water annulus, giving transitional flow rather than fully developed flow. The higher Fanning friction factor in the experiments than in the simulations can be due to a higher turbulence level in the experiment, which in turn can influence the core position.

## 7.2 Recommendations

Core-annular flow is an interesting and complex flow pattern, which has been studied a lot over the past decades. The present study has contributed to a better understanding of such flow, particularly in the presence of interface waves and a turbulent water annulus. But the current study is by no means complete, and more work can be done for further reference. Recommended research topics are the following:

- We found that the form drag caused by the high amplitude of the interface waves is the major contributor to the pressure drop for the oil core, while the shear stress at the interface only plays a minor role. The majority of empirical models in the literature were developed based on only an (effective) interfacial stress approach with a friction-based correlation. Further work to properly take into account the effect of the form drag in the correlations can be undertaken.
- From our current study, the RANS and DNS both predict a much higher eccentricity and a lower Fanning friction factor than the experiment. This can be due to the difference in the details of the pipe configurations. In the experiment, we used an 8 m long pipe loop with bend, and CAF is initiated by a special inlet nozzle where oil and water enter the pipe separately. In the simulations, we use a short pipe section of 25.8 mm length with periodic boundary conditions, and the initial condition is a perfect CAF (or PCAF) with a flat interface. The difference between the configurations may cause a different turbulence behaviour (particularly due to possible laminar-turbulent transition effects) and a different core position (due to a possible remain in g bend effect). There thus is a need for additional experiments and simulations to resolve the observed

deviations.

- Our current numerical method is not able to simulate very high oil viscosities, such as the value of 17.6 Pa s for the oil used in the DNS for vertical CAF by Kim & Choi (2018). Further improvement of the numerical method used in the applied OpenFOAM tool is thus needed.
- The main barrier for the current 3D RANS simulation for horizontal CAF (with gravity) is the occurrence of oil dispersion as droplets into the water annulus. The small volume of oil droplets in the water layer can have a large influence on the flow due to the much higher viscosity of the oil than of the water. Therefore, the local annulus flow is relaminarized, and the wave form changes. Probably due to the use of a uniform mesh close to the interface, DNS does not show the oil dispersion. However, the computational costs for this are high. A more efficient numerical scheme is required that also prevents the numerical dispersion of oil droplets at the interface for RANS.



# Appendix

**A.**

Flow envelope

## A.1 Introduction

Core-annular flow is a typical two-phase flow pattern in pipeline transport, where the oil core is surrounded by a thin lubricating water annulus. This type of flow pattern decreases the pressure drop dramatically especially for highly viscous oil. Core-annular flow has been applied for transporting highly viscous oil in the industry in a few cases to reduce the required pump capacity, as reviewed by Joseph et al. (1997).

Four parameters (namely: oil flow rate, water flow rate, pressure drop and water holdup fraction) are involved in the study of core-annular flow. Ullmann & Brauner (2004) developed a simple physical model based on the two-fluid approach, in which the pressure drop and water holdup are predicted based on given oil and water flow rates and their thermodynamic properties. Various experimental/modelling studies have been performed regarding the most appropriate modelling parameters. For example, Arney et al. (1993) defined a reduced Reynolds number to predict the pressure drop. Tripathi et al. (2017) studied the influence of interfacial waves on the pressure drop.

Most available numerical studies for core-annular have focused on vertical flow. Recently, Kim & Choi (2018) carried out DNS for a vertical pipe. For horizontal core-annular flow, due to the buoyancy acting perpendicular to the pipe axis, interfacial waves play an important role to provide the levitation, as studied for example by Ooms et al. (1984). Furthermore, Ooms et al. (2013) performed simulations for laminar horizontal core-annular flow to study the levitation physics. Li et al. (2021) carried out RANS simulations for the horizontal core-annular flow where the water annulus remained turbulent, and they studied the levitation physics related to the interfacial waves.

This chapter focuses on the numerical simulation of both 2D axi-symmetric two-phase core-annular flow and 3D single-phase annulus flow. The simulation set up is based on experiments by Van Duin et al. (2017) in a horizontal pipe at 40 °C where the viscous oil core is laminar and the water annulus is turbulent. For the 2D, two-phase simulations, with respect to the numerical interface tracking, the Coupled Level Set and Volume of Fluid (CLSVOF) method is found to be quite adequate. With this method, the numerical oil dispersion is much smaller than what is found with the Volume of Fluid (VOF) method. For 3D, single-phase simulations, we assume a highly viscous oil core to appear as a solid inner wall, and the single phase solver is modified so that the shear force properly balances the pressure force on the solid “oil core”. The numerically found relationship between the four hydraulic parameters is also compared with the physical model developed by Ullmann & Brauner (2004). In addition, single-phase DNS are performed for the 3D geometry. A comparison is made between the RANS and DNS results.

## A.2 Governing equation and numerical method

### A.2.1. Governing Equations

The mass and momentum conservation equations for an incompressible, isothermal fluid are :

$$\nabla \cdot \vec{u} = 0 \quad (\text{A.1})$$

$$\frac{\partial(\rho \vec{u})}{\partial t} + \nabla \cdot (\rho \vec{u} \vec{u}) = -\nabla p + \nabla \cdot (\mu(\nabla \vec{u} + \nabla \vec{u}^T)) + \rho \vec{g} + \vec{F}_\sigma \quad (\text{A.2})$$

Where  $\vec{u}$  is the velocity vector,  $\rho$  and  $\mu$  are the fluid density and viscosity, respectively.  $\vec{g}$  is the gravitational acceleration,  $p$  is the pressure and  $\vec{F}_\sigma$  is the interfacial tension force.

### A.2.2. Numerical method

#### A.2.2.1. Interface capturing method

In multiphase flow simulations, interface capturing is the most important and challenging part. In our

study of highly viscous oil-water core annular flow, the viscosity ratio between oil and water can be larger than 1000. When using the Volume of Fluid method, the numerical dispersion of oil through the interface can cause a large increase of the fluid viscosity in the water annulus, which can thus give a large inaccuracy in the prediction of the relationship between the flow rate and pressure drop. The Coupled Level Set and Volume of Fluid (CLSVOF) method, however, can overcome this problem. In the CLSVOF method, the level set function is used to calculate the surface tension and it smoothens the interface. In this way, a good numerical result is found in our study, as will be shown in a later section.

The CLSVOF solver, which was developed by Yamamoto et al. (2017), is based on the Volume of Fluid (VOF) solver in the “InterFoam” package in OpenFOAM. Starting from the VOF method, the volume fraction  $\alpha$  is introduced to distinguish between the two fluid phases:  $\alpha = 0$  is the oil phase,  $\alpha = 1$  is the water phase, and  $0 < \alpha < 1$  denotes the oil-water interface. Then the fluid density and viscosity in Equation A.2 are:

$$\rho = (1 - \alpha)\rho_o + \alpha\rho_w \quad (\text{A.3})$$

$$\mu = (1 - \alpha)\mu_o + \alpha\mu_w \quad (\text{A.4})$$

$\alpha$  is calculated from the advection equation:

$$\frac{\partial \alpha}{\partial t} + \nabla \cdot (\alpha \vec{u}) + \nabla \cdot ((1 - \alpha)\alpha \vec{u}_r) = 0 \quad (\text{A.5})$$

The third term on the left-hand side is the compressive term, in which  $\vec{u}_r = \vec{u}_w - \vec{u}_o$ . The level set function  $\Phi$  is initialized by using the volume of fluid function, in which the interface is defined as the location with  $\alpha=0.5$ :

$$\Phi_0 = (2\alpha - 1)\Gamma \quad (\text{A.6})$$

$$\Gamma = 0.75\Delta X \quad (\text{A.7})$$

Here  $\Delta X$  is the minimum mesh size. Thereafter the re-initialized equation is solved to get a continuous level set function and a smooth interface:

$$\frac{\partial \Phi}{\partial \tau} = \text{sign}(\Phi_0)(1 - |\nabla \Phi|) \quad (\text{A.8})$$

Here  $\tau = 0.1\Delta X$  is the iteration time step of  $\Phi$  and the sign function denotes:

$$\text{sign}(\Phi) = \begin{cases} 1 & \Phi > 0, \text{ water} \\ 0 & \Phi = 0, \text{ interface} \\ -1 & \Phi < 0, \text{ oil} \end{cases} \quad (\text{A.9})$$

Then the surface tension force is calculated as:

$$\vec{F}_\sigma = \sigma \kappa(\Phi) \delta_\phi \nabla(\Phi) \quad (\text{A.10})$$

Here  $\sigma$  is the surface tension coefficient and  $\delta_\phi$  is the delta function:

$$\delta_\phi = \begin{cases} \frac{1}{2\varepsilon} \left( 1 + \cos\left(\frac{\pi\Phi}{\varepsilon}\right) \right) & \text{for } |\Phi| < \varepsilon \\ 0 & \text{elsewhere} \end{cases} \quad (\text{A.11})$$

The quantity  $\varepsilon$  is the interface thickness coefficient (see Yamamoto et al. [10]) and  $\kappa(\Phi)$  is the interface curvature:

$$\kappa(\Phi) = -\nabla \cdot (\vec{n}_c \cdot \vec{S}_f) \quad (\text{A.12})$$

$$\vec{n}_c = \frac{(\nabla \Phi)_f}{|(\nabla \Phi)_f|} \quad (\text{A.13})$$

Here  $\vec{n}_c$  is the surface unit normal vector and  $\vec{S}_f$  is the surface vector of the cell face. The contact angle  $\theta$  between the interface and the pipe wall is defined as:

$$\cos(\theta) = \vec{n}_c \cdot \vec{n}_w \quad (\text{A.14})$$

With  $\vec{n}_w$  being the unit normal vector at the wall. The contact angle is set to  $90^\circ$  in our simulations.

### A.2.2.2. Simulation set-up and mesh verification

A perfect core-annular flow (which means that the oil core is cylindrical and concentric) is set as an initial condition. The well-known analytical (laminar) velocity profile (see e.g. Li & Renardy, 1999) is set for the whole flow domain.

The pressure drop in the flow direction is added as an extra body force term to the right-hand side of Equation A.2, with periodic boundary conditions on the left and right side of the pipe. For the 2D two-phase simulations, the value of the pressure drop is directly imposed. For the 3D single-phase simulations, the simpleFoam solver from OpenFOAM is modified so that the pressure drop can be calculated from the force balance:

$$-\frac{dp}{dz}A = \bar{\tau}_w S \quad (\text{A.15})$$

Here  $A = \pi R^2$  is the cross sectional area of the pipe,  $S = 2\pi R$  is the perimeter of the pipe, and  $\bar{\tau}_w$  is space-averaged wall shear stress. Equation A.15 guarantees that the single-phase solver can well represent the two-phase flow. The comparison of the single-phase solver with the two-phase solver is illustrated in detail by Li et al. (2022). Under the imposed pressure drop, the flow will develop until a stable final state is obtained.

Besides the CLSVOF solver for the interface tracking as discussed in the previous section, the low-Reynolds number  $k-\varepsilon$  model of Launder Sharma is used to represent the turbulence. The numerical discretisation scheme is: backward Euler in time, the limited linear scheme for the advection of the interface, the Van Leer scheme for the advection of the velocity, and the first-order upwind scheme for the advection of the turbulent properties  $k$  and  $\varepsilon$ . We have used the symmetric PBiCG solver for the velocity and for the turbulent quantities, the GAME solver for the pressure, and the PIMPLE solver for the velocity-pressure coupling. The numerical time step is controlled by the maximum value of the Courant number and by the interface Courant number, which are both set to 0.01. The gravitational acceleration is set perpendicularly to the main flow direction.

The simulation conditions were the same as in the experiments by Van Duin et al. (2017). The pipe radius is  $R=10.5$  mm. The length of the pipe section is set to 25.6 mm, which is twice the most dominant wavelength, as estimated from a linear instability analysis by Beerens et al. (2014). The fluid properties are set as follows: the oil and water kinematic viscosity are  $7.73 \times 10^{-4}$  m<sup>2</sup>/s and  $6.7 \times 10^{-7}$  m<sup>2</sup>/s, the oil and water densities are 902 kg/m<sup>3</sup> and 993 kg/m<sup>3</sup>, and the interfacial tension between oil and water is 0.016 N/m (Shell oil Morlina S2 B 680 at 40 °C was used in the experiments). Note that the ratio between the kinematic viscosities of oil and water is 1150.

To verify the numerical accuracy of the simulation results, one case with fixed total flow rate 0.43 L/s (0.00043 m<sup>3</sup>/s) and a prescribed water holdup fraction of 0.26 was simulated with various mesh resolutions. A stretch function is used in the radial direction, the stretch function will make the mesh smooth (which improves the numerical accuracy and increases the simulation speed):

$$\frac{r_j}{r_{j\max}} = 1 + \frac{\tanh[\alpha_1(j/j\max - 1)/2]}{\tanh(\alpha_1/2)}, \quad j = 0, 1, \dots, j\max \quad (\text{A.16})$$

Where  $j\max$  is the total number of mesh points and  $r_j$  is the coordinate of the  $j^{\text{th}}$  node. A proper value of  $\alpha_1$  is used to ensure that sufficient grid points are in the viscous sublayer ( $y^+ < 5$ ) both near the pipe wall and near the interface. In streamwise direction, a uniform mesh is used. An example of the mesh distribution is shown in Figure A.1.

Four mesh resolutions were tested, they are:  $50 \times 50$ ,  $100 \times 100$ ,  $200 \times 200$ ,  $400 \times 400$  number of grid points in streamwise  $\times$  radial directions. Transient simulations were carried out and if a stable state



was reached, the flow rate and velocity profiles were determined by averaging the results over a sufficiently long time. Table A.1 gives the pressure drop, averaged watercut and averaged wave amplitude for the four simulations. It can be seen that the accurate prediction of wave requires a fine numerical mesh. Even on the finest meshes, the pressure drop still shows some mesh dependence: from 814 Pa/m on the  $100 \times 100$  mesh to 748 Pa/m for the  $400 \times 400$  mesh.

Figure A.2 shows the averaged velocity profile and volume fraction. Since the total flow rate is fixed, the averaged velocity profile indicates the apparent slip effect between the oil and water. The volume fraction represents the distribution of the two fluids and the interface. The volume fraction is 1 when there is always water passing by, and the volume fraction is 0 when there is always oil passing by. The volume fraction is in between 0 to 1 when the interfacial waves are passing by. The curves on  $200 \times 200$  and  $400 \times 400$  meshes almost coincide, which confirms the good numerical accuracy of the simulation results. The other 2D simulations, as presented in the next sections, were obtained on the  $200 \times 200$  mesh, as this provides accurate results and at the same time is not using excessive computer power.

**Table A.1. Verification of numerical accuracy (total flow rate 0.43 L/s and water holdup fraction set to 0.26).**

Number of mesh points: streamwise $\times$ radial	Pressure drop (Pa/m)	Average watercut	Wave amplitude (mm)
50 $\times$ 50	772	20.8%	0.37
100 $\times$ 100	814	21.4%	0.60
200 $\times$ 200	818	21.9%	0.71
400 $\times$ 400	748	22.2%	0.73

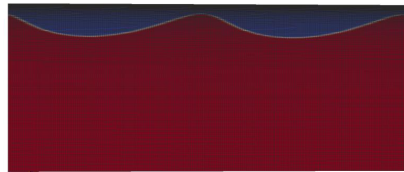


**Figure A.1. Example of the mesh distribution with travelling waves at the oil-water interface,  $200 \times 200$  mesh.**

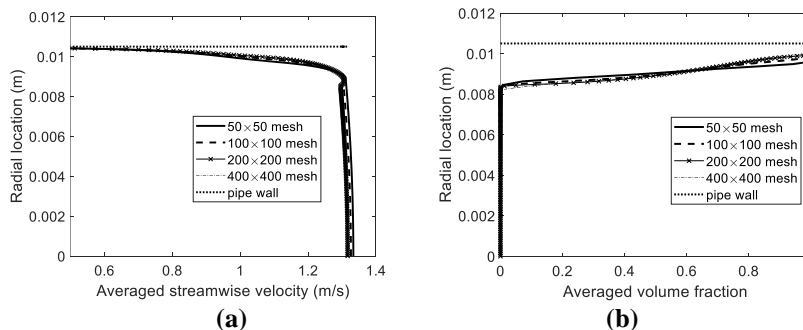


**Figure A.2. Comparison of averaged profiles with various mesh sizes; (a) streamwise velocity, (b) volume fraction. The total flow rate is 0.43 L/s and the total water holdup fraction set to 0.26.**

## A.3 Results

### A.3.1. Comparison of numerical, modelling and experimental results

In this section, the 2D numerical results are compared with both the modelling and experimental results. The physical model was developed by Ullmann & Brauner (2004) and the experiments were obtained by Van Duin et al. (2017). The relationship between four hydraulic parameters are studied: the oil flow rate  $Q_o$ , the watercut  $\varepsilon_w$ , the pressure drop and the water holdup fraction. The watercut is defined as the ratio of the water volumetric flow rate and the total volumetric flow rate:  $\varepsilon_w = Q_w / (Q_o + Q_w)$ . The water holdup fraction is defined as the ratio of the in-situ water volume in the pipe and the total volume of oil and water:  $\alpha_w = V_w / (V_w + V_o)$ . A related parameter is the holdup ratio  $h$ , which is an indicator for the slip between oil and water:

$$h = \frac{Q_o / Q_w}{V_o / V_w} \quad (\text{A.17})$$

(Note that  $h=1$  if there is no slip between the bulk oil and water velocities).

The results obtained with the physical model of Ullmann & Brauner (2004) are shown in Table A.2 and in Figure A.4. In that model, first the water holdup fraction is calculated, based on the input values for the oil and water flow rates:

$$\alpha_w = \frac{V_w}{V_w + V_o} = \frac{c_i/2 - \chi^2(Q_o/Q_w)/F_i + c_i/2\sqrt{1 + 4\chi^2(Q_o/(Q_w c_i))^2}/F_i}{c_i + Q_o/Q_w - \chi^2(Q_o/Q_w)/F_i} \quad (\text{A.18})$$

Where  $\chi^2$  is defined as:

$$\chi^2 = \frac{c_w}{c_o} \frac{Re_{ws}^{-n_a}}{Re_{os}^{-n_c}} \frac{\rho_w}{\rho_o} \left( \left| \frac{Q_o}{Q_w} \right| \frac{Q_o}{Q_w} \right)^{-1} \quad (\text{A.19})$$

Here  $Re_{ws}$  and  $Re_{os}$  are the Reynolds numbers, based on the superficial water velocity and the superficial oil velocity, respectively:

$$Re_{ws} = 4Q_w / (\pi D v_w) \quad \text{and} \quad Re_{os} = 4Q_o / (\pi D v_o) \quad (\text{A.20})$$

The coefficient  $c_i$  in Equation A.19 is the ratio of the approximation of the interfacial velocity and the average velocity in the water annulus, and its value is set to 1.16 (assuming a turbulent water annulus), whereas  $n_a = n_c = 0.2$  (as recommended by Ullmann & Brauner, 2004). The coefficient  $c_o$  is the friction factor in the oil core, and its value is set to 16 (assuming a laminar oil core). The coefficient  $c_w$  is the wall friction factor for the water annulus; its value is 0.046 in the turbulent case (as taken from the Blasius friction correlation for single phase turbulent pipe flow).  $F_i$  is a modification factor due to the apparent roughness of the interface; in oil-water core-annular flow, the interface is less rough (due to the relatively low amplitude of the waves) and this effect can thus be neglected (its value is set to 1, see Ullmann and Brauner, 2004). The pressure drop is calculated by:

$$dp/dp_{oil} = \chi^2 / \alpha_w^2 \quad (\text{A.21})$$

Here  $dp_{oil}/dz = -(128v_o\rho_o Q_o)/(\pi D^4)$  is the pressure drop when the pipe transports single-phase oil with the flow rate  $Q_o$  (and  $z$  is the streamwise pipe coordinate). In this model, the oil core is assumed to be wavy and concentric (eccentricity is thus not accounted for in this model).

The pressure drop for the water only pipe flow with the same total flow rate is also shown in Table A.2. As found by Li et al. (2022), the friction factor of core-annular flow at higher watercut is close to the single-phase water flow under the same total flow rate. To calculate the Fanning friction factor of single phase water pipe flow, the Blasius equation can be used:  $f_w = \frac{0.046}{Re_w^{0.2}}$ . Where the Reynolds

number is defined as:  $Re_w = \frac{\rho_w D u_m}{\mu_w}$ . As the shear stress is  $\tau_w = \frac{1}{2} \rho_w f_w u_w^2$ , the pressure drop is found from  $-\frac{dp}{dz} = 2\tau_w/R$ . The mixture velocity is defined as  $u_m = (Q_o + Q_o)/A$ , with  $A = \pi R^2$ .

Table A.2 compares the pressure drop and water holdup fraction results from the RANS-CFD simulations, the physical model, and the experiments at three conditions. The water holdup fractions from the Ullmann & Brauner model agree well with the RANS-CFD simulation results, but the model predicts a higher pressure drop than the RANS-CFD results. With increased watercut, this deviation becomes smaller. The water only pipe flow correlation (which is known to very accurate) gives a lower pressure drop than the core-annular flow results, but the deviation becomes smaller with increased watercut. The deviation between the RANS-CFD prediction and the Delft experiment by Van Duin et al. (2017) is larger, especially at larger watercuts, namely an under prediction of up to 23% at the watercut of 20%.

As shown in Figure A.3, the flow visualization of the experiments and the RANS-CFD simulations are quite similar. The interfacial waves become shorter with a smaller amplitude when the watercut is decreased.

To obtain the correlation map of the four hydraulic parameters, multiple simulations were performed. In each simulation, a certain value of the pressure drop and of the water holdup fraction was prescribed, and the oil and water flow rates (and herewith the watercut) followed as output values from the simulation. Note that the LSVOF method preserves the water and oil volumes, which means that (together with the periodic boundary conditions) the initially imposed water holdup fraction at time zero is preserved over the transient simulation. The simulation results are shown as the coloured symbols in Figure A.4. The symbols represent 5 different pressure drops, and there are several points for each pressure drop, which represent different water holdup fractions. A lower water holdup fraction corresponds to a lower watercut. The water holdup fractions for each pressure drop in Figure A.4 from left to right are: 750 Pa/m: 0.05, 0.125, 0.15, 0.2, 0.26; 900 Pa/m: 0.1, 0.13, 0.15, 0.16, 0.2, 0.23; 1100 Pa/m: 0.1, 0.13, 0.14, 0.16, 0.2, 0.21, 0.23; 1300 Pa/m: 0.1, 0.13, 0.14, 0.15, 0.2, 0.21, 0.24; 1500 Pa/m: 0.1, 0.13, 0.14, 0.21, 0.23, 0.24. Among all the cases, the water layer stays turbulent while the oil core stay laminar, except for one laminar-laminar case (shown as open triangle in the figure) at pressure drop 750 Pa/m and watercut 3%. The figure also includes the experimental results (shown as the black squares). The measured pressure drops from left to right are: 725 Pa/m, 828 Pa/m, 906 Pa/m and 1122 Pa/m.

**Table A.2. Comparison of the RANS-CFD modelling results with 3 experimental cases.**

Oil flow rate: 0.00035 m <sup>3</sup> /s		Exp. Van Duin et al.	RANS CFD	Ullmann & Brauner Model	Water only pipe flow
Watercut: 9%	Pressure drop (Pa/m)	725	644	665	663
	Water holdup fraction		0.125	0.1	
Watercut: 12%	Pressure drop (Pa/m)	828	670	799	704
	Water holdup fraction	-	0.16	0.14	

Watercut: 15%	Pressure drop (Pa/m)	906	720	822	750
	Water holdup fraction	-	0.20	0.17	
Watercut: ~20%	Pressure drop (Pa/m)	1120	748	881	836
	Water holdup fraction	-	0.26	0.23	

For a fixed pressure drop in the Ullmann & Brauner model, the total flow rate decreases monotonically with decreasing watercut. Comparison of the total flow rate in Figure 8.4a shows that a certain pressure drop level in the RANS-CFD simulations a slightly higher total flow rate than the physical model. The data from Figure A.4a are re-plotted in Figure A.4b, now showing only the oil flow rate (instead of the total flow rate) on the vertical axis. It is found that for the same value of the pressure drop, when decreasing the watercut, the oil flow rate first increases and then decreases. A peak value for the oil flow rate exists at a watercut of around 0.08 in model of Ullmann & Brauner: this is where the lubrication effect of the water annulus on the oil flow is maximum. As shown in detail in Figure A.5 for a fixed pressure drop of 750 Pa/m, for the RANS-CFD simulations the peak occurs at a watercut of about 5%. Both the oil flow rate and the superficial oil flow rate are shown (the latter being the oil flow rate divided by the pipe cross sectional area). At the mentioned low watercut, the water annulus has been fully relaminarized, and the amplitude of the interfacial waves has become very small. Figure A.5 also includes the analytical solution for perfect core annular flow (PCAF; laminar oil core, laminar water annulus, no interfacial waves). The 2D RANS approaches PCAF, giving a decreasing oil flow rate, when the watercut vanishes.

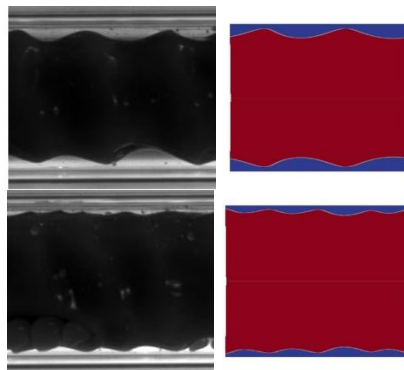


**Figure A.3.** Flow visualization of (left) experiment in horizontal pipe (2017) and (right) 2D simulation. Top graphs have 20% watercut and bottom graphs 12% watercut.

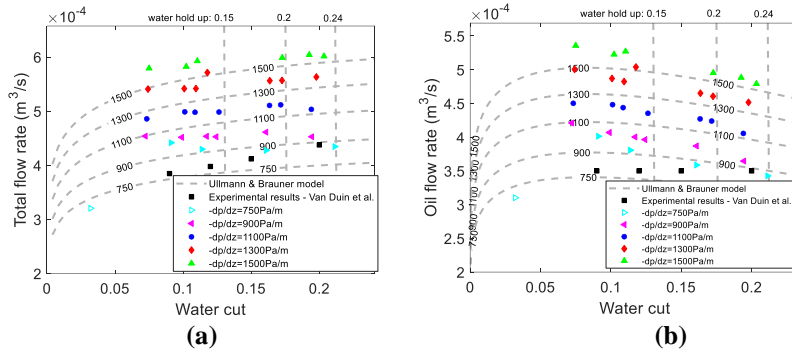


**Figure A.4. Relation between the total flow rate, watercut, pressure drop and water holdup fraction; (a) total flow rate, (b) oil flow rate.**

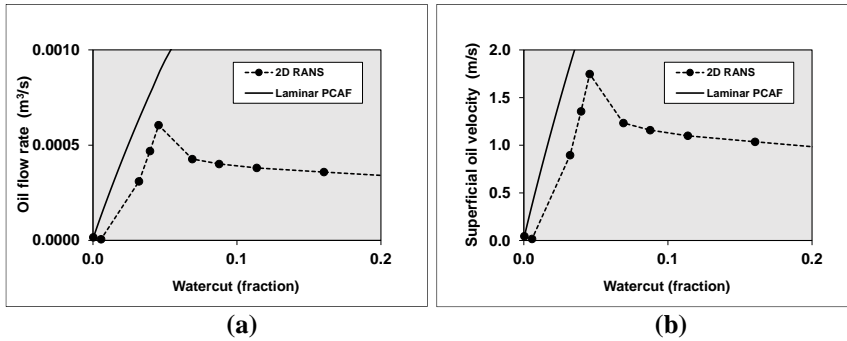


**Figure A.5. Comparison of RANS-CFD with the analytical solution for perfect core-annular flow at low watercut for a fixed pressure drop of 750 Pa/m; (a) oil flow rate, (b) superficial oil velocity.**

The holdup ratio, as defined in Equation (A.17), is shown for the RANS-CFD simulations in Figure A.6a. It is found that the numerical holdup ratio decreases with increasing watercut. This is because the wave amplitude is higher at higher watercut; the wave trough transports a certain amount of water together with the oil core flow. In this way, the water flow rate is locally enhanced and the slip effect between oil and water becomes smaller. When the water flow is in the turbulent region, the values of the holdup ratio are close to the value of 1.39 found in the experiments by Bai et al. (1996). The model of Ullmann & Brauner (2004) gives a smaller value of 1.16 (which is in fact the parameter  $c_i$  in the model). For the laminar-laminar flow condition (pressure drop 750 Pa/m, watercut 3%), the holdup ratio is much higher (near 1.6). Figure A.6b shows RANS-CFD results for the maximum turbulent viscosity in the water annulus. As expected, the water annulus becomes more turbulent for increasing watercut and pressure drop. Figure A.6c shows the Fanning friction factor from the numerical, modelling and experimental results. The Fanning friction factor is the dimensionless representation of the pressure drop:  $f_w = -\left(\frac{dp}{dz}\right) \frac{R}{\rho_w V_m^2}$  (in which  $V_m$  is the mixture velocity). Except for the condition with a laminar water annulus at very low watercut, the Fanning friction factor is almost independent of the pressure gradient and watercut. This is true for both the Ullmann & Brauner model and the RANS-CFD simulations. Figure A.6c also shows that the value of the Fanning friction factor with RANS-CFD and with the physical model is lower than the experimental results by Duin et al. (2017).

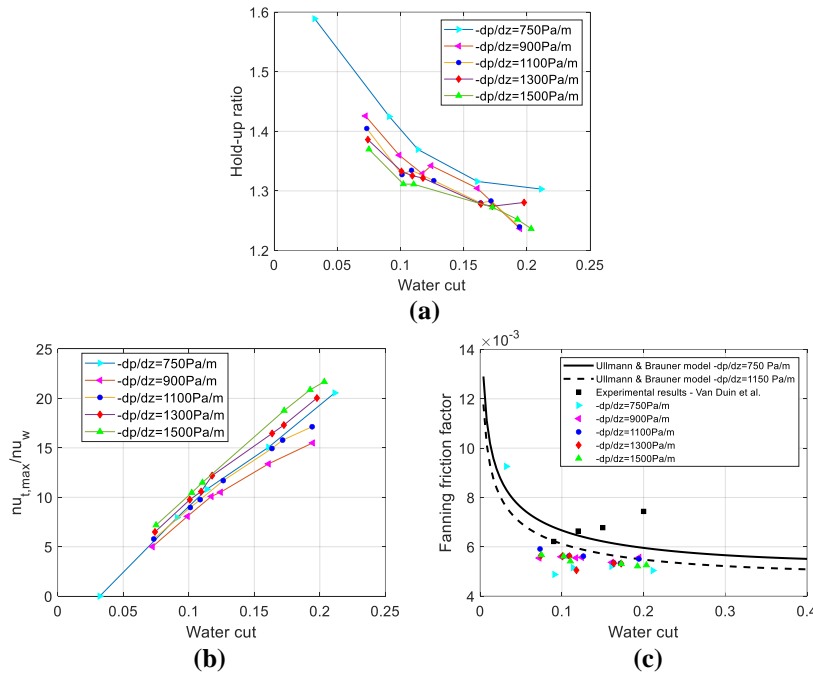


**Figure A.6. RANS-CFD results for different watercut values and pressure drop level; (a) holdup ratio, (b) averaged maximum turbulent viscosity (non-dimensionalized with the water viscosity), (c) Fanning friction factor.**

### A.3.2. 3D single-phase RANS simulation

In the 3D single-phase simulations, only the water annulus is simulated. The oil core is assumed to be solid and its presence is modelled as an imposed wavy inner wall in the simulation model. The other wall is the pipe wall. The simulation is carried out in a reference frame with respect to the travelling interface waves; thereto the pipe wall is moving with a prescribed velocity, that has the negative value of the wave velocity, and the wavy interface is not moving. In the RANS simulation, the flow is almost steady state in this reference frame.

Several 3D single-phase RANS simulations are performed to investigate the effect of an eccentric core and explain the levitation mechanism of the oil core. In the 3D single-phase model, the water holdup fraction and the total flow rate are the pre-set parameters, while the pressure drop and watercut are the outcomes from the simulation. To obtain a total flow rate of 0.43 L/s and a watercut of 20%, the water holdup fraction had to be set to 0.24 and the interface wave velocity to 1.3 m/s. In the single-phase approach, the deformation of wave is ignored and steady state simulation is performed. The interface waves have a prescribed amplitude of 0.71 mm and wave length 12.8 mm (based on the 2D two-phase simulation results).

To create an eccentric oil core in the single-phase simulation, the imposed interface with waves was moved in the direction of the pipe top. If the (average) water layer thickness at the top and bottom are denoted as  $d_{top}$  and  $d_{bottom}$ , respectively, the eccentricity is defined as  $e = \frac{d_{bottom} - d_{top}}{d_{bottom} + d_{top}}$ . Thus  $e = 0$  for a concentric oil core, and  $e = 1$  for a fully eccentric oil core. The mesh has  $100 \times 200 \times 160$  points in streamwise-radial-circumferential direction.

The simplified 3D geometry for core-annular flow makes it possible to study the dynamic force on the oil core in a horizontal pipe in detail. The reduced pressure and shear stresses are integrated along

the oil-water wavy interface to obtain the pressure force and shear force. Reduced pressure means that the pressure has been corrected for the water hydrostatic head. Figure A.7 shows these forces as a function of eccentricity. The values are non-dimensionalized with the water density  $\rho_w$ , and the oil core velocity  $U_o$  (which is 1.3 m/s) and the averaged water layer thickness  $d$ . It is found that with increased eccentricity, the vertical forces are acting downward: both the reduced pressure force and the shear force. These forces will balance the upward buoyancy force of the oil core in a horizontal pipe. The vertical force increases with an increasing eccentricity, though it decreases at an eccentricity of 0.31; actually, at this point, we found that relaminarization occurred in the top layer. While further increasing the eccentricity the vertical force increased again. This indicates that when the density difference between oil and water is high, a higher eccentricity will be required to balance the buoyancy force.

In the horizontal direction, both the pressure force and shear force (working on the wavy surface of the oil core) are acting in the opposite direction of the main flow. These forces will balance the induced pressure drop in the streamwise direction. The horizontal force does not change much with increased eccentricity, which means that the pressure drop working on the cross section of the oil core also does not change much. The pressure drop only decreases slightly when there is re-laminarization in the top layer, i.e. eccentricity is higher than 0.31.

From Figure A.7 it is clear that the pressure force on the core surface is dominant in both the vertical and horizontal directions. Since the pressure force for perfect core-annular flow (no waves) is zero, the presence of interfacial waves significantly re-distributes the pressure, and dominates the flow physics. The pressure distribution along the core surface in the flow direction is shown in Figure A.8. The increased eccentricity significantly re-distributes the pressure at the top wave, while at the bottom wave, almost no difference is found.

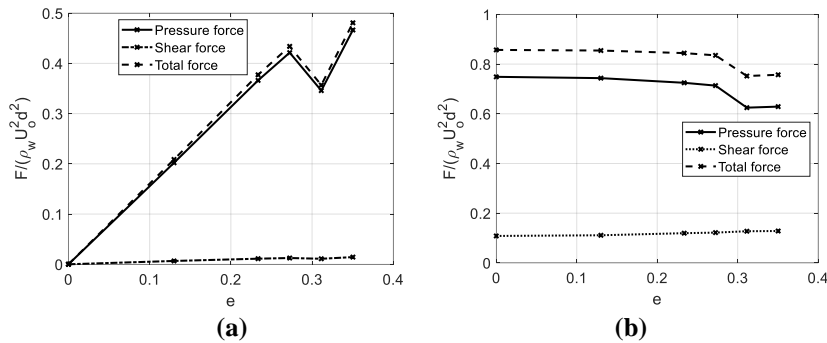


**Figure A.7. Forces on the wave surface of the eccentric oil core; (a) vertical force , (b) horizontal force.**

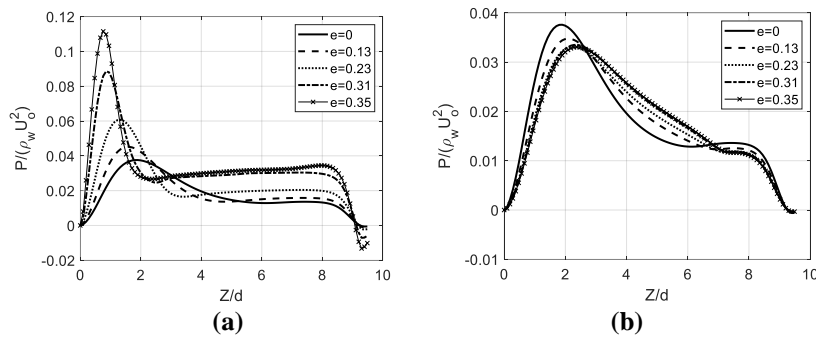


**Figure A.8.** Reduced pressure distribution in streamwise direction along the wave surface of the oil core; (a) bottom, (b) top.

### A.3.3. Comparison of DNS/RANS

According to Table A.1, there is a noticeable difference between the RANS predictions for the pressure drop and the experimental values. This can either be due to an inaccuracy in the measurements, or an inaccuracy in the RANS model. To investigate the latter, single-phase DNS were performed. The flow geometry in the DNS is the same as the one used for the 3D, single-phase RANS, but eccentricity was not considered. The considered flow conditions are: total flow rate of 0.43 L/s, water holdup of 0.24, eccentricity  $e=0$  (imposed interface wave velocity is 1.3 m/s). The mesh is refined so that flow structure on the Kolmogorov length scale can be represented. There are  $225 \times 150 \times 680$  points in the streamwise, radial, and circumferential directions. This mesh resolution is close to the mesh used by Eggels (1994) for turbulent single-phase pipe flow. We have verified that the DNS results are almost mesh independent.

To study the performance of RANS model, different RANS model are tested and the results are compared with the DNS result. The tested RANS models are: low-Re  $k - \varepsilon$ ,  $k - \omega$ , and  $k - \omega$  SST turbulent model. As shown in Table A.3, the DNS result indeed gives a larger pressure drop, which makes the deviation between numerical and experimental values smaller. The  $k - \omega$  and  $k - \omega$  SST models give an even lower pressure drop than the low-Re  $k - \varepsilon$  model, which can be linked to the under-estimation of the kinetic energy. The watercut is less sensitive to the applied turbulence model.

**Table A.3.** Comparison of the DNS/RANS result with the oil flow rate 0.35 L/s and water holdup 0.24;  $k^+ = k/u_\tau^2$  and  $-\overline{vw}^+ = k - \overline{vw}/u_\tau^2$ , in which  $u_\tau = \sqrt{\tau_w/\rho_w}$  is the wall shear velocity and  $\tau_w$  is the wall shear stress.

	DNS	Low-Re $k - \varepsilon$	$k - \omega$	$k - \omega$ SST
Pressure drop	899 Pa/m	783 Pa/m	730 Pa/m	689 Pa/m
Watercut	20%	20%	20%	20%
Max. $k^+$	5.54	4.93	3.91	3.77
Max. $-\overline{vw}^+$	1.22	1.51	1.24	1.16



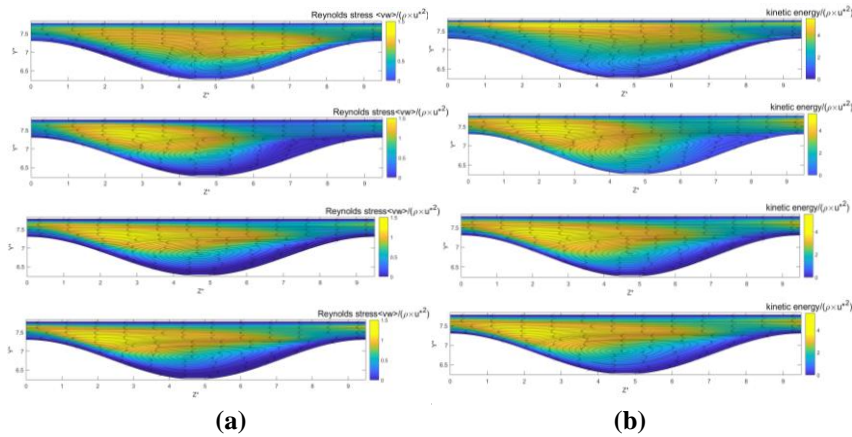


**Figure A.9. Averaged single-phase results for the water annulus, (a) the Reynolds stress, and (b) the turbulent kinetic energy. The streamlines are also shown. From top to bottom: DNS, low-Re  $k - \varepsilon$ ,  $k - \omega$  and  $k - \omega$  SST.**

Contour plots of the kinetic energy and Reynolds stress together with the streamlines are shown in Figure A.9. To obtain the 2D averaged plane, the DNS results are averaged over time and in the circumferential direction. DNS gives a smaller recirculation zone in the wave trough than RANS. Also, DNS gives lower Reynolds stress at the reattachment location than the RANS models. In DNS a higher Reynolds stress exists at the right hand side of the wave trough in the figure, which is the flow separation point, while RANS results all have a higher Reynolds stress at the flow re-attachment point. RANS with low Re  $k - \varepsilon$  results are closest to DNS. The low Re  $k - \varepsilon$  model has the largest tendency to relaminarize. This can be seen near the separation point (left graph in the second row in Figure A.9), where the Reynolds stress is close to zero.

## A.4 conclusions

2D and 3D numerical simulations were performed with OpenFOAM for core-annular flow with a turbulent water annulus. For the 2D two-phase simulations, the Coupled Level Set and Volume of Fluid (CLSVOF) method was used for the interface tracking, and RANS with the low-Reynolds number  $k - \varepsilon$  model for the turbulence. For the 3D single-phase simulations, the highly viscous oil core is assumed to be solid, and the single phase solver is modified to make it satisfy the force balance for core-annular flow. The number of mesh points in the CFD simulations was verified to be sufficiently high to give a good numerical accuracy of the results.

The results of the RANS simulations were compared with the physical model developed by Ullmann & Brauner (2004), with the water only pipe flow case and with the lab experiments by Van Duin et al. (2017). The numerical results for the pressure drop (for a given total flow rate and watercut) are lower than for the Ullmann & Brauner model and higher than for the case with water-only pipe flow. The agreement is better at higher watercuts. The water holdup fractions predicted by the Ullmann & Brauner model are quite close to the RANS results. The deviation between the RANS results and the experiments is larger, namely an under prediction of the pressure drop by up to 23% at the higher watercut of 20%. Multiple 2D two-phase simulations are performed to obtain the correlation map of the four hydraulic parameters: total flow rate, watercut, pressure drop and water holdup. It is found that for the same value of the pressure drop in the Ullmann & Brauner model, when decreasing the watercut, the total flow rate decreases. The oil flow rate first increases to reach a maximum and then decreases. At the peak value with a watercut of 8% the lubrication effect of the water annulus on the oil flow is maximum. The RANS results follow a fairly similar trend, and have a peak value for the oil flow rate at a watercut of about 5%. For lower watercut values the water annulus becomes laminar and the interfacial waves disappear, approaching perfect-core annular flow (for which an analytical

solution exists). When the Fanning friction factor is used to represent the pressure drop and flow rate, it turns out that its value is almost independent of the pressure drop level and of the watercut, unless the watercut becomes too small.

3D single-phase simulations were performed to study the forces on the oil core. It is found that increasing eccentricity of the oil core to the top of a horizontal pipe will introduce an increased downward force on the oil core. The force primarily comes from the pressure re-distribution in the top layer. Pressure dominates the flow physics both in the vertical direction and in the horizontal direction. 3D single-phase DNS were performed for comparison with the RANS model. It is found that the DNS simulation gives a higher pressure drop than the RANS prediction. This partly repairs the deviation found in RANS with the Delft experiment. Results from the low Reynolds  $k - \epsilon$  RANS are the closest to the DNS results, while the  $k - \omega$  model and  $k - \omega$  SST model underestimate the kinetic energy, and also further underestimate the pressure drop.

## References

- Arney, M.S., Bai, R., Guevara, E., Joseph, D.D., and Liu, K., 1993. Friction factor and holdup studies for lubricated pipelining - I. Experiments and correlations. *International Journal of Multiphase Flow* 19, 1061-1076.
- Bai, R., Kelkar, K., and Joseph, D.D., 1996. Direct simulation of interfacial waves in a high-viscosity-ratio and axisymmetric core-annular flow", *Journal of Fluid Mechanics* 327, 1-34.
- Beerens, J.C., Ooms, G., Pourquié, M.J.B.M., and Westerweel, J., 2014. A comparison between numerical predictions and theoretical and experimental results for laminar core-annular flow. *AIChE Journal* 60, 3046-3056.
- Eggels, J. G. M., 1994. Direct and large eddy simulation of turbulent flow in a cylindrical pipe geometry. PhD Thesis, Delft University of Technology.
- Joseph, D.D., Bai, R., Chen, K.P., Renardy, Y.Y., 1997. Core-annular flows. *Annual Review of Fluid Mechanics* 29, 65-90.
- Kim, K. and Choi, H., 2018. Direct numerical simulation of a turbulent core-annular flow with water-lubricated high viscosity oil in a vertical pipe. *Journal of Fluid Mechanics* 849, 419-447, 2018.
- Li, H., Pourquié, M. J. B. M., Ooms, G., Henkes, R. A. W. M., 2021. Simulation of turbulent horizontal oil-water core-annular flow with a low-Reynolds number  $k-\epsilon$  model. *International Journal of Multiphase Flow*, 142, 103744.
- Li, H., Pourquié, M. J. B. M., Ooms, G., Henkes, R. A. W. M., 2022. Simulation of a turbulent annulus with interfacial waves in core-annular pipe flow", *International Journal of Multiphase Flow*, 104152.
- Li, J. and Renardy, Y., 1999. Direct simulation of unsteady axisymmetric core-annular flow with high viscosity ratio. *Journal of Fluid Mechanics* 391, 123-149.
- Ooms, G., Segal, A., Van der Wees, A.J., Meerhoff, R., and Oliemans, R.V.A., 1984. A theoretical model for core-annular flow of a very viscous oil core and a water annulus through a horizontal pipe. *International Journal of Multiphase Flow* 10, 41-60.
- Ooms, G., Pourquié, M.J.B.M., and Beerens, J.C., 2013. On the levitation force in horizontal core-annular flow with a large viscosity ratio and small density ratio. *Physics of Fluids* 25, 032102.
- Tripathi, S., Tabor, R.F., Singh, R., and Bhattacharya, A., 2017. Characterization of interfacial waves and pressure drop in horizontal oil-water core-annular flows. *Physics of Fluids* 29, 082109.
- Ullmann, A. and Brauner, N., 2004. Closure relations for the shear stress in two-fluid models for core-annular flow. *Multiphase Science and Technology* 16.4, 355-387.
- Van Duin, E., Henkes, R., & Ooms, G., 2019. Influence of oil viscosity on oil-water core-annular flow through a horizontal pipe. *Petroleum*, 5(2), 199-205.
- Yamamoto, T., Okano, Y., and Dost, S., 2017. Validation of the S-CLSVOF method with the density scaled balanced continuum surface force model in multiphase systems coupled with

---

thermocapillary flows. *International Journal for Numerical Methods in Fluids* 83, 223-244.



---

# Acknowledgements

The journey of pursuing my PhD is an exceptional one and has been an invaluable experience for me. During this period I learnt how to conduct research as a junior researcher and I gained experience working on challenging scientific topics. Besides, I got good memories with people whom I worked with. I would like to show my gratitude to many people who have supported me during the PhD study.

I would like to express my utmost gratitude to my promoter Prof. Ruud Henkes who gave me the chance to work on this excellent topic: core-annular flow. The simulation of multiphase flow and turbulence came with significant challenges, but your encouragement was the source of my motivation. You helped me a lot during my PhD: from suggestions on the research direction, to the analysis of the data, to the draft paper editing. I enjoyed the insightful discussions during our weekly meetings. I am greatly influenced by and impressed by the way you work. I learned from your critical and rigorous scientific attitude and I appreciate your high efficiency of working.

I want to thank my daily supervisor Dr. Mathieu Pourquoié. You gave me strong support with the CFD simulations, and the use of OpenFOAM. You always provided very helpful suggestions whenever I had problems. I learned a lot from you about CFD simulation of multiphase flow and of turbulence. You are always dedicated to the problems and eager to share your knowledge with me. Thanks also for your help in the CPU hour application on the SurfSara cluster. I like your sense of humour and I enjoy talking with you.

I want to thank my supervisor Prof. Gijs Ooms. You have a rich experience in core-annular flow, and you helped me to understand the basic physics of core-annular flow. Your articles have been important references throughout my PhD period. Your fancy ideas in research inspired me a lot and you are always so kind to encourage me in my work which strengthened my confidence.

No words can adequately describe my thanks for the past years of support and assistance from this core team, for which I feel very fortunate to have had the opportunity to work with. My lifelong memory will be of this incredible experience.

It also has been a pleasure for me to collaborate with others on the interesting topic of core-annular flow. Thank you Daan Vrijlandt. The experimental data obtained in your Master project are a valuable source for comparison with the numerical results. Thank you Kevan Ketanbhai Parikh for your Master project contribution to the simulation work in my thesis chapter on vertical core-annular flow. Thank you Fan Jiang for your collaborative work on fouling in core-annular flow.

I want to thank all my colleagues for the pleasant office atmosphere: Junaid Mahmood, Koen Muller, Sowmya Kumar, Teng Dong, Bob Mulder, Jesse Reijtenbagh, Willian Hogendoorn, Gem Rotte, Rens Stigter, Nicola Savelli, Parviz Ghoddoosi Dehnavi, Arnoud Greidanus, John Buchner, Wout Cornel, Amitosh Dash, Udhav Gawandalkar, Yavuz Emre Kamis, Lina Nikolaidou, Luuk Altenburg, Wouter Peerbooms, Tariq Shajahan, Ankur Kislaya, Mike van Meerkerk, Ernst Jan Grift, Melika Gül, etc. Thanks are also due to Dr. Wim-Paul Breugem: I really liked the multiphase flow course, which was very helpful to me. I want to thank my friends in Delft for exploring Chinese food and celebrating Chinese New Year together: Heng Li, Rong Fan, Shilong Fu, Qi An, Mengmeng Zhang, Liangyuan Wei, Pingping Cui, Bin Fang, Wenze Guo, Zac Leong, and An Zhao. Thank you Qi An for sending me the tasty vegetable soup you made and the medicine when I had Covid. I want to thank Ze Chang and Lu Chen for organizing the board games. I appreciate the assistance of Caroline Legierse with the secretarial support.

Finally, I want to thank my parents Wenchao Li and Zhenping Chen, as well as my brother Chuyu Li for their support and concern throughout the years that I have spent away from home due to the epidemic. I hope I will spend more time with you in the future as a compensation. Thanks Yang Chen for your companionship during these years!

Haoyu Li  
Delft, the Netherlands  
August 2023

# Curriculum Vitae

Name : Haoyu Li

Born in Luohe of Henan province, China, 7<sup>th</sup> April 1994

## Education and employment:

2011-2015

Harbin Engineering University

Major: Naval Architecture and Ocean Engineering

Graduation thesis: Simulation of hydrodynamic characteristics of a trimaran

Supervisor: Prof. Shan Ma

2015-2018

Shanghai Jiao Tong University

Major: Fluid Mechanics

Graduation thesis: Simulation of tip-vortex cavitation flow behind hydrofoil

Supervisor: Prof. Benlong Wang

2018-2023

Delft University of Technology

PhD Candidate in Fluid Mechanics

Department: Process and Energy

PhD thesis: Waves and Turbulence in Core-Annular Pipe Flow

Supervisors: Dr. Mathieu Pourquié, Prof. Gijs Ooms

Promotor: Prof. Ruud Henkes

2023-now

ASML, The Netherlands

Lithography system performance engineer





# List of publications

## Main publications

Li, H., Pourquié, M.J.B.M., Ooms, G., & Henkes, R.A.W.M. (2021). Simulation of turbulent horizontal oil-water core-annular flow with a low-Reynolds number  $k-\epsilon$  model. *International Journal of Multiphase Flow* 142, 103744.

Li, H., Pourquié, M.J.B.M., Ooms, G., & Henkes, R. A. W. M. (2022). Simulation of a turbulent annulus with interfacial waves in core-annular pipe flow. *International Journal of Multiphase Flow* 154, 104152.

Li, H., Pourquié, M.J.B.M., Ooms, G., & Henkes, R.A.W.M. (2023). Simulation of vertical core-annular flow with a turbulent annulus. *International Journal of Multiphase Flow* 167, 104551.

Li, H., Pourquié, M.J.B.M., Ooms, G., & Henkes, R.A.W.M. (2023). Turbulence and waves in oil-water pipe flow. *Proceedings of the 20<sup>th</sup> International Conference on Multiphase Production Technology*, Nice, France, 26<sup>th</sup>–28<sup>th</sup> June 2023, pp. 291-305.

Li, H., Pourquié, M.J.B.M., Ooms, G., & Henkes, R.A.W.M. (2023). Wave growth in horizontal core annular flow with turbulent annulus. Submitted for publication.

Li, H., Pourquié, M. J. B. M., Ooms, G., & Henkes, R.A.W M. (2023). DNS and RANS for core-annular flow with a turbulent annulus. Submitted for publication.

## Other publications

Jiang, F., Li, H., Pourquié, M., Ooms, G., & Henkes, R. (2021). Simulation of the hydrodynamics in the onset of fouling for oil-water core-annular flow in a horizontal pipe. *Journal of Petroleum Science and Engineering* 207, 109084.

Xiaoxing Peng, Benglong Wang, Haoyu Li, Lianghao Xu, and Mingtai Song (2017). Generation of abnormal acoustic noise: singing of cavitating tip vortex. *Physical Review Fluids* 2, 053602.

Wang, B.L., Liu, Z.H., Li, H.Y., Wang, Y.Y., Liu, D.C., Zhang, L.X., & Peng, X.X. (2017). On the numerical simulation of vortical cavitating flows around various hydrofoils. *Journal of Hydrodynamics, Ser. B*, 29(6), 926-929.



## **Propositions**

accompanying the dissertation

### **Waves and Turbulence in Core-Annular Pipe Flow**

by

**Haoyu Li**

1. Spurious dispersion of droplets from the viscous core into the less viscous annulus is the major problem in the numerical simulation of core-annular flow; the problem can be mitigated by using a fine and uniform mesh across the liquid-liquid interface. (This thesis, Chapters 2 and 6).
2. The value of the Fanning friction factor for core-annular flow with a turbulent annulus of water is close to the value for water only pipe flow when the friction factor is based on the mixture velocity, the pipe diameter, the water density, and the water viscosity. (This thesis, Chapter 3).
3. Compared with the simulation of core-annular flow with a laminar annulus, interfacial waves in a simulation of core-annular flow with a turbulent annulus grow much faster under the same time scaling; in the latter a stable core-annular flow is obtained more easily because of the turbulence in the annulus. (This thesis, Chapter 4).
4. The need to quickly reduce fossil fuel consumption to save the environment will make future core-annular flow research more delicate. However, from a fundamental fluid mechanics perspective it is intriguing to know how additional research will be able to resolve the deviation found between the simulations (RANS/DNS) and the experiments. (This thesis, Chapter 6).
5. Breakthroughs in a scientific study do normally not happen by accident, but they require a continuous effort, with careful thinking and hard working.
6. Developments in Artificial Intelligence (AI) can enhance our quality of life and increase our society's productivity, but it can also lead to the loss of job opportunities and to more social inequality, similar to what occurred in the industrial revolution.
7. While doing a PhD, having a clear research goal in the first place is more important than producing data. However, the produced data themselves may require to re-formulate the research goal.
8. We often prefer to hear words that we expect to hear, but this will limit the ability to grow.
9. When working from home during COVID-19, a too quiet environment could cause a lower working efficiency; this negative influence was felt even stronger by young people and internationals.
10. The West tends to have a relatively stronger sense of relationship boundaries than the East. This discrepancy may decrease through the ongoing process of cross-cultural interaction.

These propositions are regarded as opposable and defendable, and have been approved as such by the promotor prof. dr. ir. R.A.W.M. Henkes and copromotor dr. M.J.B.M. Pourquié.

